# ANTONIA GRAUERT



# Modulation of GABA$_A$ receptor-mediated synaptic transmission by Zn$^{2+}$ at a dentate gyrus circuit

Thesis submitted in accordance with the requirements of The School of Pharmacy, University of London for the degree of Doctor of Philosophy

## Department of Pharmacology, The School of Pharmacy

## University of London

## June 2012

# PLAGIARISM STATEMENT

This thesis describes research conducted in The School of Pharmacy between March 2009 and March 2012 under the supervision of Dr Arnaud Ruiz. I certify that the research described is original and that any parts of the work that have been conducted by collaboration are clearly indicated. I also certify that I have written all the text herein and have clearly indicated by suitable citation any part of this dissertation that has already appeared in publication.

**Signature:** _____ **Date:** _____

# ACKNOWLEDGEMENTS

First and foremost, I am indebted to Dr. Arnaud Ruiz for the excellent supervision throughout this PhD project. You have given me enormous support and motivation with your positive and enthusiastic nature which made these three years an invaluable experience for me! I am incredibly grateful for having learnt so much from you which I will look back on for future times to come. Thank you!!

I would also like to thank my second supervisor Dr. Jasmina Jovanovic for the support during the PhD. Furthermore, I would like to acknowledge the School of Pharmacy for providing me financial support during the PhD project.

I would like to particularly thank Dr. Dominique Engel for scientific advice, assistance and great collaborative work on the zinc project!

I would like to express my thanks to Dr. Rahima Begum at the Institute of Neurology, who helped me immensely with the Timm's staining. Thanks for your patience and endurance!
Also, I would like to thank Dr. Caroline Le Duigou, who was very helpful in taking time to assist me with the perforated-patch technique.

I would like to thank Dr. Anna Gross for being such a great lab mate. Thanks for all the support and scientific advice on the thesis... and for your companionship in making those uncountable hours patching in the dark lab more enjoyable than they would have otherwise been!

I want to thank my work colleagues at the Department of Pharmacology who I have all at some point sought for help and who have always been friendly and supportive. Huge thanks go to: Joseph, Katiuscia, Sam, Antoine, Agota, Johnny, Nicola, Blanka, Audrey, Karine, Celine, Nazir, Adam, Martin and Dave!
Also, I want to thank my friends Ina, Britta, Sarah, Rita, Inês, Luis, Gary, Bruno and Antonio for all the great memories that I had with you in London!

# ABSTRACT

Zinc (ionic form $Zn^{2+}$) is a common trace element in the forebrain, and is especially enriched in the hippocampus, a brain structure important for learning and memory. A large amount of vesicular $Zn^{2+}$ which is thought to be released upon presynaptic depolarisation is found at synapses formed by the axons of dentate granule cells (GCs), known as mossy fibres (MFs). $Zn^{2+}$ inhibits NMDA and $GABA_A$ receptors (NMDAR and $GABA_A$R) at mono-synaptic inputs between MFs and CA3 pyramidal neurons but its role in synaptic integration in the dentate gyrus remains elusive. Whole-cell recordings were obtained from GCs held in voltage-clamp in acute rat hippocampal slices. One tungsten electrode was positioned in stratum lucidum (SL) of CA3b to activate MFs and another in stratum granulosum (SG) to directly stimulate dentate interneurons. Evoked synaptic currents were blocked by superfusion of the $GABA_A$R antagonist bicuculline implying that they were mediated by $GABA_A$Rs. In contrast, the AMPA/kainate receptor antagonist NBQX abolished SL evoked inhibitory postsynaptic currents (IPSCs) but had little effect on IPSCs evoked by SG stimulation. Similarly, the group 2 metabotropic receptor agonist DCG-IV depressed SL but not SG evoked IPSCs. These results imply a poly-synaptic inhibitory feedback projection from CA3 to the dentate gyrus via recurrent MFs, and a mono-synaptic input from dentate interneurons to GCs. $Zn^{2+}$ reversibly depressed evoked IPSCs whereas superfusion of different $Zn^{2+}$ chelators had the opposite enhancing effect. Blocking T-type $Ca^{2+}$ channels abolished the effect of $Zn^{2+}$ chelators. When recording from dentate basket cells, $Zn^{2+}$ chelation increased spike width, decreased spike threshold, enhanced NMDAR-mediated excitatory postsynaptic currents (EPSCs) and facilitated T–type $Ca^{2+}$ currents. Finally, chelation of $Zn^{2+}$ narrowed the time window for integration of perforant path inputs and facilitated GC spiking. Together, the results demonstrate that $Zn^{2+}$ modulates MF–interneuron–GC communication and thus regulates information transfer to dentate and hippocampal networks.

# CONTENTS

# LIST OF FIGURES

# LIST OF TABLES

# LIST OF ABBREVIATIONS

| | |
|---|---|
| °C | degree Celsius |
| μ +[unit] | micro, factor $10^{-6}$ |
| Ω | Ohm, unit of electrical resistance |
| τ | time membrane constant |
| 4-AP | 4-aminopyridine |
| A | ampere, unit of electrical current |
| ACSF | artificial cerebrospinal fluid |
| AfP | antidromic field potential |
| AHP | after-hyperpolarisation |
| AMPA | $\alpha$-amino-3-hydroxy-5-methyl-4-isoxazolepropionic acid |
| BC | basket cell |
| Ca, $Ca^{2+}$ | calcium, calcium ion |
| CA3/2/1 | cornu ammonis, fields of the hippocampus |
| CA3b | subarea of the CA3 – middle part, nearest to the fimbria/fornix connection |
| CaEDTA | calcium-ethylenediaminetetraacetic acid |
| CI-AMPAR | calcium impermeable-AMPA receptor |
| Cl, $Cl^-$ | chloride, chloride ion |
| CNS | central nervous system |
| CP-AMPAR | calcium permeable-AMPA receptor |
| DIC | differential interference contrast |
| dV/dt | time derivative of the voltage |
| EAAT1/2 | excitatory amino-acid transporter 1/2 |
| $E_{Cl^-}$ | reversal potential for chloride |
| $E_{GABA}$ | reversal potential for GABA |
| EPSCs | excitatory postsynaptic currents |
| EPSPs | excitatory postsynaptic potentials |
| Erk1/2 | extracellular-signal-regulated kinases 1/2 |
| $E_{syn}$ | reversal potential for evoked synaptic current/potential |
| g | gram, unit of weight |

| | |
|---|---|
| G +[unit] | Giga, factor $10^9$ |
| GABA | γ-aminobutyric acid |
| $GABA_AR$ | γ-aminobutyric acid receptor A |
| $GABA_BR$ | γ-aminobutyric acid receptor B |
| GAD67 | glutamate decarboxylase 67 |
| GAT | GABA transporter |
| GC | granule cell |
| GCL | granule cell layer |
| GlyR | glycine receptor |
| h | hour, unit of time |
| $H^+$ | proton |
| HCN channel | hyperpolarisation-activated cyclic nucleotide-gated channel |
| $HCO_3^-$ | bicarbonate |
| HEK cells | human embryonic kidney cells |
| HICAP cells | Hilar Commissural-Associational pathway related cells |
| HIPP cells | Hilar Perforant Path-associated cells |
| Hz | hertz, unit of frequency, number of cycles per second |
| I | current |
| $IC_{50}$ | half-maximal inhibitory concentration |
| $I_h$ | h-current |
| $I_{holding}$ | holding current |
| $I_{max}$ | maximum current |
| IPSCs | Inhibitory postsynaptic currents |
| IPSPs | Inhibitory postsynaptic potentials |
| I-V relationship | current-voltage relationship |
| k +[unit] | kilo, factor $10^3$ |
| K, $K^+$ | potassium, potassium ion |
| KCC2 | Potassium/chloride co-transporter 2 |
| $K_d$ | stability constant of forming a complex |
| L | litre, unit of volume |
| LJP | liquid junction potential |
| LTD | long-term depression |
| LTP | long-term potentiation |

| | |
|---|---|
| m | metre, unit of distance |
| m +[unit] | milli, factor $10^{-3}$ |
| M +[unit] | Mega, factor $10^{6}$ |
| M | Molar (mol/L) |
| MAPK | Mitogen-activated protein kinase |
| MF | mossy fibre |
| MFB | mossy fibre bouton |
| Mg, $Mg^{2+}$ | magnesium, magnesium ion |
| mGluR | metabotropic glutamate receptor |
| min | minute, unit of time |
| ML | molecular layer |
| MOPP cells | Molecular layer Perforant Path-associated cells |
| mRNA | messenger ribonucleic acid |
| mZnR | metabotropic $Zn^{2+}$ sensing receptor |
| n +[unit] | nano, factor $10^{-9}$ |
| N.S. | non-significant, $P > 0.05$ |
| Na, $Na^{+}$ | sodium, sodium ion |
| NMDA | *N*-Methyl-D-aspartic acid |
| $O_2$ | oxygen |
| $O_2/CO_2$ | carbogen |
| *P* | P-value in statistical analysis |
| p +[unit] | pico, factor $10^{-12}$ |
| PBS | phosphate buffered saline |
| PCR | polymerase chain reaction |
| PPR | Paired Pulse Ratio |
| PSC | postsynaptic current |
| psi | pound-force per square inch, unit of pressure |
| $R_N$ | input resistance |
| $R_{ser}$ | series resistance |
| s | second, unit of time |
| SEM | standard error of the mean |
| SG | stratum granulosum |
| SL | stratum lucidum |

| | |
|---|---|
| spPSC | spontaneous postsynaptic current |
| TEA | tetraethylammonium |
| THDOC | tetrahydrodeoxycorticosterone |
| TPEN | N,N,N'N'-tetrakis(-)[2-pyridylmethyl]-ethylenediamine |
| TrkB | Neurotrophic tyrosine kinase receptor type 2 |
| TTX | tetrodotoxin |
| UK | United Kingdom |
| US | United States |
| V | volt, unit of electric potential |
| V | voltage |
| VGCC | voltage-gated $Ca^{2+}$ channel |
| $V_{holding}$ | holding potential |
| $V_m$ | membrane potential |
| $V_{rest}$ | resting membrane potential |
| $V_{thr}$ | voltage threshold |
| ZIP | $Zn^{2+}$ importing proteins |
| Zn, $Zn^{2+}$ | zinc, zinc ion |
| ZnT | $Zn^{2+}$ transporter |

# 1. Introduction

## 1.1. $Zn^{2+}$ IN THE BODY AND BRAIN

### 1.1.1. $Zn^{2+}$ in health and disease

Zinc (ionic form $Zn^{2+}$) was declared an essential nutrient by the Food and Nutrition Board of the US National Academy of Sciences in 1974 (Prasad, 2003), evidently acknowledging the wide range of biological actions of $Zn^{2+}$ in the human body. Although the first manifested symptoms associated with $Zn^{2+}$ deficiency were reported to be growth retardation, rough and dry skin, mental lethargy and testicular hypofunction, the importance of $Zn^{2+}$ in the brain was later acknowledged in several studies, reporting neuronal dysfunction and behavioural changes in $Zn^{2+}$ deficient rats (Hesse, 1979; Hesse *et al.*, 1979). Many studies since have reported on the biological actions of $Zn^{2+}$ in the brain and its crucial roles in physiological and pathophysiological processes (Sensi *et al.*, 2009).

### 1.1.2. Abundance of $Zn^{2+}$ in the brain

The most widely used method for $Zn^{2+}$ staining is Timm's staining which precipitates $Zn^{2+}$ as Zn-sulfides, which are then visualised by silver amplification (Timm, 1958; Danscher, 1981). This method, as well as the later use of more selective fluorescent probes, such as TSQ or ZP1/4 (Frederickson, 2003), have shown that the distribution of $Zn^{2+}$ is widely abundant but selective to certain areas (**figure 1.1**).

A
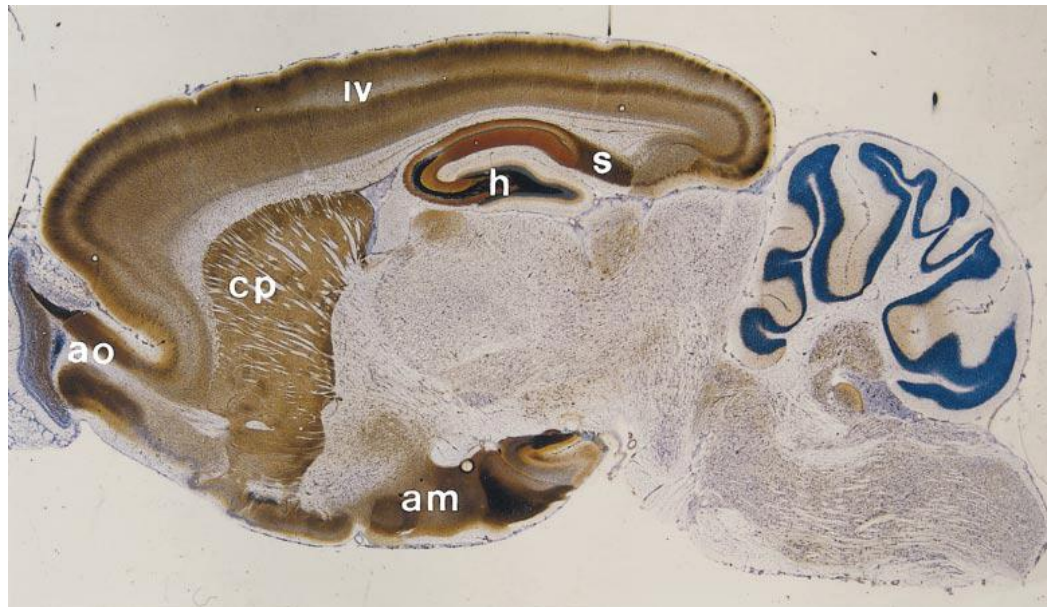


B
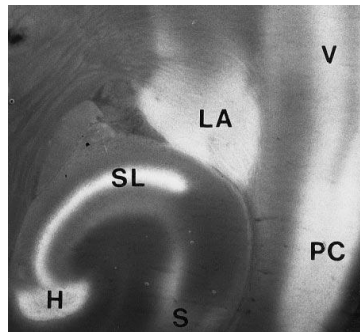
C
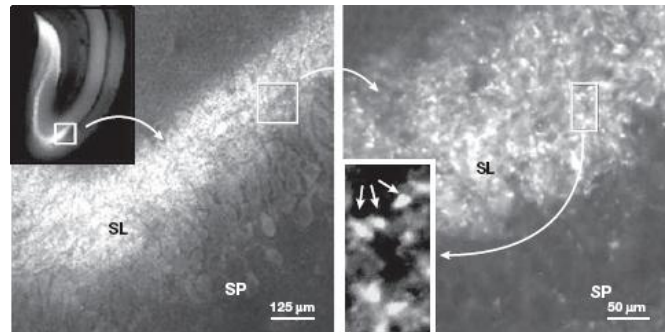


**Figure 1.1 – Zn$^{2+}$ imaging. A:** Digital image showing a sagital rat slice which has been stained for Zn$^{2+}$. The brown-black areas account for staining by the Timm-Danscher method and the blue represent Nissl stained areas. Staining is found in the neuropil, and in presynaptic terminals of Zn$^{2+}$-containing neurons. Note the dense staining in the hilus (h) and subiculum (s), the accessory olfactory bulb (ao), the caudato putamen (cp) and the amygdala (am). Little staining is present in layer IV of the cerebral cortex or the olfactory bulb proper, adjacent to ao. **B:** Image showing a rat slice that has been stained with TSQ which forms a bright fluorescent TSQ:Zn$^{2+}$ complex. H hilus; SL stratum lucidum, S subiculum, V layer V of the cerebral cortex, PC perirhinal cortex, LA lateral amygdala. **C:** Zn$^{2+}$ staining in stratum lucidum of the CA3 area of the hippocampal formation with the fluorescent probe ZP1. SL stratum lucidum, SP stratum pyramidale. Figure modified from Frederickson *et al.* (2000) and (2005).

Selective $Zn^{2+}$ staining is layer restricted to areas amongst the forebrain including stratum lucidum (SL) in CA3 area of the hippocampus and the hilus of the dentate gyrus, as well as the amygdala and the caudatoputamen (**figure 1.1A,B**). These neurons came to be known as "$Zn^{2+}$-containing neurons" and are defined as all "cells that are required to contain intracellular $Zn^{2+}$ that is loosely bound and mobile, with a predominant presence in vesicles of the axonal terminal boutons" (Smart *et al.*, 2004). The connectivity of $Zn^{2+}$-containing neurons within the brain, especially to and from the hippocampal formation, is described in more detail in **section 1.3**.

## 1.1.3.   $Zn^{2+}$ in synaptic vesicles

The use of Timm's staining combined with electron microscopy has shown that $Zn^{2+}$ is contained within clear synaptic vesicles which predominantly form asymmetric synapses with dendritic spines (Haug, 1967; Frederickson *et al.*, 1987; Perez-Clausell and Danscher, 1985). These $Zn^{2+}$-containing neurons were predominantly found to be glutamatergic in the hippocampus or the visual cortex (Beaulieu *et al.*, 1992; Slomianka, 1992). In the spinal cord, some GABAergic and glycinergic neurons were also found to contain $Zn^{2+}$ (Birinyi *et al.*, 2001; Danscher *et al.*, 2001). $Zn^{2+}$ is not essential for glutamate or GABA packaging within the terminals and is, with the exception of the mossy fibres (MFs), interspersed with non $Zn^{2+}$-containing terminals (Slomianka, 1992). $Zn^{2+}$ is transported into vesicles via the $Zn^{2+}$ transporter ZnT3, a $H^+/Zn^{2+}$ co-transporter from the ZnT family. It is expressed in $Zn^{2+}$-containing neurons and its immunoreactivity coincides with that of Timm's staining (Palmiter *et al.*, 1996). Specifically in the MF pathway, which has possibly the densest $Zn^{2+}$ staining, electron microscopic studies showed that ZnT3 is expressed at vesicles in MF terminals (Wenzel *et al.*, 1997). ZnT3 is responsible for the inclusion of $Zn^{2+}$ within the same vesicles as glutamate, where they can reach a concentration up to 1.4mM (Frederickson *et al.*, 2000). Indeed, knockout-mice that lack the gene for expressing ZnT3 were shown to have no histochemical staining for $Zn^{2+}$ (Cole *et al.*, 1999). Interestingly the phenotype of these mice, as well as the ultrastructure of MF terminals, was reported to be normal. In contrast, the so-

called mocha mice which lack the δ subunit of the AP-3 vesicular chaperone complex show hearing impairments, hypersynchronised theta rhythms and spontaneous bursts of epileptiform activity. These mice also show a dramatic reduction in vesicular $Zn^{2+}$. Due to the much more universal role of AP-3 in vesicular protein complexes, this phenotype is much more severe (Kantheti *et al.*, 1998).

## 1.1.4. $Zn^{2+}$ concentration in the synaptic cleft

The dense Timm's staining (that coincides with the terminals of $Zn^{2+}$-containing neurons) suggested that $Zn^{2+}$ is co-released together with glutamate or GABA (Wenzel *et al.*, 1997). However, the concentration of $Zn^{2+}$ in the synaptic cleft after vesicular release is still unknown. Initially, $Zn^{2+}$ was measured in a perfusate following high frequency stimulation of MFs in two independent studies (Assaf and Chung, 1984; Howell *et al.*, 1984). Both studies reported that the $Zn^{2+}$ concentration in the extracellular tissue was as high as 300µM following release. However, this estimate was revised by later studies that used more advanced technology. The use of novel $Zn^{2+}$ sensitive fluorescent probes and ZnT3 knock-out mice has provided evidence that $Zn^{2+}$ acts as a co-transmitter. Qian and Noebels (2005) have used FluoZin-3, a membrane impermeable fluorescent probe, to demonstrate that action potential dependent release of $Zn^{2+}$ is associated with glutamate release, which depended on vesicular exocytosis, however without an estimate of a concentration. In addition, they showed that $Zn^{2+}$ release is absent in ZnT3 knock-out mice. In a follow-up study, the authors also showed that there was even $Zn^{2+}$ release at the CA3-CA1 Schaffer collateral synapse (Qian and Noebels, 2006), even though it has previously been shown that only half of these terminals contain $Zn^{2+}$ (Sindreu *et al.*, 2003). Using the membrane permeable fluorescent probe ZnAF-3, Komatsu *et al.* (2005) estimated a $Zn^{2+}$ concentration of 1µM, whereas Li *et al.* (2001) reported a $Zn^{2+}$ concentration of 30µM with the use of the membrane impermeable fluorescent probe Newport Green. However, once released, the transient $Zn^{2+}$ concentration is likely to drop quickly to a nanomolar range by means of diffusion and clearance. In a recent study, the $Zn^{2+}$ concentration in the extracellular fluid has

been estimated to be ~19nM (Frederickson *et al.*, 2006), however measurements for dynamic processes of $Zn^{2+}$ within the synaptic cleft are nonetheless still lacking. In contrast, not all research groups support the view of active $Zn^{2+}$ release. Using the fluorescent probes ZnAF-2 and ZP4, Kay and Toth (2006) showed that changes in fluorescence can be used to monitor presynaptic activity. The results did not support the release of $Zn^{2+}$ from the presynaptic membrane upon synaptic activation.

## 1.1.5. $Zn^{2+}$ homeostasis

There are many transporters and receptors involved in $Zn^{2+}$ homeostasis (reviewed by Sensi *et al.*, 2009). $Zn^{2+}$ has been shown to translocate into the postsynaptic cell with physiological stimulations (Li *et al.*, 2001). For example, voltage-gated $Ca^{2+}$ channels (VGCCs) and $Ca^{2+}$ and $Zn^{2+}$ permeable, GluA2 subunit lacking, AMPA receptors (AMPARs) are two main ways of entering the postsynaptic cell. Another mechanism by which $Zn^{2+}$ is transported into the cell involves $Zn^{2+}$ importing proteins (ZIP), which are $H^+$ or $HCO_3^-$ - $Zn^{2+}$ co-transporters. $Zn^{2+}$ transporters from the ZnT family, such as ZnT1, are mediating the $Zn^{2+}$ efflux (Palmiter and Findley, 1995). Finally, $Na^+/Zn^{2+}$ exchanger, situated within the plasma membrane mediate $Zn^{2+}$ influx or efflux, depending on the $Zn^{2+}$ gradient. Once inside the cell, buffering proteins of the cytoplasm including metallothioneins are likely to bind $Zn^{2+}$ and are thus important contributors for $Zn^{2+}$ homeostasis. Cote *et al.* (2005) have demonstrated that the intracellular concentration of $Zn^{2+}$ following seizures is cell specific, with relatively high concentrations in interneurons causing cell death, and low concentrations in pyramidal cells, promoting their survival arguing that the $Zn^{2+}$ homeostasis is cell-type specific. In addition, a recent study has shown that following epileptic seizures, $Zn^{2+}$ is released from internal stores rather than presynaptic vesicles, suggesting that the intracellular $Zn^{2+}$ concentration is modulated by activity (Lavoie *et al.*, 2007).

## 1.2.   EFFECTS OF $Zn^{2+}$ ON NEURONAL FUNCTION

Genetically modified mice whose $Zn^{2+}$ transporter ZnT3 has been deleted lack vesicular $Zn^{2+}$, meaning that the contribution of $Zn^{2+}$ in physiological processes, especially those mediated by MFs, could be studied. Lopantsev *et al.* (2003) did not find any differences in field potential recordings, input-output curves, short-term plasticity as well as pharmacological isolated currents mediated by NMDA receptors (NMDARs), non-NMDARs, $GABA_A$ receptors ($GABA_A$Rs) or $GABA_B$ receptors ($GABA_B$Rs) between ZnT3 knock-out mice and wildtype mice when recording from a CA3 pyramidal cell and stimulating MFs. Similarly, Vogt *et al.* (2000) did not find a significant difference in the degree of paired-pulse facilitation, frequency-dependent facilitation or NMDAR independent long-term potentiation (LTP) when using mocha mice compared to wildtype mice. Nevertheless, several studies have found an involvement of $Zn^{2+}$ in various physiological processes, including receptors or transporters mediating excitatory and inhibitory neurotransmission. In addition, subtypes of VGCCs are also known to be modulated by $Zn^{2+}$ which highlights the importance of the ion on neuronal function.

## 1.2.1.   Effects of $Zn^{2+}$ on glutamatergic transmission

### 1.2.1.1.  NMDA receptors

NMDARs are tetrameric ionotropic glutamate receptors that consist of two obligatory GluN1 subunits and two GluN2A-D subunits, forming a stoichiometry of $(GluN1)_2(GluN2)_2$. NMDAR mediated signals have characteristically slow kinetics (hundreds of milliseconds), are highly permeable to $Ca^{2+}$ and their open probability and gating is subunit specific (Gielen *et al.*, 2009). At resting membrane potential, NMDARs are blocked by $Mg^{2+}$, which is relieved by a transient depolarisation of the membrane, displaying a characteristic outward rectification in the I-V relationship of NMDAR-mediated currents.

Studies in cultured cortical and hippocampal neurons have shown that NMDAR-mediated currents are selectively sensitive to $Zn^{2+}$ at low micromolar concentrations (Peters *et al.*, 1987; Westbrook and Mayer, 1987; Paoletti *et al.*, 2009). Studies on recombinant NMDARs demonstrated that NMDARs are blocked by $Zn^{2+}$ in a subunit specific manner. NMDAR containing GluN1/GluN2A subunits have two binding sites for $Zn^{2+}$: a high-affinity, voltage independent binding site that blocks the receptor with an $IC_{50}$ of ~ 0.005-0.08μM and a low-affinity, voltage dependent binding site with an $IC_{50}$ of ~ 26-79μM (Paoletti *et al.*, 1997; Rachline *et al.*, 2005). The location of the binding site of $Zn^{2+}$ has been shown to be located at the interface between GluN1/GluN2A of the N-terminal of the receptor promoting the domain closure (Low *et al.*, 2000; Gielen *et al.*, 2008). Knock-in mice carrying a single point mutation at the histidine residue, which mediates $Zn^{2+}$ binding at the high-affinity site, have been shown to display sensorimotor deficits and impaired pain processing, demonstrating an important role of $Zn^{2+}$ in analgesia (Nozaki *et al.*, 2011). NMDAR containing GluN1/GluN2B or GluN1/GluN2C,D subunits were shown to be inhibited by $Zn^{2+}$ with $IC_{50}$ values of ~ 1μM and >10μM respectively (Williams, 1996; Paoletti *et al.*, 1997). While the GluN1 subunit is ubiquitously expressed throughout the brain (Moriyoshi *et al.*, 1991), GluN2A and GluN2B subunits have been shown to prevail in the hippocampus (Monyer *et al.*, 1994). Vogt *et al.* (2000) investigated the effect of endogenous $Zn^{2+}$ at the MF-CA3 synapse in hippocampal rat slices. The authors found evidence that the high-affinity $Zn^{2+}$ binding site at NMDARs is tonically occupied by endogenous $Zn^{2+}$, a finding that has been corroborated by the estimation that the extracellular fluid contains 0.02μM of $Zn^{2+}$ (Frederickson *et al.*, 2006). Moreover, tetanic stimulation of MFs caused endogenous $Zn^{2+}$ to bind to the low-affinity binding site at a concentration of 10-100μM as the perfusion of CaEDTA enhanced NMDAR-mediated currents (Vogt *et al.*, 2000). In accordance with this result, chelation of $Zn^{2+}$ also enhanced the NMDA component of excitatory transmission in epileptic animals in response to MF activation, but not the perforant path (Molnar and Nadler, 2001b). Whether released $Zn^{2+}$ can also influence NMDARs at neighbouring synapses remains a matter of debate and is linked to the conflict of how much $Zn^{2+}$ is actually released during synaptic activity. While Ueno *et al.* (2002) have provided evidence that released $Zn^{2+}$ can

diffuse as far as 100μm to modulate NMDARs at synapses located in stratum radiatum, Vogt *et al.* (2000) have observed no modulatory effect of $Zn^{2+}$ at synapses formed by associational/commissural fibres.

### 1.2.1.2. AMPA and kainate receptors

Few studies have examined the modulation of AMPARs by $Zn^{2+}$. Mayer *et al.* (1989) have reported that AMPARs in hippocampal cultures are insensitive to submicromolar concentrations of extraneous $Zn^{2+}$ application. At higher concentrations homomeric GluA3 containing AMPARs are potentiated by $Zn^{2+}$, whereas homomeric GluA1 containing AMPARs did not show any sensitivity for $Zn^{2+}$ (Dreixler and Leonard, 1994).

Kainate receptors also participate in synaptic transmission and are expressed and characterised at the MF-CA3 synapse. Postsynaptic kainate receptors contribute to the temporal summation of synaptic inputs (Frerking and Ohliger-Frerking, 2002), whereas presynaptic kainate receptors are important in short-term plastic properties such as frequency-dependent facilitation (Schmitz *et al.*, 2001) and also modulate axonal excitability of MFs (Schmitz *et al.*, 2000; for review see Kullmann, 2001). In recombinant GluK2/GluK5 containing kainate receptors, Fukushima *et al.* (2003) have found that low micromolar $Zn^{2+}$ application inhibited these receptors. In acute slices, $Zn^{2+}$ blocks kainate receptor-mediated spontaneous and evoked synaptic transmission at the MF-CA3 synapse which was shown to be subunit specific to GluK4 and dependent on the pH (Mott *et al.*, 2008).

## 1.2.2. Effects of $Zn^{2+}$ on inhibitory transmission

### 1.2.2.1. $GABA_A$ receptors

There have been many studies on the modulation of $GABA_ARs$ by $Zn^{2+}$ in the central nervous system (CNS). Experiments in embryonic hippocampal neurons have identified $Zn^{2+}$ as an antagonist of $GABA_ARs$ (Westbrook and

Mayer, 1987). This inhibition was observed to depend on the stage of development, as embryonic neurons showed a considerable inhibition by $Zn^{2+}$, whereas adult neurons were almost insensitive (Smart and Constanti, 1990). It was demonstrated that the inclusion of the γ subunit in recombinant $GABA_A$Rs made them insensitive to $Zn^{2+}$ inhibition, compared to a 3,400-fold higher potency of $Zn^{2+}$ inhibition at αβ recombinant $GABA_A$Rs (Draguhn *et al.*, 1990). Molecular modelling studies identified $Zn^{2+}$ binding sites at the αβ interface which were disrupted after co-assembly of a γ subunit into the receptor pentamer (Hosie *et al.*, 2003). However, the $Zn^{2+}$ sensitivity of $GABA_A$Rs can also be influenced by the α subunit. It has been demonstrated that α6β3γ2 containing $GABA_A$Rs have a micromolar sensitivity to $Zn^{2+}$, which depended on a histidine residue at the α6 subunit, whereas α1β3γ2 containing $GABA_A$Rs were $Zn^{2+}$ insensitive (Saxena and Macdonald, 1996; Fisher and Macdonald, 1998). In addition, $GABA_A$Rs in dentate basket cells (BCs) were tested for their $Zn^{2+}$ sensitivity with nucleated patch recordings (Berger *et al.*, 1998). Pressure application of GABA on BC nucleated patches revealed that low micromolar concentrations of $Zn^{2+}$ caused a block in the peak amplitude by modulating the receptor desensitisation kinetics. Single cell polymerase chain reaction (PCR) experiments also revealed the presence of $γ_1$ and $γ_2$ subunit mRNA, but no α1, implying that additional factors apart from the presence or absence of a γ subunit seem to be important for the $Zn^{2+}$ sensitivity of $GABA_A$Rs.

### 1.2.2.2. $GABA_A$ receptors in epileptic animals

In pathological animal models, such as the kindling or the pilocarpine-induced model of temporal lobe epilepsy, alterations in the sensitivity of postsynaptic $GABA_A$Rs to $Zn^{2+}$ inhibition became apparent and were reported in several studies (Gibbs, III *et al.*, 1997; Buhl *et al.*, 1996). The induction of epileptic seizures was shown to enhance the number of $GABA_A$Rs at postsynaptic sites (Nusser *et al.*, 1998). As these $GABA_A$Rs were shown to display a higher $Zn^{2+}$ sensitivity, it was suggested that $Zn^{2+}$ induced a collapse of this augmented inhibition in temporal lobe epilepsy models (Buhl *et al.*, 1996). These findings were explained by an alteration in the subunit composition

induced by epileptic seizures. Indeed, Brooks-Kayal *et al.* (1998) showed a selective increase in the expression of the $\alpha_4$ subunit and a down-regulation of $\alpha_1$ subunits, which can promote epileptiform activity in the dentate gyrus. However, this disinhibition theory by $Zn^{2+}$ stands in contrast to the findings of Molnar and Nadler (2001a). The authors also reported an enhanced inhibition of GABA$_A$Rs by $Zn^{2+}$ in epileptic animals, however they could not see a modification of GABA$_A$R-mediated responses evoked by photo-uncaged GABA, when MFs were stimulated in these animals. In support of this result, it was demonstrated in a recent study that fast GABAergic transmission between basket cells (BCs) and granule cells (GCs) was disrupted in models of temporal lobe epilepsy (Zhang and Buckmaster, 2009). The authors showed that the excitatory drive by MFs to these BCs was reduced despite MF sprouting and the readily releasable pool of vesicles in BCs was smaller, resulting in lower amplitude inhibitory post-synaptic currents (IPSCs).

## 1.2.2.3. Synaptic and extrasynaptic GABA$_A$ receptors at the MF-CA3 synapse

With regard to evidence provided for GABAergic signalling at the MF-CA3 synapse, Ruiz *et al.* (2004) tested the possibility that, following MF stimulation, endogenous $Zn^{2+}$ could block GABA$_A$Rs which has been shown to be expressed at the postsynaptic membrane (Bergersen *et al.*, 2003). Indeed, the authors demonstrated that $Zn^{2+}$ tonically blocked GABA$_A$Rs by showing a pathway-specific enhancement of GABAergic signalling following the perfusion of a $Zn^{2+}$ chelator.

Extrasynaptic GABA$_A$Rs, which contain a subunit composition $\alpha\beta\delta$ reside at GC dendrites and mediate a tonically active GABAergic current. By using recombinant $\delta$ subunit containing GABA$_A$Rs expressed in oocytes as well as cerebellar GC cultures, Krishek *et al.* (1998) have shown that the inclusion of a $\delta$ subunit conferred a high sensitivity to $Zn^{2+}$ inhibition. A study in cultured hippocampal pyramidal neurons revealed that tonic GABAergic currents consisted of heterogeneous receptor subunit compositions, including $\alpha5\beta\gamma$, $\alpha4\beta\delta$

and $\alpha\beta$. The latter receptor isoforms accounted for up to 10% of the compound current and in addition was shown to be benzodiazepine insensitive and had a low micromolar sensitivity to $Zn^{2+}$ (Mortensen and Smart, 2006). Whether dentate GC $\alpha\beta\delta$ subunit containing GABA$_A$Rs may be sensitive to $Zn^{2+}$ spillover from MF synapses needs to be demonstrated. Similarly, it is unknown whether presynaptic GABA$_A$Rs may be sensitive to $Zn^{2+}$ since a subset of tonically active GABA$_A$Rs have revealed pharmacological properties consistent with $\delta$ subunit containing GABA$_A$Rs (Ruiz *et al.*, 2010).

### 1.2.2.4. Glycine receptors

Glycine receptors (GlyRs) are also sensitive to $Zn^{2+}$. A study in cultured rat spinal cord neurons as well as expression of recombinant GlyRs in human embryonic kidney (HEK) cells showed that $Zn^{2+}$ modulated the receptor concentration dependently in a biphasic fashion. Low concentrations (<10µM) potentiated GlyR-mediated currents whereas higher concentrations inhibited the currents (Bloomenthal *et al.*, 1994). Again, molecular binding studies have shown that the $Zn^{2+}$ binding site at the $\alpha$ subunit contained a histidine residue responsible for its high sensitivity (Miller *et al.*, 2005). Interestingly, knock-in mice carrying a single-point mutation that eliminates the high-affinity potentiating binding site of $Zn^{2+}$ (at the $\alpha 1$ subunit) have shown reduced IPSC amplitudes and shorter decay time constants, while there was no overall change in the level of GlyR expression or its sensitivity to glycine (Hirzel *et al.*, 2006). This type of knock-out mice had the motor phenotype with symptoms similar to the ones found in hyperekplexia. Thus, the authors have identified $Zn^{2+}$ as an essential modulator for glycinergic neurotransmission.

## 1.2.3. Transporters

Glutamate transporters are also sensitive to $Zn^{2+}$ which has been demonstrated by overexpression of the most abundant excitatory amino acid transporters, EAAT1 and EAAT2 in *Xenopus leavis* oocytes (Vandenberg *et al.*,

1998). The authors demonstrated that low micromolar concentrations of $Zn^{2+}$ selectively blocked EAAT1 in a non-competitive fashion.

In another study, GABA transporter (GAT) isoforms GAT1-4 were overexpressed in *Xenopus leavis* oocytes. Results have revealed that GAT4 and GAT2 were potently inhibited by $Zn^{2+}$, whereas GAT1 and GAT3 have shown little and partial sensitivity respectively. Interestingly, GAT4 immunostaining has revealed that this isoform is widely expressed within the dentate gyrus and the hippocampus, thereby coinciding with $Zn^{2+}$-containing fibres (Cohen-Kfir *et al.*, 2005).

## 1.2.4. Voltage-gated conductances

### 1.2.4.1. Voltage-gated $Ca^{2+}$ channels

Voltage-gated $Ca^{2+}$ channels (VGCCs) are a group of ion channels that are involved in a variety of processes including neurotransmitter exocytosis, synaptic plasticity or gene expression. The group of VGCCs is classified according to their $\alpha_1$ subunit. At least 10 genes have been cloned so far. High-voltage activated channels consist of the $Ca_v1$ and $Ca_v2$ subfamilies. These include L-type ($Ca_v1.1$-1.4), P/Q-type ($Ca_v2.1$), N-type ($Ca_v2.2$) and R-type ($Ca_v2.3$) VGCCs. In contrast, low-voltage activated channels carry the $Ca_v3$ subfamily, consisting of T-type ($Ca_v3.1$-3.3) VGCCs. For fast neurotransmitter release from presynaptic terminals during an action potential driven event, P/Q-type and N-type VGCCs are the most important subtypes to ensure efficient and rapid exocytosis. At MF terminals, together these two subtypes contribute to more than 90% of all VGCCs. The remaining fraction consists of R-type VGCCs which have been shown to be important for synaptic plasticity (Li *et al.*, 2007; Dietrich *et al.*, 2003). Moreover, L-type VGCCs, expressed at postsynaptic membranes, have been shown to be important for synaptic plasticity, including one form of LTP at the MF-CA3 synapse (Kapur *et al.*, 1998). Finally, low-voltage activated T-type VGCCs can play an important role as a pacemaker in some neurons and are additionally involved in the generation of low-threshold spikes

which may contribute to burst firing activity (Destexhe *et al.*, 1996; Cueni *et al.*, 2009).

The sensitivity of VGCCs to a modulation of $Zn^{2+}$ has been tested in many types of neurons including dorsal root ganglion neurons (Busselberg *et al.*, 1994), thalamic relay neurons (Noh and Chung, 2003), hypothalamic neurons (Muller *et al.*, 1992) and paleocortical neurons (Magistretti *et al.*, 2003). Expression of VGCCs in HEK cells and systematical testing for $Zn^{2+}$ modulation has shown that the VGCC subtype $Ca_v1.2$ (L-type, $IC_{50}$ = 11µM) and $Ca_v3.2$ (T-type, $IC_{50}$ = 24µM) had the highest sensitivities, whereas other high-voltage activated VGCCs had low sensitivities to $Zn^{2+}$ modulation (Sun *et al.,* 2007). In comparison, a similar study that only expressed T-type isoforms ($Ca_v3.1$, $Ca_v3.2$, $Ca_v3.3$) in tsA-201 cells reported a slightly higher sensitivity with an $IC_{50}$ = 0.8µM for the $Ca_v3.2$ isoform (Traboulsie *et al.*, 2007). It has also been demonstrated in dissociated thalamic relay neurons and dissociated CA1 neurons that low-threshold T-type $Ca^{2+}$ currents are reduced by $Zn^{2+}$ in a concentration dependent manner (Noh and Chung, 2003; Takahashi and Akaike, 1991). A recent study also linked tonic $Zn^{2+}$ inhibition of T-type $Ca^{2+}$ channels with analgesia, as the authors found that $Zn^{2+}$ chelation also sensitised dorsal root ganglion nociceptors by relieving the tonic inhibition of T-type $Ca^{2+}$ channels by $Zn^{2+}$, thus enhancing $Ca_v3.2$ currents (Nelson *et al.*, 2007).

Genes encoding for T-type $Ca^{2+}$ channels are expressed in the dentate gyrus and the hippocampus proper (Craig *et al.*, 1999; Talley *et al.*, 1999). The expression pattern of T-type $Ca^{2+}$ channel subunits is also known for interneurons (Vinet and Sik, 2006). For instance, in all parvalbumin positive cells in the dentate gyrus and the hippocampus proper, staining for $Ca_v3.1$ subunits could be observed, whereas only 30% of all parvalbumin positive cells stained for $Ca_v2.3$ (R-type). However, whether $Zn^{2+}$ might modulate T-type $Ca^{2+}$ channels at these cells has not been explored.

### 1.2.4.2. Other voltage-gated conductances

A possible modulation of voltage-gated $Na^+$ channels by $Zn^{2+}$ has also been studied. White *et al.* (1993) reported a tetrodotoxin (TTX)-resistant $Na_v1.5$ containing $Na^+$ current in acutely dissociated neurons in the entorhinal cortex. This $Na^+$ current could also be distinguished from the TTX sensitive $Na^+$ current by its highly potent block by $Zn^{2+}$ ($IC_{50}$ = 9µM). Moreover, Sim and Cherubini (1990) have reported a modulation of the outward current underlying the afterhyperpolarization (AHP) of action potentials by low concentrations of $Zn^{2+}$, and a subsequent enhancement in cell excitability using intracellular recordings from CA1 and CA3 pyramidal cells. In addition, intracellular $Zn^{2+}$ has recently been shown to activate large-conductance voltage and $Ca^{2+}$-activated $K^+$ (BK) channels in HEK cells (Hou *et al.*, 2010). Other voltage-gated conductances such as various voltage-gated $K^+$ conductances have been investigated and reviewed in Mathie *et al.* (2006).

## 1.2.5. Potassium/chloride co-transporter 2

The potassium/chloride co-transporter 2 (KCC2) is the main $Cl^-$-extruding transporter in neurons that regulates the intracellular $Cl^-$ concentration. Its expression profile is developmentally regulated and increases with age, which shifts the reversal potential for GABA ($E_{GABA}$) in the majority of neurons to more hyperpolarised potentials compared to the membrane potential ($V_m$) and renders GABA hyperpolarising. Recent evidence suggests that $Zn^{2+}$ also acts on KCC2. In HEK cells, it has been shown that an increase in the intracellular $Zn^{2+}$ concentration with Zn-pyrithion decreases KCC2 function, monitored by pH changes with the aid of a fluorescent dye (Hershfinkel *et al.*, 2009). It was also shown that the intracellular $Zn^{2+}$ chelator N,N,N'N'-tetrakis(-)[2-pyridylmethyl]-ethylenediamine (TPEN) reversed this effect indicating that intracellular $Zn^{2+}$ tonically inhibits $Cl^-$ extrusion. This study associates for the first time elevation in intracellular $Zn^{2+}$ with the decreased function of KCC2. Although KCC2 is ubiquitously expressed, different intensities in KCC2 labelling have been reported in different areas of the hippocampus (Gulyas *et al.*, 2001). KCC2 expression has

been shown to coincide with excitatory synapses to set the driving force for fast neurotransmission.

## 1.2.6. Metabotropic signalling

$Zn^{2+}$ has also been described to modulate metabotropic signals. Metabotropic receptors are critical for slow synaptic transmission, activation of intracellular pathways and changes in synaptic plasticity. Besser *et al.* (2009) have shown that $Zn^{2+}$ activates a postsynaptic metabotropic $Zn^{2+}$ sensing receptor (mZnR) that has been previously identified on epithelial cells (Hershfinkel *et al.*, 2001). Activation of mZnR has been shown to induce intracellular $Ca^{2+}$ elevation and phosphorylation of $Ca^{2+}$/calmodulin kinase II. Furthermore, it has been reported that MF stimulation resulted in the activation of mZnR which induced the expression of KCC2. Interestingly, this vesicular $Zn^{2+}$ dependent increase in KCC2 expression caused a hyperpolarisation in $E_{GABA}$ whereas Hershfinkel *et al.* (2009) reported a depolarisation in $E_{GABA}$ by intracellular $Zn^{2+}$. In addition, using ZnT3 knock-out mice, it has been demonstrated that $Zn^{2+}$ modulates presynaptic MAP kinase (MAPK) signalling by activating Erk1/2 pathway and inhibiting MAPK tyrosine phosphatase activity in mossy fibre boutons (MFBs) (Sindreu *et al.*, 2011). The authors described deficits in contextual discrimination and spatial working memory and thus found that it is necessary for hippocampal dependent learning tasks.

## 1.3. $Zn^{2+}$ IN THE LIMBIC SYSTEM AND HIPPOCAMPAL FORMATION

$Zn^{2+}$-containing neurons form an elaborate associational network which generally interconnects cerebral cortices and limbic structures in the form of cortico-cortical, cortico-limbic or limbic-cortico projections (Frederickson *et al.*, 2000). In contrast, long-range projections from and towards lower brain regions such as the brain stem and spinal cord, or subcortical structures such as the thalamus are usually devoid of $Zn^{2+}$. The majority of $Zn^{2+}$-containing somata are found in the cerebral cortex and amygdala, from where they project locally to the

cerebral cortex or amygdala but also to the accessory olfactory bulb, caudate putamen and limbic targets such as the hippocampal formation, septum, nucleus of the diagonal band and medial hypothalamus (Slomianka *et al.*, 1990). Most amygdalar nuclei including pyramidal cells in the lateral amygdala, receive $Zn^{2+}$-containing boutons. Their $Zn^{2+}$-containing fibres project via the amygalofugal system to the pyriform cortex, striatum and periamygdalar cortices (Christensen and Frederickson, 1998).

The hippocampal formation plays a central role in learning and memory and it is the structure of the limbic system, which harbours the greatest abundance of $Zn^{2+}$ in the entire brain, the anatomical structure of which will be reviewed in detail.

The rat hippocampal formation is an elongated C-shaped structure with its long axis spanning rostrodorsally from the septal nuclei near the midline of the brain to caudoventrally behind the thalamus of the temporal lobe (Amaral and Witter, 1989, **figure 1.2A**). The long axis is also called the septotemporal axis, whereas the transverse axis spans the width of the hippocampal formation. The term "hippocampal formation" refers to six regions which are functionally connected in a uni- or bi-directional fashion: The dentate gyrus, the CA regions (also termed hippocampus) consisting of CA3, CA2 and CA1, the subiculum, the presubiculum, the parasubiculum and the entorhinal cortex (**figure 1.2B,C**). Initially, it was thought and coined a uni-directional "trisynaptic" loop between the entorhinal cortex, dentate gyrus, CA3 and CA1 (Anderson *et al.*, 1971), however today it is known that not only the subiculum and its adjacent parts (the pre- and parasubiculum) play an important role, but also that the different regions are interconnected.

A

B
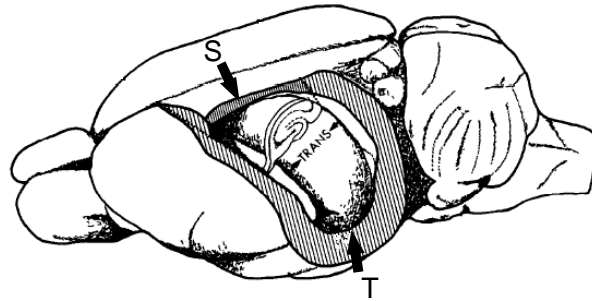
C
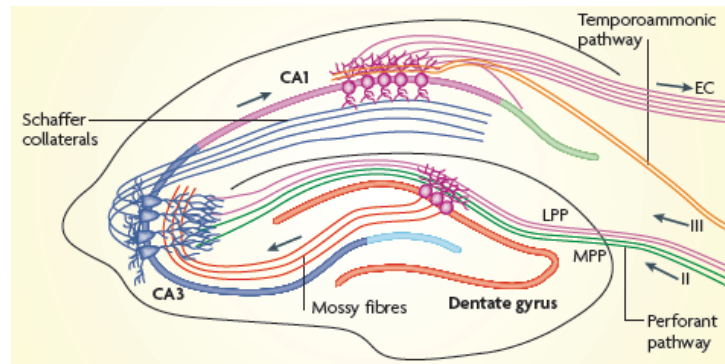
**Figure 1.2 – Rodent hippocampal formation within the brain and its connectivity.**
**A**: Picture taken from Amaral and Witter (1989) showing a drawing of the hippocampal formation and its anatomical location within the rodent brain. The long or septotemporal axis extends from the septal nuclei (S) towards the thalamus of the temporal lobe (T). The transverse axis is depicted as (TRANS). **B**: Picture adapted from Andersen *et al.* (2007) illustrating a simplistic diagram of the connectivity of the hippocampal formation. **C**: Cartoon taken from Deng *et al.* (2010) showing a simplistic illustration of the trisynaptic loop of the hippocampal formation.

Apart from intrinsic connections, the hippocampus is also highly connected to other brain structures (Andersen *et al.*, 2007). One of the main fibre systems that mediates such extrahippocampal connections is the angular bundle. This fibre bundle includes direct connections from layer III neurons of the entorhinal cortex to CA1 neurons via the temporoammonic pathway. Furthermore, direct connections to and from the basal lateral amygdala originate from CA1 and the ventral subiculum. In addition, neurons of the presubiculum project directly to the septum. The other bundle which provides connections to and from the main subcortical hippocampal targets is the fimbria-fornix pathway. This bundle originates closest to CA3 and is referred to as fimbria at this level and as fornix at a lower trajectory. Afferent fibres connect to subcortical structures such as the septal nuclei, nucleus accumbens, striatum, and also connect to serotonergic system at the raphe nuclei. In addition, they also connect to neurons of the cingulate cortex which project to neurons of the entorhinal cortex, closing the circle. Finally, the fornix also projects to the mammillary nuclei of the hypothalamus and the anterior thalamic nuclei. Neurons of the latter nucleus also project to neurons of the cingulate cortex closing a circular projection from the hippocampus to the entorhinal cortex via thalamic projections.

The principal cells of the dentate gyrus, the GCs, receive their main input from the entorhinal cortex via the perforant path and project their axon (or MF) to form the main excitatory input to the hippocampus proper, the CA3 pyramidal cells. All vesicles in MFBs are $Zn^{2+}$-containing, which accounts for the exceptionally dense staining in the hilus and SL. The axons of CA3 pyramidal cells, the Schaffer Collaterals, bypass the CA2 region and provide inputs to the CA1 pyramidal cells, but also to other cortical and limbic targets. In addition, CA3 pyramidal cells also back-project to the dentate gyrus to innervate hilar cells or even GCs (Scharfman, 2007). It has been demonstrated that nearly half of the vesicles of CA3 pyramidal cells contain $Zn^{2+}$ (Sindreu *et al.*, 2003). Finally, the CA1 region innervates the subiculum, which in turn provides the main neocortical output of the hippocampal formation by sending its fibres back to the entorhinal cortex via the pre- and parasubiculum. The neurons of the presubiculum, which project to the septum, subiculum and other hippocampal fields are entirely $Zn^{2+}$-containing.

In contrast, none of the subicular neurons which provide projections to the basal forebrain and the brain stem contain $Zn^{2+}$ in their vesicles (Long *et al.*, 1995).

## 1.4.  ANATOMY OF THE DENTATE GYRUS

The dentate gyrus is an exceptionally organised cortical structure associated with the hippocampal formation whose inputs are structured in a lamellar fashion (reviewed by Amaral *et al.*, 2007). The principal cells, the GCs, receive the main neocortical input from layer II neurons of the entorhinal cortex (minor input also comes from layer V, VI) via the perforant path (**figure 1.2C**). This can be seen as the first gateway for the processing of episodic memories. The dentate gyrus is divided into three parts: the relatively cell-free molecular layer (ML), the granule cell layer (GCL), also referred to as stratum granulosum (SG) and the polymorph layer, also referred to as the hilus, where pyramidal BCs, mossy cells and other interneurons reside. GCs have a characteristic dendritic trunk that spans the entire ML, however only two thirds, the outer and middle third of the ML, are innervated by the lateral and medial perforant path respectively. The inner third receives input from commissural/associational fibres mediating signals from the ipsi- and contralateral dentate gyrus. The GCL is also divided into three parts: the infrapyramidal blade, which is the part furthest away from the hippocampal subarea CA1, the suprapyramidal blade, which is situated between CA3 and CA1 and the crest which is situated in between the blades. MFs form synapses with proximal dendrites of CA3 pyramidal cells, however their main targets are interneurons in the hilus and CA3 (Acsady *et al.*, 1998). Its projection zone in CA3 is mainly restricted to SL, which accounts for the dense $Zn^{2+}$ staining in hippocampal slices.

### 1.4.1.  Dentate granule cells

#### 1.4.1.1. Cellular anatomy and microphysiology

In the dentate gyrus, the principal excitatory cell type is the GC. There are approximately 1 million GCs within the rat dentate gyrus, with their somata

situated in the GCL and their dendrites extending into the ML. GCs have a small (10-18μm) elliptical cell body and a cone-shaped spiny dendritic tree, which spans the whole ML to the hippocampal fissure (Claiborne *et al.*, 1990). Per GC there is usually one MF that extends to CA3. Compared to other principal cell connections, MFs innervate their main excitatory targets only sparsely with ~50 synapses per CA3 cell (Amaral *et al.*, 1990). However, within the hilus MFs have been shown to branch extensively (Claiborne *et al.*, 1986). The axonal plexus of MFs is refined to the hilus, although some fibres occasionally enter the GCL to terminate onto proximal dendrites of BCs. Recurrent excitation of GC dendrites by MF collaterals is observed very rarely in rodents compared to GCs in monkeys which extend basal dendrites into the hilus and are therefore innervated by MFs more frequently (Austin and Buckmaster, 2004). Although MF projections are confined to the hilus and SL in CA3 at their transverse axis, MFs can travel up to 400μm in their septotemporal plane (Acsady *et al.*, 1998).

Ramón y Cajal recognized early in his studies of the MF system that the terminals of MFs are unique as these axons possess more than one terminal (Ramón y Cajal, 1911). Today, it is known that MFs possess three morphologically different terminals: the large MF boutons (MFBs), filopodial extensions of the MF terminals and small *en passant* synaptic varicosities (Claiborne *et al.*, 1986). MFBs terminate onto CA3 pyramidal cells within SL, but are also present, albeit slightly smaller in size, within the hilus where they terminate onto mossy cell dendrites. Interestingly, the small varicosities considerably outnumber MFBs (160-200 small varicosities versus ~20 MFBs) and synapse onto dendrites of local interneurons within SL or the hilus, showing that the main postsynaptic target of MFs are in fact inhibitory cells (Acsady *et al.*, 1998). Using electron microscopy, the authors showed that the nature of the GABAergic postsynaptic targets was diverse, with some postsynaptic cells immunoreactive to parvalbumin, calretinin as well as substance P. Using MFB – interneuron paired recordings, Szabadics and Soltesz (2009) showed that MFs targeted perisomatically projecting parvalbumin positive BCs and regular spiking BCs, as well as dendritically projecting ivy cells and the septum projecting spiny SL cells.

MFBs contain the excitatory neurotransmitter glutamate in their vesicles (Sindreu *et al.*, 2003), but are also immunoreactive for neuromodulators such as dynorphin and $Zn^{2+}$. Furthermore, MFs show intense immunoreactivity for GABA (Sandler and Smith, 1991) and have also been reported to contain the GABA synthetic enzyme glutamate decarboxylase (GAD) 67 (Schwarzer and Sperk, 1995). The finding that GABA can be released at rat MF synapses following seizure-like activity raised the possibility that GABA release was only associated to a pathological condition (Gutierrez, 2000). However, the first electrophysiological evidence that GABA can be released from a subset of MFBs in normal animals came from studies in guinea-pig slices, and later in rats (Walker *et al.*, 2001; Walker *et al.*, 2002; but see Uchigashima *et al.*, 2007). Studies in neonatal rats additionally showed mono-synaptic GABAergic signalling at the MF synapse in young animals (Bergersen *et al.*, 2003; Safiulina *et al.*, 2006). As postsynaptic $GABA_A$Rs were identified at synapses formed by MFBs to CA3 pyramidal cells and to hilar neurons, the subcellular distribution of $Zn^{2+}$ and GABA immunogold particles have also been described (Ruiz *et al.*, 2004).

The mossy fibre synapse was described as a powerful "conditional detonator" due to its ability to discharge its postsynaptic target, both interneuron and pyramidal cell, reliably in response to a train of action potentials. The prefix 'conditional' is owed to the observation that in response to a single action potential, postsynaptic targets have a very low probability to be discharged *in vivo* (Henze *et al.*, 2002). Granule cells fire at very low discharge rates (Jung and McNaughton, 1993). Such low firing rates are difficult to temporally integrate by an ordinary synapse. However, it has been shown that mossy fibre synapses possess two unique forms of short-term plasticity which occur at low enough frequencies to facilitate temporal signal integration which are relevant for granule cell firing: paired-pulse facilitation and frequency dependent facilitation. Paired-pulse facilitation refers to the phenomenon that the second pulse has a larger amplitude than the first pulse following an evoked high-frequency paired pulse, commonly of 20Hz (Salin *et al.*, 1996). The authors observed that the paired-pulse facilitation at MF synapses was ~2 fold greater compared to associational/commissural fibres. Similarly, switching stimulation frequency from

0.0125 to 0.3 Hz facilitated postsynaptic responses whose magnitude was ~6 fold greater at mossy fibre synapses compared to associational/commissural synapses. These two properties enhance synaptic transmission at MF synapses enormously which turns MFs into reliable detonators under certain conditions. $Ca^{2+}$ imaging and buffering studies have shown that internal $Ca^{2+}$ pools are mainly responsible for short-term plasticity at mossy fibre synapses (Regehr *et al.*, 1994; Salin *et al.*, 1996; Scott and Rusakov, 2006). Moreover, presynaptic kainate receptors and $A_1$-receptors that reside at MFBs have been shown to contribute to short-term plastic properties (Lauri *et al.*, 2003; Schmitz *et al.*, 2003).

The size of giant MFBs (~ 4µm) has made them accessible to presynaptic patch-clamp recordings (Geiger and Jonas, 2000; Bischofberger *et al.*, 2006), a method that gained important information on synaptic transmission at MF synapses. It has been demonstrated that P/Q-type and N-type VGCCs are predominantly expressed at the bouton membrane, to ensure the efficient and precisely timed $Ca^{2+}$ influx at MFBs (Bischofberger *et al.*, 2002; Li *et al.*, 2007). Moreover, MFB recordings have revealed that not only $K_v1.1/K_v4.1$ heteromers are expressed but also $BK_{Ca}$ channels and few $K_v3$ channels which have been recently shown to be important for the repolarisation phase of action potentials at the bouton (Geiger and Jonas, 2000; Alle *et al.*, 2011). $Na^+$ channels have not only been shown to be expressed in high density but also demonstrated to display unique kinetic properties with very fast activation and inactivation kinetics to amplify and enhance the $Ca^{2+}$ inflow (Engel and Jonas, 2005). Finally, direct whole-bouton recordings have revealed that presynaptic $GABA_ARs$ are sensitive to the neurosteroid tetrahydrodeoxycorticosterone (THDOC) which is known to occur endogenously in the brain (Ruiz *et al.*, 2010). The authors showed that THDOC depolarises the MFB membrane potential, enhances $Ca^{2+}$ influx into the bouton and facilitated glutamatergic transmission to pyramidal neurons (Ruiz *et al.*, 2010).

In summary, there is conclusive evidence that GCs fire action potentials at basal rates less than 0.5Hz and do not fire for extended periods of time (Jung and

McNaughton, 1993), with the exception of certain behavioural tasks, including exploration in open field (Henze *et al.*, 2002; Wiebe and Staubli, 1999). The reasons for this low discharge frequency lie within intrinsic activities as well as network activity: 1) GCs have a very hyperpolarised membrane potential, implying that the excitatory current density needs to be high to reach threshold (Fricke and Prince, 1984), 2) Dendritic properties of GCs have been shown to act like passive cables that largely attenuate excitatory inputs (Krueppel *et al.*, 2011), 3) In addition to phasic inhibition, GCs also contain tonically activated GABA$_A$Rs that maintain a tonic inhibitory current in response to ambient concentrations of GABA (Farrant and Nusser, 2005), 4) GCs are rarely interconnected in contrast to CA3 pyramidal cells that have a dense CA3 collateral network and thus display a high background discharge rate, 5) Finally, and most importantly, the dentate network is endowed with strong feed-forward and feedback inhibition which efficiently shunts excitatory inputs to suppress GC activity (Mody *et al.*, 1992; Misgeld *et al.*, 1986). Together, these properties corroborate that the dentate gyrus is distinct from all other regions and has a unique function.

## 1.4.2. Local circuit neurons in the dentate gyrus

### 1.4.2.1. Basket cells

Local circuit neurons including GABAergic interneurons only constitute 10% of all neurons within the dentate gyrus (Czeh *et al.*, 2005). Despite their small number, many different cell types have been identified in the hilus (Freund and Buzsaki, 1996; Lubke *et al.*, 1998; Amaral, 1978), which can be categorised according to their axonal arborisation (including synaptic contacts at specific compartments of principal cells), expression of Ca$^{2+}$-binding proteins or their physiological properties (including firing pattern).

The pyramidal BCs are amongst the most studied neurons within interneurons (Ribak and Seress, 1983). The somata of BCs reside at the border of the GCL and the hilus (Ribak *et al.*, 1978; Ribak and Seress, 1983) and are considerably larger than those of GCs (25-35µm). BCs usually have one main apical dendrite

that travels through the GCL, which then branches and spans the entire ML. Unlike GCs, BCs also have basal dendrites which extend into the hilus and receive excitatory inputs via MFs (Geiger *et al.*, 1997; Acsady *et al.*, 1998). The axonal plexus branches extensively and stays contained within the GCL. Their main postsynaptic targets are GCs. The terminals contain GABA and form perisomatic inhibition with symmetric synapses onto somata and proximal dendrites of GCs (Sik *et al.,* 1997). Using double staining for $Zn^{2+}$ and parvalbumin, a $Ca^{2+}$-binding protein expressed in a subset of BCs, several studies have shown that GCs also provide the main excitatory input to BCs which makes them ideal candidates to provide local circuit inhibition (Ribak and Peterson, 1991; Seress *et al.*, 2001; Blasco-Ibanez *et al.*, 2000). In addition, morphological studies have also recently uncovered a long distance inhibition from BCs in SL to the dentate gyrus (Szabadics and Soltesz, 2009).

In general, BCs are more excitable than GCs due to their more depolarised membrane potential and their ability to fire sustained high-frequency trains of action potentials *in vitro* (Han *et al.*, 1993; Martina *et al.*, 1998) and *in vivo* (Sik *et al.*, 1997). This fast-spiking firing pattern was shown to depend on voltage-gated $K^+$ channels of the $K_v3$ family as they deactivate rapidly, have a high activation threshold and lack inactivation (Martina *et al.*, 1998; Lien and Jonas, 2003). Within the network, BCs are able to provide fast and precise conversion of excitatory inputs to inhibitory outputs and thereby control the number of active principal cells, frequency of firing and precise timing of action potentials (reviewed by Jonas *et al.*, 2004). Paired recordings between GCs and BCs have demonstrated that AMPAR-mediated excitatory synaptic events are timed precisely to the sub-millisecond and are of large amplitude (Geiger *et al.*, 1997). MF-mediated excitatory postsynaptic potentials (EPSPs) are generated close to the soma, an electrotonic favourable location to influence action potential spike generation and to prevent filtering the fast decay of EPSPs. The fast time course of evoked EPSCs at GC-BC synapses is due to the high synchrony of transmitter release at MFBs, a low NMDAR component (Kneisler and Dingledine, 1995; Koh *et al.*, 1995) and a rapid time course of AMPAR deactivation in BCs. In addition, efficient $Ca^{2+}$ buffering properties, a uniquely high density of dendritic $K_v3$

channels and the presence of the hyperpolarising current, $I_h$ at somatodendritic synapses, accelerate and sharpen EPSP decay, implying that effective summation only occurs for synchronous events (Aponte *et al.*, 2008; Aponte *et al.*, 2006; Hu *et al.*, 2010). Similarly, BC-GC dual recordings have shown that BCs generate rapid, large amplitude inhibitory postsynaptic conductances at GCs with a synchronous release and tight coupling between $Ca^{2+}$ channels and $Ca^{2+}$ sensors of the release machinery (Kraushaar and Jonas, 2000; Bucurenciu *et al.*, 2008). The proximity of their synaptic contacts to the axon initial segment, the initiation site of the action potential, implies that these cells are in the ideal position to influence spike initiation, allowing them to contribute to feedback and feed-forward inhibition (Pouille and Scanziani, 2004).

### 1.4.2.2. Other cells in the dentate gyrus

Other cells that reside in the dentate gyrus are the GABAergic interneuron subtypes axo-axonic cells, Hilar Perforant path associated cells (HIPP cells), Hilar Commissural-Associational Pathway related cells (HICAP cells), Molecular layer Perforant path associated cells (MOPP cells), cells of the neurogliaform family, long-range projecting GABAergic cells as well as the glutamate-containing mossy cells and semilunar granule cells which will be briefly reviewed below.

The axo-axonic cell is a subtype of interneuron that has a similar dendritic and axonal arborisation to the BC. The location of the soma tends to be at the border of the GCL and the ML, and the apical and basal dendrites also extend in a bipolar fashion to the ML and the hilus respectively. Also, the axonal plexus largely remains within the GCL where they form symmetric synapses onto the axon initial segment of GCs. Here, they are in the ideal position to control action potential initiation in GCs (Freund and Buzsaki, 1996).

HIPP cells are a subtype of interneuron whose somata are located within the hilus. The dendrites remain within the hilus and have, unlike most other interneurons, spines that make synaptic contact with hilar MF terminals. The axons of HIPP cells make symmetric contacts with distal dendrites of GCs and

are (like the MOPP cell), in the anatomical position to mainly control perforant path-mediated inputs (Han *et al.*, 1993).

The cell bodies of HICAP cells are located within the hilus and their unspiny dendrites are arranged in a bipolar nature spanning the ML. The axons target GC dendrites within the inner ML and can thus control inputs made by associational/commissural fibres (Han *et al.*, 1993).

One type of interneuron whose cell bodies are located in the ML are the MOPP cells. Their cell bodies, dendritic arbors and axonal plexus are located within the outer two thirds of the ML (Freund and Buzsaki, 1996). As the name indicates, MOPP cells mainly form symmetric synapses with the distal dendrites of GCs, hence controlling inputs from the perforant path.

Recently, cells of the neurogliaform family which include neurogliaform cells and ivy cells have also been identified in the dentate gyrus (Armstrong *et al.*, 2011). The soma of neurogliaform cells are mainly located in the middle or outer ML, while the axonal arbour is branched extensively and covers the middle and outer molecular layer but also reaches to the subiculum and CA1. In contrast, the dendritic arbour is small. Neurogliaform cells form synapses with granule cells and mediate a unique type of inhibition, which has been referred to as "volume transmission". Synaptic inputs are provided by the entorhinal cortex via the perforant path, so that neurogliaform cells are involved in feed-forward inhibition (Armstrong *et al.*, 2011). In contrast, the cell bodies of ivy cells have been suggested to be located near the granule cell layer where they project to proximal dendrites of granule cells and newly generated granule cells (Armstrong *et al.*, 2012).

Interestingly, it has been recently demonstrated that neurogliaform cells, or the related ivy cells provide the initial source for GABAergic signalling to newly generated granule cells in the dentate gyrus. It was suggested that these cells regulate neurogenesis by depolarising newly generated granule cells with volume transmission while disinhibiting mature granule cells (Markwardt *et al.*, 2009; Markwardt *et al.*, 2012).

Using optogenetic tools, Melzer *et al.* (2012) have also identified interneurons in the hilus which project their axon back to the entorhinal cortex. These long-range projecting GABAergic cells were identified as somatostatin positive cells and preferentially targeted other GABAergic cells in the medial entorhinal cortex. Activation of these fibres has been demonstrated to enhance rhythmic theta activity in postsynaptic neurons of the medial entorhinal cortex.

Mossy cells (Amaral, 1978) and the recently described semilunar granule cells both contain glutamate as their neurotransmitter (Soriano and Frotscher, 1994; Williams *et al.*, 2007). The large somata and dendrites of mossy cells are located mainly within the hilus. The most distinct characteristic of mossy cells is their dense and complex thorny excrescences on their dendrites which form synapses with hilar MFBs, but also local interneurons such as axo-axonic cells, cholecystokinin-positive and parvalbumin-positive BCs (Halasy and Somogyi, 1993; Acsady *et al.*, 2000). The main targets of mossy cells are local interneurons, but they also provide excitatory inputs to granule cells. The axonal plexus of mossy cells covers 75% of the septotemporal axis of the dentate gyrus and form associational/commissural fibres that innervate GCs at the inner third of the ML. Interestingly, it has been demonstrated that the projections by mossy cells to the ML are very weak at the same septotemporal level, whereas projections get stronger the more distant the postsynaptic target is innervated from the cell of origin (Amaral and Witter, 1989).

The other glutamatergic cell type which can be found within the inner ML is a newly described cell type called semilunar granule cells (Williams *et al.*, 2007). These cells have similar properties to GCs, except for their distinct axonal arborisation within the inner ML and their persistent firing throughout a depolarising step. This has recently been uncovered to influence mossy cells and hilar interneurons, and may be important in temporal lobe epilepsy (Larimer and Strowbridge, 2010).

### 1.4.3. Principles of feed-forward and feedback inhibition

Generally within a microcircuit, interneurons are involved in two forms of inhibition: feedback inhibition and feed-forward inhibition. While other interneurons can contribute to one type of inhibition only, in the dentate gyrus, BCs are involved in both types of inhibition as depicted in **figure 1.3**.

A

dentate gyrus

**Feedback inhibition**

BC

\-

\+

CA3

\-  \+

B

PP  \+

BC

\-

GC

GCL  hilus

**Feed-forward inhibition**

\-  \+
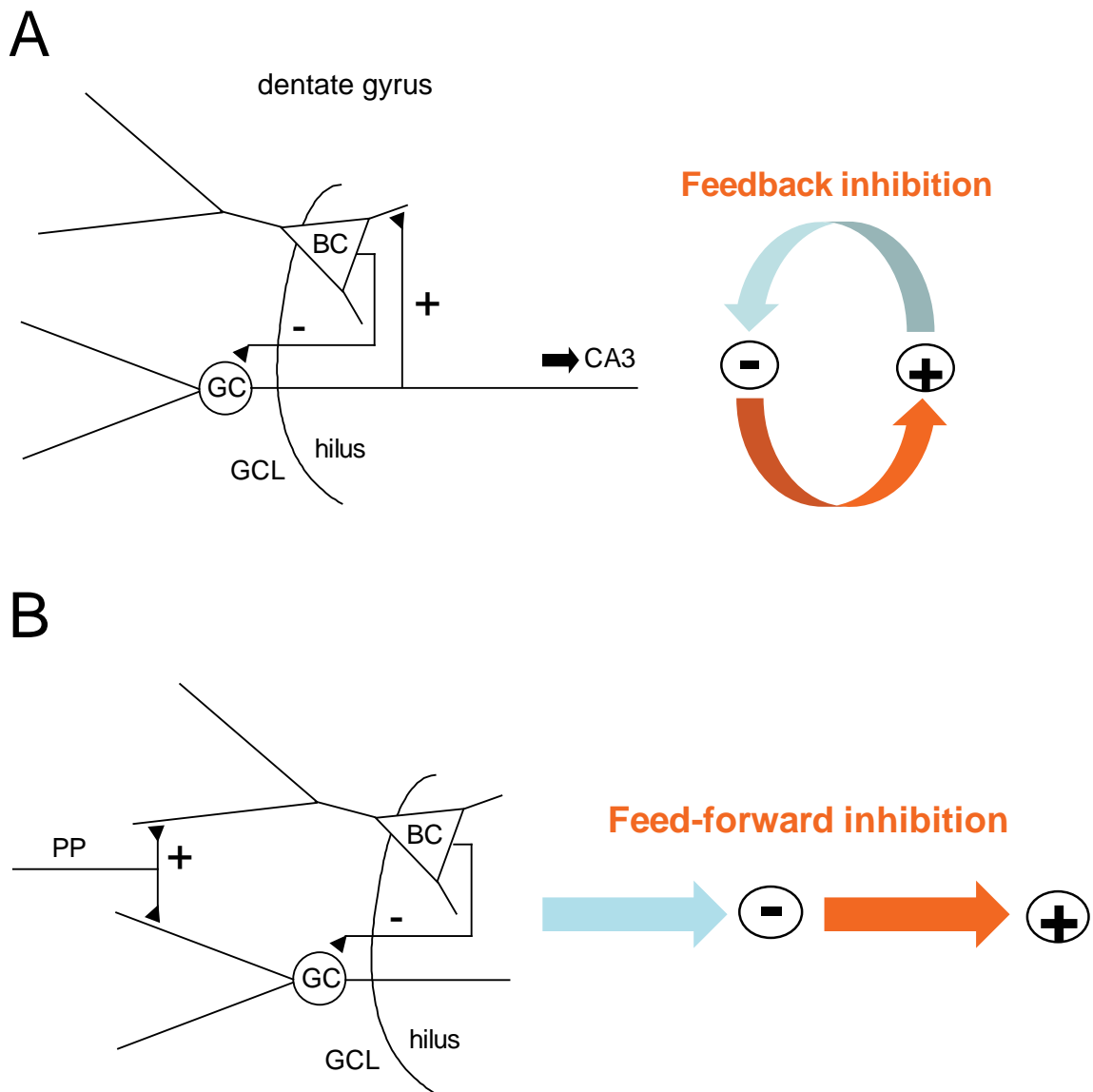
**Figure 1.3 – Principles of feedback and feed-forward inhibition. A:** (Left) Drawing showing the outline of a microcircuit between a dentate GC and a pyramidal BC. MF collaterals form excitatory synapses (**+**) with the basal dendrites of BCs. BC axons in turn form inhibitory synapses (**-**) with GCs providing feedback inhibition. **B:** (Left) Apart from forming excitatory synapses onto GCs, perforant path axons also make excitatory synapses (**+**) with BCs which in turn form inhibitory synapses with GCs providing feed-forward inhibition. General principles are represented on the right with excitatory cells in orange and inhibitory cells in blue.

BCs receive inputs from the perforant path and form connections with GCs providing strong feed-forward inhibition. In addition, they also receive inputs from MF collaterals via their basal dendrites, thus acting as a feedback inhibitory circuit (**figure 1.3**). The principle of feed-forward inhibition is supported by a number of studies. Electrical stimulation of commissural fibres was observed to not only trigger excitatory inputs to GCs, but also long-lasting inhibition mediated by BCs (Buzsaki, 1984; Buzsaki and Czeh, 1981). Similarly, local interneurons are recruited in the dentate gyrus by stimulation of the perforant path that in turn provide feed-forward inhibition to GCs *in vivo* and *in vitro* (Penttonen *et al.*, 1997; Ewell and Jones, 2010). Also, feed-forward inhibition in the CA3 area of the hippocampus is powerful. Due to higher per-site release probabilities (Lawrence *et al.*, 2004) and a higher amount of MF-interneuron synapses (Acsady *et al.*, 1998), single action potentials are rarely propagated to CA3 pyramidal cells (Henze *et al.*, 2002). However, when dentate GCs fire short, high frequency bursts, the powerful short-term dynamics of the MF-CA3 synapse increase the probability to spike and outweigh the efficient feed-forward inhibition, making MFs 'conditional detonators' (Henze *et al.*, 2002). Equally well documented is feedback inhibition in the dentate gyrus. Stimulation of the CA3 area of the hippocampus has shown to trigger MF-mediated IPSCs in GCs. Using double staining for $Zn^{2+}$ and parvalbumin, it was previously shown that BCs play a major role in local feedback inhibition (Kneisler and Dingledine, 1995; Ribak and Peterson, 1991).

Given the experimental evidence for feed-forward and feedback inhibition in the dentate gyrus, does the anatomy give clues as to how 10% of interneurons can efficiently influence 90% of principal cells? Firstly, local circuit neurons display a high degree of spatial selectivity in their axonal and dendritic arborisation in order to effectively innervate their target neurons. This has been observed not only for the dentate gyrus (Han *et al.*, 1993) but also for the CA3 area of the hippocampus (Gulyas *et al.*, 1993). The layer-specific input to GCs by local circuit neurons in the dentate gyrus is closely related to their functional role within the microcircuitry. Generally, MOPP, HIPP and HICAP cells all target GC dendrites. However, while MOPP and HIPP cells control excitatory input

associated with the perforant path, HICAP cells specifically control inputs from associational/commissural fibres. In contrast, both BCs and axo-axonic cells mediate perisomatic inhibition to the soma and the axon initial segment of dentate GCs respectively (Freund and Buzsaki, 1996). Since the dendrites and axons of MOPP cells are located in the same two outer thirds as the perforant path input, it is likely that this cell is mainly involved in feed-forward inhibition. In contrast, the dendrites of HIPP cells are contained within the hilus and receive input from MF collaterals, therefore HIPP cells are mostly likely to be involved in feedback inhibition. Secondly, MFs form 10 times more synapses onto interneurons compared to principal cells (Acsady *et al.*, 1998), ensuring an efficient and powerful inhibitory response. Thirdly, tracing studies have shown that some local circuit neurons such as BCs or HIPP cells possess very elaborate axonal arbors and thus compensate for their small quantity of cells compared to principal cells. For example, the axonal plexus of a single BC has been shown to extend 900µm in the transverse axis and ~1.5mm in the septotemporal axis thus innervating as many as 10,000 GCs (Sik *et al.*, 1997). Similarly, axonal arbors of a HIPP cell travel as much as 3.5mm along the septotemporal axis.

In addition to this efficient "task-management" of different interneurons within the dentate gyrus, they are endowed with different conductances, receptors and activity-dependent properties (Martina *et al.*, 2000; Hu *et al.*, 2010). Synapses formed by terminals from the perforant path onto BCs which mediate feed-forward inhibition, have been shown to express $Ca^{2+}$-impermeable AMPA receptors (CI-AMPARs), whereas MF-BC synapses, which mediate feedback inhibition, express $Ca^{2+}$-permeable AMPA receptors (CP-AMPARs). Unlike at MF-interneuron synapses in CA3, which have been shown to contain a high amount of NMDARs along with CI-AMPARs (Lei and McBain, 2002), MF-BC synapses at in the dentate gyrus contain CP-AMPARs and a high amount of NMDARs (Sambandan *et al.*, 2010).

In addition, interneurons mediating feedback and feed-forward inhibition may be regulated differently, as shown by Doherty *et al.* (2004). The authors showed that MF-mediated feedback inhibition is regulated by metabotropic glutamate

receptors (mGluRs), whereas mono-synaptic GABAergic inputs are insensitive to metabotropic glutamate receptor agonists.

## 1.4.4. Synaptic integration in the hippocampal network

Simultaneous activation of inputs has been used in many studies to investigate how neurons integrate inputs within the network. Calixto *et al.* (2008) found that in CA3 interneurons summation of EPSPs evoked by the perforant path and MFs is supra-linear which depended on voltage-gated T-type $Ca^{2+}$ channels and $I_h$. The latter conductance was also shown to be important in CA1 pyramidal neurons where $I_h$ enhanced the temporal precision of co-incidence detection of two excitatory - inhibitory postsynaptic current (EPSC-IPSC) sequences (Pavlov *et al.*, 2011b). In contrast, these conductances did not contribute to neuronal integration in dentate mossy cells. Simultaneous stimulation of IPSCs and EPSCs mediated by local interneurons and MFs onto mossy cells, revealed that mossy cells receive considerable input from local interneurons whose IPSCs enhanced the precision of triggering action potentials mediated by MFs, but also enhanced the gain and firing frequency in these cells (Kerr and Capogna, 2007). The authors showed that this phenomenon was not dependent on $I_h$ or T-type $Ca^{2+}$ channels, but instead was mediated by a de-activation of $Na^+$ conductances by hyperpolarisation.

### 1.4.4.1. $Zn^{2+}$ and synaptic plasticity

Many studies have investigated the role of $Zn^{2+}$ in synaptic plasticity because $Zn^{2+}$ is very abundant in corticolimbic structures which are important for learning and memory. An experimental model that is thought to underlie learning and memory is LTP of synaptic neurotransmission which is caused by high-frequency stimulation of afferent axons, including MFs (Bliss and Collingridge, 1993). Whether $Zn^{2+}$ modulates LTP at MF synapses is still a matter of debate. Several studies argue against an involvement of $Zn^{2+}$ in MF LTP. Quinta-Ferreira and Matias (2004) have studied the modulation of transient $Ca^{2+}$ signals by $Zn^{2+}$

during LTP, and have established that presynaptic $Ca^{2+}$ signals were maintained following perfusion of a $Zn^{2+}$ chelator without enhancing synaptic transmission. Similarly, the perfusion of CaEDTA did not prevent the induction of MF LTP following the delivery of a tetanus (Vogt *et al.*, 2000).

However, there are also several studies that argue in favour for an involvement of $Zn^{2+}$ in MF LTP. Lu *et al.* (2000) have used $Zn^{2+}$ deficient rats to compare the extent of enhancement in synaptic transmission. The authors found that MF LTP was impaired in $Zn^{2+}$ deficient animals while LTP induction at other synapses remained unchanged. Xie and Smart (1994) found that the perfusion of 100μM $Zn^{2+}$ prevented LTP at CA1 and CA3, arguing that $Zn^{2+}$ inhibited the high- and low-affinity binding site of GluN2A subunit containing NMDARs which has been shown to be necessary for LTP (Liu *et al.*, 2004). In line with this result, another study has found that perfusion of 10μM $Zn^{2+}$ blocks GluN2B subunit containing NMDARs, and so prevented long-term depression (LTD) which has been found to require GluN2B subunits but not LTP (Izumi *et al.*, 2006). Another study investigated the role of $Zn^{2+}$ in LTP at cortico-amygdala glutamatergic synapses, which are implicated in auditory fear conditioning (Kodirov *et al.*, 2006). The authors found that spillover of $Zn^{2+}$ which tonically acted on neighbouring $GABA_ARs$ at feed-forward GABAergic synapses was essential for the induction of LTP at cortico-amygdala synapses. This conclusion was inferred from the observation that the induction of LTP was prevented following the perfusion of CaEDTA and reversed by pharmacological suppression of GABAergic signalling. Huang *et al.* (2008) investigated the role of $Zn^{2+}$ at TrkB signalling which has been demonstrated previously to be activated by extracellular $Zn^{2+}$. The authors found that endogenous $Zn^{2+}$ transactivates the receptor tyrosine kinase, TrkB at the postsynaptic membrane via a non-neurotrophin mechanism. Furthermore, it was demonstrated that not only deletion of TrkB, or inhibition of kinase activity but also the perfusion of CaEDTA impaired MF LTP.

The most recent study that investigated $Zn^{2+}$ participation at MF LTP was carried out by Pan *et al.* (2011). The authors used the novel $Zn^{2+}$ chelator, ZX1, which is membrane impermeable and is endowed with rapid and selective $Zn^{2+}$ binding properties. The authors demonstrated that the perfusion of this novel $Zn^{2+}$

chelator prevented the induction of NMDAR independent LTP. In contrast, they also reported that postsynaptic NMDAR dependent LTP was inhibited by vesicular $Zn^{2+}$. The latter result was also corroborated by Evstratova and Toth (2011) as the authors could not find evidence for a modulation of $Ca^{2+}$ release by vesicular $Zn^{2+}$ at CA3 pyramidal cells which might be important for the induction of postsynaptic LTP.

Although, there are more studies in favour for an involvement of $Zn^{2+}$ on LTP, which highlights the importance of the ion on dynamic synaptic transmission, the amount of controversial results indicates that irrevocable evidence on the involvement is still lacking.

## 1.5. AIMS OF THE THESIS

The aim of this study was to investigate how $Zn^{2+}$ alters GABAergic signalling in the dentate gyrus network in the rodent. There is a wealth of evidence showing that $Zn^{2+}$ modulates glutamatergic transmission in various $Zn^{2+}$-enriched areas including the hippocampus, the amygdala or the retina. These studies have mainly focused on how $Zn^{2+}$ modulates mono-synaptic inputs and how this may be important for synaptic transmission or plasticity. However, little is known on how $Zn^{2+}$ alters di-synaptic events, particularly those mediated by $GABA_ARs$. Even further, nothing is known about $Zn^{2+}$ actions on dentate interneurons. Thus, the aim of this study was to dissect how $Zn^{2+}$ alters the functionality of interneuron networks in the dentate gyrus, particularly those activated by MF inputs.

The dentate gyrus proved a suitable model as not only MFs are particularly enriched in $Zn^{2+}$, but also because dentate GCs display powerful $GABA_AR$-mediated inhibition via local interneurons.

The main working hypotheses of this study were the following:

Firstly, it was hypothesised that $Zn^{2+}$ depresses GABAergic signalling in granule cells which was evoked by electrical stimulation in the dentate gyrus. This depression was postulated to be specific to axons that contain $Zn^{2+}$ in their terminals, such as the mossy fibre pathway. Furthermore, the question was investigated whether a possible $Zn^{2+}$ modulation is dependent on synaptic activity or synaptic release of $Zn^{2+}$ under the present conditions.

Secondly, I further hypothesised that a depression of GABAergic signalling by $Zn^{2+}$ is independent of synaptic or extrasynaptic $GABA_ARs$ in granule cells. Instead, the depression of GABAergic transmission in granule cells may be based on a modulation of axonal receptors on MFBs which ultimately results in a decrease in the release of GABA from interneurons. Alternatively, a tonic inhibition of NMDARs or VGCCs on interneurons may result in a decrease in GABA release at an interneuron-granule cells synapse. Therefore, it was

hypothesised that NMDARs or voltage-gated $Ca^{2+}$ channels located at interneurons are sensitive to a $Zn^{2+}$ block.

Thirdly, it was postulated that the excitability of interneurons in the granule cell layer may be subjected to a modulation of $Zn^{2+}$. A comparison of current clamp recordings from interneurons and granule cells may reveal a selective depression in the excitability of the interneuron by $Zn^{2+}$.

Finally, interneuron network excitability is an important determinant of principal cells integrative properties. Therefore, it was hypothesised that a depression in the excitability of fast-spiking interneurons by $Zn^{2+}$ may also influence the integration of the main excitatory input to the dentate gyrus, the perforant path.

# 2.  Methodology

## 2.1.  SLICE PREPARATION AND MAINTENANCE

All experiments were performed using male Sprague Dawley rats (Harlan Laboratories Ltd., Oxon, UK), age postnatal day 22-40 and followed UK Home Office regulations. Animals were anesthetised with isoflurane injection or placed inside a chamber which was saturated with an isoflurane/$O_2$ mixture. The level of anaesthesia was tested by a paw pinch.

### 2.1.1.  Dissection of the rat brain

Sprague Dawley rats were killed by decapitation and an incision in the scalp was made to expose the skull. Using scissors, the skull was cut along the midline, beginning from the foramen magnum. Two cuts in the medio-lateral direction at the cerebellum were made to facilitate the opening of the skull to expose the brain. Using a spatula, the brain was carefully scooped out of the skull by cutting the cranial nerves and quickly submerged into oxygenated ice-cold sucrose solution. The brain was placed onto a filter paper inside a petri-dish. Using a blade, the brain was trimmed in the coronal plane removing the olfactory bulb and the cerebellum. By cutting along the midline, the two hemispheres were separated and placed onto the medial side, lateral side facing up. An additional angled cut (~30⁰) was made along the dorsal side of the hemisphere (**figure 2.1**). For MFB recordings the angle was close to 0⁰ (Bischofberger *et al*., 2006).
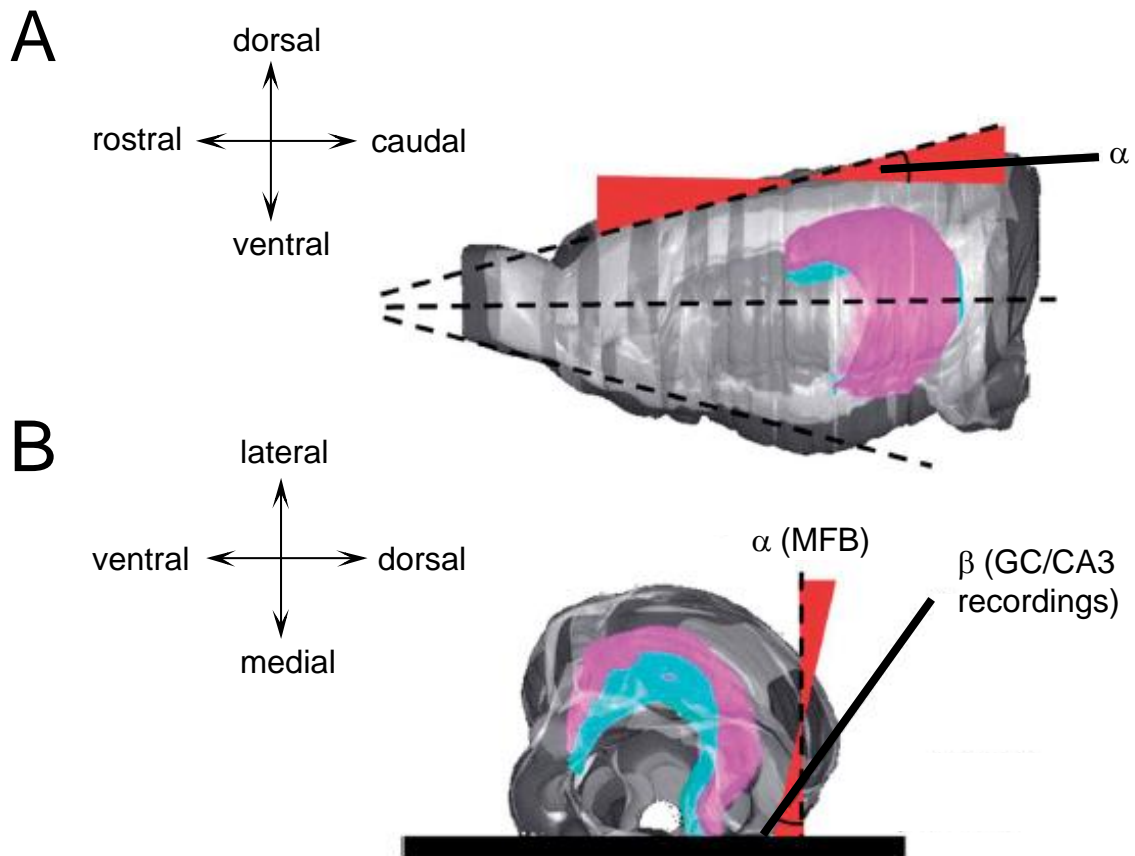
**Figure 2.1 – Dissection of the adult rat brain. A,B:** Computer reconstruction of the adult rat brain showing the hippocampal formation (pink, CA1 and CA3 areas; blue, dentate gyrus). **A** shows both hemispheres in the orientation as they were removed from the skull and **B** shows the orientation of one hemisphere after the cut along the midline and a 90⁰ turn onto the medial side. Reproduced from Bischofberger *et al.* (2006).

Using a spatula, the hemispheres were glued onto their dorsal sides on a specimen holder, placed inside a buffer tray and submerged with ice-cold sucrose solution. Transverse slices of the dorsal hippocampus were obtained using a Vibratome (Leica VT 1200S, Leica Biosystems, Nussloch, GmbH, Nussloch, Germany). Throughout the cutting process, the hemispheres were constantly oxygenated with 95% $O_2$/5% $CO_2$.

## 2.1.2. Solutions

The composition of the sucrose solution for slice cutting and slice maintenance is listed in **table 2.1**. The recipe of the artificial cerebrospinal fluid (ACSF) for perfusion during electrophysiological recordings is listed in **table 2.2**.

Table 2.1

Table 2.2

Sucrose solution

ACSF

| Substance | mM |
|---|---|
| sucrose | 75 |
| D-glucose | 10 |
| NaCl | 87 |
| $NaHCO_3$ | 25 |
| KCl | 2.5 |
| $NaH_2PO_4$ | 1.25 |
| $MgCl_2$ | 7 |
| $CaCl_2$ | 0.5 |

| Substance | mM |
|---|---|
| NaCl | 125 |
| $NaHCO_3$ | 25 |
| KCl | 2.5 |
| $NaH_2PO_4$ | 1.25 |
| D-glucose | 25 |
| $MgCl_2$ | 1 |
| $CaCl_2$ | 2 |

The osmolarity and pH of both solutions were adjusted to ~320 mOsmol/L and 7.3, respectively.

## 2.1.3.  Slice maintenance

Slices were stored in a custom-made submersion chamber, designed to optimise the oxygenation process and to reduce turbulences (**figure 2.2**). To incubate slices with toxins to block $Ca^{2+}$ channel subtypes (see figures 5.20 - 5.24), slices were maintained in an interface chamber.

A
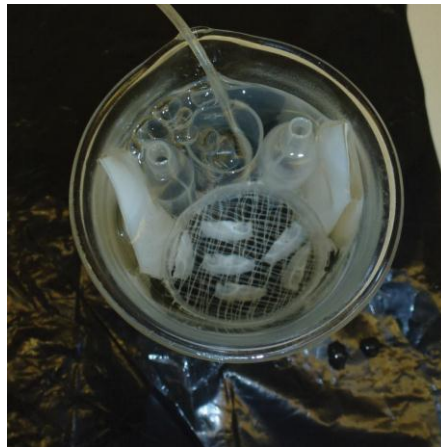


**Figure 2.2 – Submersion chamber for slice maintenance. A:** Picture of the custom-made submersion chamber showing the cotton mesh that holds the brain slices. The chamber is filled with sucrose solution which is then gassed with 95% $O_2$/5% $CO_2$ through a plastic tube to reduce turbulences.

Subsequent to slice cutting, the slices were incubated for 20min at 36°C and then stored at least 1h at room temperature. All experiments were performed at 22°C.

## 2.2.  ELECTROPHYSIOLOGICAL RECORDINGS

### 2.2.1.  Recording equipment

The experimental set-up is shown in **figure 2.3** and a schematic diagram of the recording equipment is shown in **figure 2.4**.

A
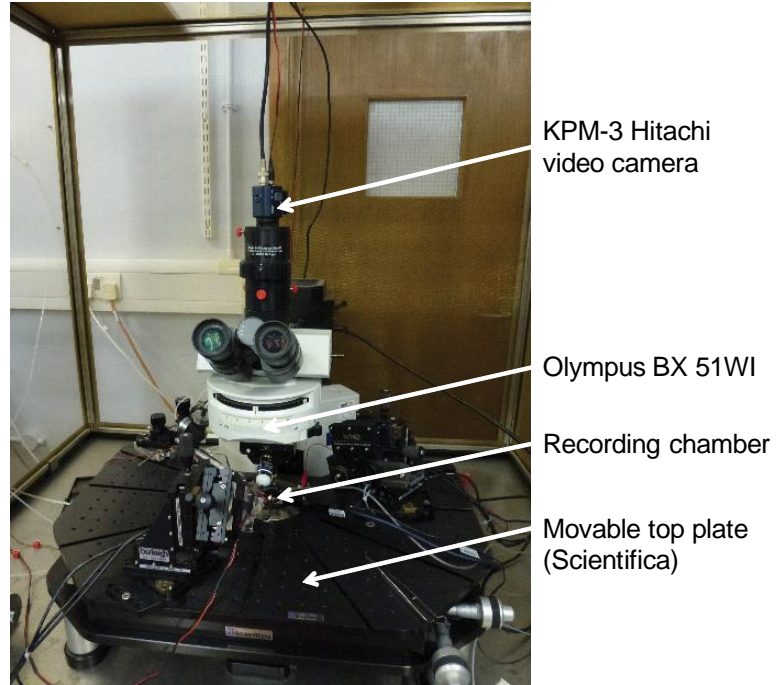


B
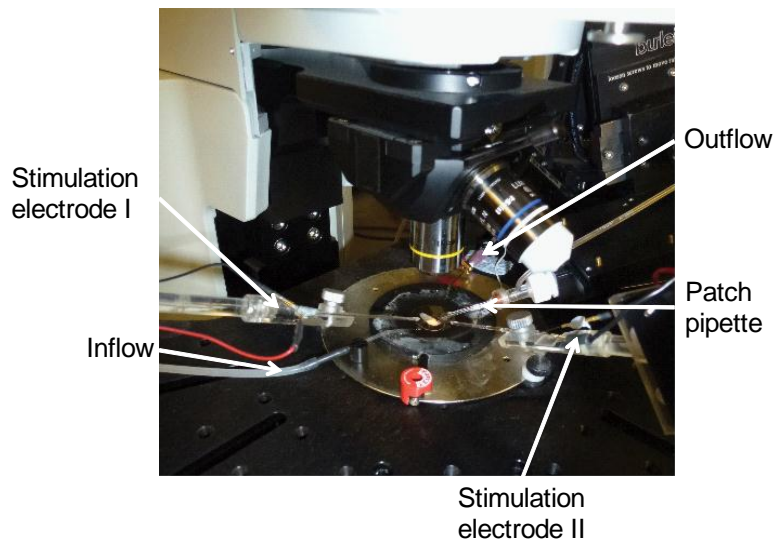


**Figure 2.3 – Experimental set-up. A:** Overview picture of the recording set-up. **B:** Close-up showing a hippocampal slice in the recording chamber with two extracellular stimulation electrodes positioned in the tissue.

A
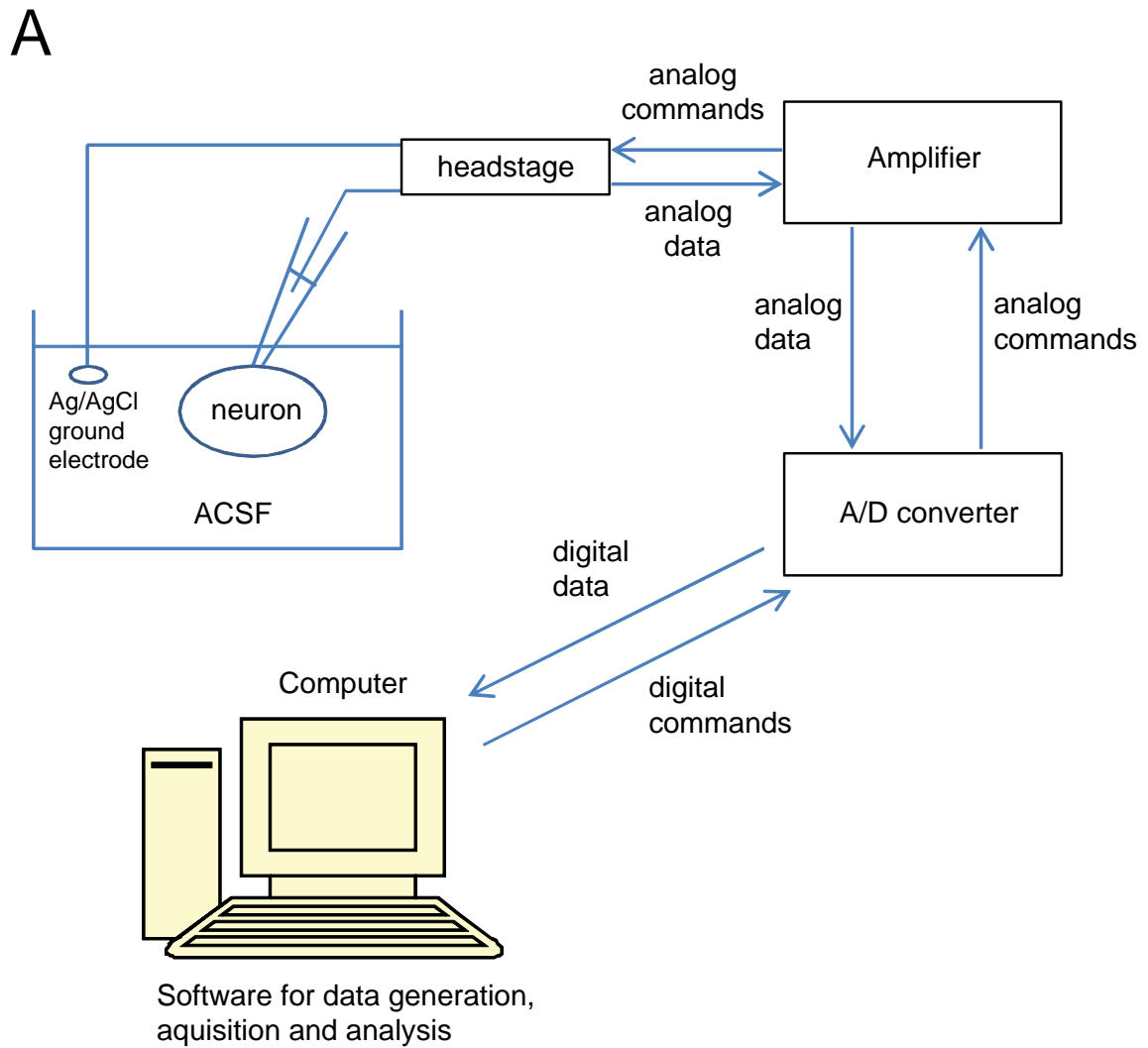


**Figure 2.4 – Schematic diagram of the recording equipment. A:** Diagram shows the wiring between the headstage, the amplifier, A/D converter and the personal computer.

A slice was transferred into the recording chamber and was secured by nylon strings attached to a platinum wire. Perfusion rate was set to 2 ml/min. The slice was visualised with an Olympus BX 51WI microscope (Olympus Europa Holding GmbH, Hamburg, Germany) which was connected to a KPM-3 Hitachi infrared (IR) video camera. Stimulation electrodes (bipolar tungsten electrodes purchased from FHC Inc. Bowdoin, Maine, USA) were positioned under a low magnification (10x) objective (Olympus) while for patch-clamp experiments neurons were visualised under IR-differential interference contrast (DIC) imaging with a water-emersion high magnification (60x) objective (Olympus) and a fourfold magnification changer (Luigs & Neumann GmbH, Ratingen, Germany). The recording equipment consisted of an Axopatch 200B amplifier (Axon Instruments, Union City, USA) that fed analog data to an A/D converter. Data were collected and analysed with custom-built routines in the LabVIEW environment (version 5.1) using National Instruments drivers and were stored on a personal computer (**figure 2.4**).

## 2.2.2. **Whole-cell patch-clamp**

### 2.2.2.1. Strategy

Whole-cell recordings were obtained from GCs, dentate BCs, SL interneurons and CA3 pyramidal neurons. In the dentate gyrus, GCs and BCs can be distinguished by their distinct size and shape of their somata under IR-DIC (GCs: ovoid 10µM somata; BCs: pyramidal 25µM somata). In addition, GCs are clustered in the GCL (**figure 2.5**), whereas BCs are mainly found at the border of the hilus and GCL.

A
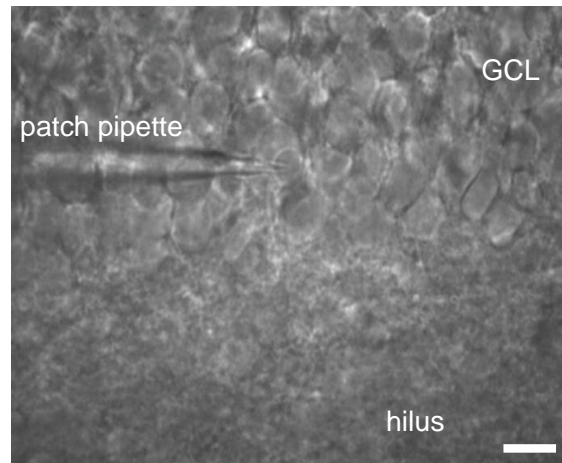


**Figure 2.5 – High magnification IR-DIC image of the GCL of the dentate gyrus. A:** The picture shows part of the crest of the GCL and the hilus while patching a GC. Scale bar 20µm.

For current-clamp recordings, BCs can also be identified by their ability to fire non-adapting trains of action potentials. Similarly, in the CA3 area of the hippocampus, SL interneurons and pyramidal cells can also be distinguished by their distinct size of their somata. In addition, 0.4% biocytin was included in the patch pipette in order to reveal their morphology *post-hoc.*

### 2.2.2.2. Patch pipettes and intracellular solutions

Patch pipettes were pulled from borosilicate capillaries (outer diameter of 1.50mm and inner diameter of 0.86mm purchased from Harvard Apparatus Ltd., Edenbridge, UK) with a Flaming/Brown micropipette puller (Model P-97, Sutter Instruments Co., California, USA). Heat settings were adjusted so that pipettes had resistances of 4-6MΩ for GCs and 2-3MΩ for BCs.

The pipette solutions used for whole-cell recordings are listed in **tables 2.3 – 2.6**.

Table 2.3

Table 2.4

Voltage-clamp - high $Cl^-$

Voltage-clamp - low $Cl^-$

| Substance | mM |
| --- | --- |
| CsCl | 120 |
| QX314 Br | 5 |
| NaCl | 8 |
| $MgCl_2$ | 0.2 |
| HEPES | 10 |
| EGTA | 2 |
| MgATP | 2 |
| $Na_3GTP$ | 0.3 |

| Substance | mM |
| --- | --- |
| Cs-gluconate | 135 |
| QX314 Br | 5 |
| NaCl | 8 |
| HEPES | 10 |
| EGTA | 0.2 |
| MgATP | 2 |
| $Na_3GTP$ | 0.3 |

Table 2.5

Table 2.6

Current-clamp - high $Cl^-$

Current-clamp - low $Cl^-$

| Substance | mM |
| --- | --- |
| KCl | 150 |
| EGTA | 10 |
| HEPES | 10 |
| NaCl | 8 |
| $MgCl_2$ | 4 |
| MgATP | 4 |
| $Na_3GTP$ | 0.3 |
| Na-phospho-creatine | 10 |

| Substance | mM |
| --- | --- |
| K-methane-sulphonate | 145 |
| EGTA | 2 |
| HEPES | 10 |
| NaCl | 5 |
| $MgCl_2$ | 2 |
| $Na_2ATP$ | 2 |
| $Na_3GTP$ | 0.5 |
| Na-phospho-creatine | 5 |

The osmolarity and pH of all intracellular solutions were adjusted to ~310 mOsmol/L and 7.3, respectively. For voltage-clamp recordings in which cells were held at $V_{holding}$ = -70mV (see figures in chapters 4 and 5), CsCl (**table 2.3**) was included in the solution in order to increase the driving force for $Cl^-$ (reversal potential for $Cl^-$, $E_{Cl^-}$ = -1mV). In contrast, for voltage-clamp recordings in which

cells were held at the reversal potential for glutamate receptors, $V_{holding}$ = 0mV (see figures 4.13, 5.11, 5.18, chapter 6), Cs-gluconate (**table 2.4**) was used instead ($E_{Cl^-}$ = -72mV). Similarly, for recordings in current-clamp mode, pipette solutions with high Cl⁻ ($E_{Cl^-}$ = +6mV, **table 2.5**, for spike-timing experiments) and low Cl⁻ concentrations ($E_{Cl^-}$ = -69mV, **table 2.6,** spiking properties of neurons) were used.

### 2.2.2.3.  Experimental approaches

For postsynaptic current (PSC) recordings, two bipolar tungsten stimulation electrodes were used to evoke PSCs. One was positioned in SL of CA3 in order to activate MFs and the other electrode was positioned in SG to recruit local interneurons (stimulus intensity range: 200 – 800µV, 50µs). The stimulus intensity was chosen in an attempt to record similar responses for both stimulation electrodes. Care was taken that the stimulation electrode was only positioned in SG to recruit GABAergic fibres as opposed to within the hilus to avoid contamination of MF-mediated inputs. Access resistances were ~10-20MΩ and were monitored online throughout the experiments using a voltage step. Results were discarded if the access resistance changed by more than 20%. PSCs were filtered at 2kHz and digitized at 5 or 10kHz. The liquid junction potential (LJP) was subtracted from the membrane potential for measurements performed with CsCl- (6.1mV, **table 2.3**), CsGluconate- (18mV, **table 2.4**), KCl- (10.6mV, **table 2.5**) or K-methanesulfonate-containing pipettes (10mV, **table 2.6**). Stimuli at each pathway were delivered every 15s (0.06Hz). For PSC trains and paired pulse ratio (PPR) measurements, stimuli were delivered at 20Hz. GABA$_B$Rs were routinely blocked by CGP-52432 (5µM). AMPA/kainate and NMDARs were left unblocked unless otherwise stated. PSC recordings evoked by SL stimulation were only taken into account if currents were reversibly depressed >40% by DCG-IV (1µM), consistent with the selective sensitivity of MF synapses (Doherty *et al.*, 2004). At the end of the experiments, PSCs were confirmed to be mediated by GABA$_A$Rs by bath-application of the GABA$_A$R antagonist bicuculline (10µM).

For PSC recordings in CA3 pyramidal cells (**figure 4.13**), one tungsten electrode was positioned in stratum radiatum ~200µm away from the soma in order to evoke responses mediated by di-synaptic associational/commissural fibres. Recordings were only taken into account if they showed no DCG-IV sensitivity. Again, PSCs were confirmed to be GABAergic by perfusion of bicuculline (10µM) at the end of the experiment.

For local puff application, a picospritzer (Picospritzer III, Intracel, Unit 4, Shepreth, Herts, UK) was connected to a pipette holder designed for pressure application. For glutamate puffs, a final concentration of 100mM glutamate was prepared in ACSF and was applied at 5-30psi, for 10-450ms. To allow complete diffusion of the reagent from the slice, puffs were applied with an intertrial interval of 20s. In current-clamp configuration, glutamate was applied to the dendrites of GCs, dentate and SL interneurons, while in voltage-clamp the puff electrode was positioned in SL or SG. In a subset of experiments, the puff electrode was carefully moved from SL towards SG, as close as 100µm away from the soma while whole-cell configuration was maintained. KCl and GABA were included in the puff pipette at a concentration of 3M and 100mM, respectively.

For recording $Ca^{2+}$ currents in voltage-clamp, slices were incubated with ω-agatoxin IVA (0.5µM), ω-conotoxin GVIA (2µM) or SNX 482 (0.5µM) to block P/Q-, N- or R-type VGCCs, respectively. Slices were maintained within an interface chamber on a petri-dish containing the toxin/sucrose mixture at their final concentration at least for 2h prior to the beginning of the recording. Series resistances ($R_{ser}$ = 11-23MΩ) were compensated (voltage-clamp 60-70% correction, time lag 10µs). BCs and GCs were held at $V_{holding}$ = -70mV and a 500ms pre-pulse followed by a 1s step protocol from -90 to +20mV with 10mV increments was applied. In order to isolate $Ca^{2+}$ currents, $K^+$ channels and $Na^+$ channels were blocked by bath-application of tetraethylammonium (TEA, 5mM), 4-aminopyridine (4-AP, 2mM) and TTX (1µM). The addition of $Cs^+$ in the ACSF to block $I_h$-currents was omitted as QX314 (5mM) was included in the Cs-gluconate based internal solution (**table 2.4**) which has previously been shown to inhibit

hyperpolarisation-activated cyclic nucleotide-gated (HCN) channels (Perkins and Wong, 1995).

To evoke action currents in GCs, one stimulation electrode was positioned in SL to evoke antidromic action currents. GCs were held at $V_{holding}$ = -70mV and patch pipettes were filled with a K-methanesulphonate based solution to evoke escape currents. The stimulation strength was adjusted to evoke action currents with a probability of 50%.

For current-clamp recordings, hyperpolarising and depolarising current steps (duration 500 - 800ms) were injected every 5s to determine the current-voltage (I-V) relationship. Potentials were recorded in current-clamp "fast mode".

For spike-timing experiments, one stimulation electrode was positioned in SL to evoke MF-mediated responses, the other electrode was placed in the outer ML ~300µm away from the soma in order to activate lateral perforant path-mediated inputs to GCs. Perforant path axons and MFs were activated concomitantly with intertrial intervals of -30, -20, -10, 0, +10, +20 and +30ms, for 10 cycles. For each cell, an internal control measuring the probability for evoking a spike in response to MF or perforant path inputs was obtained separately. Stimulus intensities were adjusted so that the spike probability was 50% when perforant path and MFs were activated simultaneously.

## 2.2.3.  Extracellular recordings

To record antidromic field potentials, electrodes (resistances ~ 3MΩ, filled with ACSF) were positioned in the GCL while an extracellular stimulation electrode was positioned in SL to activate MFs.

## 2.2.4.  Mossy fibre bouton recordings

Subsequent to slice cutting, the slices were incubated for 30min at 36ºC and immediately used for the experiment. Pipettes had resistances of 7-10MΩ and were filled with a K-methanesulphonate based solution (**table 2.6**). MFBs in

SL of the hippocampal CA3 region (mainly CA3b) were identified by their small diameter (3 – 4µm), the high input resistance ($R_N > 1G\Omega$), and action potential broadening in current-clamp (Geiger and Jonas, 2000; Bischofberger *et al.*, 2006).

## 2.3. ANALYSIS

### 2.3.1. Current-clamp recordings

The I-V relationship for each neuron was determined by calculating the deflection of hyper- and depolarising current pulses at steady state potential to the resting membrane potential $V_{rest}$, and plotting them against current injection. The input resistance was then obtained by fitting the linear portion (sub-threshold) of the I-V relationship. All traces that illustrate the I-V relationship have been averaged. "Sag" ratios were determined as the ratio between the steady-state voltage and the peak voltage in response to a current injection that resulted in a membrane potential of ≥120mV. To determine the time membrane constant ($\tau$), averaged deflections of hyperpolarising potentials (less than -10mV) were fitted by a mono-exponential function. Maximum firing rates were determined by the interval between the first and the second action potential at a current step that did not inactivate $Na^+$ channels. Action potential amplitudes were measured from $V_{rest}$ preceding the current pulse. The half-spike width was determined as the duration at half-spike amplitude and was calculated offline (**figure 2.6A**).

To measure the offset and gain in dentate interneurons, the mean firing frequency was plotted against the injected current, thus yielding an input-output (I-O) relationship of each cell. Control I-O relationships were subject to non-linear fitting using:

$$f(x) = k * \ln(x) - A \tag{1}$$

where f = firing frequency (Hz), $x$ = injected current (pA), $k$ = gain (Hz pA$^{-1}$) and exp $A/k = (x - $ offset). Fitting parameters $k$ and $A$ were then used to constrain the fitting of the I-O relationship during chelation of zinc, using:

$$f(x) = m * (k * \ln(x - C) - A) \tag{2}$$

where the gain is equal to $m * k$, and $C$ is the shift in offset ($\Delta_{offset}$) (pA).

Finally, to determine the spike threshold of a neuron, the action potential was illustrated as a phase-plane plot. Here, the time derivative of the voltage (dV/dt) was plotted against the voltage and the spike threshold was evident as the voltage at which dV/dt suddenly increased (Bean, 2007).

## 2.3.2.   Voltage-clamp recordings

PSCs were analysed for their peak amplitude, latency and decay offline using LabVIEW National Instruments routines (**figure 2.6B**).

A

## Action potential



B

## PSC
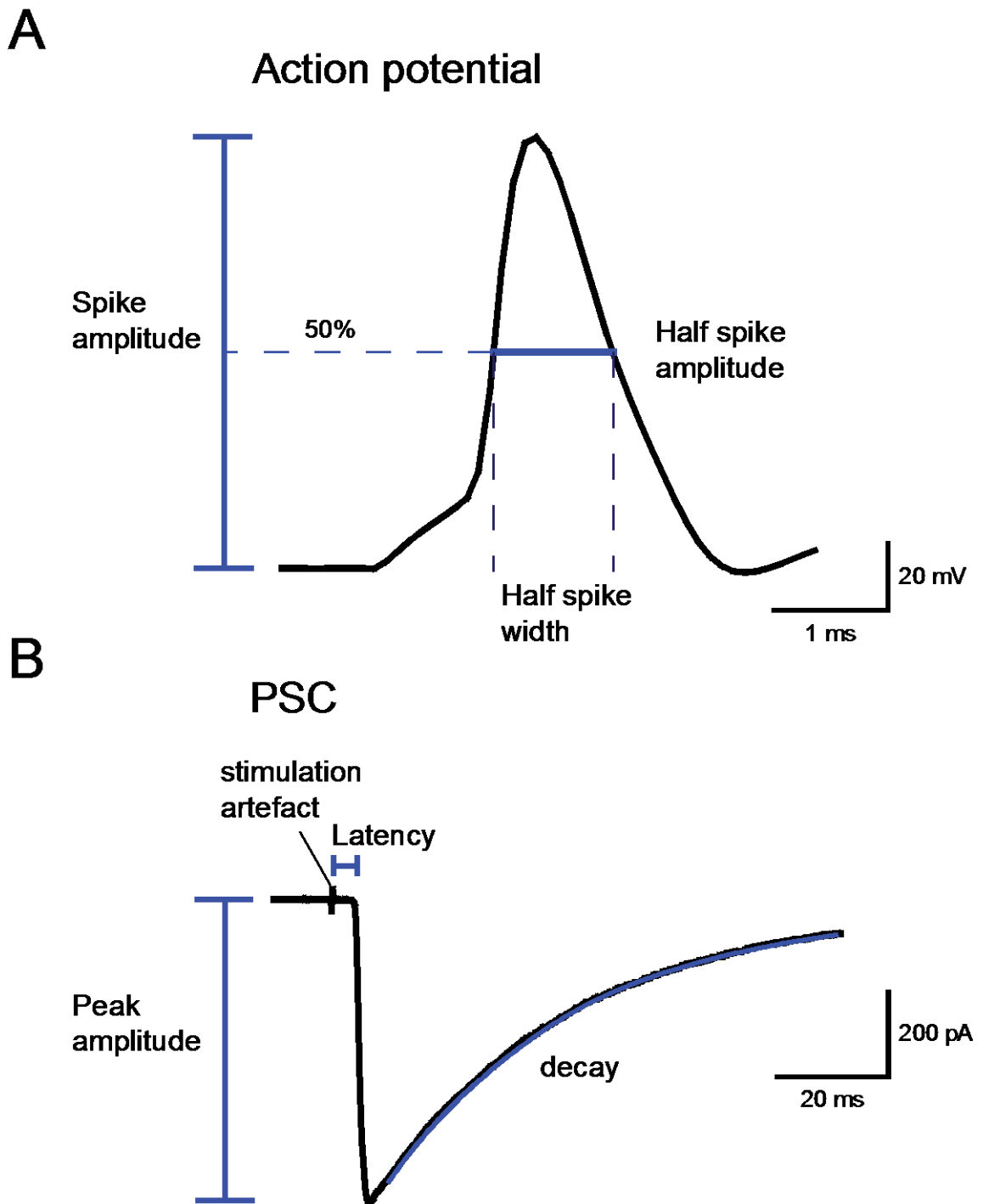


**Figure 2.6 – Analysis of action potential wave-forms and evoked PSCs. A:** Example trace of an action potential (**A**) and a PSC (**B**) with parameters which are relevant for the data analysis.

For each recording, the PSC amplitude was normalised to pre-drug PSC amplitude and the overall change in amplitude for 'n' neurons was determined by averaging normalised amplitudes expressed as a percentage. PSC traces of representative examples were averages of 10-20 traces. In some examples, stimulation artefacts were removed for clarity. The PPR was determined by dividing the peak amplitude of the second pulse by the first pulse. In order to account for insufficient neurotransmitter clearance in a high frequency train of stimuli, the response evoked by a single stimulus was subtracted from the paired responses elicited at 20Hz (50ms apart). Similarly, for train recordings, ten consecutive traces with one, two, three and four stimuli were recorded in a separate window, averaged and subsequently subtracted from the averaged train trace. The latency was determined as the time between the stimulation artefact and the onset of the response. 100 IPSC sweeps of each neuron were allotted into 1ms bins and fitted with a Gaussian distribution function to determine the mean latency. The jitter of the response was defined as the standard deviation of the latency. The decay of synaptic responses was analysed by fitting the averaged PSC with a mono-exponential function using OriginPro 8 (SR0, version 8.0724, OriginLab Corporation, Northampton, MA 01060 USA).

Spontaneous IPSC events and PSCs evoked by glutamate or KCl puffs were identified as events exceeding the threshold of three times the standard deviation of the noise level. Amplitudes and interevent intervals were analysed using KPL Analyzer (version 2.1.3, Knut P. Lehre). Events were analysed for 5min or 10min in each condition for spontaneous or puff-evoked events, respectively. "Large" events were defined as events that exceeded the amplitude of 50pA.

Mean peak $Ca^{2+}$ currents were measured by determining the peak current against the steady-state current averaged for 10 cycles in each condition. To obtain the I-V relationship, current amplitude was normalised to the maximum current ($I_{max}$) at 0mV. In figures, capacitive transients were truncated for clarity.

### 2.3.3. Mossy fibre bouton recordings

Action potentials were evoked by short (1ms) depolarising current pulses. Long (500ms) depolarising and hyperpolarising current pulses (–40 to 50pA, increment 10pA) were used to determine the I-V relationship. Action potential broadening was observed with short current pulses (1ms) elicited at 50Hz.

### 2.3.4. Statistics

Statistical significance was tested by using paired t-tests, ANOVA tests or unpaired Mann-Whitney U-tests as indicated. Data was indicated to be significant if $P < 0.05$. All data are shown as mean ± standard error of the mean (SEM).

## 2.4. DRUGS

Tetraethylammonium (TEA), 4-aminopyridine (4-AP), gramicidin from *Bacillus aneurinolyticus* (mixture of gramicidins A,B,C and D), zinc chloride, nickel(II) chloride, calcium hydroxide,  ethylenediaminetetraacetic acid (EDTA), N,N,N',N'-tetrakis (2-pyridylmethyl)ethylenediamine (TPEN), L-glutamic acid monosodium, γ-aminobutyric acid (GABA), Triton (Tx-100) and all chemicals for Timm's staining (sodium sulfide, gelatin, chromium(III) potassium sulphate solution, gum arabic from acacia tree, hydroquinone, silver nitrate, trisodium citrate dihydrate, sodium thiosulfate and DPX mounting medium) were obtained from Sigma Aldrich Company Ltd. (Dorset, UK).

6-Cyano-7-nitroquinoxaline-2,3-dione (CNQX), DL-2-Amino-5-phosphonopentanoic acid (APV), N-(2,6-Dimethylphenylcarbamoylmethyl)triethylammonium bromide (QX-314), kynurenic acid, bicuculline, tetrodotoxin (TTX), ifenprodil, ω-agatoxin IVA, ω-conotoxin GVIA, SNX-482, nifedipine and (+)-MK 801 maleate were purchased from Ascent Scientific (Abcam plc, Cambridge, UK).

3-[[(3,4-Dichlorophenyl)methyl]amino]propyl] diethoxymethyl)phosphinic acid (CGP-52432), (2*S*,2'*R*,3'*R*)-2-(2',3'-Dicarboxycyclopropyl)glycine (DCG-IV),

mibefradil and (1$S$,2$S$)-2-[2-[[3-(1$H$-Benzimidazol-2-yl)propyl]methylamino]ethyl]-6-fluoro-1,2,3,4-tetrahydro-1-(1-methylethyl)-2-naphthalenyl cyclopropanecarboxylate dihydrochloride (NNC 55-0396) were obtained from Tocris Bioscience (Bristol, UK).

Alexa Fluor® 488 streptavidin was purchased from Invitrogen (Molecular Probes®, Eugene, Oregon, USA).

## 2.4.1.  Zn$^{2+}$ chelators

Two different Zn$^{2+}$ chelators were used in the present study. N,N,N',N'-tetrakis (2-pyridylmethyl)ethylenediamine (TPEN, **figure 2.7**) was shown to have a femtomolar affinity for Zn$^{2+}$, whereas its affinity for Ca$^{2+}$ is low (Zn$^{2+}$: $K_d = 10^{-15.6}$ Ca$^{2+}$: $K_d = 10^{-4.4}$). Due to its lipophilic structure, it is able to cross cell membranes and chelate Zn$^{2+}$ within the cytosol. Its chelation kinetics are considered to be fast enough to capture a transient Zn$^{2+}$ increase (Arslan *et al.*, 1985).

A

B
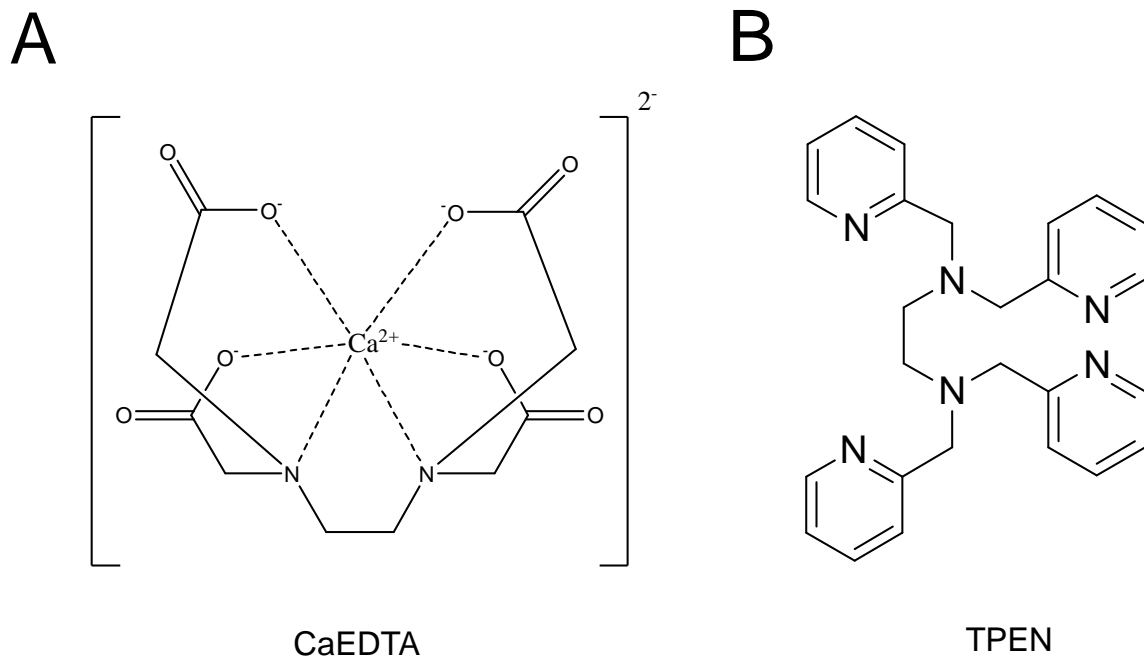
CaEDTA

TPEN

**Figure 2.7 – Chemical structures of two Zn$^{2+}$ chelators. A:** Chemical structure of the 6 co-ordinated complex between EDTA and Ca$^{2+}$. **B**: Chemical structure of the lipophilic Zn$^{2+}$ chelator TPEN**.**

In addition, a stock solution of CaEDTA was used as an alternative chelator by dissolving Ca(OH)$_2$ and ethylenediamine tetra-acetic acid (EDTA) in a 2:1 molar ratio in ACSF (**figure 2.7**). EDTA has a higher affinity to Zn$^{2+}$ than to Ca$^{2+}$ (Zn$^{2+}$: $K_d$ = 10$^{-16.4}$; Ca$^{2+}$: $K_d$ = 10$^{-10.6}$) (Dawson RMC *et al.,* 1986). The concept of saturating EDTA with Ca$^{2+}$ was first shown by Koh *et al.* (1996) and has been shown not to alter the extracellular Ca$^{2+}$ or Mg$^{2+}$ concentration. CaEDTA is membrane impermeable, so it chelates only extracellular Zn$^{2+}$.

## 2.5. HISTOLOGY

To reconstruct the morphology of neurons, 0.4% biocytin was included in the intracellular solution. To allow complete diffusion of biocytin, whole-cell mode was maintained for at least 30min. Subsequently, the patch pipette was carefully removed and slices were transferred into 4% paraformaldehyde fixative and

stored at 4ºC overnight. The fixative was exchanged with phosphate buffered saline (PBS) and washed three times 20min in PBS. Slices were permeabilised in 0.5% Triton (Tx-100). Subsequently, slices were stored in 0.1% Alexa Fluor® 488 streptavidin for 2h and then washed three times 20min in PBS. Slices were then mounted on a microscope slide in DABCO – Mowicol mounting medium and allowed to be dried overnight. Z-stacks of representative examples were obtained with a confocal laser scanning microscope (LSM 510, Carl Zeiss, Germany) and reconstructed with ImageJ (version 1.42q, Wayne Rasband, National Institutes of Health, USA).

## 2.6. TIMM'S STAINING

To stain hippocampal slices for $Zn^{2+}$ by the Timm's method, the brain of a Sprague Dawley rat was quickly removed as described in **section 2.1.1** and incubated in 0.4% sodium sulfide solution for 2h prior to fixing overnight. Hippocampal sections (40μm) were cut on a vibratome and washed several times in PBS. To coat microscope slides in gelatin, they were submerged into water for 20s and subsequently submerged into a solution of 0.5% gelatin and 0.05% K-chromiumsulfate and left to be dried overnight. Sections were then mounted on gelatin-coated microscope slides and then allowed to be dried overnight. The slides were incubated in a developer solution containing 36% gum arabic, 1.7% hydroquinone, 0.08% silver nitrate and 2.9% sodium citrate buffer in darkness for 2h. The slides were then incubated in water in darkness for 30min and subsequently incubated in a solution of 5% sodium thiosulfate for 12min to stop the reaction. After dehydration in graded ethanol (50%, 75%, 95%, 100% ethanol for 15min each) slides were cleared in xylene and then coverslipped in DPX.

# 3.	Electrophysiological and morphological properties of dentate neurons

The following chapter describes the $Zn^{2+}$ abundance of the rat hippocampal formation and the morphological and biophysical properties of dentate neurons. Because both sub-sections have been reported previously in the literature, the objective of this chapter is to demonstrate their reproducibility under the present conditions from parameters found in the literature.

## 3.1. NEO-TIMM'S STAINING IN THE HIPPOCAMPAL FORMATION

The lamellar projections of $Zn^{2+}$-containing MF terminals determine the dense staining in the hilus of the dentate gyrus and SL of the hippocampal CA3 area which has previously been described in the literature (**figure 1.1**). A refined method of the original Timm's staining, the Danscher-Timm's staining or the neo-Timm's staining, was described by Danscher (1984) and was performed in this study in order to illustrate the abundance of $Zn^{2+}$-containing terminals within the dentate gyrus.
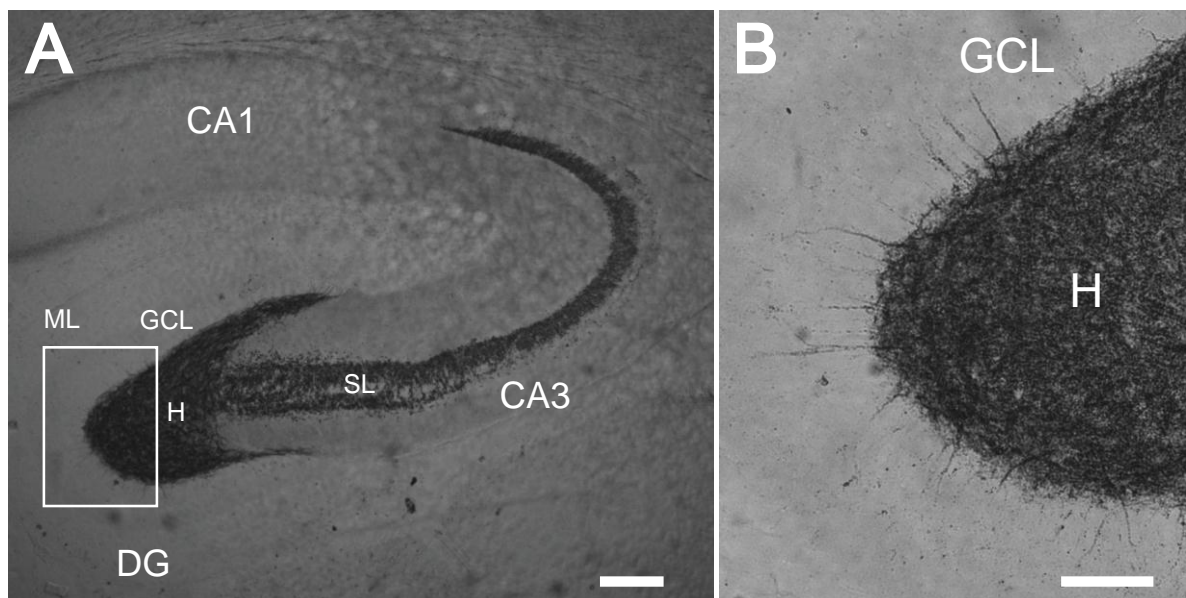


**Figure 3.1 – Neo-Timm's staining in the hippocampal formation. A:** Hippocampal rat slice stained for $Zn^{2+}$ with the Neo-Timm's method. Dense $Zn^{2+}$ staining can be observed in the hilus of the dentate gyrus and in SL of CA3. Scale bar 300µm. **B:** High-magnification image of the square box in A showing the protrusion of $Zn^{2+}$-containing fibres into the GCL. DG: dentate gyrus, H: hilus. Scale bar 100µm.

**Figure 3.1** illustrates the dense $Zn^{2+}$ staining within the hilus of the dentate gyrus and the SL of the hippocampal CA3 area. Although no $Zn^{2+}$ staining could be detected in the ML, some selective $Zn^{2+}$-containing fibres entered the GCL. Since GC - GC connections are very rare in normal rats (Claiborne *et al.*, 1986), this staining may originate from innervations of $Zn^{2+}$-containing terminals onto proximal dendrites of interneurons within the GCL such as parvalbumin positive BCs as previously reported (Ribak and Peterson, 1991; Seress *et al.*, 2001).

## 3.2. MORPHOLOGY AND BIOPHYSICAL PROPERTIES OF DENTATE NEURONS

### 3.2.1. Granule cells

In order to illustrate the electrophysiological properties of dentate GCs in this study, current-clamp recordings were performed from 11 GCs. **Figure 3.2A** shows an example of the characteristic morphology of a GC. The spiny dendrites extend into all three layers of the ML in a brush-like fashion, while the axonal collaterals remain within the hilus. Arrows indicate the giant MFBs with their filopodial extentions (inset). Few single long MFs enter SL of CA3 from which many boutons emerge.

Injections of rectangular current steps with increments of 10 or 20pA revealed an I-V relationship with a relatively high input resistance compared to other principal cells in the hippocampal formation (**figure 3.2B,C**). The majority of GCs showed a slow firing pattern with only few spikes which revealed strong adaptation and a decrease in action potential amplitude. A subset of GCs showed a small "sag", presumably due to $I_h$. Indeed, immunostaining in the dentate gyrus has shown weak HCN1 isoform expression of mRNA (Santoro *et al.*, 2000; Moosmang *et al.*, 1999), but $I_h$ was nevertheless previously recorded in GCs (Mellor *et al.*, 2002; Chevaleyre and Castillo, 2002). The intrinsic characteristics such as membrane potential ($V_m$), input resistance ($R_N$), "sag" ratio, maximum firing rate, half-amplitude spike width and spike amplitude of 11 GCs are listed in **table 3.1**. The data are displayed as histograms in **figure 3.3**. The listed parameters found

under the present conditions were comparable to those reported previously (Lubke *et al.*, 1998).

A



B



C



$R_N = 441M\Omega$

D



E
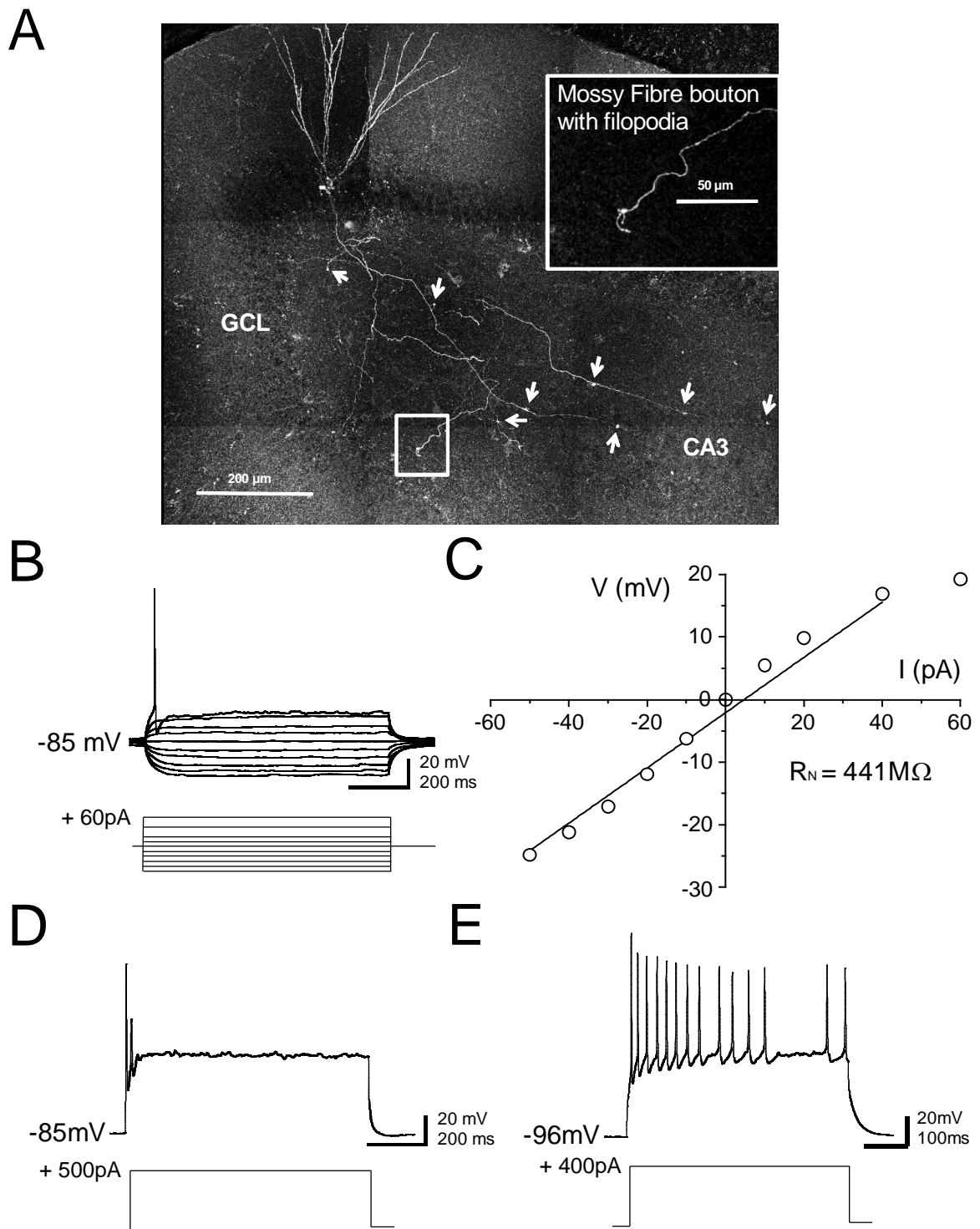


**Figure 3.2 – Morphology and electrical properties of a dentate GC. A:** Characteristic morphology of a dentate GC. Arrows indicate giant MFBs. Inset shows a MFB with filopodia. Scale bar 200µm, Inset 50µm. **B**: Voltage responses to 800ms current injections of -50 to 60pA in 10pA and 20pA increments. **C**: I-V relationship for the data shown in **B**, "sag" ratio = 0.993, $R_N$ = 441.2MΩ. **D**: Maximum firing rate was 62.5Hz (500pA current injection). **E:** Another example of a granule cell recording showing a maximum firing rate of 143Hz (400pA current injection).

Chapter 3 – Properties of dentate neurons

Table 3.1

Physiological properties of granule
cells (n = 11) in the dentate gyrus

| Parameter | Mean ± SEM | Max, Min |
|---|---|---|
| Resting Membrane Potential, mV | -82.4, ± 2.1 | -91, -72 |
| $R_N$, MΩ | 358 ± 45 | 579, 160 |
| "Sag" Ratio | 0.993 ± 0.004 | 1.006, 0.973 |
| Max. Firing Rate, $s^{-1}$ | 90.2 ± 10.9 | 167, 48 |
| Spike Width, ms | 2.65, ± 0.3 | 3.54, 1.15 |
| Spike Amplitude, mV | 100.4 ± 3.2 | 116.5, 76.7 |

A

B

C

D

E

F
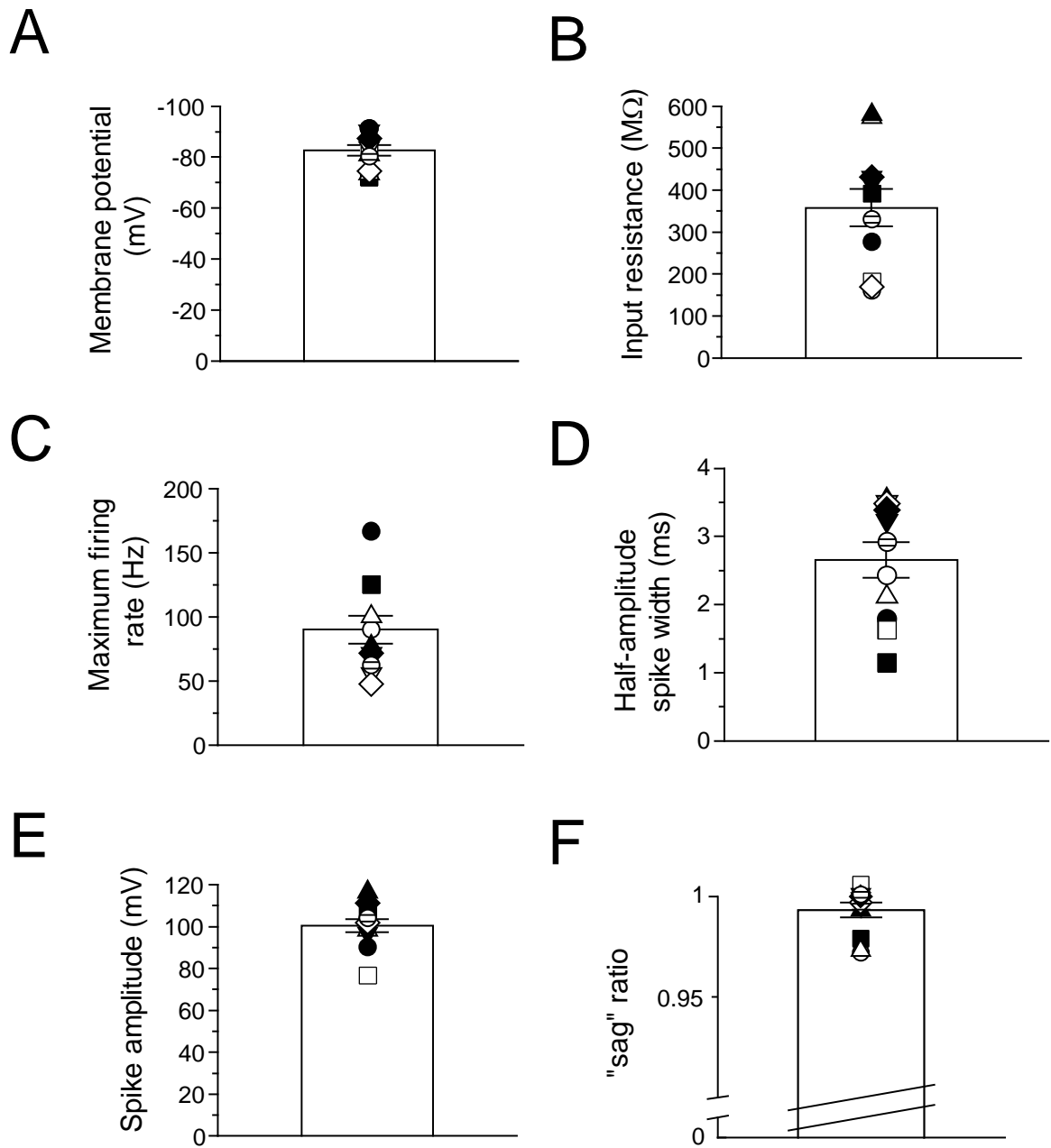
**Figure 3.3 – Passive and active properties of dentate GCs. A:** Bar graphs summarising the data for membrane potential ($V_m$, **A**), input resistance ($R_N$, **B**), maximum firing rate (**C**), half-amplitude spike width (**D**), spike amplitude (**E**) and "sag" ratio (**F**) in 11 GCs.

It has been reported by Acsady *et al.* (1998) that MFs travel a vertical distance of 400µm within the transverse axis of the hippocampus and thus may be cut during the slicing procedure. 20 GCs were filled with biocytin and their morphology was reconstructed (**figure 3.4**). Those cells whose axons were cut less than 100µm away from the soma were defined as "severed MF" whereas cells whose MFs reached the CA3 region were defined as "preserved MF". The percentage of severed and preserved MFs is shown in **table 3.2**.

Table 3.2

MF integrity of GCs in slices

| | |
|---|---|
| GCs (# total) | 20 |
| MF integrity | |
|     preserved axon | 12 (60%) |
|     severed axon | 8 (40%) |

A

preserved axon

B

cut axon with axonal "bleb"
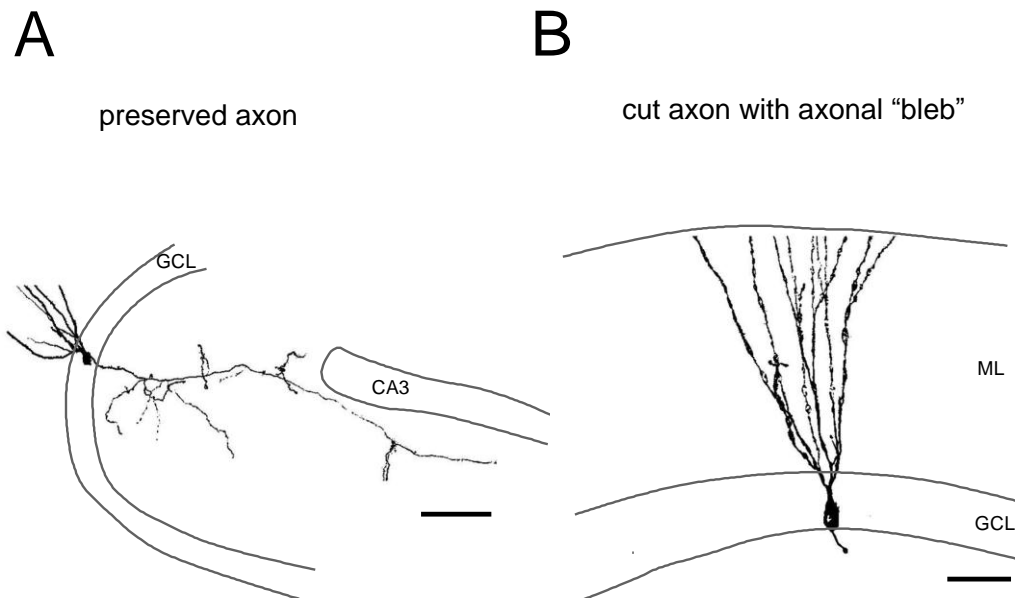


**Figure 3.4 – MF integrity of GCs in slices. A,B:** Reconstructed GCs with a preserved axon (**A**, Scale bar 100µm) and a cut axon with an axonal "bleb" (**B**, Scale bar 50µm).

The reconstruction of the morphology revealed that in a subset of GCs (8 out of 20 cells) MFs were cut by the slicing procedure (**table 3.2**). 60% of recorded GCs had intact MF collaterals and at least one MF reaching CA3 whereas 40% of GCs had severed MFs by the slicing procedure.

### 3.2.2.  Other dentate neurons

Current-clamp recordings were also obtained from non-principal dentate neurons, including interneurons which are involved in feedback and feed-forward inhibition within local networks of the dentate gyrus. To characterise their active and passive properties as well as their morphology, the I-V relationship of each neuron was obtained and biocytin was included in the pipette. There are known to be a vast variety of interneurons within the dentate gyrus (Freund and Buzsaki, 1996; Lubke *et al.*, 1998; Amaral, 1978), however for the purpose of this study, the cells were divided into non-adapting fast-spiking and adapting regular-spiking cells according to their firing pattern.

**Figure 3.5A** shows an example of the morphology of a fast-spiking interneuron. The soma was located at the border of the GCL and the hilus. Similar to GCs, the dendrites of fast-spiking interneurons spanned all layers of the ML. In contrast to GCs, the dendrites were unspiny. The axonal arbour did not enter CA3, but rather remained largely within the GCL.

The I-V relationship showed a relatively low input resistance (**figure 3.5B,D**). In a subset of cells, hyperpolarising steps showed a very small "sag" which has been previously reported in fast-spiking interneurons (Aponte *et al.*, 2006). An injection of the rheobase current, the minimal amount of current needed to reach threshold, resulted in action potentials with short duration and large AHP. Injection of high amounts of current (1nA) yielded a non-adapting high frequency firing pattern (**figure 3.5C**).

A



Hilus

GCL

ML

B

-71mV

20 mV
200 ms

+ 50pA

C

-71mV

20 mV
200 ms

+ 400 pA

D

V (mV)

20

10

-200    -150    -100    -50          50

-10

I (pA)

$R_N$ = 191MΩ

-20

-30

-40
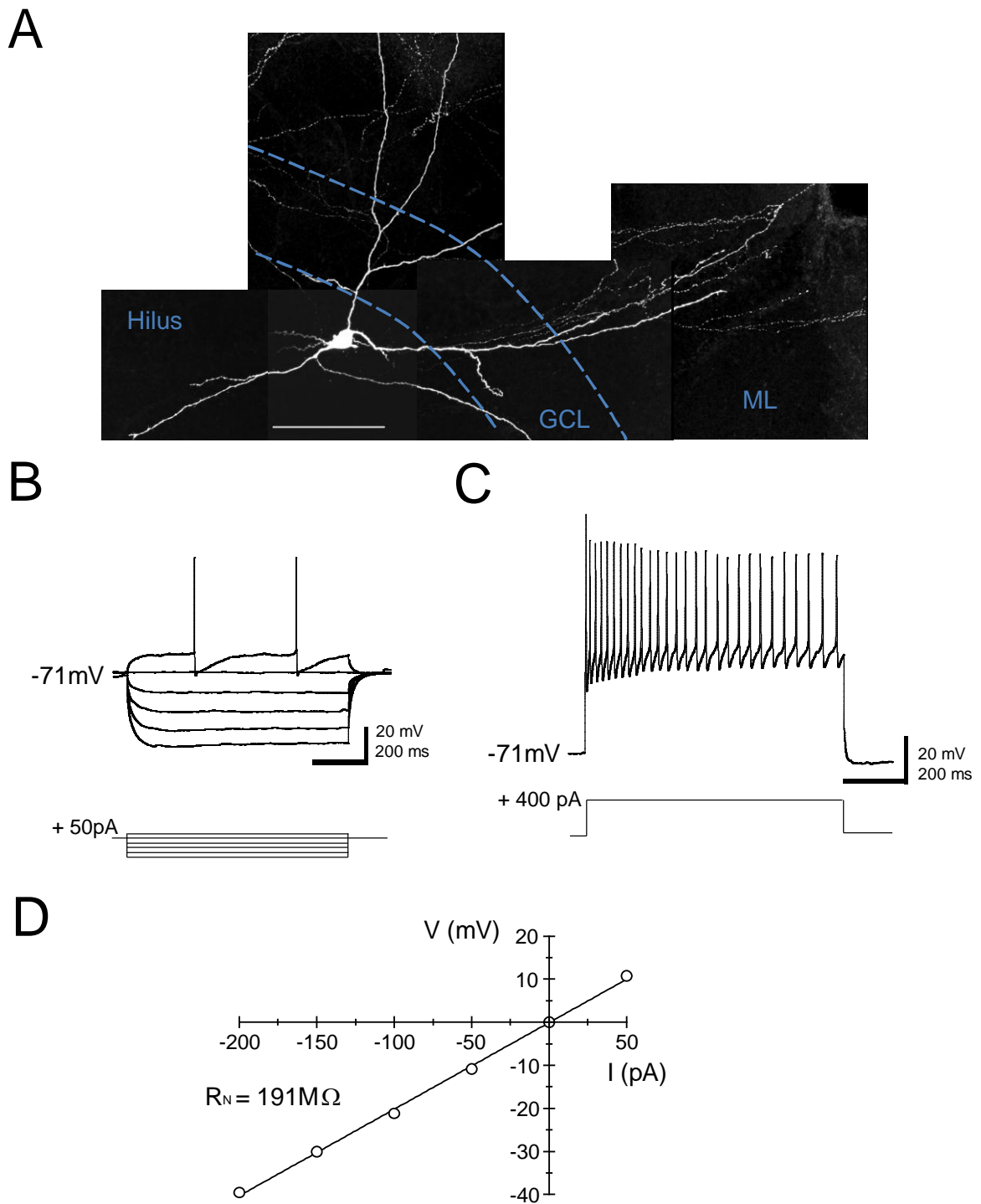
**Figure 3.5 – Electrical properties of a fast-spiking interneuron. A**: Morphology of a fast-spiking dentate interneuron. Scale bar 100µm. **B**: Voltage responses to 800ms current injections of -200 to +50pA in 50pA increments. **C**: The firing pattern is non-adapting (maximum firing rate = 90Hz for a current injection of 400pA). **D**: I-V relationship for the data shown in **B**, "sag" ratio = 0.981, $R_N$ = 191MΩ.

In contrast, **figure 3.6A** shows an example of a regular-spiking interneuron. The confocal picture shows part of the unspiny dendrites which extended both into the ML and the hilus. The soma was located at the border of the GCL and the hilus. Moreover, the axonal plexus was largely confined to the GCL resembling the morphology of an axo-axonic cell or a regular-spiking BC. The I-V relationship showed a low input resistance and a considerable "sag" following a hyperpolarising current injection (**figure 3.6B,D**). The maximum firing rate was 71Hz following moderate current injections. In contrast to the non-adapting firing pattern of a fast-spiking interneuron, the firing pattern of regular-spiking interneurons was stuttering and adapting (**figure 3.6C**).
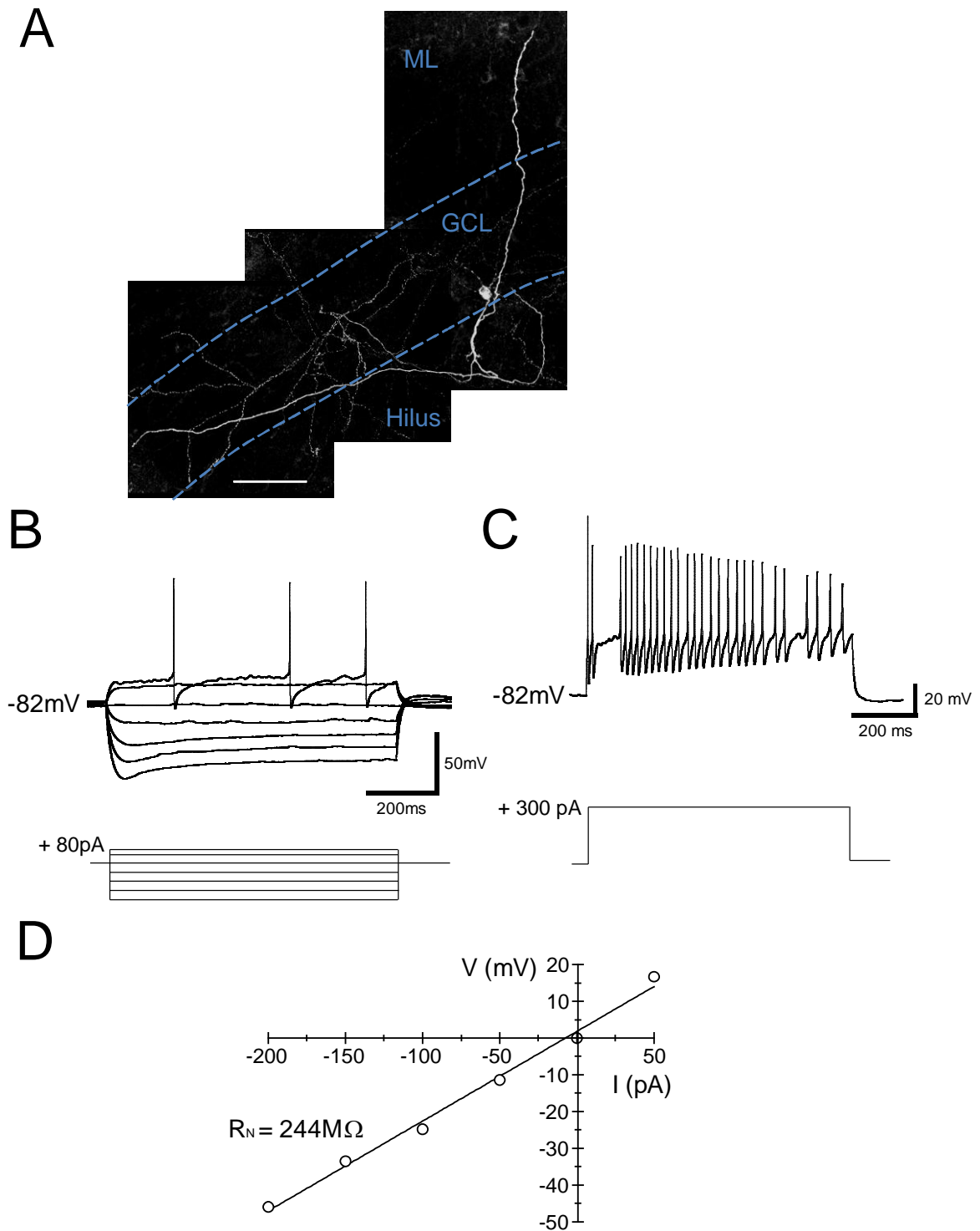
**Figure 3.6 – Electrical properties of an adapting regular-spiking interneuron. A**:
Tiled image of a dentate interneuron observed with confocal microscopy. Scale bar
100μm. **B**: Voltage responses to 800ms current injection (-200 to +80pA in 50 and 30pA
increments). Note the "sag" in response to hyperpolarising current injection and the
considerable AHP following the action potential. **C**: The maximum firing pattern is
irregular and stuttering (71Hz for a current injection of 300pA). **D**: I-V relationship for the
data shown in **B**, "sag" ratio = 0.894, $R_N$ = 244MΩ.

**Figure 3.7** shows a further example of a dentate neuron. The soma was located in the hilus and the dendritic tree was also refined to the hilus. The dendrites were covered with large spines (see inset, **figure 3.7A**) which are known to only exist in mossy cells or HIPP cells. The neuron had a relatively hyperpolarised membrane potential, and a moderate input resistance. High amounts of current injection (+400pA) yielded a firing pattern which was slow and adapting with a maximum firing rate of 48Hz.

**Table 3.3** shows the intrinsic characteristics of fast-spiking interneurons and regular-spiking interneurons such as membrane potential ($V_m$), input resistance ($R_N$), "sag" ratio, maximum firing rate, half-amplitude spike width and spike amplitude. The data are displayed as histograms in **figure 3.8**.

A



B



C



D
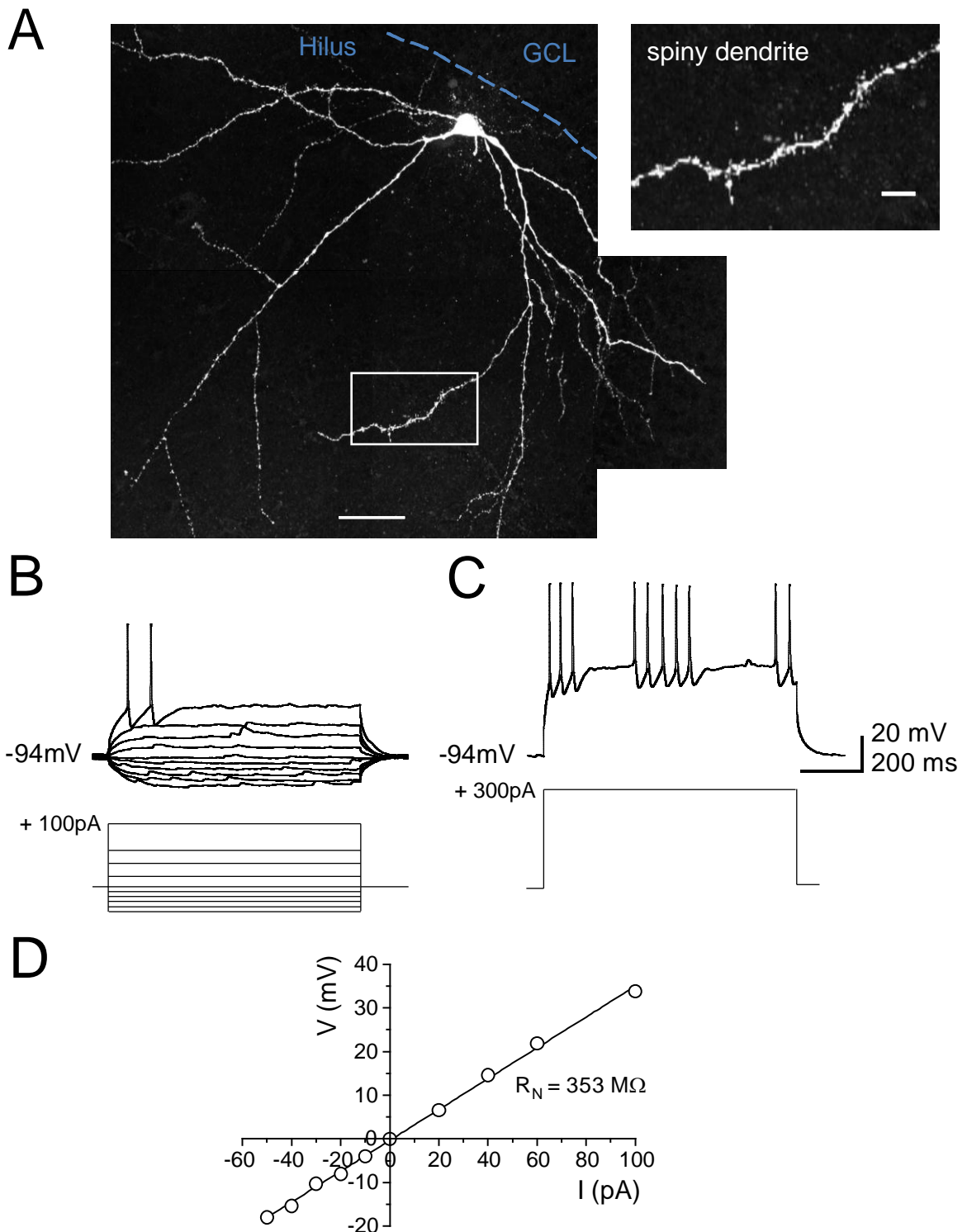


**Figure 3.7 – Electrical properties of an adapting regular-spiking neuron. A**: Confocal image of a hilar neuron. Inset shows a section of a spiny dendrite. Scale bar 50µm, inset 10µm. **B**: Voltage responses to 800ms current injection (-50 to +100pA in 10, 20 and 40pA increments). **C**: The maximum firing pattern is slow and adapting (47.6Hz for a current injection of +300pA). No "sag" is observed at the onset of a hyperpolarising current step. **D**: I-V relationship for the data shown in **B**, $R_N$ = 353MΩ.

Table 3.3

## Physiological properties of dentate interneurons

| Parameter | fast-spiking interneurons (n = 3) | | regular-spiking interneurons (n = 7) | |
|---|---|---|---|---|
| | Mean ± SEM | Max, Min | Mean ± SEM | Max, Min |
| Resting Membrane Potential, mV | -78.5, ± 3.3 | -83, -72 | -74.8, ± 3.54 | -85, -61 |
| $R_N$, MΩ | 322 ± 66.2 | 405, 191 | 262 ± 38.8 | 406, 77 |
| "Sag" Ratio | 0.943 ± 0.06 | 1.023, 0.824 | 0.913 ± 0.02 | 0.849, 1.001 |
| Max. Firing Rate, Hz | 114.3 ± 14.3 | 143, 100 | 83.9 ± 13.8 | 143, 22 |
| Spike Width, ms | 1.59, ± 0.09 | 1.71, 1.42 | 1.26, ± 0.07 | 1.59, 1.11 |
| Spike Amplitude, mV | 105 ± 12.1 | 123, 82 | 106 ± 5 | 122, 81 |
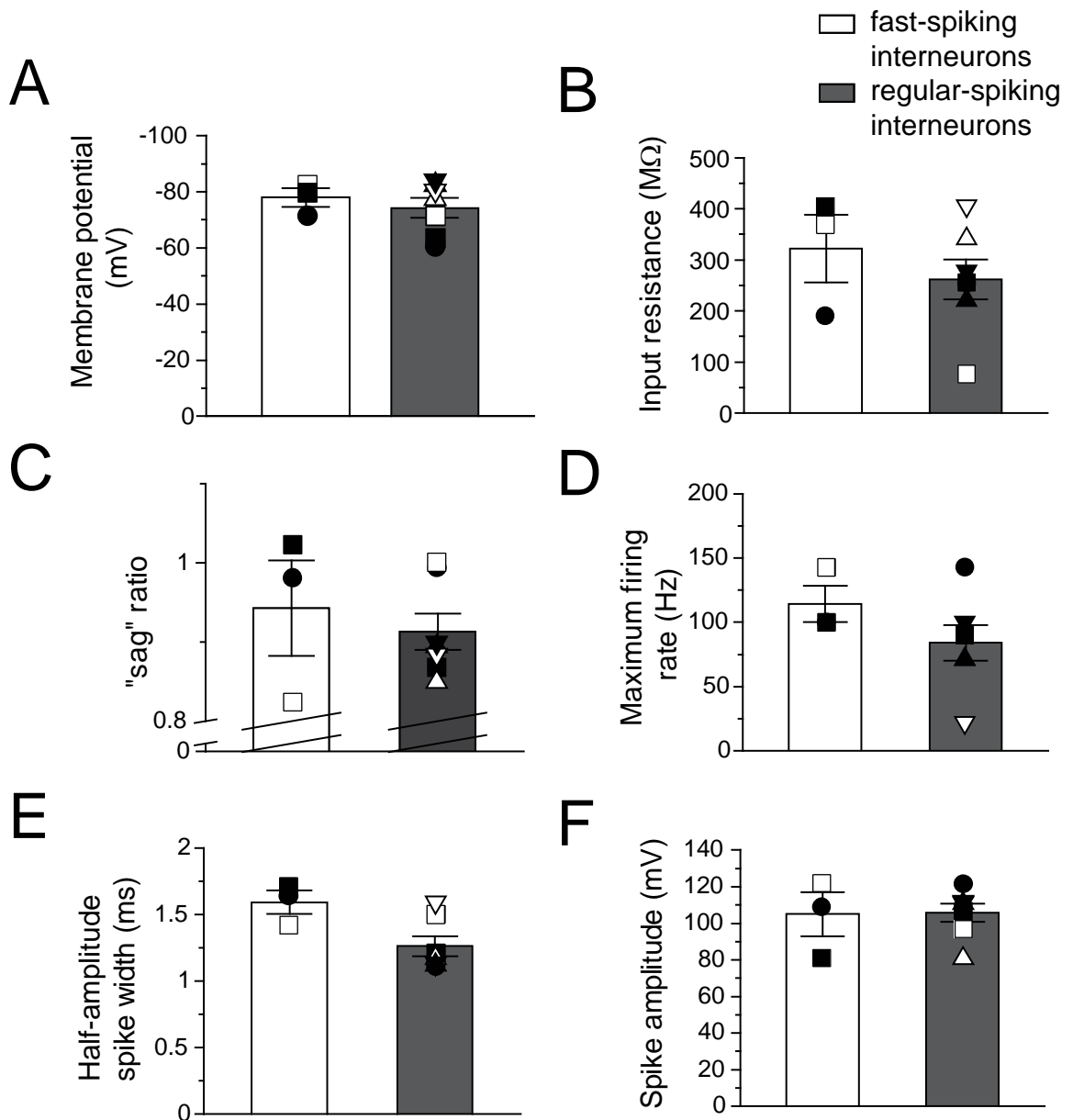
**Figure 3.8 – Passive and active properties of dentate interneurons. A:** Summary bar graphs showing the distribution of membrane potential ($V_m$, **A**), input resistance ($R_N$, **B**), "sag" ratio (**C**), maximum firing rate (**D**), half-amplitude spike width (**E**) and spike amplitude (**F**) in fast-spiking (white bars) and regular-spiking interneurons (grey bars).

Both classes of interneurons showed distinct biophysical properties from one another. Regular-spiking interneurons had slower and more stuttering firing patterns which ranged from 143 to 22Hz. In contrast, fast-spiking interneurons could be described with a non-adapting firing pattern following a current injection up to 1nA suggesting that $Na^+$ channels of these cells were much more resistant to inactivation compared to those of regular-spiking interneurons. Generally, the majority of interneurons were observed to have a more depolarised membrane potential ($V_m$), lower input resistances and usually a more pronounced "sag" compared to GCs.

In summary, active and passive properties as well as morphological differences of the main excitatory principal GCs and other dentate neurons, including fast-spiking interneurons and regular-spiking interneurons were characterised and their electrical properties compared. It was demonstrated that under the present experimental conditions, electrophysiological recordings can be made in routine and that their electrical properties are comparable to the ones found in the literature (Lubke *et al.*, 1998).

**4. Zn$^{2+}$ chelators modulate evoked IPSCs at different pathways in dentate granule cells**

## 4.1. DIFFERENTIAL ACTIVATION OF STRATA LUCIDUM AND GRANULOSUM EVOKED PATHWAYS

One tungsten electrode was positioned in SL of area CA3 to activate MFs and their collaterals and another in SG to stimulate GABAergic fibres of dentate interneurons (**figure 4.1**). To enhance the connectivity between GCs and local interneurons including dentate BCs, all experiments were performed on dorsal hippocampal slices. Dorsal slices not only have been shown to have an increased ratio of BCs to GCs (Seress and Pokorny, 1981), but also have reduced CA3 pyramidal cell collaterals compared to ventral slices (Li *et al.*, 1994).

Postsynaptic currents (PSCs) elicited at both pathways were analysed in order to measure their reversal potential, latency, pharmacological properties as well as the short-term plasticity dynamics.
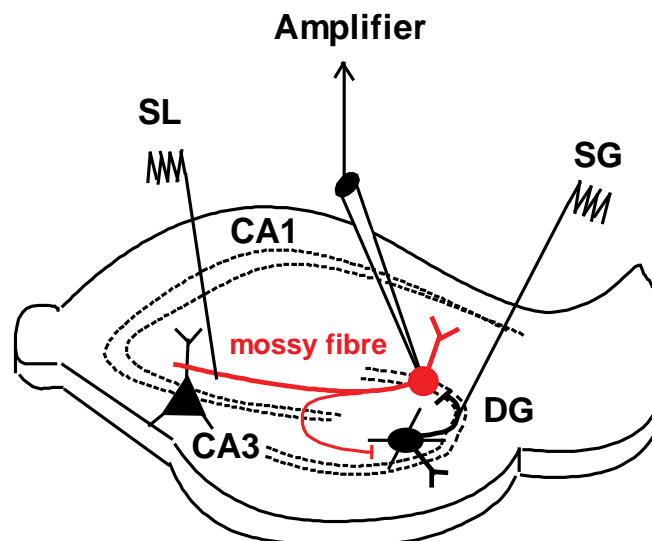


**Figure 4.1 – Experimental design. A:** Drawing of a hippocampal slice showing a stimulation electrode in SL of CA3, a second stimulation electrode in SG of the dentate gyrus and the recording electrode in a GC.

## 4.1.1. Reversal potential of PSCs

In whole-cell mode, GCs were held at $V_{holding}$ = -70mV and PSCs were inward. The reversal potential of evoked PSCs, $E_{syn}$, depended on the Cl$^-$ concentration (**figure 4.2**). When recording with a high Cl$^-$-containing intracellular solution (CsCl electrode; calculated $E_{Cl-}$ = -1mV), evoked currents had a reversal potential of $E_{syn}$ = +7.2mV and +4.6mV (corrected for LJP) for SL and SG evoked PSCs, respectively. In addition, little current rectification was observed. In contrast, when patching GCs with a low Cl$^-$-containing intracellular solution (Cs-gluconate; calculated $E_{Cl-}$ = -71.6mV), evoked currents reversed at $E_{syn}$ = -57.2mV (SL stimulation – corrected for LJP) and -45.4mV (SG stimulation – corrected for LJP) and were accompanied by a marked outward rectification, presumably following the Goldman-Hodgkin-Katz equation. The values obtained for $E_{Cl-}$ and $E_{syn}$ as well as the dependence of $E_{syn}$ on the Cl$^-$ concentration argued that the PSCs evoked at both pathways were largely mediated by a Cl$^-$ conductance.
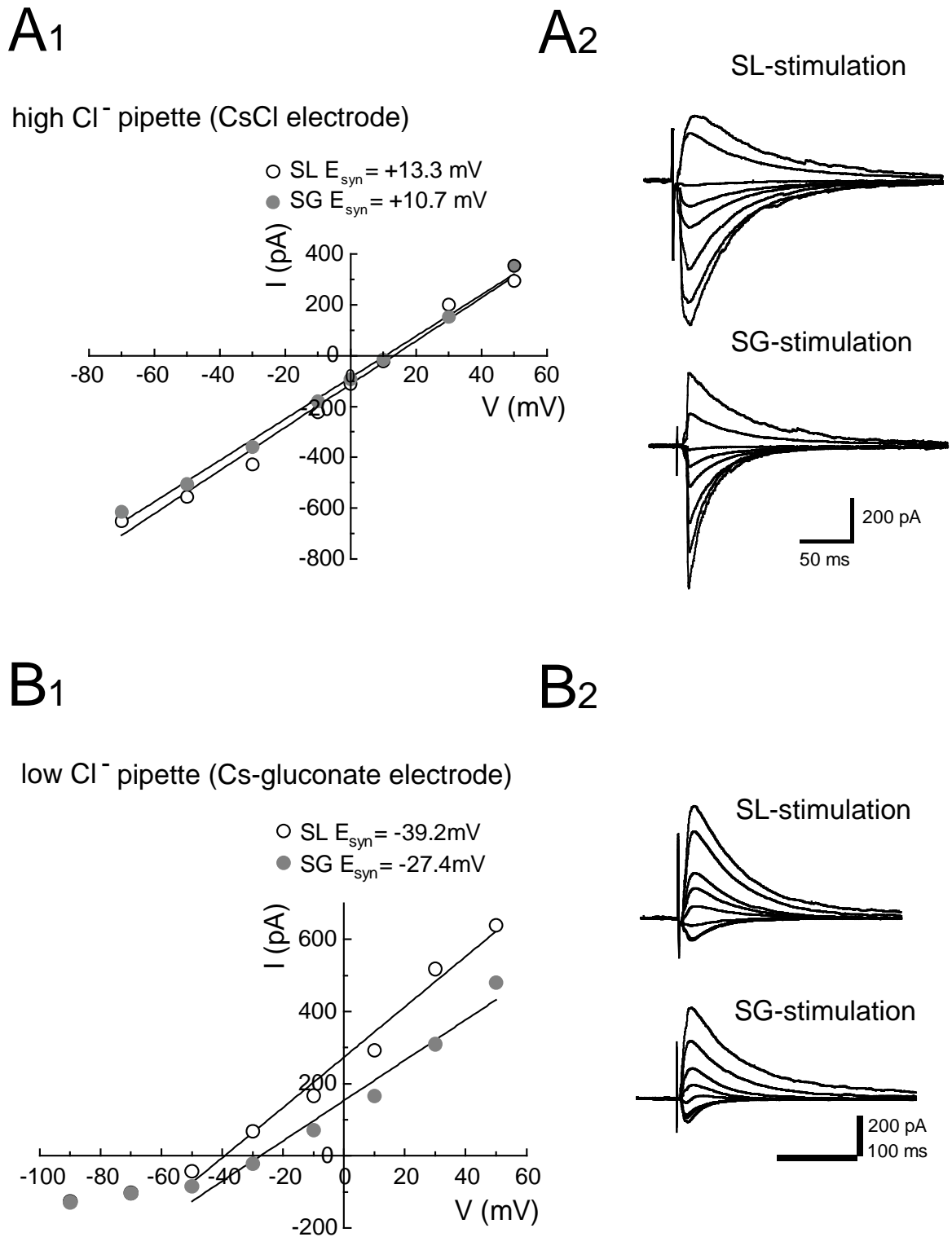
**Figure 4.2 – The reversal potential for evoked PSCs depends on the intracellular Cl⁻ concentration. A1,B1:** I-V relationship of SL (white) and SG (grey) evoked PSCs in a GC recorded with a high Cl⁻-containing pipette solution (**A1**) and a low Cl⁻ pipette solution (**B1**). A linear fit was applied to the linear portion of the data. **A2, B2:** Averaged traces of PSCs held at $V_{holding}$ = -70, -50, -30, -10, 0, 10 and 30mV.

## 4.1.2. Latency

PSCs evoked at both pathways had different latencies. Fitting the distributions of evoked PSC latencies in 15 cells with a Gaussian model yielded a latency of 7.4 ± 2.4ms (mean ± standard deviation) for SL stimulation and 3.9 ± 1.9ms for SG stimulation. The longer latency for PSCs evoked by SL stimulation accounted for the further distance of the SL stimulation electrode from the patch pipette compared to the much closer stimulation electrode in SG. Furthermore, the latency of evoked PSCs at the SL pathway had a much broader distribution, as shown by the greater standard deviation, or jitter (standard deviation SL stimulation: 2.1 ± 0.2ms). In contrast, SG evoked PSCs had a reliable unchanged onset (standard deviation SG stimulation: 1.3 ± 0.1ms, **figure 4.3A**).

# A$_1$



# A$_2$

# B
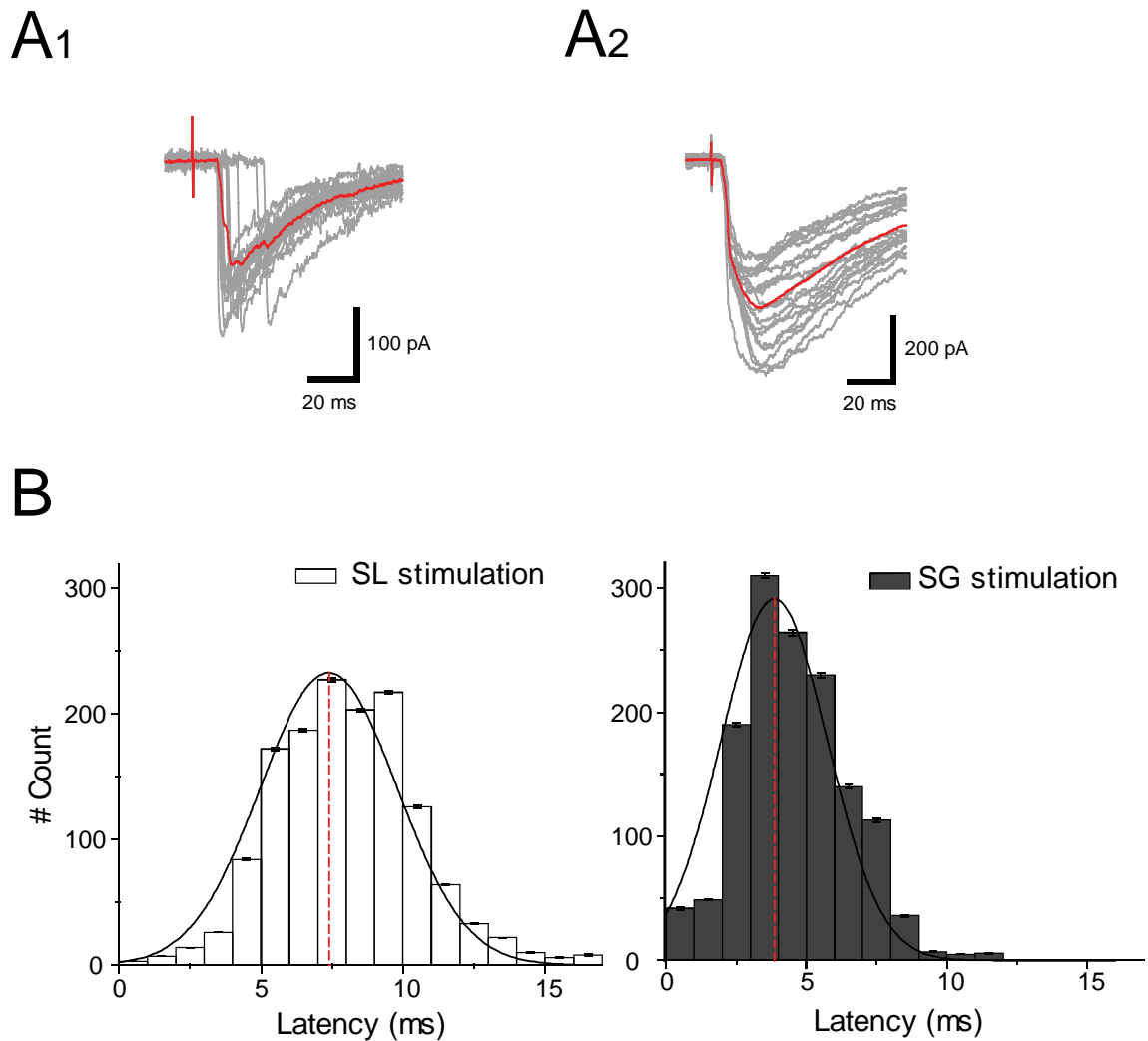


**Figure 4.3 – Distinct latencies of SL and SG evoked PSCs. A1, A2:** Example recording showing 20 consecutive traces (grey) and their mean (red) for SL evoked PSCs (**A1**) and SG evoked PSCs (**A2**). Note the jittering of the onset of the response elicited by SL stimulation. **B:** Distribution of PSC latencies for SL and SG stimulation. Data were fitted with a Gaussian function. Red dashed lines represent the mean latency of each distribution.

### 4.1.3. Pharmacology

PSCs evoked at both pathways had very different pharmacological properties. As seen in **figure 4.4**, evoked PSCs showed a differential sensitivity to bath-application of the AMPA- and kainate receptor antagonist NBQX (20µM) whereas the sensitivity to the GABA$_A$R antagonist bicuculline (10µM) was similar.

A



B



C
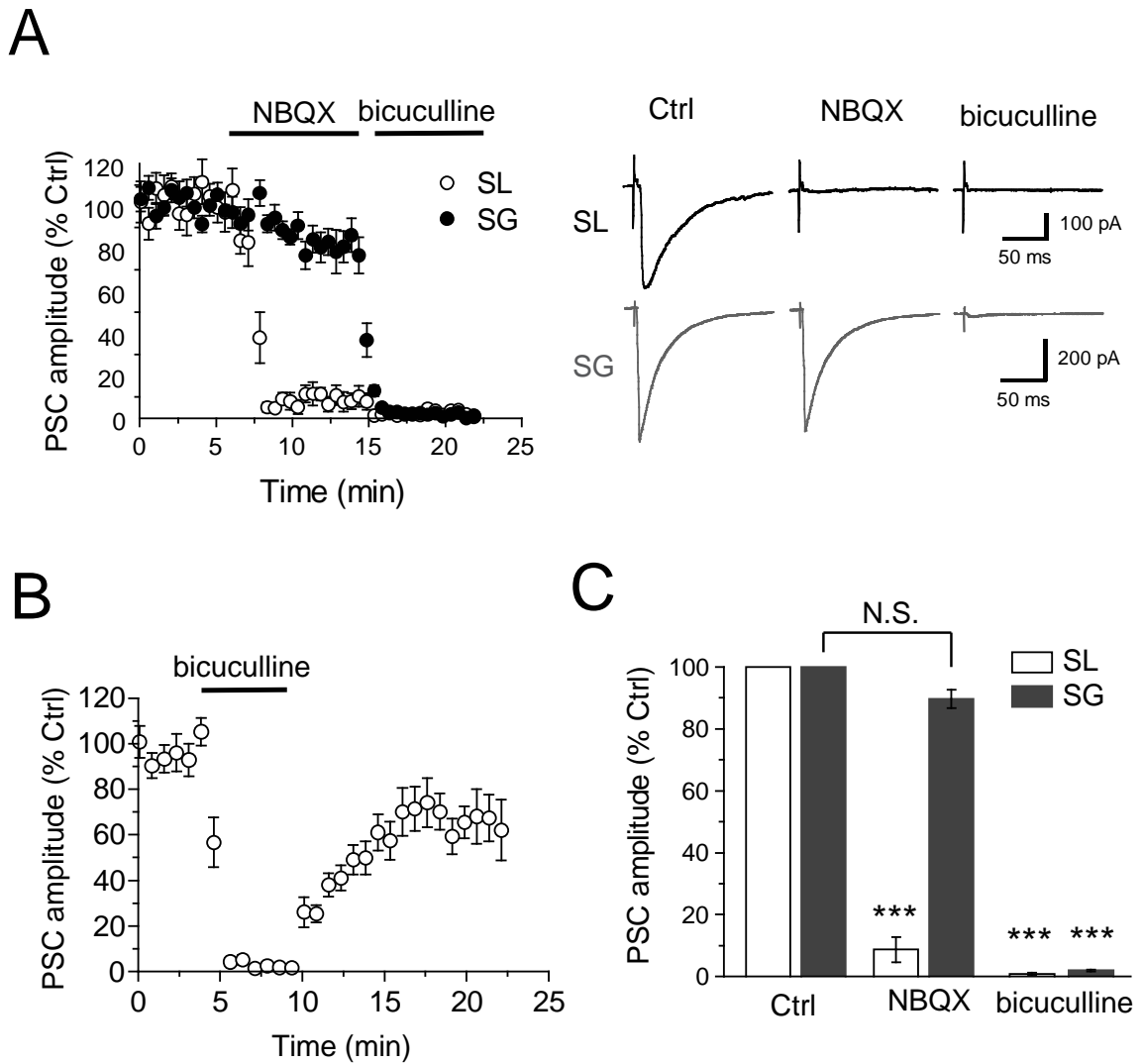


**Figure 4.4 – SL and SG evoked PSCs can be dissected pharmacologically. A:** Plot showing the amplitude of evoked PSCs against time for n = 8 cells. Superfusion of NBQX (20µM) nearly abolished SL evoked PSCs without affecting SG evoked PSCs. Bicuculline (10µM) abolished both SL and SG evoked PSCs. Traces of PSCs evoked by SL (black) and SG (grey) are shown on the right for each indicated pharmacological condition. **B:** Effect of bicuculline at the SL pathway showing the washout of bicuculline. **C:** Summary histogram of the data shown in A.

The abolishment of the currents in response to bicuculline (SL: 1.3 ± 0.4%, n = 8; SG: 2 ± 0.31%, n = 8, $P$ < 0.001 for both; **figure 4.4**) clearly indicated that the PSCs recorded at GC somata were mediated by GABA$_A$Rs. The differential sensitivity to NBQX also indicated that the responses evoked by the SL pathway were driven by excitatory fibres, releasing glutamate (SL: 11.4 ± 2.6%, n = 8, $P$ < 0.001, **figure 4.4**). This, together with the high degree of jittering in response to SL stimulation (**figure 4.3**) suggested that a poly-synaptic circuit was activated. In contrast, SG stimulation showed only little NBQX sensitivity (SG: 81.7 ± 3.2%, n = 8, $P$ > 0.1; **figure 4.4A-C**), indicating that these responses were largely driven by GABAergic fibres. The little degree of jittering (**figure 4.3**) also suggested that it may be mediated by a mono-synaptic GABAergic pathway.

To test whether SL evoked IPSCs were mediated by MF collaterals, the sensitivity of IPSCs to group II mGluRs on MF terminals was tested. The group II mGluR agonist DCG-IV down-regulates the amount of glutamate (and Zn$^{2+}$) released from the vesicles (Conn and Pin, 1997) and proved therefore a useful tool to indicate whether evoked IPSCs were indeed mediated by MFs (**figure 4.5**).

A



B
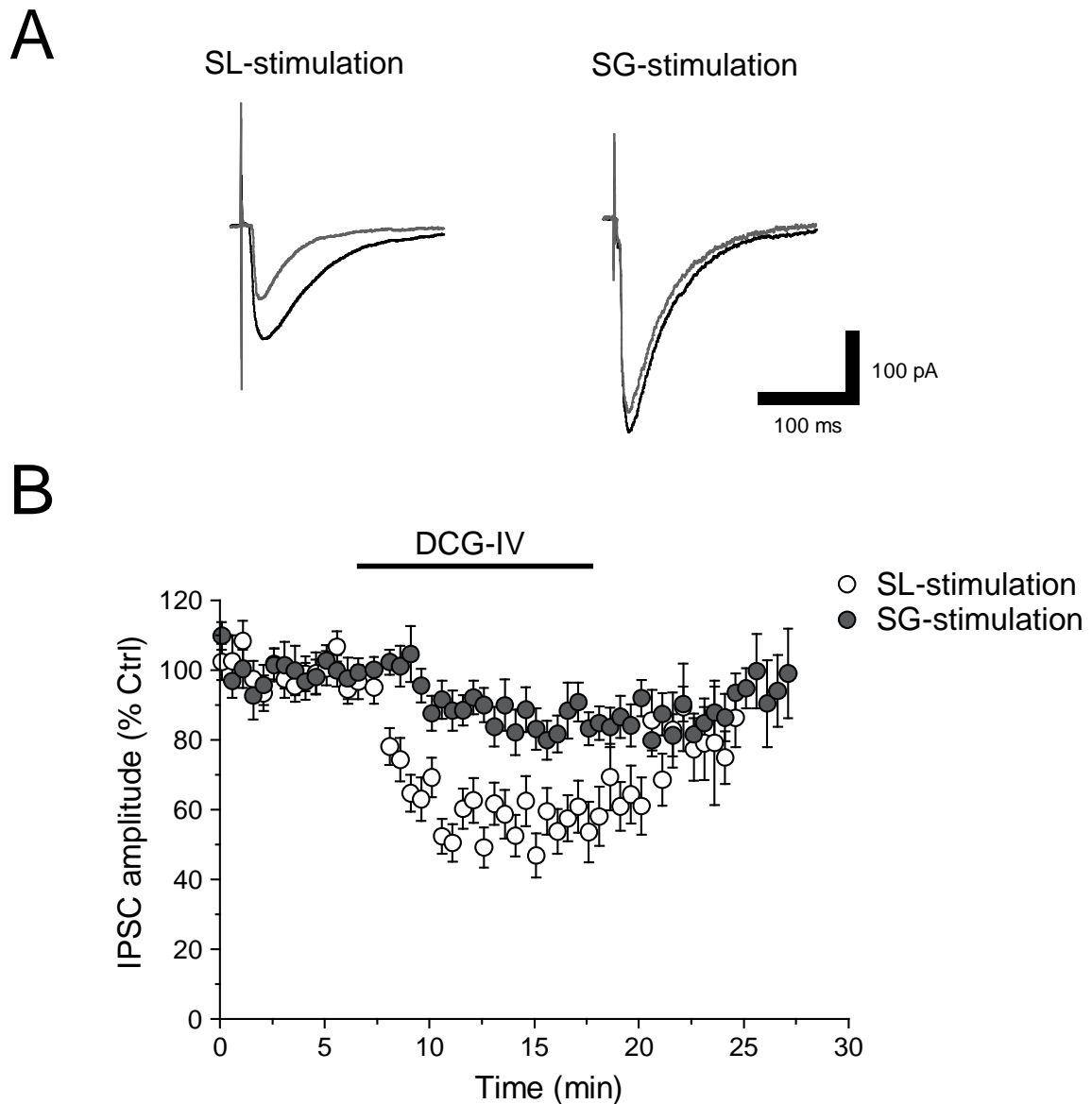


**Figure 4.5 – Differential sensitivity of SL and SG evoked IPSCs to the group II mGluR agonist DCG-IV. A:** Representative traces of IPSCs for control (black) and in the presence of DCG-IV (1µM, grey) for SL and SG stimulation. **B:** Time course of the effect of DCG-IV on the IPSC amplitude showing that SL evoked IPSCs are more sensitive to DCG-IV than those evoked by SG stimulation.

SL evoked IPSCs showed a higher sensitivity to DCG-IV (1µM) than SG evoked IPSCs (SL: 44.3 ± 2.9% depression, n = 18, $P < 0.001$; SG: 11.5 ± 2.9% depression, n = 18, $P > 0.1$, unpaired Mann-Whitney U test $P < 0.003$, **figure 4.5**), implying that SL stimulation recruited MFs. Although MF sensitivity to group II/III mGluR activation was shown to be much higher at a mono-synaptic GC-CA3 pathway (Manzoni *et al.*, 1995), the result was consistent with a study by Doherty *et al.* (2004) that also stimulated MFs in SL. The high degree of sensitivity of SL evoked IPSCs to DCG-IV and NBQX strengthened the concept that MFs activated local interneurons. In contrast, little sensitivity to both NBQX and DCG-IV indicated that SG stimulation mainly elicited mono-synaptic IPSCs with little jitter in their synaptic onset.

## 4.1.4.  Short-Term Plasticity

The short-term plastic properties of evoked IPSCs are important determinants for synaptic efficacy and have been investigated with paired recordings and high-frequency stimulation protocols previously (Kraushaar and Jonas, 2000; Doherty *et al.*, 2004). In the present conditions, the PPR for two consecutive IPSCs elicited with a 50ms interval (20Hz) was 1.31 ± 0.46 (n = 7, **figure 4.6A**) following stimulation in SG. The majority of neurons (5 out of 7 neurons) showed a depression which was in line with previous work (Kraushaar and Jonas, 2000). However, the high variability in PPR values may suggest that subsets of interneurons mediate distinct responses, as it was previously shown for CA3 and their target-specific MF synaptic transmission (Maccaferri *et al.* 1998). Although short-term dynamic properties had limited relevance for the SL pathway due to poly-synaptic activation, the PPR was compared and observed to be facilitating (PPR 1.33 ± 0.12, n = 20, **figure 4.6A**). When switching stimulation frequencies from 0.06 to 0.6Hz, evoked IPSCs underwent a reversible depression whose magnitude was similar (SL: 16.8 ± 8.2% depression, n = 18, $P > 0.05$; SG 18.3 ± 11.5% depression, n = 12, $P > 0.1$, **figure 4.6B**). Similarly, switching stimulation frequency also caused a facilitation in the IPSC amplitude in a subset of neurons, raising the possibility of target-specific MF mediated plasticity at dentate synapses.

# A

## Paired-Pulse Ratio (PPR)
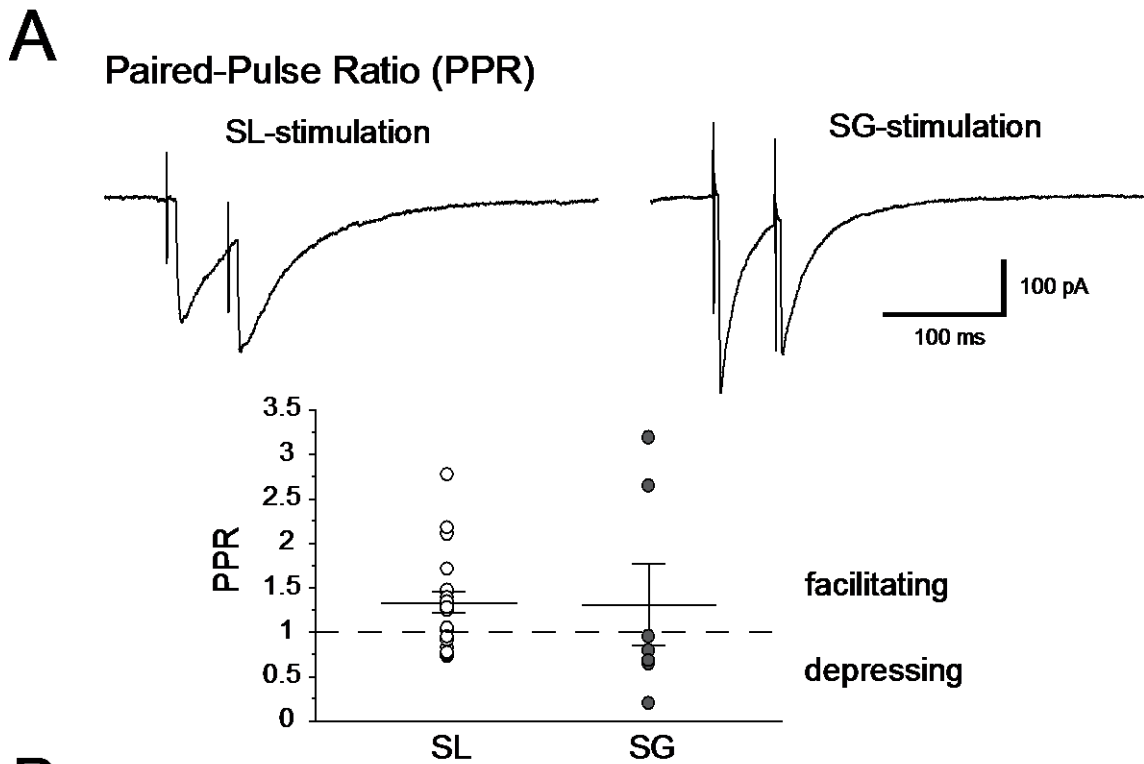


# B

## frequency dependent facilitation test
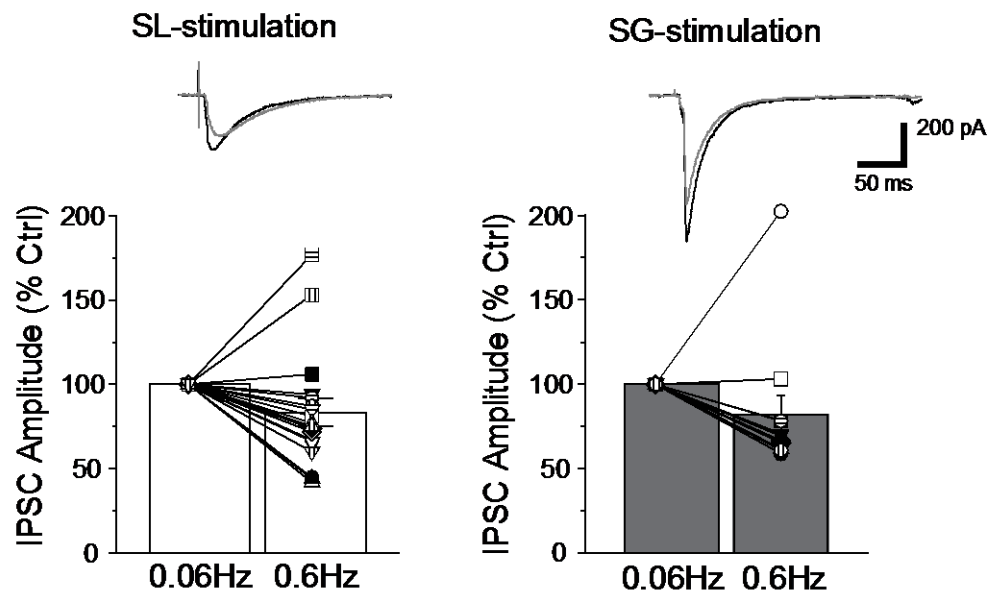


**Figure 4.6 – Short-term plasticity of SL and SG evoked IPSCs. A:** Chart showing the PPR for a 20Hz paired-pulse delivered in SL and SG. Horizontal lines depict the mean PPR. Traces of IPSC paired-pulses evoked by SL (left) and SG stimulation (right) are shown on top. **B:** Summary bar charts showing a reduction in IPSC amplitude when switching the stimulation frequency from 0.06 to 0.6Hz at the SL (white bars) and the SG pathway. IPSC traces evoked at 0.06Hz (black) and 0.6Hz (grey) are shown for both pathways.

Together these results show that due to their differential sensitivities to NBQX and abolishment of both currents by bicuculline, SL and SG stimulation may be considered in "functional" terms to activate local dentate feedback and feed-forward pathways, respectively.

## 4.2. Zn$^{2+}$ CHELATORS AND EXOGENOUS Zn$^{2+}$ MODULATE STRATA LUCIDUM AND GRANULOSUM EVOKED IPSCs IN OPPOSITE DIRECTIONS

Having described the properties of evoked IPSCs at both pathways, I investigated whether these currents are modulated by endogenous Zn$^{2+}$. In order to chelate endogenous Zn$^{2+}$, two different Zn$^{2+}$ chelators were used: 1) the membrane impermeable Zn$^{2+}$ chelator CaEDTA and 2) the membrane permeable chelator TPEN (for chemical structures refer to **figure 2.7**). **Figure 4.7 and 4.8** show examples of typical two-pathway experiment conducted in GCs.
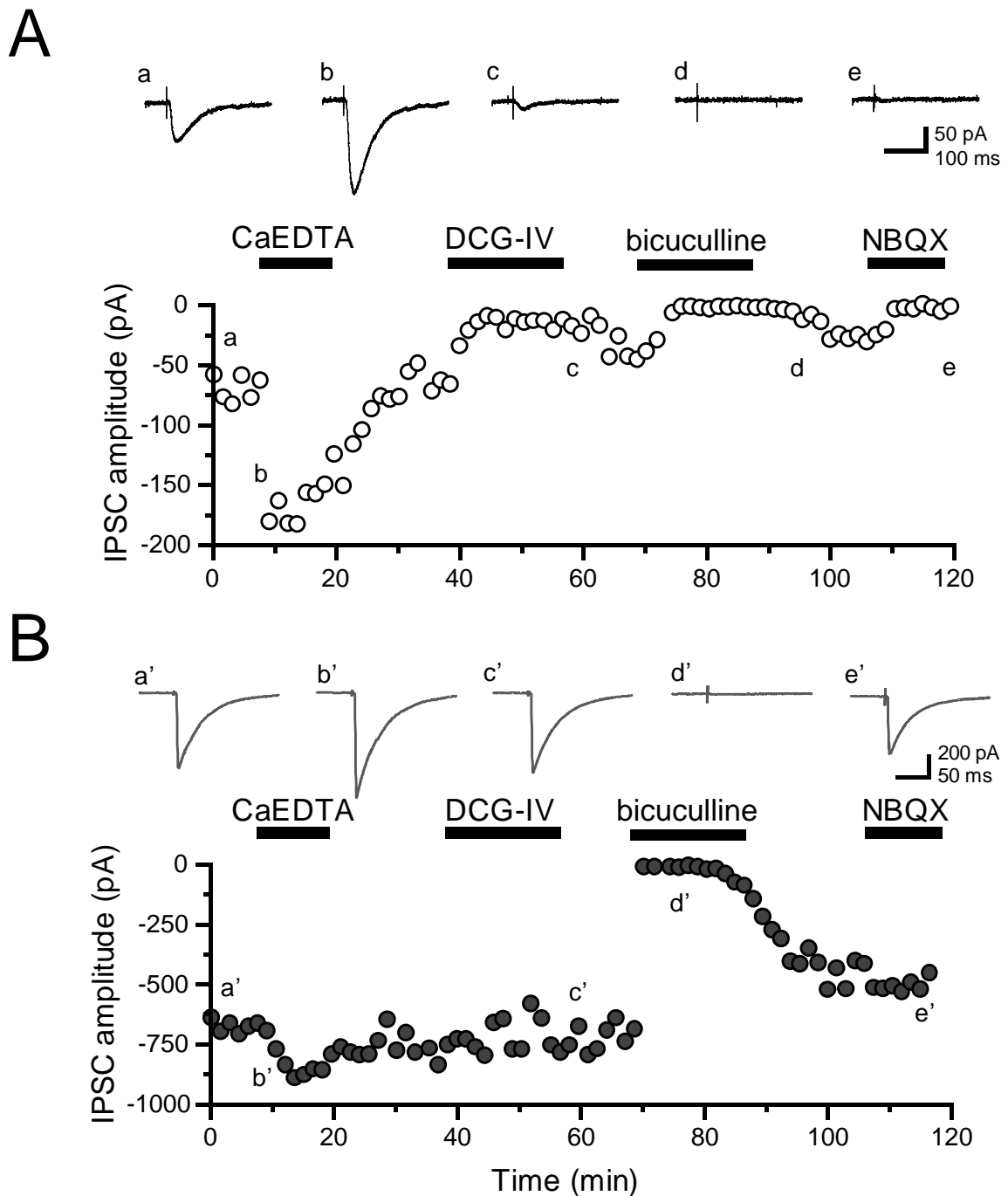
**Figure 4.7 – CaEDTA increases IPSC amplitude at both pathways. A, B:** Example taken from a GC recording showing PSCs evoked by SL (**A**, white circles) and SG (**B**, grey circles) stimulation. Superfusion of CaEDTA (2mM) increases PSC amplitude at both pathways whereas DCG–IV (1µM) selectively depresses PSCs elicited by SL stimuli. Evoked PSCs are fully abolished by addition of bicuculline (10µM) whereas addition of NBQX (20µM) only depresses SL evoked PSCs. Traces of PSCs for SL (a–e) and SG stimulation (a'–e') are shown at time indicated.
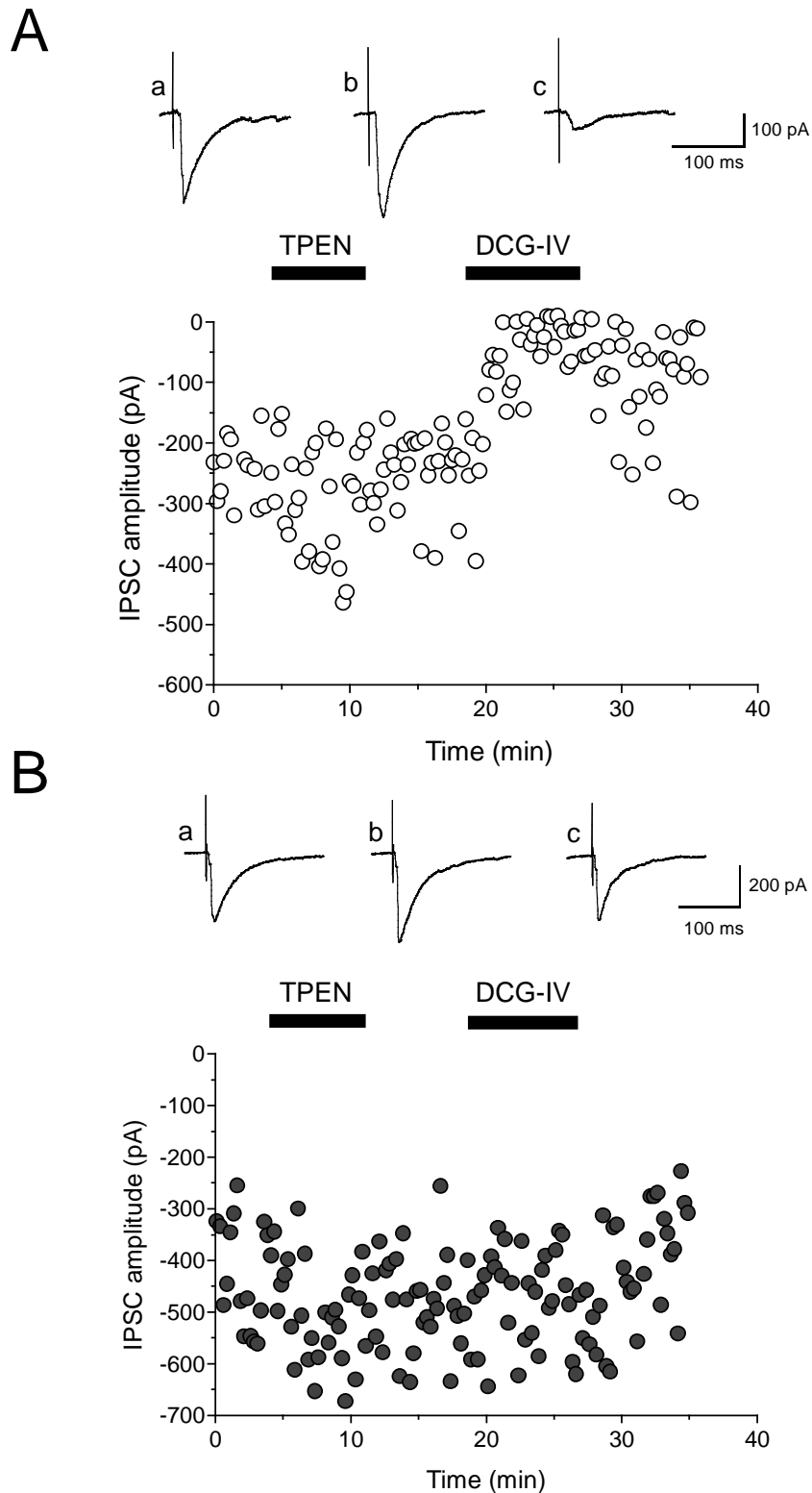
**Figure 4.8 – TPEN increases IPSC amplitude at both pathways. A, B:** Example taken from a GC recording showing PSCs evoked by SL (**A**, white circles) and SG (**B**, grey circles) stimulation. Superfusion of TPEN (1μM) increases PSC amplitude at both pathways whereas DCG–IV (1μM) selectively depresses PSCs elicited by SL stimuli.

Bath-application of CaEDTA (2mM) reversibly facilitated SL evoked IPSCs by 69% (**figure 4.7A**). Furthermore, the IPSC amplitude was reduced by DCG-IV (1µM) and was abolished by bicuculline (10µM) and subsequent application of NBQX (20µM) showing the differential sensitivity and MF component of a di-synaptic GABAergic current. Interestingly, evoked IPSCs by SG stimulation also showed a facilitation following CaEDTA application of 32%. IPSCs were less sensitive to DCG-IV (14% depression) and only bicuculline abolished the currents, whereas in the background of NBQX, amplitudes remained unchanged (**figures 4.4, 4.5**). Similarly, bath-application of TPEN (1µM) reversibly increased the amplitude of SL evoked IPSCs by 29% while SG evoked IPSCs facilitated by 19%. SL evoked IPSCs were more sensitive to DCG-IV (70% depression) than SG evoked IPSCs (5% depression, **figure 4.8**).

Pooled data from several repetitions showed that CaEDTA increased the amplitude of SL evoked IPSCs on average by 75.2 ± 18.4% (n = 13, $P < 0.001$). Similarly, perfusion of TPEN (1µM) enhanced SL evoked IPSCs by 31.6 ± 5.2% (n = 20, $P < 0.05$, **figure 4.9**). CaEDTA and TPEN yielded a significantly different amount of facilitation when SL was stimulated ($P < 0.002$, unpaired t-test). Both chelators also increased the amplitude of SG evoked IPSCs (CaEDTA: 53.4 ± 24.3%, n = 6, $P < 0.05$; TPEN: 23.4 ± 5.1%, n = 8, $P < 0.05$; unpaired t-test between the chelators $P > 0.1$) implying that endogenous Zn$^{2+}$ levels modulate GABAergic transmission at dentate gyrus synapses. These results showed that Zn$^{2+}$ chelators facilitate GABAergic IPSCs in GCs.
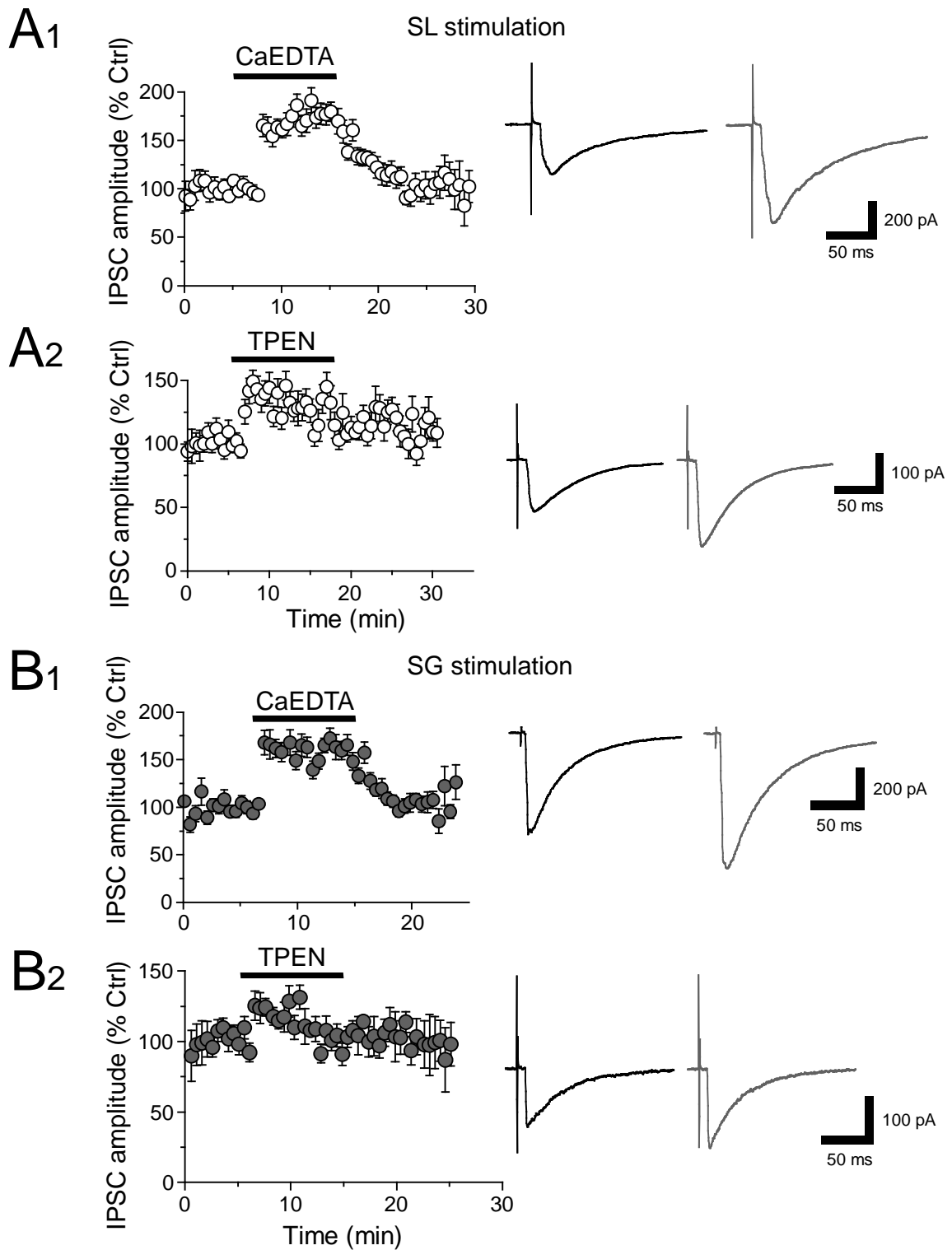
**Figure 4.9 – Zn$^{2+}$ chelators facilitate GABAergic signalling.** Summary plot of SL (**A**) and SG (**B**) evoked PSC amplitude against time showing a reversible facilitation in the presence of CaEDTA (2mM; n = 13). Time courses of the effects of TPEN (1µM) on SL (**A2**) and SG (**B2**) evoked PSCs similarly show a facilitation. Representative PSC traces are shown on the right in control (black) and in the presence of the Zn$^{2+}$ chelator (grey).

Next, the effect of exogenously applied Zn$^{2+}$ on the evoked IPSC amplitude in response to SL stimulation in granule cells was tested, hypothesising that the IPSC amplitude would depress. The Zn$^{2+}$ concentration within the synaptic cleft is still a matter of debate as studies have estimated the concentration to range between 1µM and 30µM (Komatsu *et al.*, 2005; Li *et al.*, 2001). Other studies estimated the Zn$^{2+}$ concentration to reach even as high as 100µM (Vogt *et al.*, 2000). Taking these estimations into consideration, this set of experiment was performed using a concentration of 10µM ZnCl$_2$.
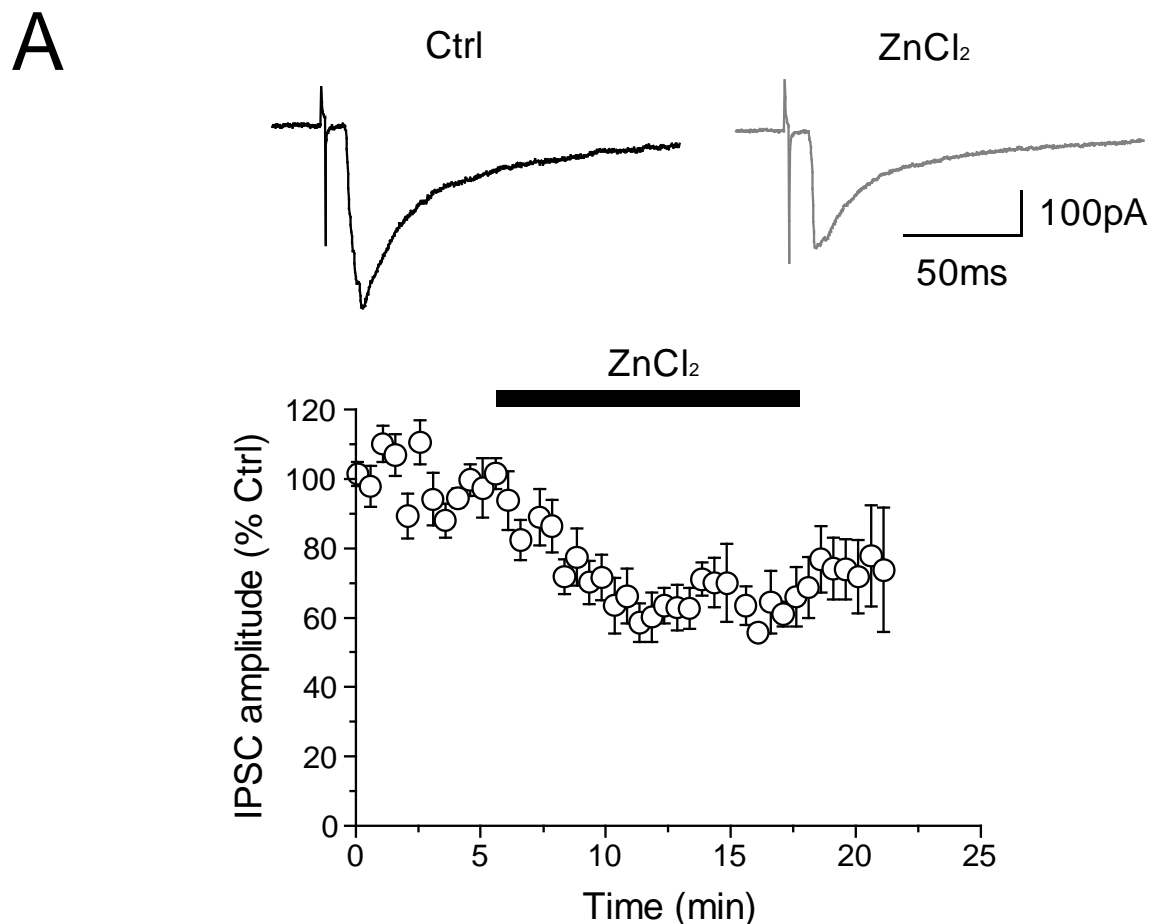


**Figure 4.10 – Perfusion of ZnCl$_2$ depresses IPSCs in GCs. A:** Plot of IPSC amplitude against time showing the effect of ZnCl$_2$ (10µM) on SL evoked responses. Traces on the right show IPSCs in control condition (black) and in the presence of ZnCl$_2$ (grey).

As seen in **figure 4.10**, when perfusing the slice with ZnCl$_2$ (10µM), the amplitude of evoked IPSCs was depressed by 37.9 ± 3.16% (n = 5, $P < 0.05$).

IPSCs in response to SL stimulation were analysed for a possible change in the decay time constant τ when the Zn$^{2+}$ chelators or ZnCl$_2$ were perfused compared to control, hypothesising that currents should decay faster as the closure configuration of GABA$_A$Rs is stabilised by the allosteric binding site of Zn$^{2+}$ at the subunit-specific isoform (Hosie *et al.*, 2003).
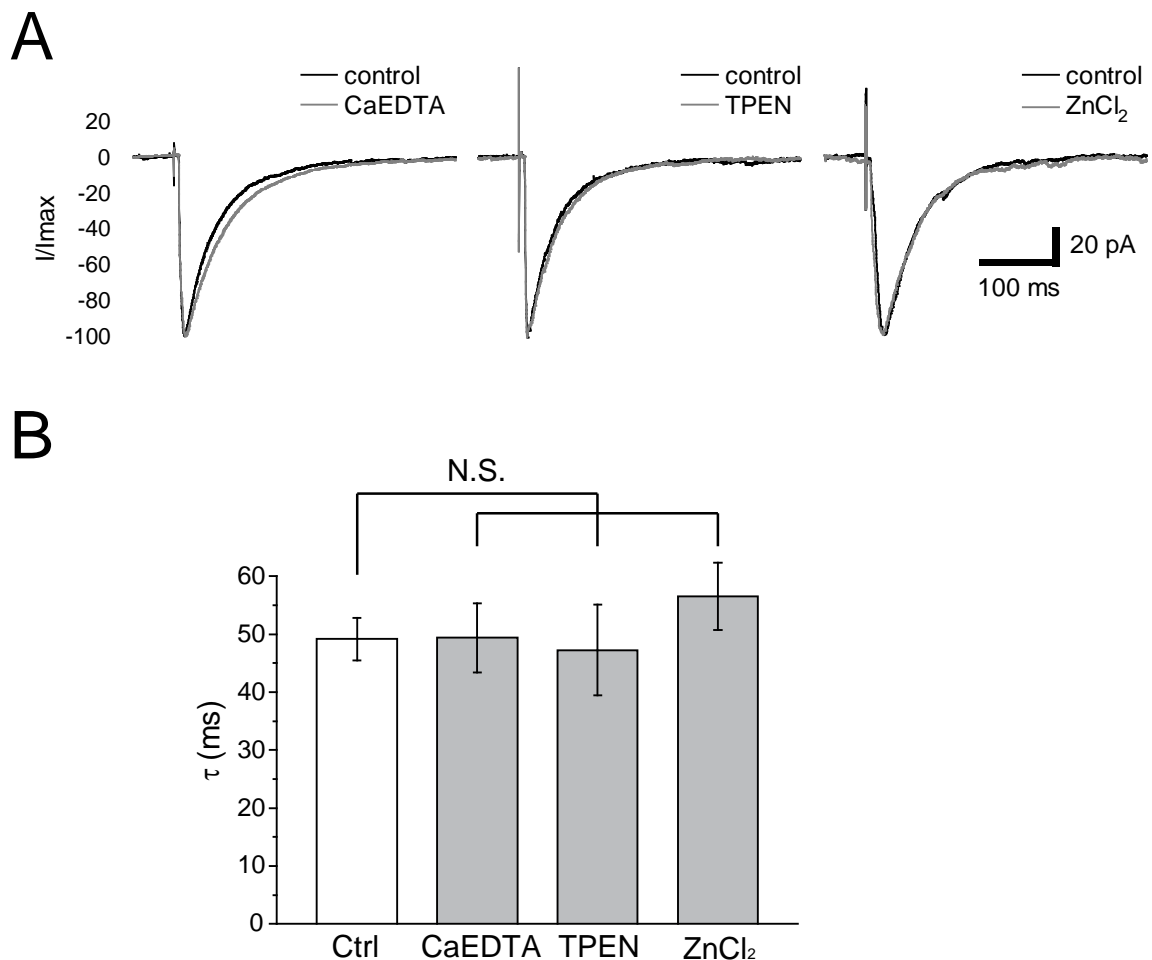


**Figure 4.11 – Perfusion of Zn$^{2+}$ chelators or ZnCl$_2$ does not change the decay time constant τ. A:** Peak-scaled IPSCs taken from three representative cells perfused with CaEDTA (2mM), TPEN (1µM) or ZnCl$_2$ (10µM, grey). **B:** Summary bar plot showing no significant difference in IPSC decay time between control and any of the drugs.

However, as shown in **figure 4.11**, there was no significant change of $\tau$ in any of the conditions that could indicate a modulation of synaptic GABA$_A$Rs ($\tau$ Ctrl: 49.1 ± 3.6ms; $\tau$ CaEDTA: 49.4 ± 5.9ms; $\tau$ TPEN: 47.3 ± 7.8ms; $\tau$ ZnCl$_2$: 56.5 ± 5.8ms, n = 5, *P* > 0.08).

## 4.3. MODULATION OF SPONTANEOUS PSCs BY TPEN

In addition to evoked responses, a modulation of spontaneous neurotransmitter release onto GCs by Zn$^{2+}$ chelation was tested which could hind towards a change in network activity. Long epochs of spontaneous PSCs were thus recorded in control condition and after superfusion of TPEN for 5min and analysed for their amplitude and frequency (**figure 4.12**).

Because BC-GC transmission was reported to be reliable and of large quantal size (Kraushaar and Jonas, 2000) and because the frequency of large spontaneous events (amplitude > 50pA) appeared to differ as shown in a cumulative frequency plot **(figure 4.13A)**, those events were analysed separately to test whether a subset of events was modulated (**figure 4.13**).

A

Ctrl

TPEN

50 pA

20 ms

B

* *P* < 0.05

C

N.S.    N.S.
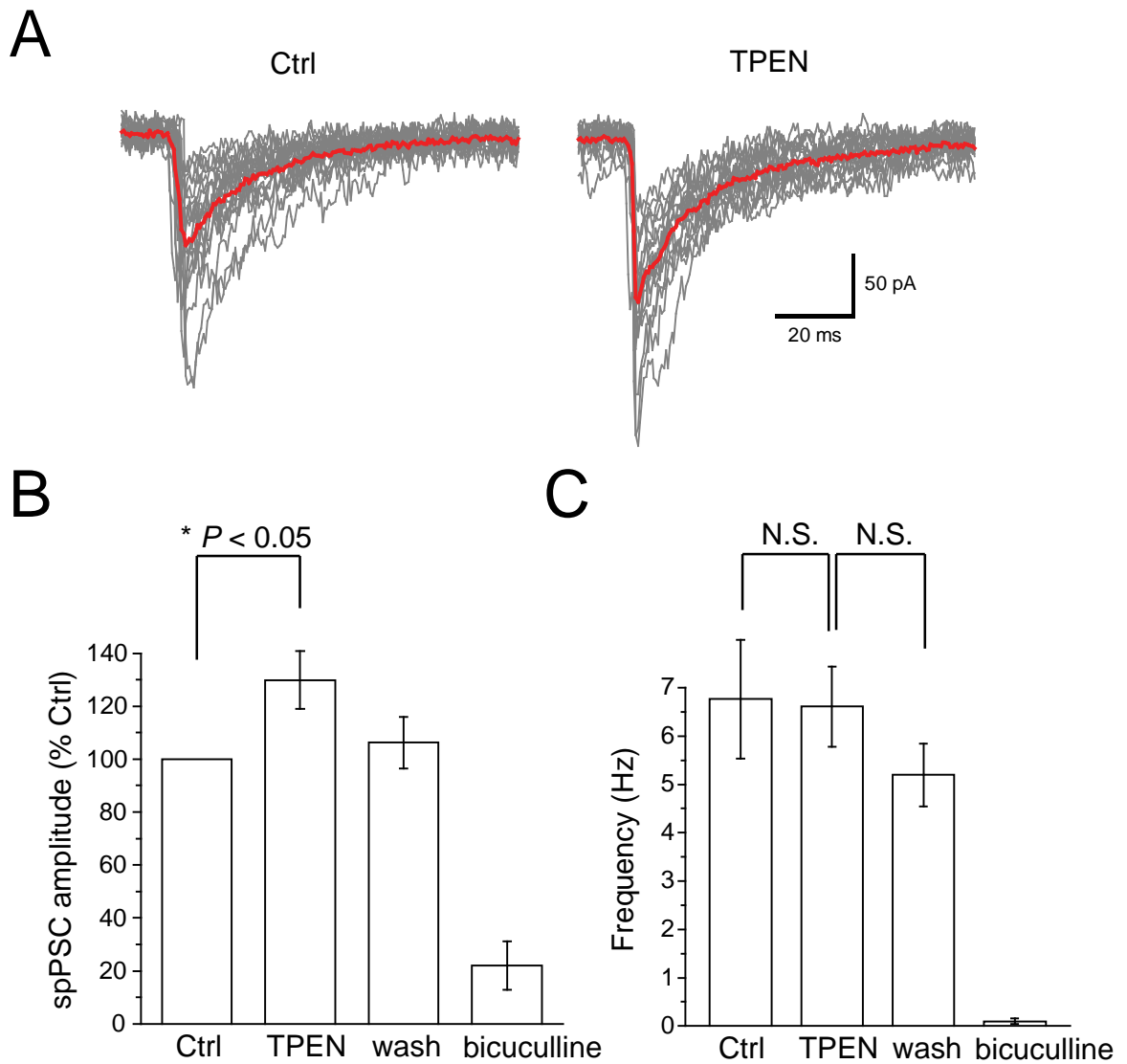
**Figure 4.12 – TPEN enhances the amplitude of spontaneous PSCs. A:** Traces showing 20 superimposed spontaneous PSCs (spPSCs, average in red) in control condition and with TPEN (1µM). **B,C:** Summary bar graph from 6 cells showing an increase in the amplitude of spontaneous PSCs (**B**) without change in their frequency (**C**).

**A**



**B**



**C**



**D**



**E**
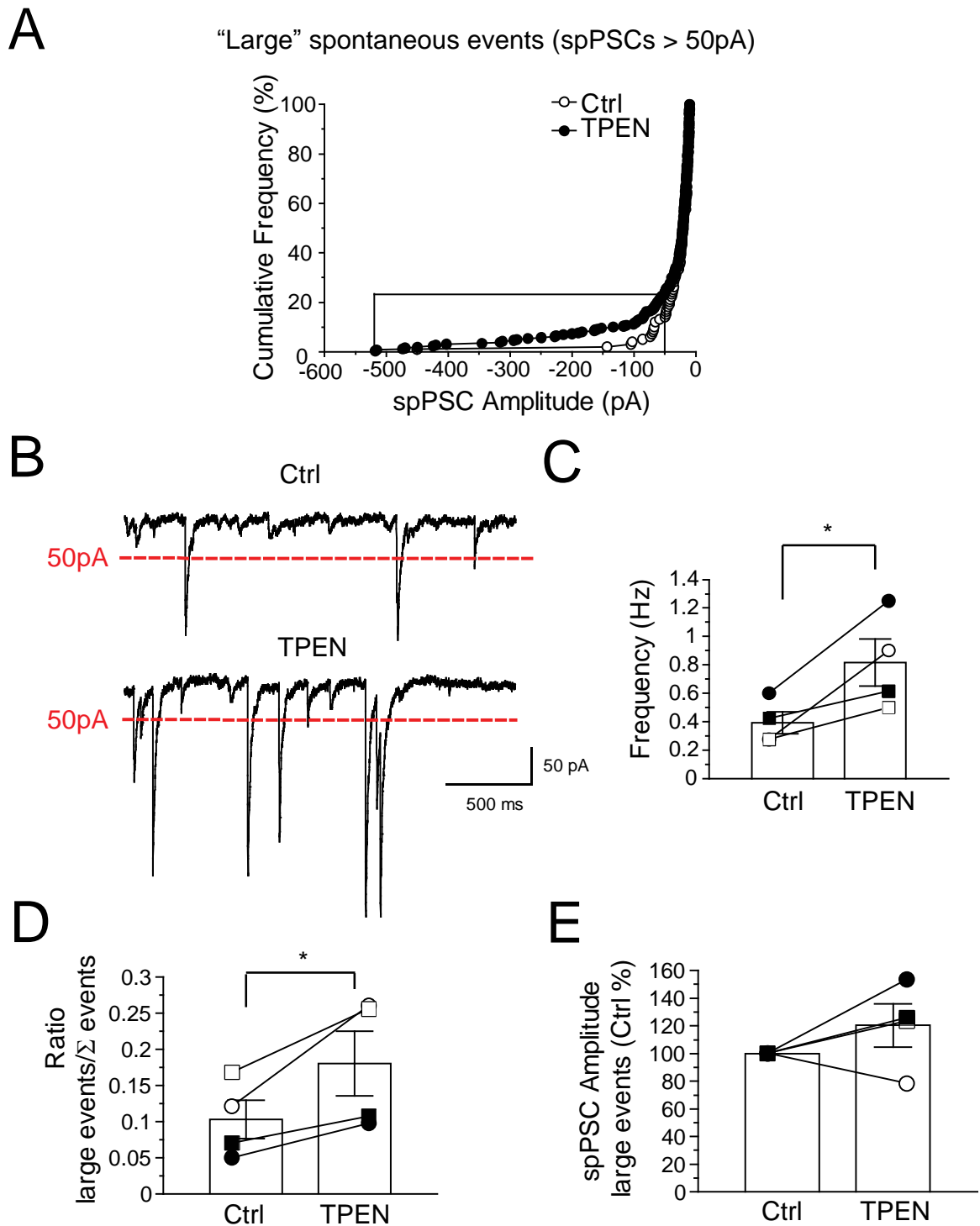


**Figure 4.13 – TPEN enhances the amplitude and frequency of large spontaneous PSCs. A:** Cumulative frequency plot of spPSC amplitude in control condition (white symbols) and in TPEN (black symbols). The black box delineates large events. **B**: Traces showing an increase in amplitude and frequency in large spPSCs (>50pA) following perfusion of TPEN (1μM). **C**: Summary bar graph showing the effect of TPEN on the frequency of large events. **D**: Bar graph showing the ratio of large events to the sum of all events, in control condition and following superfusion of TPEN. **E**: Bar chart showing the effect of TPEN on the amplitude of large events.

The amplitude of spontaneous PSCs reversibly increased without any change in the frequency (amplitude: TPEN 29.9 ± 10.9% increase, n = 6, *P* < 0.05; frequency: Ctrl 6.8 ± 1.2Hz, TPEN 6.6 ± 0.8Hz, wash 5.2 ± 0.6Hz, *P* > 0.8, **figure 4.12**). Bicuculline (10µM) depressed PSC amplitude to 22 ± 9.1% and reduced the frequency to 0.1 ± 0.1Hz indicating that these spontaneous events were largely mediated by GABA$_A$Rs. A change in the amplitude of spontaneous events may be the result of a modification of postsynaptic receptors in granule cells or alternatively can also be caused by a change in the vesicular filling (Edwards, 2007).

In addition, analysis of large events (>50pA) also showed that a subset of spontaneous IPSCs is modulated by endogenous Zn$^{2+}$. Perfusion of TPEN showed that the frequency and amplitude of this subset was augmented (**figure 4.13**) suggesting that those interneurons that mediate large quantal events may be predominantly modulated. A change in the frequency of large events whilst small events remained unchanged may suggest a modulation in release probability of GABA in cells that predominantly mediate large events. Alternatively, the possibility cannot be excluded that large events stem from action potential dependent events and the majority of spontaneous events result from spontaneous action potential independent release of GABA.

Together, these results suggest that endogenous Zn$^{2+}$ also tonically depresses spontaneous IPSCs to a similar extent as Zn$^{2+}$ depresses evoked IPSCs, when MFs are stimulated for phasic Zn$^{2+}$ release.

## 4.4.  EFFECT OF Zn$^{2+}$ CHELATORS IS PATHWAY SPECIFIC

To test whether the effect of Zn$^{2+}$ chelators on IPSCs was restricted to a network that is enriched with Zn$^{2+}$, the effect of Zn$^{2+}$ chelators was next investigated at a pathway that does not contain Zn$^{2+}$, such as the commissural/associational pathway to CA3. A stimulation electrode was positioned in stratum radiatum of CA3 to activate commissural/associational fibres and GABAergic fibres of local interneurons. Apart from providing excitatory

input to CA3 pyramidal cells, commissural/associational fibres also impinge onto local interneurons, which provide feed-forward inhibition to CA3 pyramidal cells (**figure 4.14A$_1$**). As CA3 collaterals could also be stimulated with this experimental paradigm, pyramidal cells were held at the reversal potential for glutamate receptors $V_{holding}$ = 0mV in order to isolate GABAergic IPSCs. Patch pipettes contained a K-gluconate-based solution and, in addition, the use-dependent NMDAR blocker MK-801 (1mM) was included to block NMDARs in CA3 cells which are normally inhibited by ambient Zn$^{2+}$ (Vogt *et al.*, 2000).

In these conditions, bath-application of bicuculline (10µM) completely abolished the response, indicating that IPSCs were mediated by GABA$_A$Rs (bicuculline 1.6 ± 0.9%, n = 6, *P* < 0.001, **figure 4.14B**). In contrast to MF-mediated responses, the group II mGluR agonist DCG-IV (1µM) only minimally affected the amplitude of evoked IPSCs by stratum radiatum stimulation (DCG-IV 6.9 ± 2.1% depression, n = 5, *P* > 0.4, **figure 4.14C**). Finally, superfusion of either CaEDTA or TPEN left the amplitude of IPSCs unchanged (TPEN 4.3 ± 3.4% depression, *P* > 0.8; CaEDTA 3.5 ± 3.1% facilitation, n = 4, *P* > 0.9, **figure 4.14D,E**) implying that endogenous Zn$^{2+}$ has little effect on GABAergic signalling at this pathway.
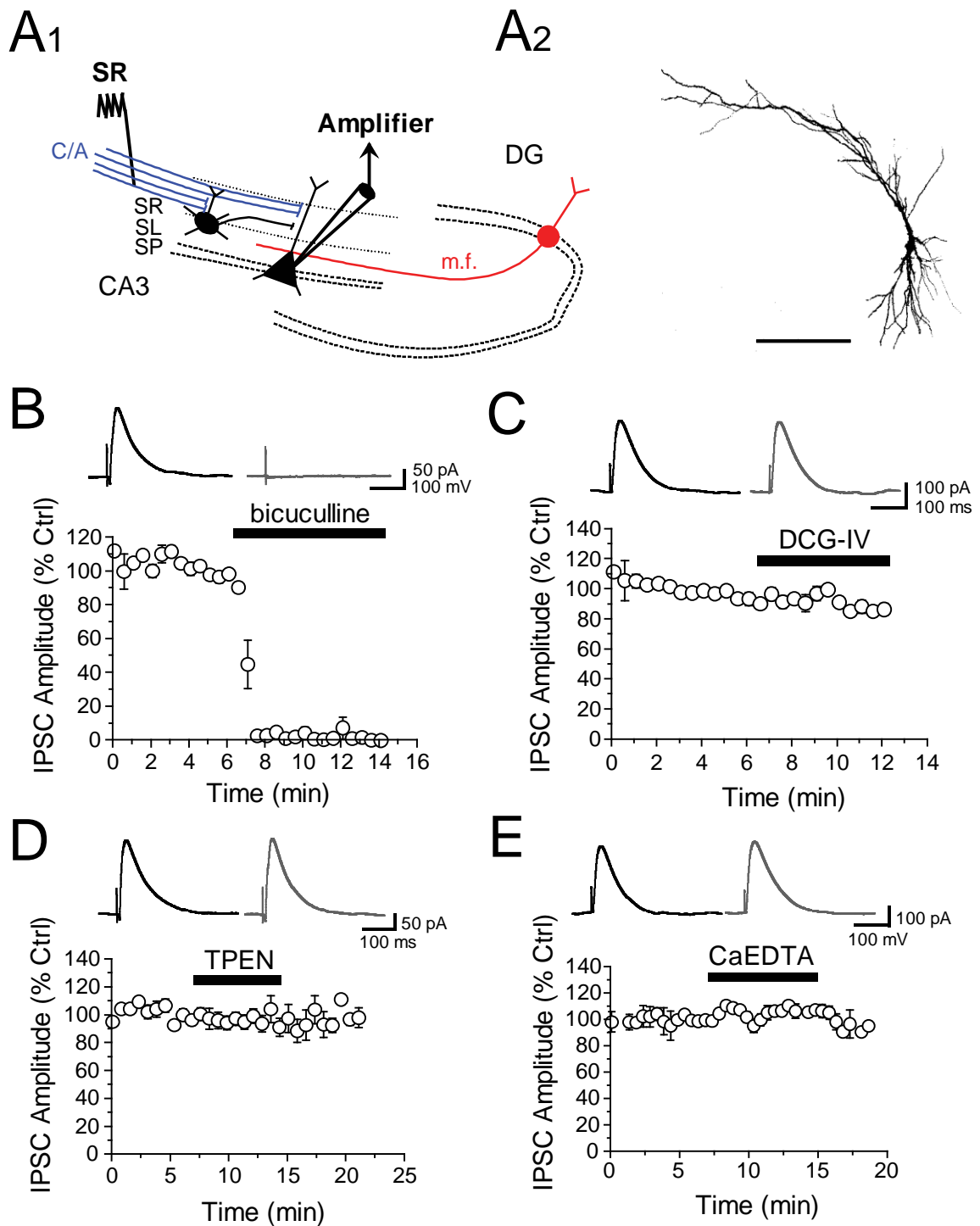
**Figure 4.14 – Zinc chelators do not affect stratum radiatum evoked IPSCs. A1**:
Cartoon of a hippocampal slice showing the experimental approach. **A2**: Reconstruction
of a CA3 pyramidal neuron, Scale bar 200μm. **B-E**: Plots of the effects of bicuculline
(10μM), DCG-IV (1μM), TPEN (1μM) and CaEDTA (2mM) on IPSC amplitude against
time. Bicuculline abolishes evoked IPSCs whereas DCG-IV, TPEN and CaEDTA have
no effect. Corresponding traces are displayed for control condition (black) and for the
corresponding drug (grey). SP stratum pyramidale, SR stratum radiatum, C/A
Commissural/Associational pathway.

Together, these results indicate a modulatory, pathway-specific role for endogenous Zn$^{2+}$ on mono-synaptic and di-synaptic GABAergic signalling.

## 4.5. Zn$^{2+}$ RELEASE AND ACTIVITY-DEPENDENT EFFECTS OF Zn$^{2+}$ CHELATORS

### 4.5.1. Source of endogenous Zn$^{2+}$

So far the results indicate a modulatory role of endogenous Zn$^{2+}$ on GABAergic signalling mediated by poly-synaptic recurrent MF inputs as well as mono-synaptic inputs mediated by local interneurons, but where is the Zn$^{2+}$ coming from? It was next tested whether MFs provide a source for ambient Zn$^{2+}$ which may spill-over to dentate synapses, thus contributing to the "tonic" effect of endogenous Zn$^{2+}$ on evoked IPSCs (**figure 4.15A$_1$**). If this would be the case, the group II mGluR agonist DCG-IV should occlude the effect of Zn$^{2+}$ chelators on evoked IPSCs. To answer this question, DCG-IV (1µM) was bath-applied prior to the Zn$^{2+}$ chelator to reduce the release of glutamate (and Zn$^{2+}$) selectively from MF terminals. The AMPA and kainate receptor antagonist NBQX (20µM) was also applied to reduce poly-synaptic activity. Although SL evoked IPSCs were completely abolished by NBQX (**figure 4.15A**) and only SG evoked IPSCs were analysed for an effect of TPEN, the SL pathway was stimulated to evoke Zn$^{2+}$ release from mossy fibres.
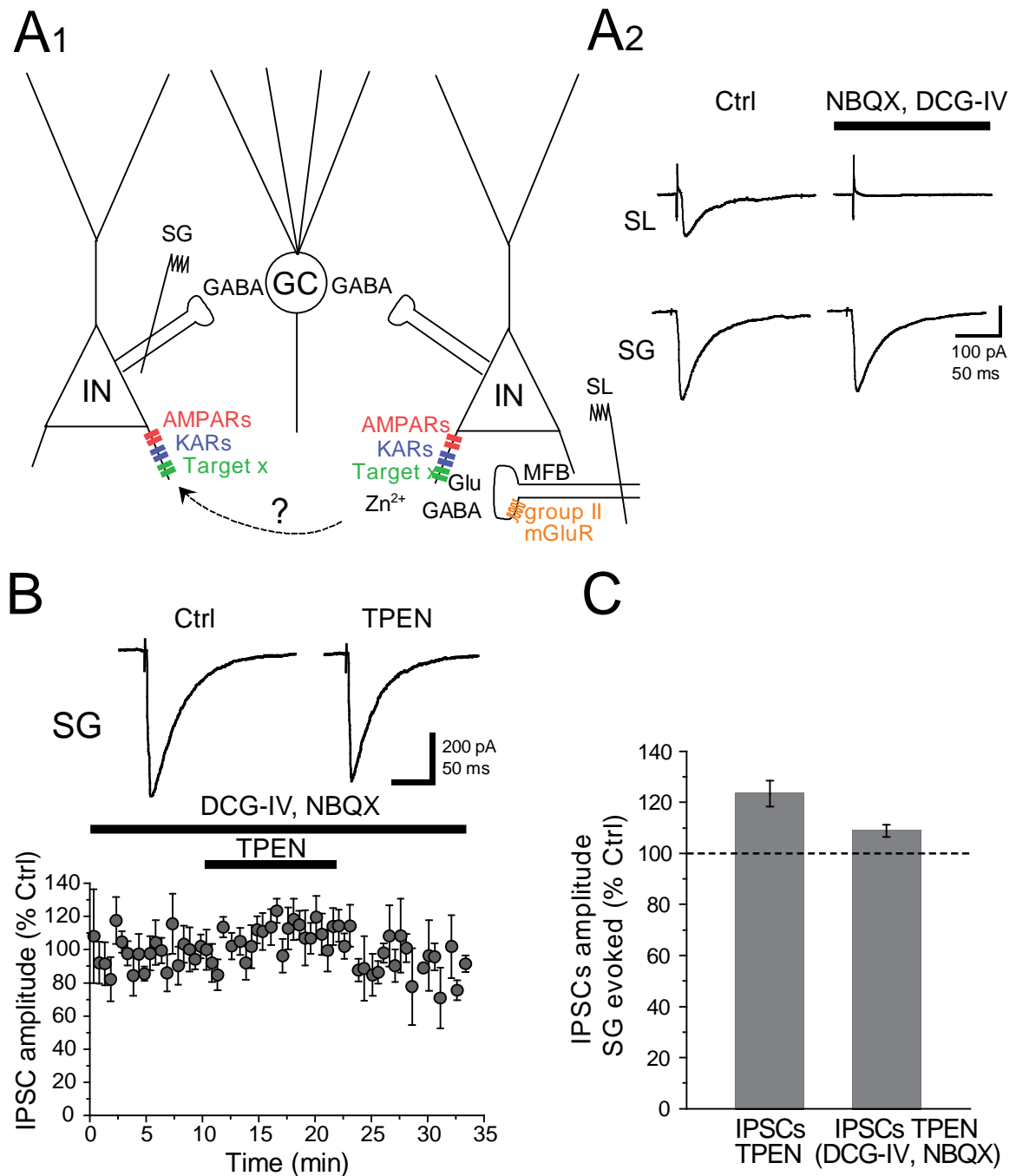
**Figure 4.15 – Decreasing MF release probability reduces the chelator effect. A1:** Cartoon describes the experimental design and the putative Zn$^{2+}$ targets. Zn$^{2+}$ may spill-over to other synapses made by interneurons. **A2:** Averaged traces showing the complete blockade of SL evoked IPSCs by DCG-IV (1µM) and NBQX (20µM) whereas IPSCs evoked by SG stimulation remain unchanged. **B:** Time course showing the effect of TPEN (1µM) on the amplitude of SG evoked IPSCs in conditions where MF release probability is reduced. Traces before and during bath-application of TPEN are shown on top. **C:** Bar plot showing the effect of TPEN on SG evoked IPSCs with and without DCG-IV.

**Figure 4.15B,C** shows that SG evoked IPSCs were minimally affected by the perfusion of the Zn$^{2+}$ chelator TPEN (DCG-IV: 8.9 ± 2.4% facilitation, n = 6, *P* > 0.7, paired t-test), in comparison to the increase in IPSC amplitude without DCG-IV and NBQX (23.4 ± 5.1% facilitation, **figure 4.9**). These results suggest that the facilitatory effect of TPEN on the IPSC amplitude is reduced if Zn$^{2+}$ release from MFs is reduced. They also raise the possibility that endogenous Zn$^{2+}$ in the dentate gyrus might originate from MFs, thus providing a source for ambient Zn$^{2+}$. This also supplies evidence for a possible spill-over of Zn$^{2+}$ from Zn$^{2+}$-containing MFs to neighbouring synapses, such as connections between interneurons and GCs.

## 4.5.2. High frequency paired pulses and trains of stimuli

Next, the possibility was tested whether the effects of endogenous Zn$^{2+}$ on GABAergic signalling were activity dependent. If this was the case, the amount of IPSC facilitation following Zn$^{2+}$ chelation should increase as a function of the IPSC number within the train, thus reflecting increasing amounts of Zn$^{2+}$ release along the train of stimuli. The two-pathway experiments were repeated this time evoking a paired pulse or a train (5 stimuli, 20Hz), with the assumption that the facilitation of IPSC amplitude is greater at the end of a 20Hz train. **Figure 4.16** shows the effect of both Zn$^{2+}$ chelators on the PPR whereas **figure 4.17** shows the effect of the chelators on a train of 5 stimuli, normalised to the first stimulus.

A$_1$

SL stimulation



A$_2$



B

SG stimulation
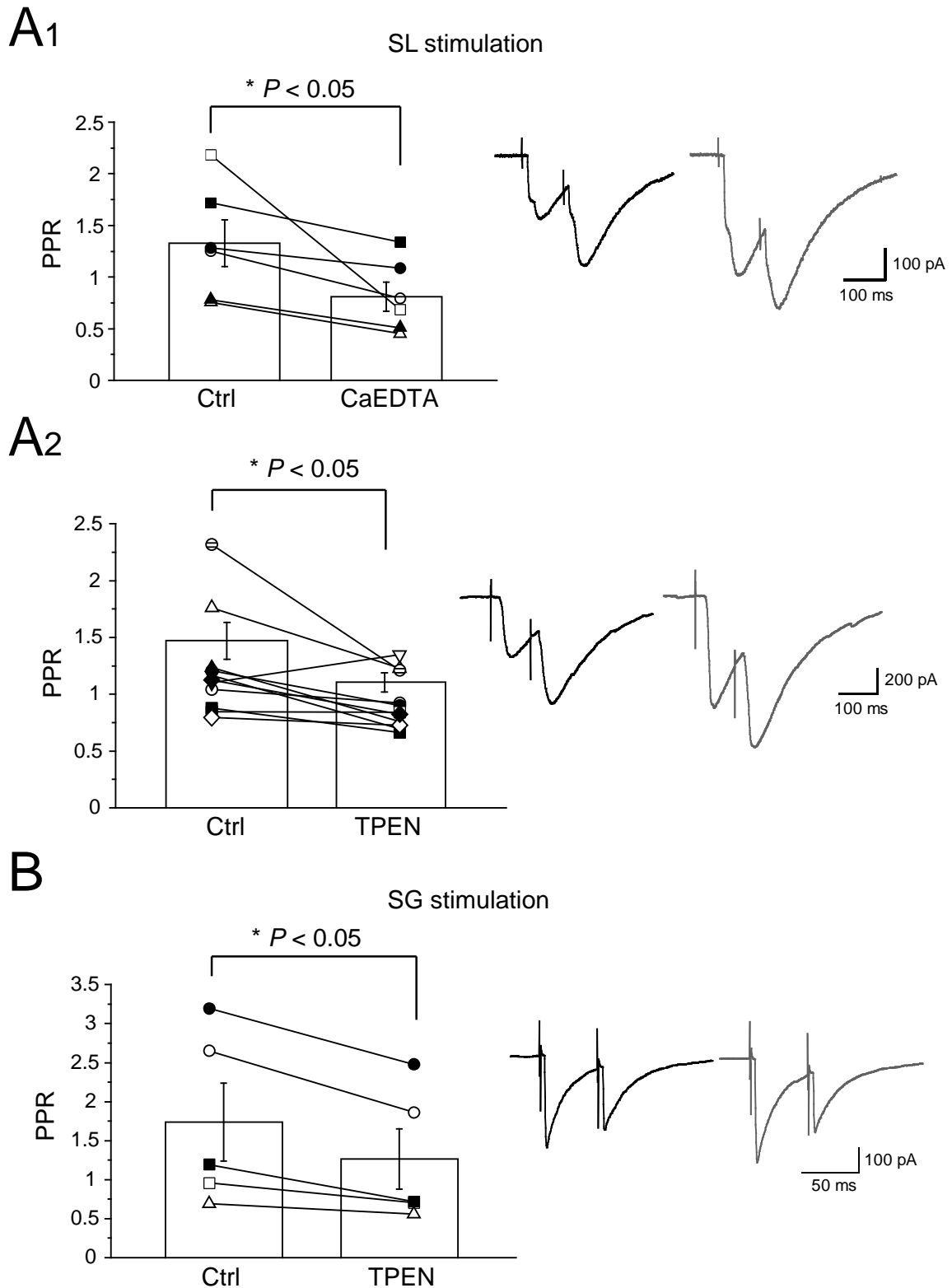


**Figure 4.16 – Effect of Zn$^{2+}$ chelators on the PPR of SL and SG evoked IPSCs. A,B:** Bar charts showing the PPR in control condition and in the background of CaEDTA (2mM, **A1**) or TPEN (1µM, **A2,B**) for both pathways. Traces on the right show IPSCs in control condition (black) and in the background of the chelator (grey).
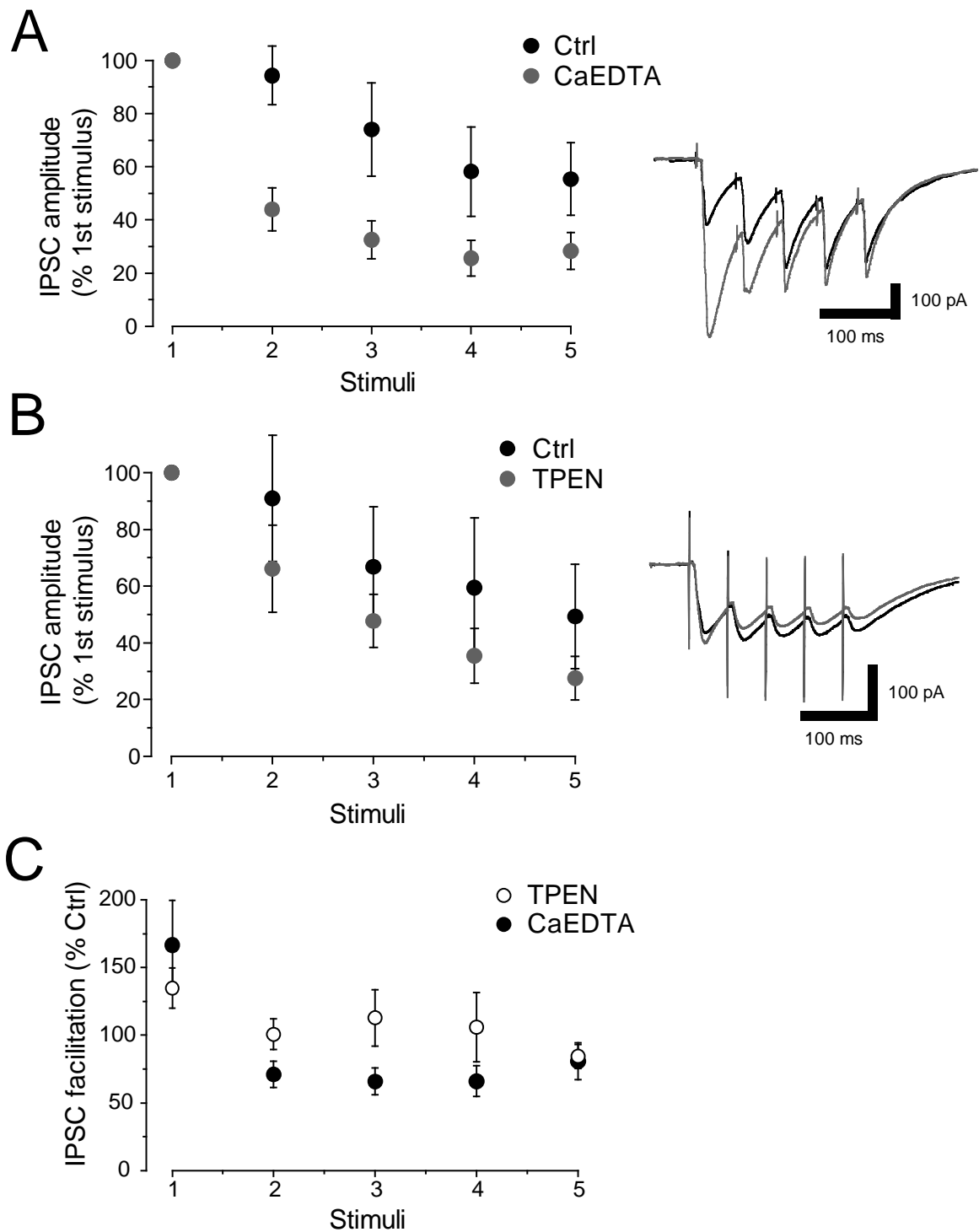
**Figure 4.17 – Effect of Zn$^{2+}$ chelators on the amplitude of IPSCs in a 20Hz train of stimuli evoked by SL stimulation. A, B:** Plot showing the effect of Zn$^{2+}$ chelators CaEDTA (2mM, **A**) and TPEN (1µM, **B**) on the amplitude of the 2$^{nd}$, 3$^{rd}$, 4$^{th}$ and 5$^{th}$ IPSC normalised to the 1$^{st}$ IPSC. Traces in control (black) and in the background of the chelator (grey) are shown on the right. **C:** Plot shows the IPSC facilitation against the stimulus number for experiments performed with TPEN (white symbols) and CaEDTA (black symbols).

**Table 4.1** shows a decrease in the amplitude ratios (stimulus 2/stimulus 1) following perfusion of a Zn$^{2+}$ chelator when IPSCs are evoked using a paired-pulse protocol.

Table
4.1

**PPR (amplitude ratio of 2 pulses)**

| chelator | SL | stats (n, $P$) | SG | stats (n, $P$) |
|---|---|---|---|---|
| Ctrl | 1.3 ± 0.2 | | N/A | |
| CaEDTA | 0.8 ± 0.1 | 6, $P$ < 0.05 | N/A | N/A |
| Ctrl | 1.5 ± 0.2 | | 1.7 ± 0.5 | |
| TPEN | 1.1 ± 0.1 | 11, $P$ < 0.05 | 1.3 ± 0.4 | 5, $P$ < 0.05 |

statistical test: paired t-test

For IPSC measurements in a train of 5 stimuli, IPSC amplitudes measured in response to the 2$^{nd}$, 3$^{rd}$, 4$^{th}$ and 5$^{th}$ pulses were normalised to the response elicited by the 1$^{st}$ pulse, in each condition (**table 4.2**). A two-way ANOVA was performed to determine whether the effect of zinc chelation with bath application of CaEDTA or TPEN depended upon the IPSC number within the train.

Table 4.2

| Control | IPSC1 | IPSC2 | IPSC3 | IPSC4 | IPSC5 |
|---|---|---|---|---|---|
| Mean | 100.00 | 86.09 | 68.57 | 53.97 | 54.89 |
| S.E.M. | 0 | 12.19 | 15.32 | 14.36 | 13.01 |
| N | 6 | 6 | 6 | 6 | 6 |

| CaEDTA | IPSC1 | IPSC2 | IPSC3 | IPSC4 | IPSC5 |
|---|---|---|---|---|---|
| Mean | 100.00 | 43.99 | 32.59 | 25.58 | 28.34 |
| S.E.M. | 0 | 8.10 | 7.11 | 6.68 | 6.97 |
| N | 6 | 6 | 6 | 6 | 6 |

| Sum Table | IPSC1 | IPSC2 | IPSC3 | IPSC4 | IPSC5 |
|---|---|---|---|---|---|
| Control | 100.00 | 86.09 | 68.57 | 53.97 | 54.89 |
| CaEDTA | 100.00 | 43.99 | 32.59 | 25.58 | 28.34 |
| T(A) | 200.00 | 130.08 | 101.16 | 79.55 | 83.23 |
| Sum (x^2) | 20000.00 | 9346.49 | 5764.03 | 3567.16 | 3815.95 |

**ANOVA Table for Unbalanced Case**

| Factor | SS | Df | Ms | F(cal) | |
|---|---|---|---|---|---|
| A (Columns) | 27327.48 | 4.00 | 6831.87 | 7.59 | *** (P <=0.001) |
| B (Rows) | 9831.91 | 1.00 | 9831.91 | 10.93 | ** (P<=0.01) |
| AxB (Interaction) | 2886.31 | 3.99 | 721.58 | 0.80 | N.S. (P>0.05) |

Bath-application of CaEDTA caused a significantly greater depression in IPSC amplitude compared to control conditions ($P < 0.001$). This depression was greater for subsequent IPSCs within the train ($P < 0.01$). Repeating this analysis for experiments performed with TPEN yielded no significant difference ($P > 0.05$; not shown).

Table 4.3

**TRAIN (SL - normalised to control, %)**

| chelator | 1 | 2 | 3 | 4 | 5 |
|---|---|---|---|---|---|
| Ctrl | | | | | |
| CaEDTA | 66.6 ± 32.8 | -29 ± 9.6 | -34.1 ± 10 | -34 ± 11.3 | -19.3 ± 13.5 |
| Ctrl | | | | | |
| TPEN | 34.7 ± 14.8 | 0.7 ± 11.3 | 12.8 ± 20.7 | 5.9 ± 25.8 | -15.7 ± 8.7 |

The degree of IPSC facilitation induced by both chelators was greatest on IPSCs evoked by the first stimulus (**table 4.3**).

Together, these results do not favour the hypothesis of dynamic release by endogenous Zn$^{2+}$. They support the notion that a quick depletion of Zn$^{2+}$ occurs from the vesicles, as previously reported (Kay, 2003; Smart *et al.*, 2004).

## 4.6. EFFECT OF Zn$^{2+}$ CHELATORS ON HOLDING CURRENT AND LOCAL APPLICATION OF GABA

This facilitatory modulation of IPSC amplitude in GCs could be explained by an inhibitory action of Zn$^{2+}$ at tonically active GABA$_A$Rs on the dendrites of GCs. Some extrasynaptic GABA$_A$Rs in GCs contain δ subunits which makes them tonically active and highly sensitive to neurosteroids (Stell *et al.*, 2003). It has been long known that GABA$_A$Rs with the subunit composition αβ or αβδ are sensitive to Zn$^{2+}$ inhibition (Draguhn *et al.*, 1990). Thus, inhibition of tonically-active GABA$_A$Rs would be a ready explanation for this phenomenon. In order to test this possibility, the holding current (I$_{holding}$) was analysed as tonically active GABA$_A$R activation promotes a shift in I$_{holding}$ (Brickley *et al.*, 1996; Nusser and Mody, 2002; for review see Semyanov *et al.*, 2004).

# A
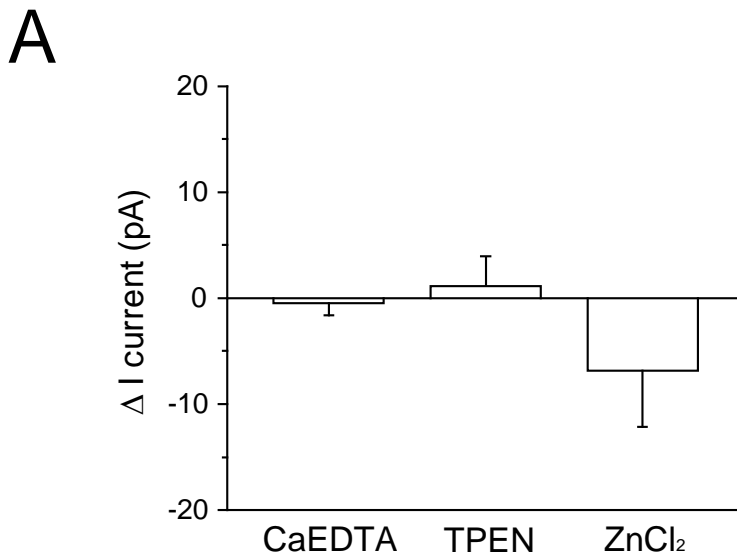


**Figure 4.18 – Perfusion of Zn$^{2+}$ chelators or ZnCl$_2$ does not change I$_{holding}$. A:** Bar graph showing the change ($\Delta$) in I$_{holding}$ in the presence of CaEDTA (2mM), TPEN (1µM) or ZnCl$_2$ (10µM).

There was no significant difference in I$_{holding}$ following perfusion of CaEDTA, TPEN or ZnCl$_2$ compared to control condition ($\Delta$I$_{holding}$ CaEDTA -0.4 ± 1.2pA, n = 9; $\Delta$I$_{holding}$ TPEN 1.2 ± 2.6pA, n = 17; $\Delta$I$_{holding}$ ZnCl$_2$ -6.9 ± 5.3pA, n = 5, *P* > 0.2, **figure 4.18**), arguing that a modulation of tonically active GABA$_A$Rs by endogenous Zn$^{2+}$ or exogenous Zn$^{2+}$ at GC dendrites may not be involved.

Although the lack of change in I$_{holding}$ is an initial indication against a possible inhibition of GABA$_A$Rs, only the local application of GABA on GC dendrites can provide robust evidence that Zn$^{2+}$ has a direct effect on GCs. Whole-cell recordings were obtained from GCs and GABA was locally applied to GC dendrites with a pressure application system (**figure 4.19A**). Recordings were performed in 0mM Ca$^{2+}$ to block spontaneous activity and in the background of NBQX (20µM) and CGP-52432 (5µM) to isolate GABA$_A$R-mediated responses. **Figure 4.19** shows the effect of TPEN on GABA currents recorded from GCs held at various holding potentials.
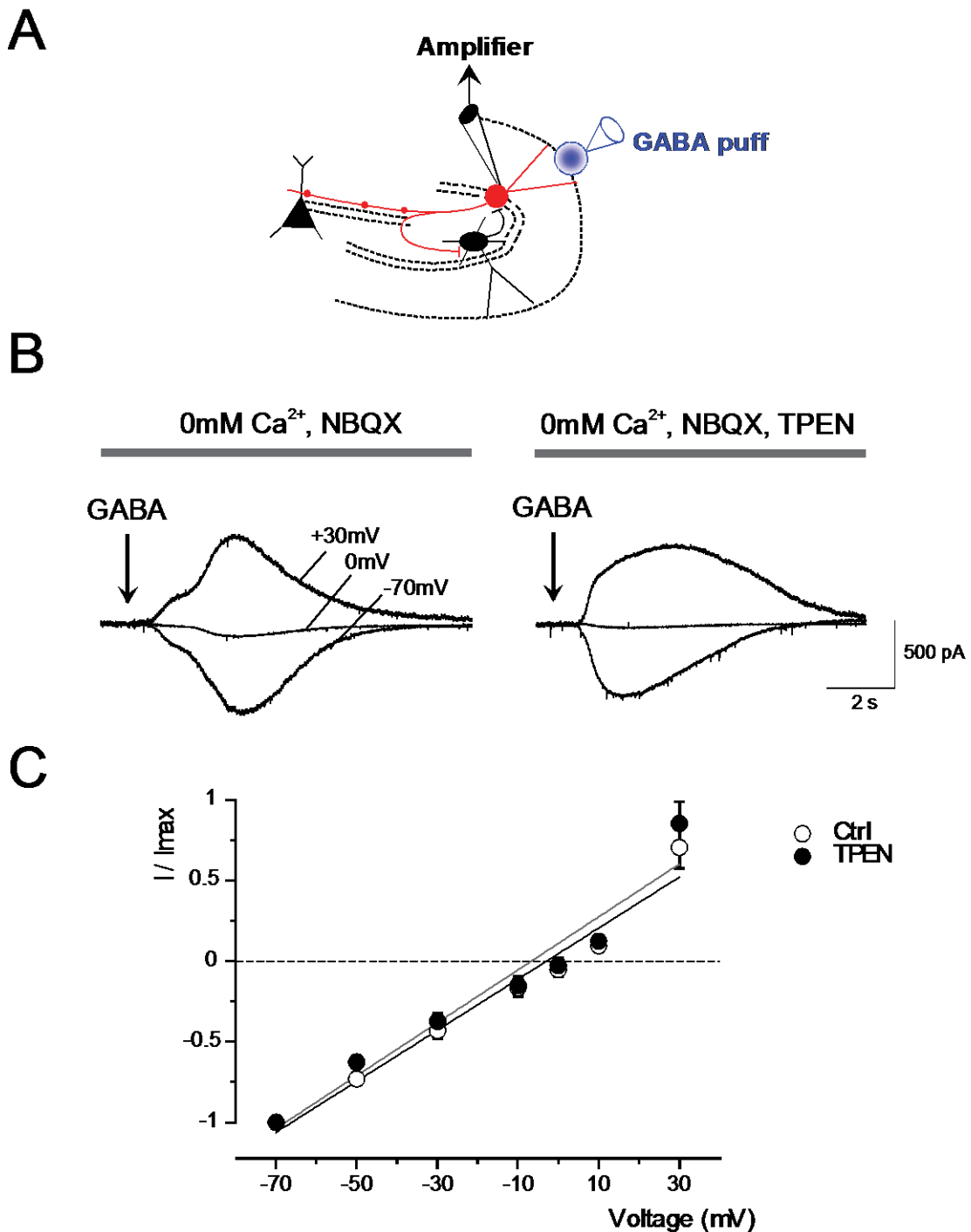
**Figure 4.19 – Effect of TPEN on GABA currents evoked by local GABA puff on the dendrites of GCs. A:** Drawing of a hippocampal outline showing the location of GABA puffs in the ML. **B:** Averaged traces of currents elicited by local GABA puffs at $V_{holding}$ = -70, 0 and +30mV. Arrows indicate puffing of GABA (100mM). **C:** I-V relationship (normalised to $I_{max}$ at -70mV) in control (white symbols, black fitting) and in the presence of TPEN (1µM, black symbols, grey fitting). Recordings were performed in 0mM Ca$^{2+}$ to block spontaneous activity and in the background of CGP 52345 (5µM) and NBQX (20µM).

The traces of the example recording (**figure 4.19B**) show an inward current ($V_{holding}$ = -70mV) that reversed at $E_{GABA}$ ~ 0mV following local pressure application of GABA (100mM) with a high Cl$^-$ pipette solution. Superfusion of TPEN caused no significant change in the amplitude of GABA evoked currents or $E_{GABA}$ (**figure 4.19C**). This result, together with a lack of change in the holding current and decay time constant of evoked IPSCs, indicates that synaptic or extrasynaptic GABA$_A$Rs on GC dendrites are unlikely to contribute to a modulation in the amplitude of evoked IPSCs by Zn$^{2+}$.

In summary, this chapter showed evidence for a modulation of GABAergic signalling by endogenous Zn$^{2+}$ at two different pathways. Firstly, Zn$^{2+}$ depressed SL-, MF-driven, evoked IPSCs whose kinetics and pharmacological properties served as a model for a di-synaptic feedback pathway. Secondly, Zn$^{2+}$ also depressed, albeit to a lesser extent, IPSCs evoked by SG stimulation, thus also modulating a mono-synaptic feed-forward pathway. The modulation at the latter pathway showed that Zn$^{2+}$ also contributed to heterosynaptic interactions at dentate neighbouring synapses. Furthermore, the modulation was dependent on neurotransmitter release from MFs but was activity independent. Finally, it was demonstrated that Zn$^{2+}$ chelation had little effect on direct activation of GABA$_A$Rs at GC dendrites when using focal GABA application.

5.  **Potential targets mediating a depression in the amplitude of evoked IPSCs by endogenous $Zn^{2+}$**

A modulation of GABA release onto GCs by endogenous Zn$^{2+}$ may have repercussions for the signalling in the dentate gyrus and possibly also towards CA3. Therefore, it was important to investigate the mechanisms by which endogenous Zn$^{2+}$ mediates this effect. Several targets were examined which could be modulated by Zn$^{2+}$ and could mediate the phenomenon described in the previous section. Firstly, a modulation of axonal receptors at MFs by Zn$^{2+}$ could translate in a change in axonal excitability and thus may explain a modulation of GABA release. Secondly, NMDARs are known to be inhibited by endogenous Zn$^{2+}$ and their inhibition by Zn$^{2+}$ could result in a reduction of GABA release from interneurons. Finally, the group of VGCCs were examined whose subtypes have various sensitivities for Zn$^{2+}$ and could equally mediate a reduction in GABA release.

## 5.1. Zn$^{2+}$ CHELATION MODULATES AXONAL EXCITABILITY

An increase in the amplitude of evoked IPSCs in GCs following Zn$^{2+}$ chelation may be due to a change in axonal excitability of MFs themselves. Such a modulation would account for enhanced neurotransmitter release at MF-interneuron synapses at the feedback circuit to GCs. It has become evident that presynaptic ionotropic receptors on MFBs can alter axonal excitability and neurotransmitter release (Ruiz *et al.*, 2010). Hence, the action of Zn$^{2+}$ on ionotropic receptors that control the presynaptic membrane potential could result in a modulation of axonal excitability.

### 5.1.1. Field potential recordings

To test whether Zn$^{2+}$ chelation modulates axonal excitability, antidromic field potentials (AfPs) were recorded. A stimulation electrode was positioned into SL to activate a bulk of MFs while monitoring antidromically evoked population spikes in GC somata by recording from the suprapyramidal blade of the GCL. AfPs had a short-latency wave-form and application of pharmacological agents such as DCG-IV (1µM), bicuculline (10µM) and NBQX (20µM) did not alter their

amplitude indicating that this response was mediated by an antidromic population spike (**figure 5.1A**). If Zn$^{2+}$ chelation alters axonal excitability, it should be reflected on the AfP wave-form, whose amplitude is directly correlated to the number of GC spiking in response to electrical stimulation and subsequent antidromic propagation of action potentials.

**Figure 5.1 – TPEN does not modulate the amplitude of AfPs. A:** (Left) Experimental approach to record AfPs. The recording electrode is placed in the GCL while the stimulation electrode is placed in SL. (Right) Averaged AfP evoked by SL stimulation. **B:** Averaged AfPs in control condition and in the background of DCG-IV (1µM), bicuculline (10µM) or NBQX (20µM). **C:** Time plot showing no effect of TPEN on the amplitude of AfPs. Corresponding traces are shown on the right (black – control, grey – TPEN).

As seen in **figure 5.1B**, there was no significant change in the amplitude of AfPs following application of TPEN (2.68 ± 1.2% depression, n = 6, *P* > 0.3) suggesting that chelation of Zn$^{2+}$ does not modulate the excitability when stimulating the axon directly. However, there can be many reasons as to why there was no apparent change in the AfP amplitude after Zn$^{2+}$ chelation. Firstly, all fibres could be activated supra-threshold so that a change in firing will not be detected. Alternatively, some fibres close to the extracellular stimulation electrode could be activated supra-threshold, while others will be activated progressively sub-threshold depending on the distance to the stimulation electrode. Thus, a potential effect of Zn$^{2+}$ on antidromic firing may remain undetected because of a large population of fibres that are activated supra-threshold. Finally, TPEN could have potential effects on somato-dendritic receptors at GCs which would be overlooked with the above approach.

## 5.1.2. Action currents

GCs were next held in voltage-clamp and antidromic action currents were evoked by SL stimulation to examine the effect of TPEN on axonal excitability more directly. This approach allowed a more precise investigation of the effect of Zn$^{2+}$ chelation on MF excitability without a possible action of somato-dendritic receptors. In total, recordings from 7 GCs were obtained. Pharmacological agents (**figure 5.3**) and/or the Zn$^{2+}$ chelator TPEN (**figure 5.5**) were applied to characterise evoked action currents and to test their sensitivity to Zn$^{2+}$ chelation, respectively. Evoked action currents could be divided into two different groups distinguished by their latencies. Antidromic action currents had short latencies of 2.7 ± 1.1ms (n = 4) while orthodromic action currents had longer latencies with a mean of 11.7 ± 0.9ms (n = 5, *P* < 0.0004, unpaired t-test, **figure 5.2**). Also the jitter of the spike latency was distinct in these two populations. For antidromic action currents the standard deviation was 0.3 ± 0.08ms, whereas for orthodromic action currents the standard deviation was 1.8 ± 0.2ms, indicating a much broader distributed latency compared to antidromic action currents.

A

B
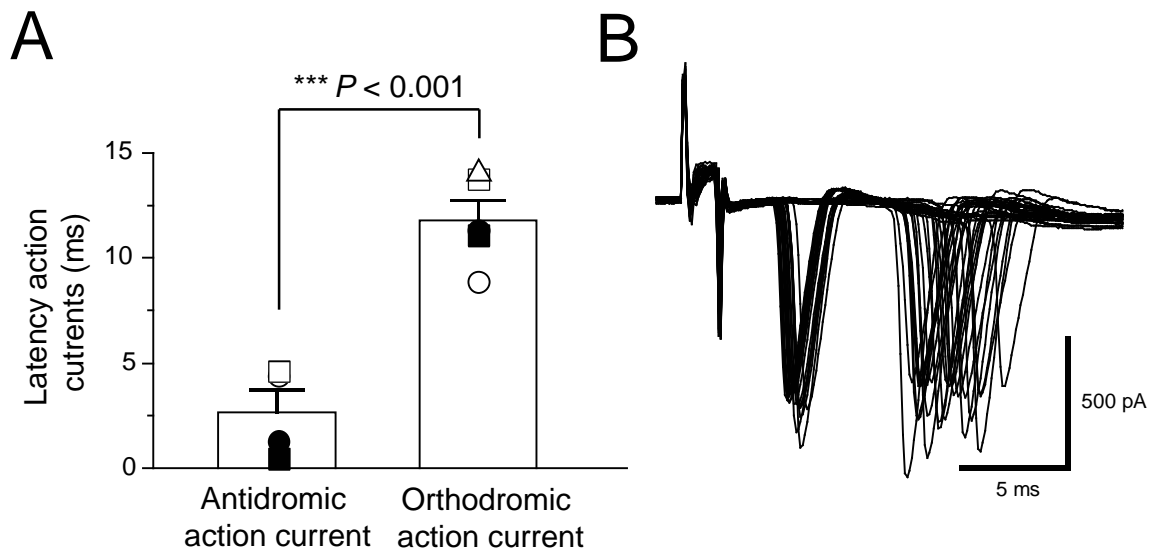


**Figure 5.2 – SL stimulation elicits two groups of action currents with distinct latencies in GCs. A:** Bar graph showing the mean latency for antidromic and orthodromic action currents. **B:** 20 superimposed traces showing the fixed latency of antidromically evoked action currents and the jitter in the latency of orthodromically evoked action currents.

Changes in axonal excitability were monitored by analysing the success rate for evoking an antidromic action current. In contrast, orthodromic action currents were mediated by recurrent MFs and should be therefore sensitive to DCG-IV and NBQX and should be completely abolished by bicuculline.

**A**

Orthodromic action currents



**B**
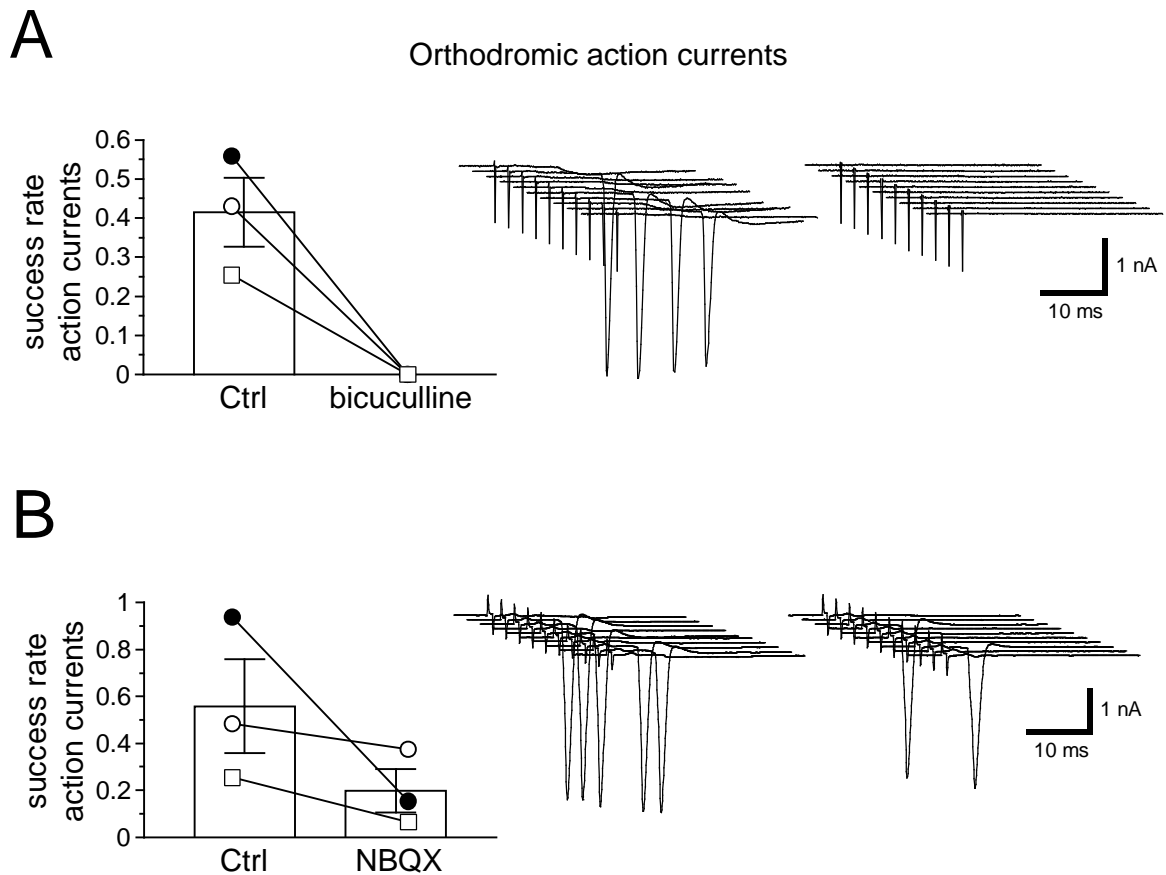


**Figure 5.3 – Pharmacological sensitivities of orthodromic action currents. A,B:** Bargraphs showing the effect of bicuculline (10µM, **A**) and NBQX (20µM, **B**) on the success rate for evoking orthodromic action currents. Traces show 10 consecutive trials in control condition and the corresponding drug on the right.

Bath-application of bicuculline (10µM) abolished all orthodromic action currents (Ctrl: 0.41 ± 0.09, bicuculline: 0 ± 0, n = 3, $P$ < 0.05, **figure 5.3**) and application of NBQX (20µM) more than halved the success rate for evoking orthodromic action currents (Ctrl: 0.56 ± 0.2, NBQX: 0.2 ± 0.09, n = 3, **figure 5.3**). In addition, DCG-IV (1µM) reduced the success rate for evoking orthodromic action currents in one recording (Ctrl: 0.28, DCG-IV: 0.08). In contrast, the application of NBQX (20µM) slightly increased the success rate for evoking antidromic action currents (Ctrl: 0.24, NBQX: 0.37, n = 1). These results together with the distinct latencies in both population of action currents, suggest that antidromically evoked action currents are the result of the direct stimulation of MFs in SL, whereas orthodromic action currents are evoked by a di-synaptic MF-mediated GABAergic conductance reaching threshold.

In 4 out of 7 cells, both antidromic and orthodromic action currents could be recorded, whereas in the remaining cells, antidromic action currents were absent. This closely correlates with the fact that MFs were found severed in 40% of neurons within a representative subset of recorded GCs by reconstructing the morphology of those neurons (**table 3.2 and figure 3.4**). Accordingly, in 3 out of 7 neurons, both types of action currents could not be recorded simultaneously as GCs may have had a severed axon, whereas in the remaining 4 recordings the presence of both antidromic and orthodromic action currents points to an intact axon that reaches the CA3 area as shown in the example in **figure 5.4**.
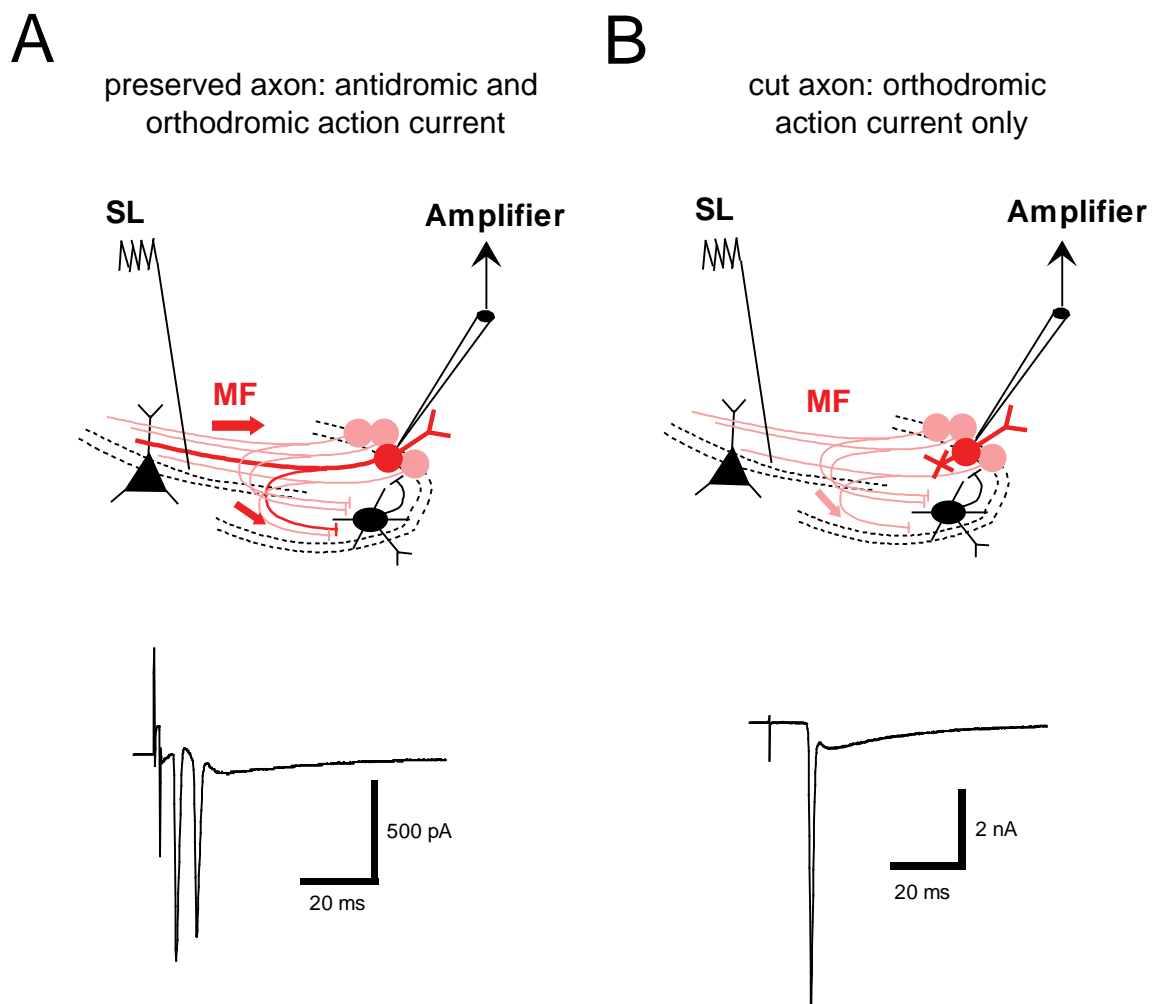


**Figure 5.4 – Influence of MF integrity and correlation with antidromic or orthodromic action currents. A,B:** (Top) Cartoons showing the effect of severing MFs on action currents recorded in GCs. (Bottom) In slices where MFs are preserved, antidromic and orthodromic action currents can be detected (**A**), whereas slices with severed MFs only show orthodromic action currents (**B**).

To test whether $Zn^{2+}$ may be modulating the success rate for evoking either antidromic or orthodromic action currents, the stimulation strength was set to evoke 50% action current success rate.

## A



## B
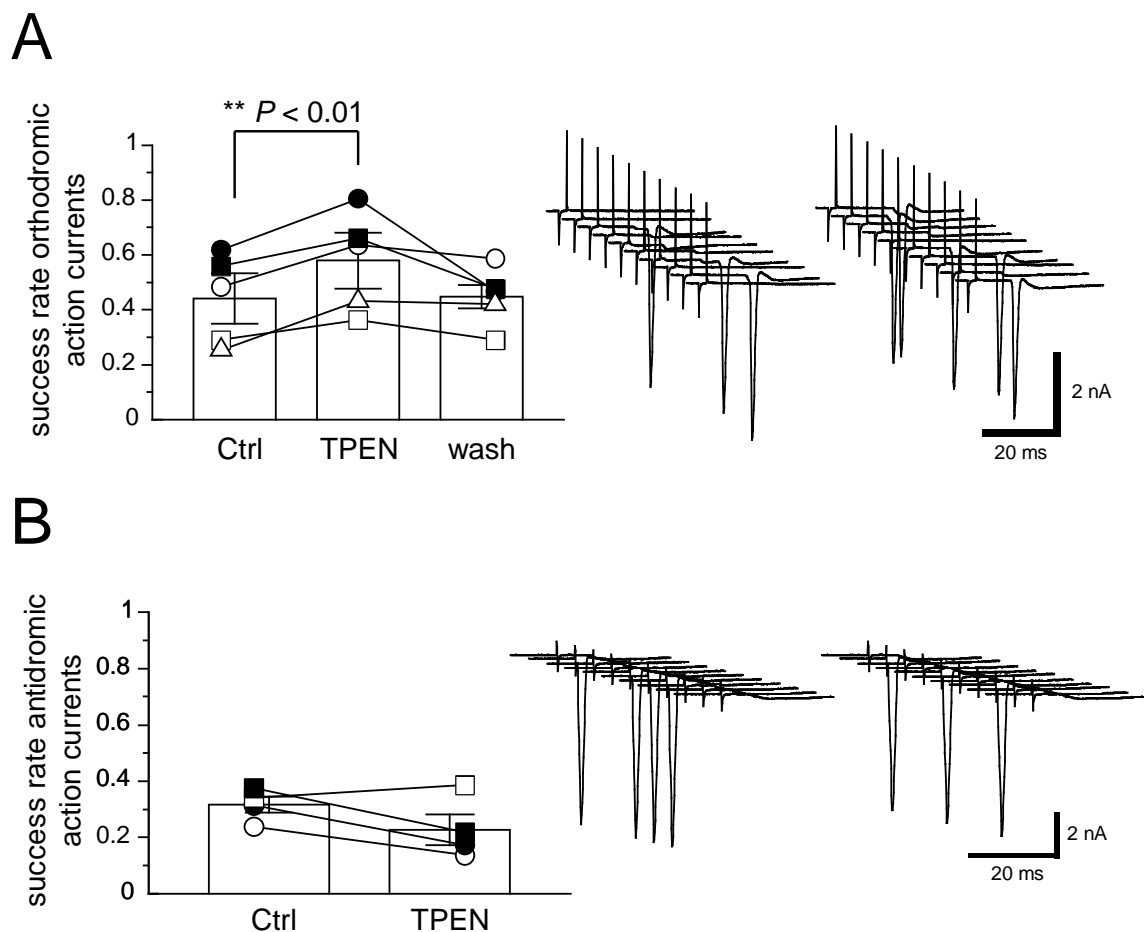


**Figure 5.5 – TPEN enhances the success rate for evoking orthodromic action currents but not antidromic action currents. A,B:** Bar plots showing the success rate for evoking orthodromic (**A**) and antidromic action currents (**B**) in control and in the background of TPEN (1μM). Traces show 10 consecutive trials before (left) and after application of TPEN (right).

Bath-application of TPEN significantly enhanced the success rate for evoking orthodromic action currents (Ctrl: 0.44 ± 0.09, TPEN: 0.58 ± 0.1, n = 5, $P < 0.004$, **figure 5.5**) while the success rate for evoking an antidromic action current

remained unchanged (Ctrl: 0.32 ± 0.03, TPEN: 0.23 ± 0.06, n = 4, *P* > 0.1, **figure 5.5**). This result suggested that the success rate for evoking an action current by direct activation of MFs was not altered in the presence of TPEN, while the probability for evoking orthodromic action currents was enhanced. Although this approach cannot distinguish between a pre- or postsynaptic origin of an enhancement in the success rate for evoking orthodromic action currents, this result suggested that stimulation of recurrent MFs can trigger action currents in voltage-clamp which were elicited as a result of $GABA_A R$-mediated IPSCs and whose success rate was modulated by endogenous $Zn^{2+}$.

### 5.1.3.  Presynaptic recordings from mossy fibre boutons

The most direct way to look for an effect of $Zn^{2+}$ on axonal excitability is to record from MFBs. An example of a MFB recording is shown in **figure 5.6**. MFBs were visualised with IR-videomicroscopy in SL in CA3 area. MFBs were identified by their very high input resistance and marked inward rectification in their I-V relationship (**figure 5.6B$_1$**). Another hallmark of MFBs is spike-broadening in response to repetitive stimulation (**figure 5.6C$_1$**). Following perfusion of CaEDTA (2mM) or TPEN (1µM), the action potential duration at half-maximal amplitude was increased from 894 ± 29µs to 956 ± 44µs (n = 8, *P* < 0.05) and from 1007 ± 39µs to 1092 ± 52µs (n = 8, *P* < 0.05), respectively (**figure 5.7**; data shown in this figure have been performed by Dr. Dominique Engel). Furthermore, there was a decrease in the input resistance following perfusion of CaEDTA (Ctrl 2.31 ± 0.3GΩ, CaEDTA 1.64 ± 0.18GΩ, n = 9, *P* < 0.05). In contrast, bath-application of TPEN had no effect on the input resistance (*P* > 0.05). The action potential amplitude remained unaffected following bath-application of both chelators (Ctrl 115.2 ± 2.1mV, CaEDTA 113.7 ± 2.5mV, n = 9, *P* > 0.05; Ctrl 112 ± 2.3mV, TPEN 105.6 ± 13.4mV, n = 8, *P* > 0.05). These small but significant changes in action potential spike width suggested that endogenous $Zn^{2+}$ affects axonal excitability. Whether this increase provides a ready explanation for the facilitation of evoked IPSCs remains to be elucidated.

A



$B_1$



-80 mV

20 mV

100 ms

$B_2$



20

I (pA)

-40   -20      20   40   60   80

20

-40

V (mV)

$C_1$



-79 mV

10 mV

5 ms

$C_2$



200 pA

20 ms

-83 mV

20 mV

100 ms
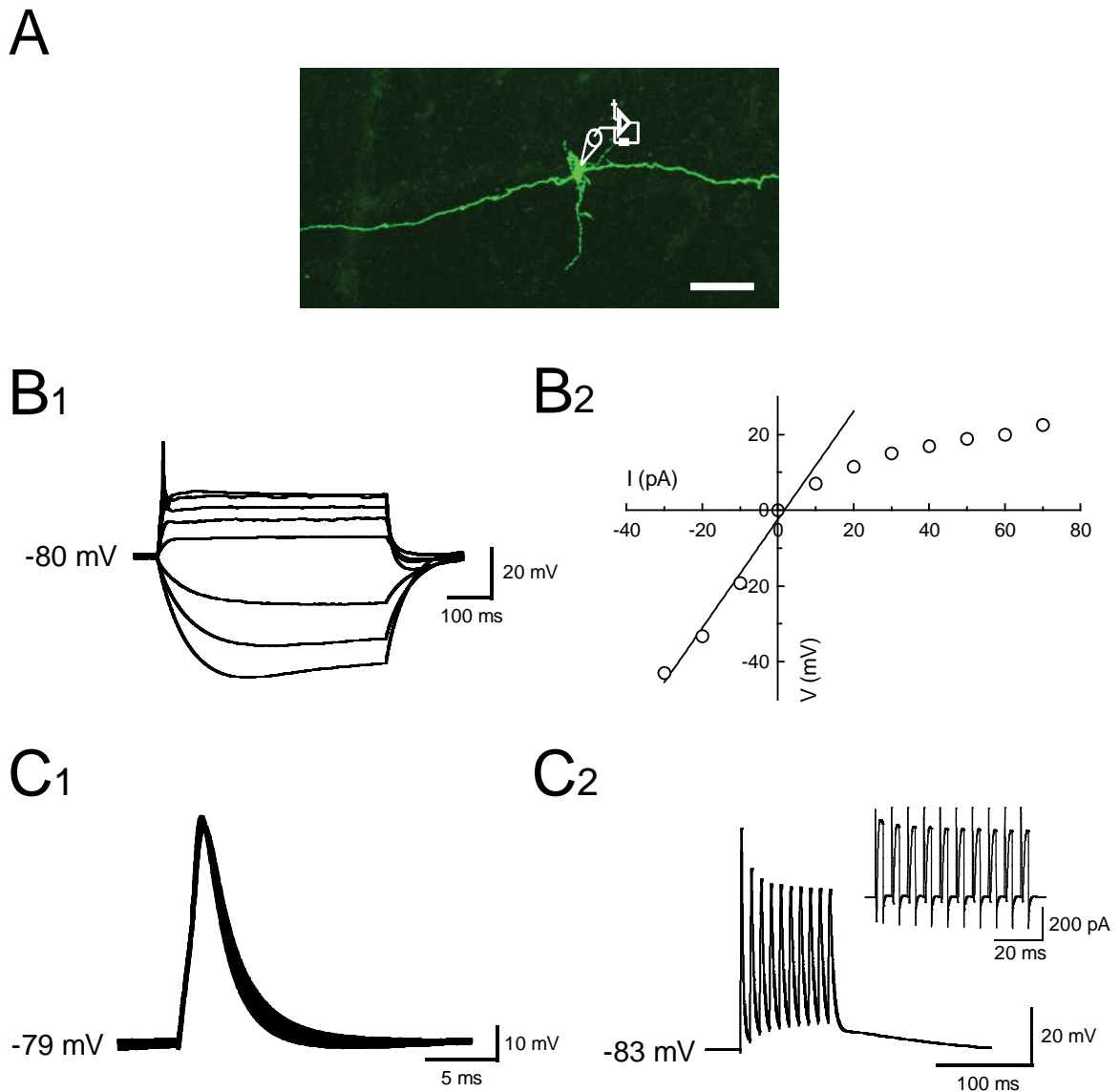
**Figure 5.6 – Electrophysiological properties of MFBs. A:** Confocal image from a MFB in CA3. **B1:** Voltage responses for negative and positive current injection (-30, -20, -10, +10, +30, +50, +70, +80pA) showing a marked inward rectification at negative potentials. **B2:** I-V relationship for the data shown in B1. The input resistance is 1.69 GΩ. **C1:** Superimposed action potentials elicited at 50Hz (1ms current injection of 1nA). The action potential shows the characteristic spike broadening typical of MFBs **C2:** Averaged action potentials at 100Hz in current-clamp and at 150Hz in voltage-clamp.
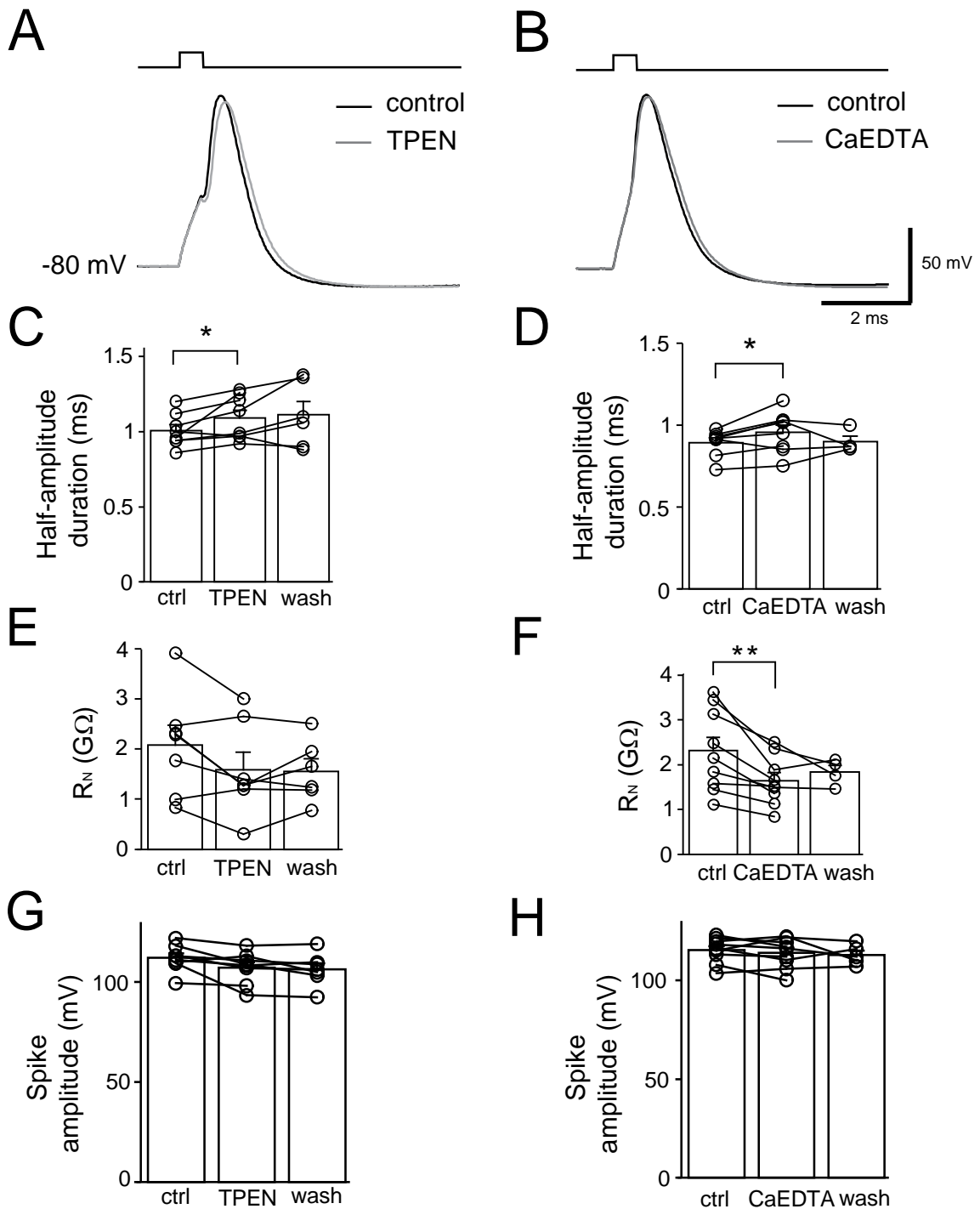
**Figure 5.7 – Zn$^{2+}$ chelators modulate the action potential wave-form in MFBs. A,B:** Wave-form of the action potential in response to a 0.5ms current injection of 800pA in control condition (black) and in TPEN (1µM, **A**, grey) or CaEDTA (2mM, **B**, grey). **C-H:** Summary histograms showing the effects of the Zn$^{2+}$ chelators TPEN (1µM, **C,E,G**) or CaEDTA (2mM, **D,F,H**) on action potential duration at half–maximal amplitude (n = 8), input resistance, $R_N$ (n = 7) and spike amplitude (n = 8). Data shown in this figure were obtained in collaboration with Dr. Dominique Engel.

In conclusion, AfP-, action current- and MFB recordings have been obtained to look at $Zn^{2+}$ actions on presynaptic excitability. The results suggest that changes in axonal excitability are unlikely to be a major contributor to the facilitatory effect of $Zn^{2+}$ chelators on evoked IPSCs in GCs. Importantly, the success rate for synaptically evoking orthodromic action currents was higher in the presence of the $Zn^{2+}$ chelator reflecting increased GC spiking activity.

## 5.2. MODULATION OF NMDA RECEPTORS

Another possibility that would account for a facilitation of IPSC amplitude in GCs following $Zn^{2+}$ chelation is a modulation of receptors or channels at the level of interneurons which would then result in an increase in GABA release. NMDARs are known to be tonically blocked by endogenous $Zn^{2+}$ at MF-CA3 synapses (Vogt *et al.*, 2000; Paoletti *et al.*, 1997), but it remains to be investigated whether such a phenomenon occurs at MF–interneuron synapses.

A stimulation electrode was positioned in SL while recording di-synaptic IPSCs from GCs held at $V_{holding}$ = -70mV in the background of the NMDAR antagonist D-APV (50µM, **figure 5.8A**). If NMDARs are tonically blocked by $Zn^{2+}$ then the degree of facilitation should be prevented or become smaller when chelating $Zn^{2+}$ in the presence of a NMDAR antagonist (**figure 5.8B,C**).
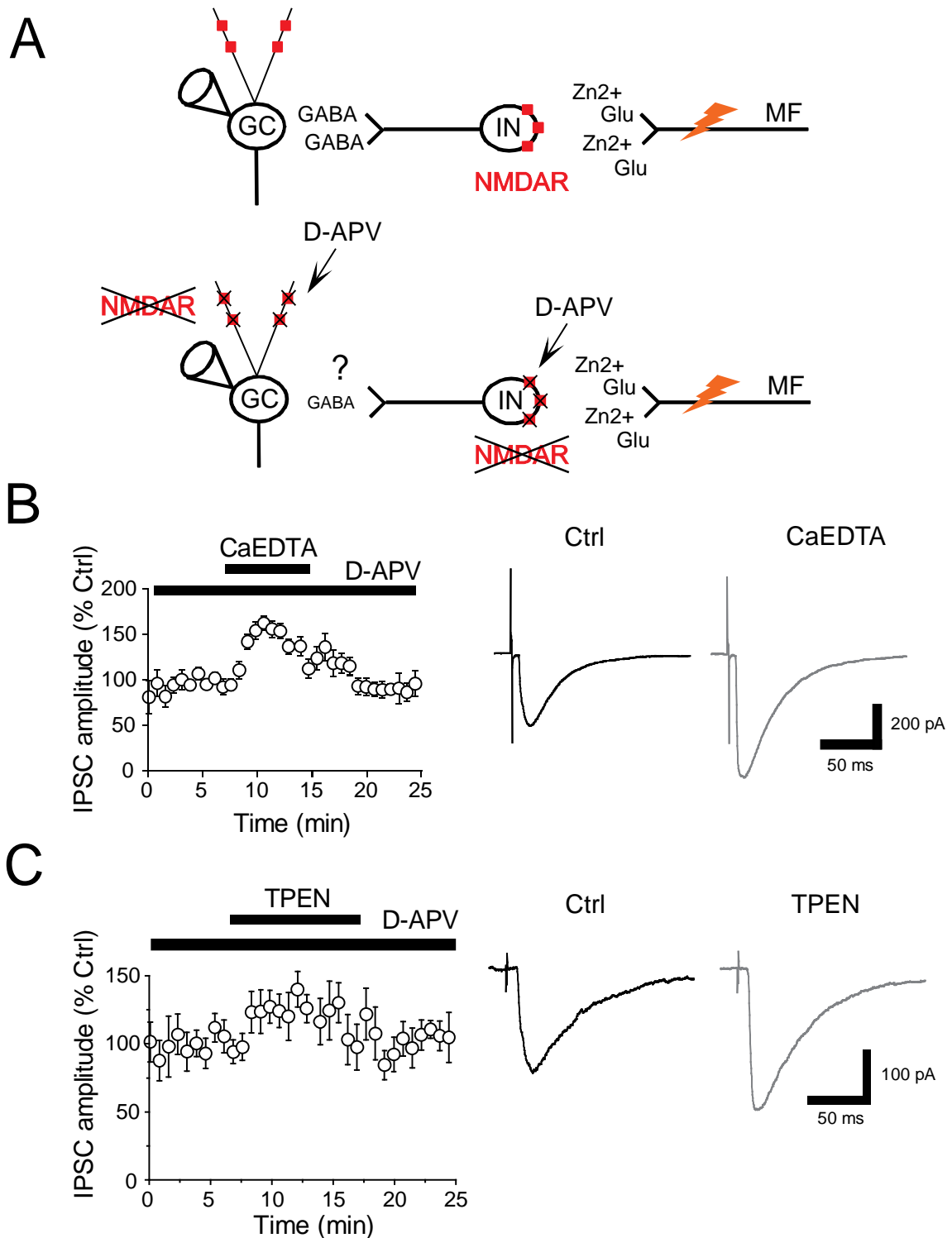
**Figure 5.8 – Modulation of NMDARs by endogenous Zn$^{2+}$. A:** Cartoon showing the experimental approach and the location of NMDARs at interneurons and GCs. Bath-application of D-APV blocks NMDARs at both cell types. **B,C:** Plot of the amplitude of SL evoked IPSCs against time showing the effect of CaEDTA (2mM) and TPEN (1μM) in the background of the NMDAR antagonist D-APV (50μM). Averaged traces for control (black) and the corresponding chelator (grey) are shown on the right.

When NMDARs were blocked with the subunit unspecific antagonist D-APV (50µM), perfusion of the $Zn^{2+}$ chelator CaEDTA (2mM) caused a significant reduction in the facilitation of IPSCs in GCs (without D-APV 75.2 ± 18.4% facilitation, with D-APV 46.1 ± 5.5% facilitation, n = 7, $P < 0.05$, unpaired t-test, **figure 5.8**). Interestingly, the effect of the membrane permeable chelator TPEN was very similar whether NMDARs were blocked or left intact suggesting differences in the mechanism of action (without D-APV 31.6 ± 5.2% facilitation, with D-APV 28.8 ± 7.9% facilitation, n = 6). Furthermore, removing $Mg^{2+}$ from the perfusion medium did not change this result, so that all recordings were pooled.

A modulation of NMDARs by endogenous $Zn^{2+}$ can occur either at postsynaptic NMDARs at dendrites of interneurons, or alternatively, $Zn^{2+}$ can act on dendritic NMDARs in GCs. In order to distinguish between these two possibilities, control experiments were performed, where GCs were held at the reversal potential for glutamate receptors ($V_{holding}$ = 0 mV) in order to isolate GABAergic transmission. The use-dependent NMDAR antagonist MK-801 (1mM) was also included in the pipette in order to block NMDARs specifically in GCs. If a facilitation of IPSC amplitude became smaller, this result would indicate towards an involvement of dendritic NMDARs at GCs (**figure 5.9A**).
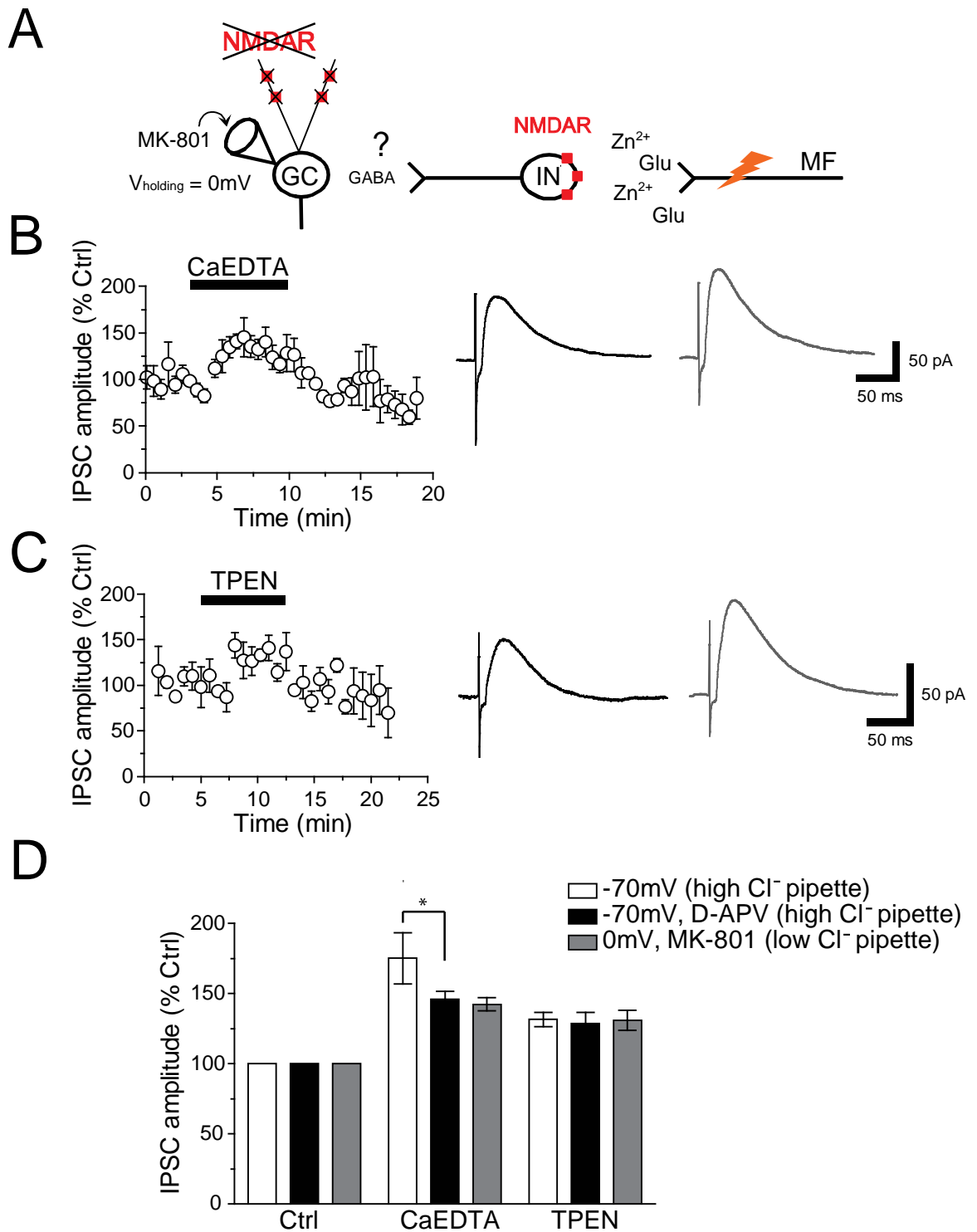
**Figure 5.9 – Effect of Zn$^{2+}$ chelators on IPSC amplitude in GCs with glutamatergic transmission blocked. A:** Cartoon showing the experimental design and the pharmacological approach. **B,C:** Plots of the amplitude of SL evoked IPSCs against time for CaEDTA (2mM) or TPEN (1µM) application. Corresponding traces for control (black) and the corresponding chelator (grey) are shown on the right. **D:** Summary bar plot comparing the extent of IPSC facilitation for each chelator in conditions where NMDARs are left unlocked (white bars), NMDARs are blocked by D-APV (black bars) and when glutamatergic transmission is blocked by MK-801 and V$_{holding}$ = 0mV (grey bars).

**Figure 5.9** shows a significant increase in the amplitude of IPSCs in response to perfusion of CaEDTA (42.4 ± 4.8%, n = 4, $P < 0.004$) and also TPEN (31 ± 7.1%, n = 4, $P < 0.05$). The degree of facilitation recorded at $V_{holding}$ = 0mV with Cs-gluconate was indeed similar to recordings in the background of D-APV recorded with CsCl (**figure 5.9D**). These results suggest that dendritic NMDARs at GCs may be also sensitive to perfusion of CaEDTA.

Because NMDARs partly contribute to the effect of CaEDTA on IPSC amplitude, IPSCs were recorded in the background of the GluN2B subunit specific blocker ifenprodil (3-10µM, **figure 5.10**) as CaEDTA has been shown to be unable to relieve the high-affinity block of GluN2A subunits by $Zn^{2+}$ (Vogt *et al.*, 2000).
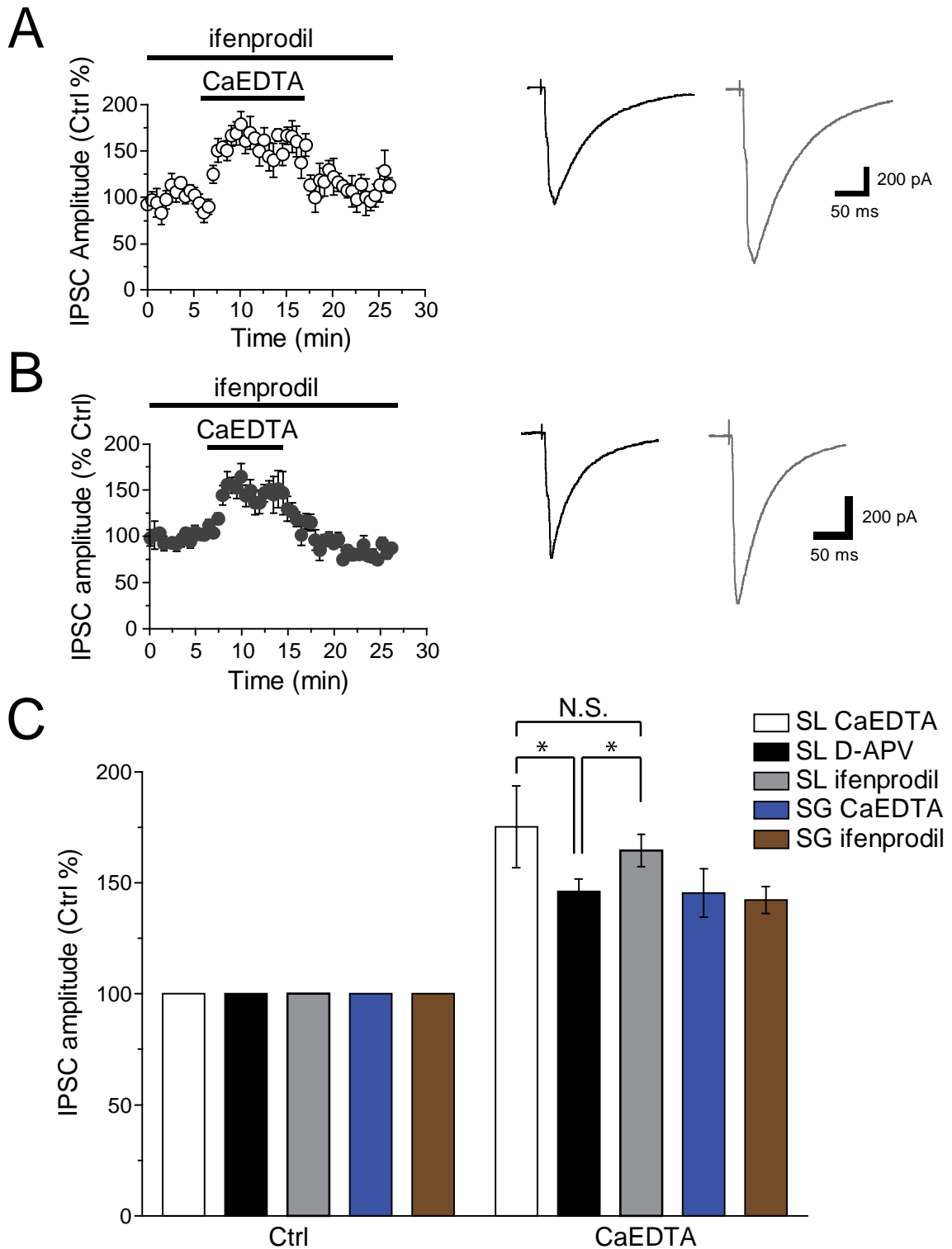
**Figure 5.10 – Chelator effect in the presence of the GluNR2B antagonist ifenprodil.** **A,B:** Plots showing the effect of CaEDTA (2mM) on IPSCs evoked by SL (**A**, white symbols) or SG stimulation (**B**, grey symbols) in the presence of ifenprodil (3-10μM). Traces on the right show control IPSCs before (black) and after superfusion of CaEDTA (grey). **C:** Summary diagram showing a modest contribution of GluN2B subunits to the chelator effect of CaEDTA.

When GluN2B subunits were blocked by the subunit specific antagonist ifenprodil (3-10μM), perfusion of CaEDTA (2mM) led to a significantly higher facilitation in IPSC amplitude compared to conditions when both NMDA subunits GluN2A and GluN2B were blocked with D-APV (CaEDTA [D-APV]: 46.1 ± 5.5%, CaEDTA [ifenprodil]: 64.6 ± 7.2%, n = 4, $P < 0.02$ Mann Whitney U-test, **figure 5.10C**). Thus, CaEDTA did not significantly alter the degree of facilitation of IPSCs when GluN2B subunit-containing receptors were blocked compared to conditions in which NMDARs were left unblocked (CaEDTA 75.2 ± 18.4%, CaEDTA [ifenprodil] 64.6 ± 7.2%) suggesting that GluN2B containing NMDARs do not contribute to the mechanism of action of CaEDTA. Similar results were obtained for IPSCs evoked by SG stimulation (CaEDTA 45.4 ± 10.9%, CaEDTA [ifenprodil] 42.3 ± 6%). Together, these results suggest that extracellular $Zn^{2+}$ chelation with CaEDTA involves NMDARs which do not contain GluN2B subunits.

## 5.3. LOCATION OF LOCAL CIRCUIT INTERNEURONS INVOLVED IN A MODULATION BY ENDOGENOUS $Zn^{2+}$

The modulation of evoked IPSCs in dentate GCs by endogenous $Zn^{2+}$ may be mediated via a local interneuron or distant projections among different hippocampal subfields. It is known that $Zn^{2+}$-containing MFs preferentially target interneurons in the CA3 area (Acsady *et al.*, 1998). These CA3 interneurons provide most of feed-forward inhibition to CA3 pyramidal cells (Buzsaki, 1984). Besides, some anatomical studies have also described CA3 interneurons which send their axon back to the dentate gyrus (Szabadics and Soltesz, 2009; Sik *et al.*, 1994). Also, in the dentate gyrus recurrent MF collaterals target local interneurons which also innervate GCs. Thus, interneurons in CA3 or in the dentate gyrus could be the target of endogenous $Zn^{2+}$. The location of the stimulation electrode is unable to dissect between these two possibilities as stimuli delivered in SL can activate MFs whose action potentials propagate antidromically to GC somata or terminals made on to interneurons. Alternatively, electrical stimulation in SL can directly activate axons from CA3 interneurons whose projections extend to the dentate gyrus and synapse on to GCs.

Therefore, local glutamate application was used, originally developed by Weisskopf and Nicoll (1995), in an attempt to uncover the location of relay interneurons which may indirectly mediate the modulation described above.

### 5.3.1. Direct excitation of dentate granule cells or local interneurons by local glutamate application

A puff electrode was positioned in the outer ML to excite GC dendrites (**figure 5.11A**). **Figure 5.11B** shows that local glutamate application (puff duration 50ms, puff pressure 10psi, 100mM glutamate) in the ML elicited a train of EPSCs recorded in voltage-clamp mode whose reversal potential was ~0mV. The magnitude of glutamate evoked EPSCs also depended on the duration of the glutamate application (**figure 5.11C**).
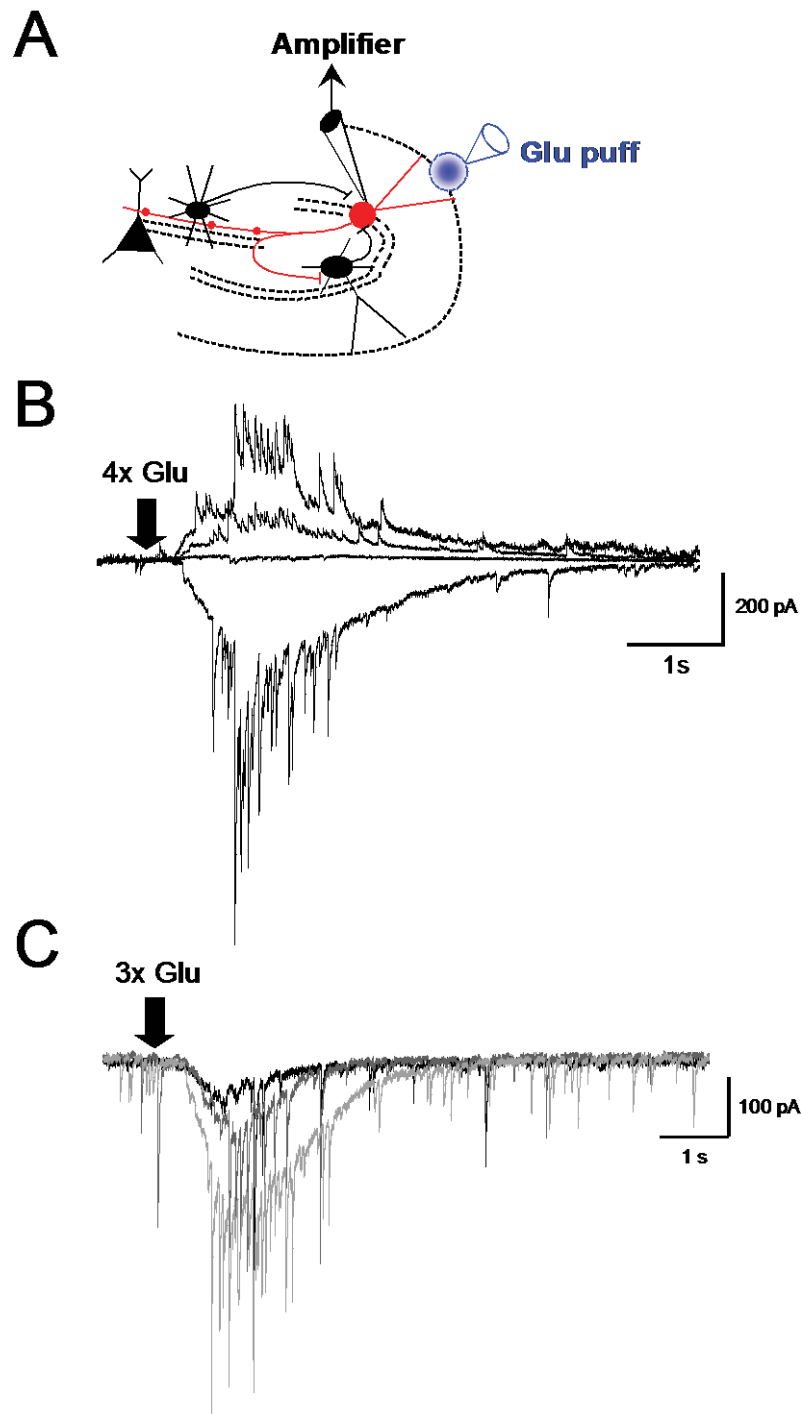
**Figure 5.11 – Local glutamate application in the dentate gyrus elicits slow currents superimposed with bursts of phasic currents in GCs. A:** Drawing of a hippocampal outline showing the location of glutamate puffs in the ML. **B:** Superimposed current traces in response to glutamate puffs ($V_{holding}$ = -70mV, 0mV, +20mV, +40mV). PSCs reverse at 0mV (Puff duration 50ms, 10psi). **C:** Superimposed current traces in response to increased puff duration shows that glutamate puff application is time-dependent. 20ms (black), 30ms (dark grey), 40ms (light grey), ejection pressure 10psi.

In current-clamp mode, glutamate puffs in the ML of the dentate gyrus depolarised and evoked trains of action potentials in GCs or hilar interneurons such as BCs whose dendrites span the ML (**figure 5.12**). Similarly, positioning the puff pipette in SL also evoked action potentials in SL interneurons (**figure 5.13**).
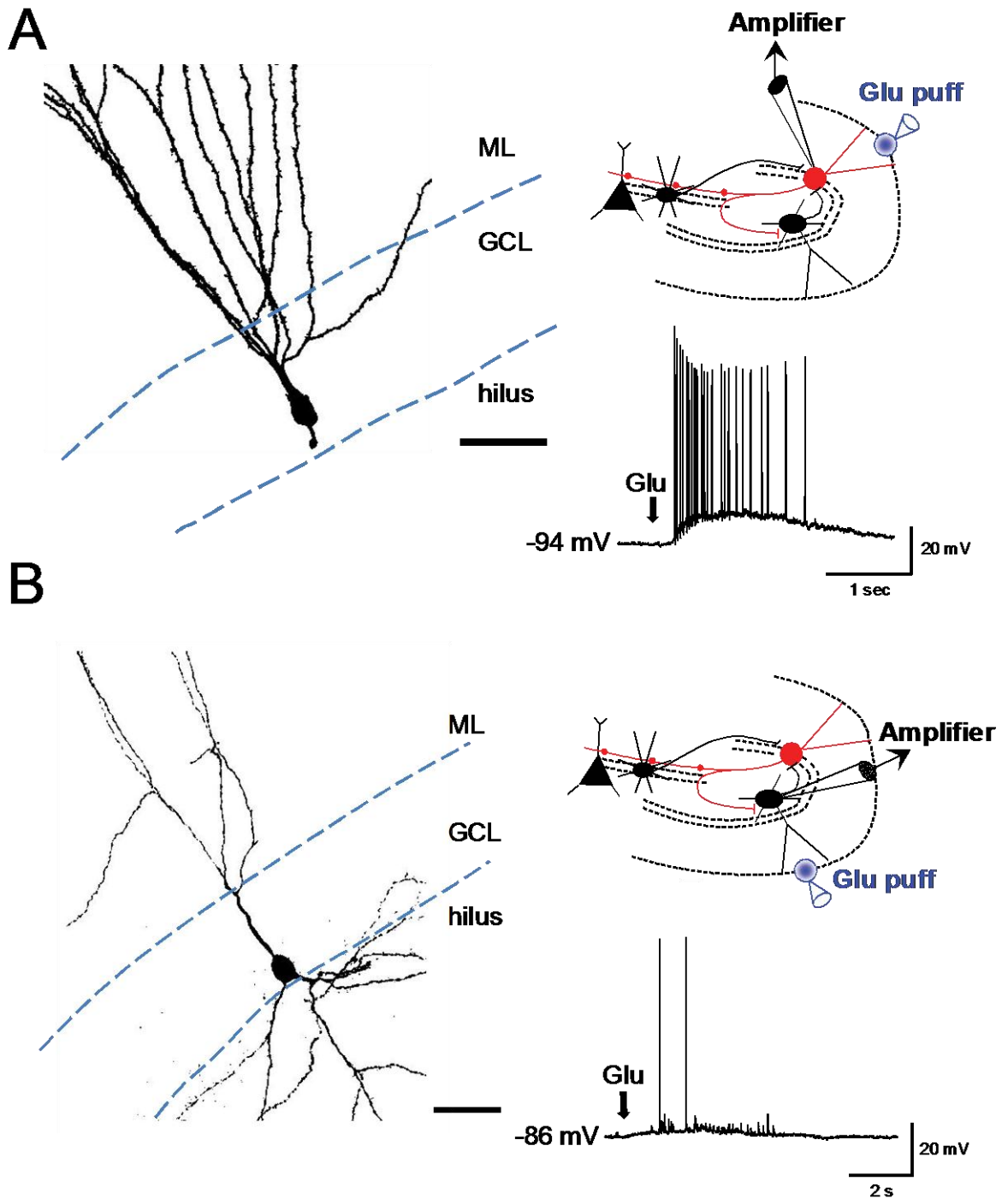
**Figure 5.12 – Local glutamate application in the ML in current-clamp mode. A,B:** (Top right) The cartoons show the location of the glutamate application for GC or dentate interneuron recordings. (Bottom right) Local glutamate application to the dendritic tree of a GC elicits a depolarisation and a train of action potentials in (**A**). A similar glutamate puff evokes a depolarisation and spiking in a dentate interneuron (**B**). (Left) The morphology and location of representative cells is also shown. Scale bars in A and B: 50µm. Puff duration 20-40ms, 6-12psi.

# A$_1$

# A$_2$

**Amplifier**

**Glu puff**

**Glu**

−87 mV

20 mV

500 ms

# B

SL

SP

SO
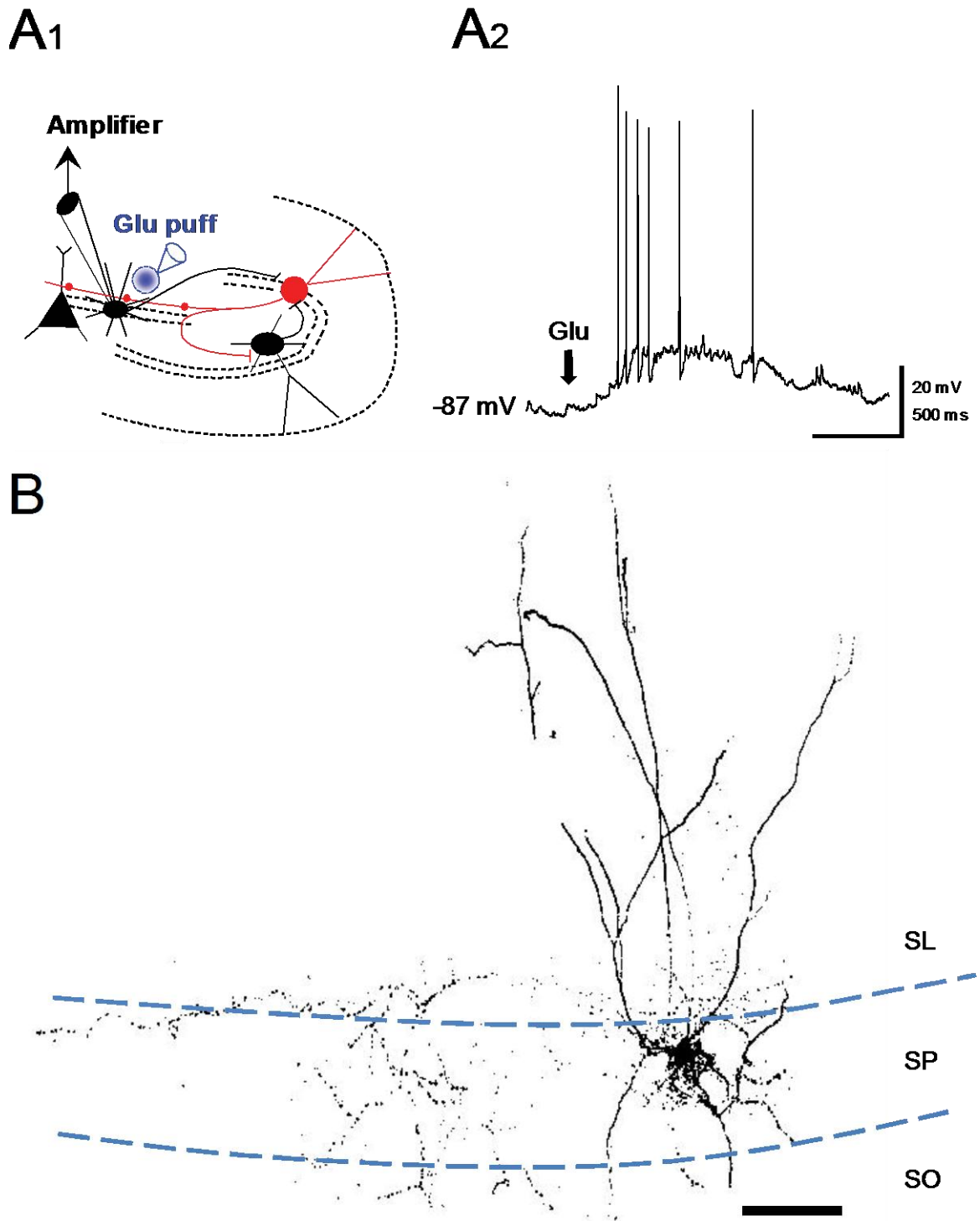
**Figure 5.13 - Local glutamate application in SL recruits interneurons in CA3. A1:** Cartoon showing a glutamate puff application in SL while recording from an interneuron in CA3. **A2:** Voltage trace from a CA3 interneuron showing a depolarisation and a train of action potentials in response to a glutamate puff in SL. **B:** The image shows the morphology and location of the recorded neuron. Scale bar in B 50μm. SP stratum pyramidale, SO stratum oriens. Puff duration 20-40ms, 6-12psi.

These results show that under the present conditions, local puff application of glutamate is a suitable method to test whether interneurons which may be modulated by endogenous Zn$^{2+}$ are located in SL and/or in SG.

## 5.3.2. Differential sensitivity of granule cells to local glutamate application in strata lucidum and granulosum

To distinguish between these two possible locations, the puff electrode was positioned in SL and responses evoked by glutamate puffs in SL and SG were compared while recording from GCs (**figure 5.14A1,2)**. When applying glutamate in SL the mean interevent interval or frequency of PSCs did not differ from that of spontaneously occurring PSCs before the puff (interevent interval control: 355.5 ± 77.3ms, puff: 387.9 ± 94.1ms, frequency: control 2.81 ± 0.61Hz, frequency puff 2.58 ± 0.56Hz, n = 4, *P* > 0.1). In contrast, simultaneous electrical stimulation in SL evoked IPSCs in GCs demonstrating that synapses onto interneurons could be activated. When moving the puff electrode from SL to SG, glutamate puffs evoked PSCs whose interevent interval significantly decreased or frequency significantly increased compared to spontaneously evoked events (interevent interval control: 305.8 ± 71.3 ms, puff: 83.5 ± 8.8, frequency: control 3.27 ± 0.71 Hz, frequency puff 11.97 ± 2.60 Hz, n = 4, *P* < 0.001, **figure 5.14**). These results suggest that, interneurons can be chemically activated by positioning the puff electrode in SG indicating an interneuron-GC circuit within the dentate gyrus.
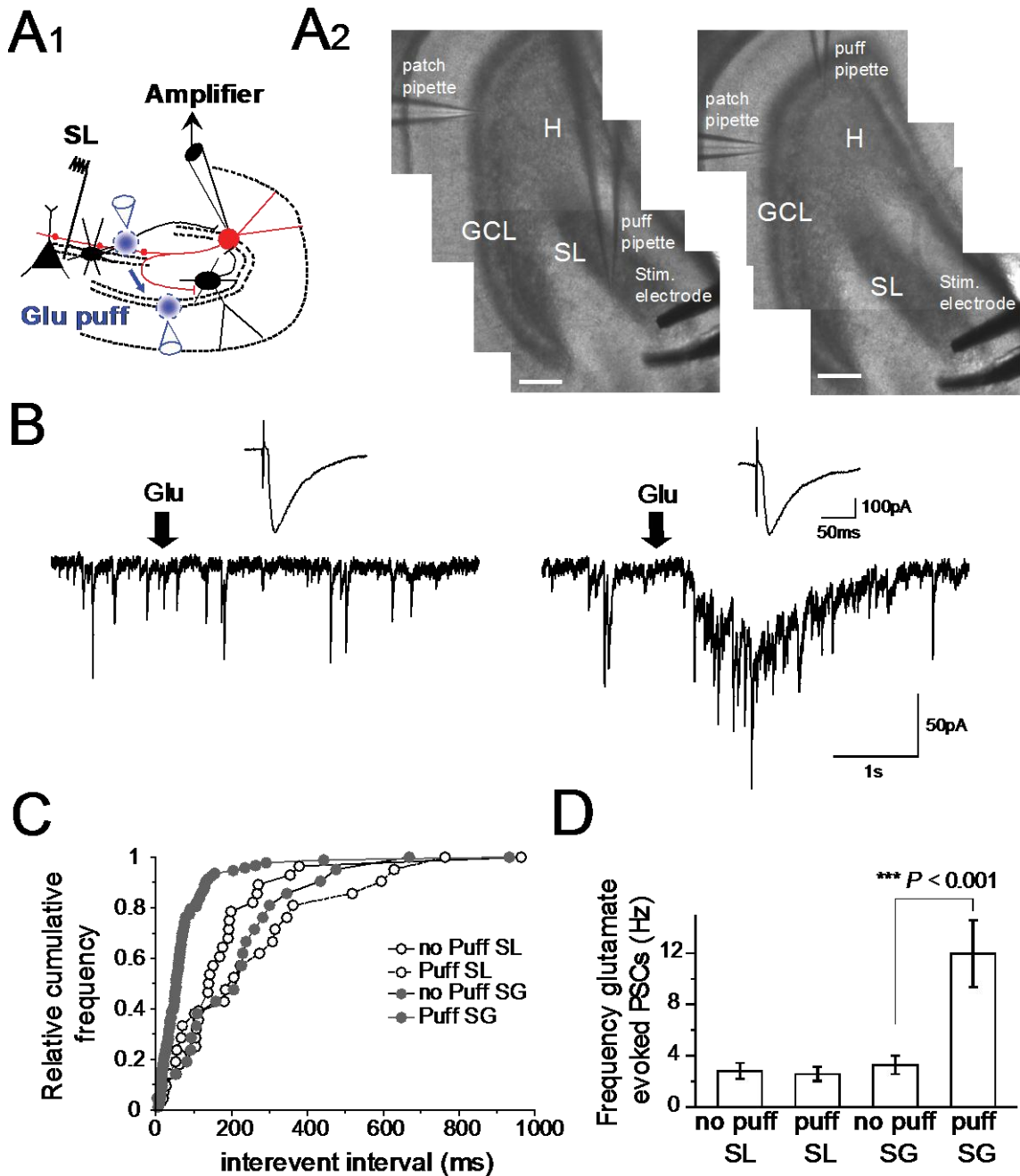
**Figure 5.14** – **Local glutamate application in SG evokes PSCs in GCs. A1:** Cartoon showing the position of the stimulation electrode in SL and a puff pipette (blue) in SL. In these experiments, the puff pipette is moved from SL to SG. **A2:** DIC images of the patch-, puff- and stimulation electrodes. Scale bars 200μm **B:** Representative traces showing the response elicited by a glutamate puff in SL and in SG. SL evoked IPSCs are shown on top. **C:** Cumulative distributions of inter-event intervals for SL and SG glutamate puffs. **D:** Summary bar graph showing a significant increase in PSC frequency for SG puffs.

### 5.3.3. Modulation of glutamate evoked responses by Zn$^{2+}$ chelators

Having shown that electrically-evoked IPSCs facilitate in the presence of Zn$^{2+}$ chelators, it was next tested whether this effect also persisted when synapses were chemically activated (**figure 5.15**). A puff electrode was positioned in SG in order to stimulate interneuron-GC connections similar to the experimental approach when interneurons were recruited electrically. Here, the AMPA- and kainate receptor antagonist NBQX (20µM) was also applied in order to minimise poly-synaptic activity. NMDARs were left unblocked.
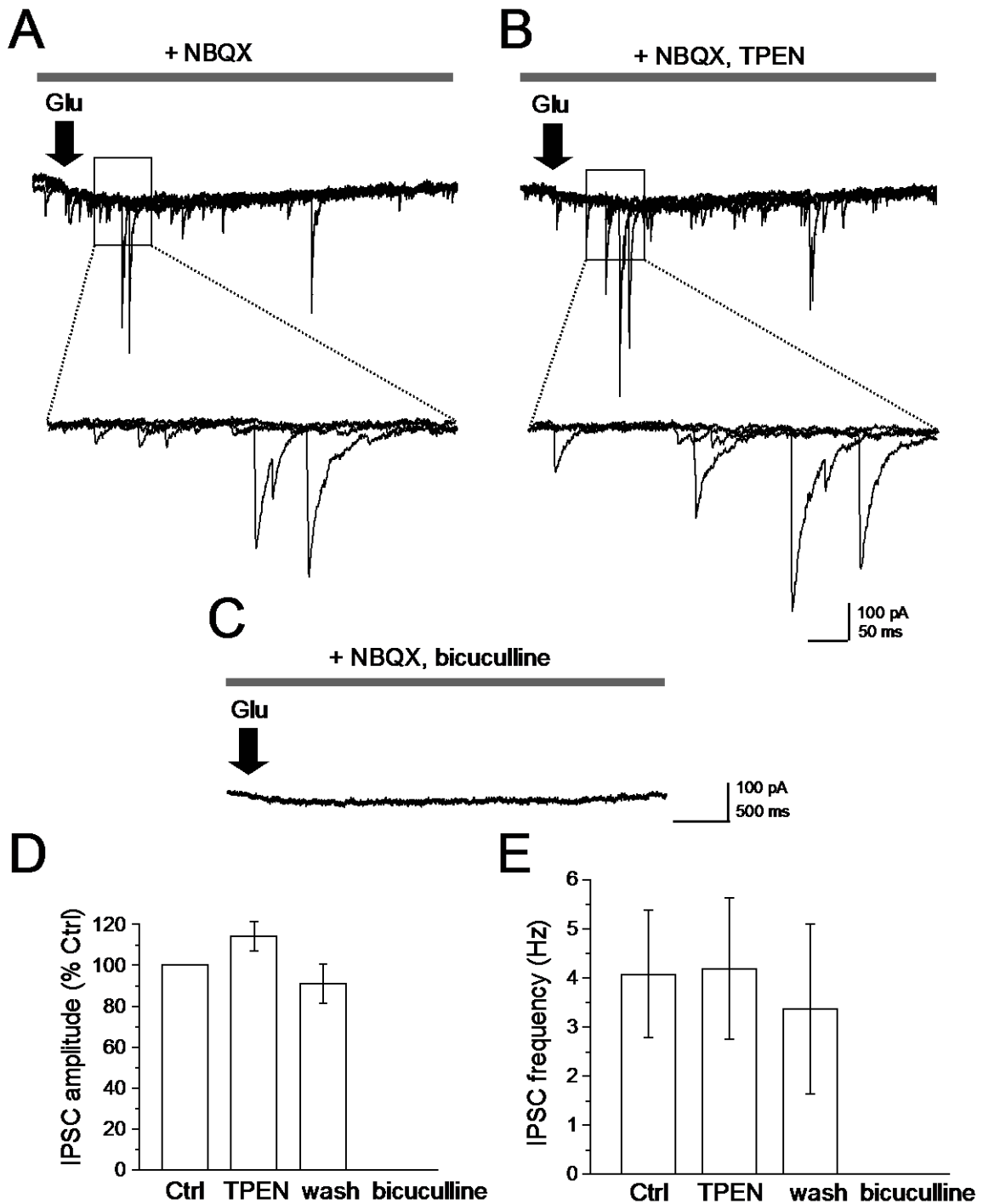
**Figure 5.15 – TPEN enhances glutamate evoked IPSCs in GCs. A-C:** 4 representative traces have been superimposed to show the effect of TPEN (1µM) and bicuculline (10µM) on the amplitude and frequency of glutamate evoked IPSCs in GCs. Calibration bars in **C** apply to all enlarged traces whereas calibration bars in **B** apply only for magnified traces. Arrows indicate the glutamate application. **D:** Summary histograms showing the effect of TPEN on the amplitude (**D**) and on the frequency (**E**) of IPSCs in GCs.

As shown in **figure 5.15**, perfusion of the Zn$^{2+}$ chelator TPEN caused a small increase in the amplitude of glutamate evoked PSCs (TPEN 14.4 ± 7.1% facilitation, washout 9 ± 9.7% depression, n = 4, $P$ > 0.05), without affecting the frequency of events (control 4.1 ± 1.3Hz, TPEN 4.2 ± 1.4Hz, washout 3.4 ± 1.7Hz, n = 4, $P$ > 0.05). Perfusion of bicuculline (10µM) completely abolished all PSCs indicating that they were mediated by GABA$_A$Rs. These results suggest that bath-application of TPEN enhanced IPSCs in GCs which have been evoked by local glutamate puffs binding to glutamate receptors including NMDARs in dentate interneurons.

The rather small degree of facilitation in glutamate evoked IPSC amplitude may be caused by the blockade of AMPARs by NBQX which deprives NMDARs of their depolarisation making them partly inactive. The experiment was thus repeated with the omission of NBQX in one GC which was held at the reversal potential for glutamate receptors (V$_{holding}$ = 0mV) to isolate GABAergic transmission in GCs. The use-dependent NMDAR blocker MK-801 (1mM) was also included in the recording pipette to ensure the block of dendritic NMDARs in the recorded GC only. In addition, a stimulation electrode was positioned into SL to simultaneously record changes in the amplitude of electrically evoked IPSCs (**figure 5.16E**).
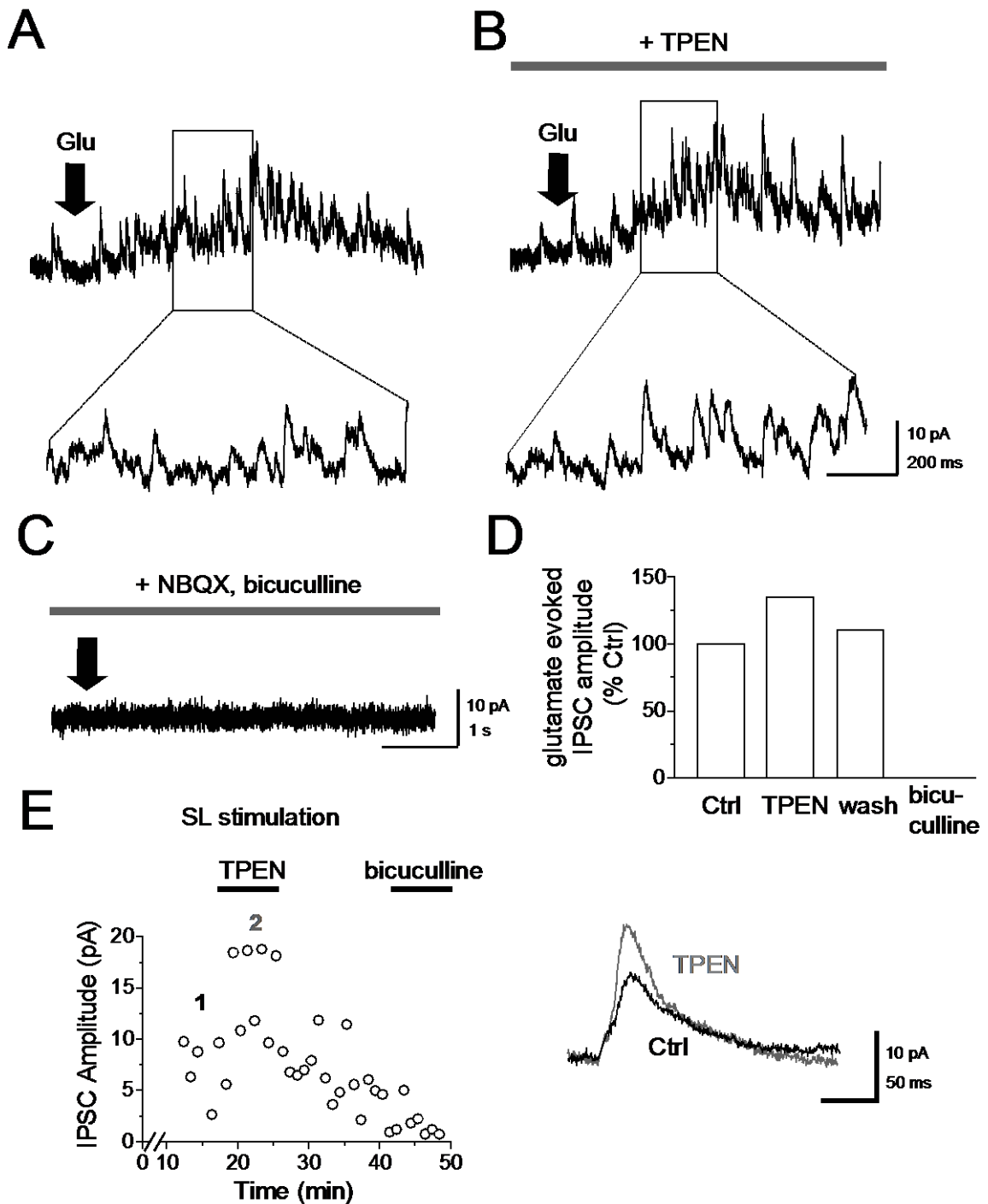
**Figure 5.16 – Effect of TPEN on the amplitude of glutamate evoked IPSCs in GCs with glutamatergic transmission blocked. A-C:** Representative traces showing the effect of local glutamate application ($V_{holding}$ = 0mV) in control condition (**A**), in the presence of TPEN (1μM, **B**) and after superfusion of NBQX (20μM) and bicuculline (10μM, **C**). **D:** Summary bar chart showing an increase in IPSC amplitude following the superfusion of TPEN, and a full blockade after application of NBQX and bicuculline. **E:** TPEN also increases the amplitude of SL evoked IPSCs. Traces in control condition (black) and in TPEN (grey) are shown on the right.

Perfusion of TPEN facilitated the amplitude of glutamate evoked IPSCs by 34.6% (**figure 5.16D**). Also, SL stimulation enhanced the amplitude of evoked IPSCs by 59.5%. This result raises the possibility that Zn$^{2+}$ chelation indirectly causes an increase in IPSC amplitude in GCs by modulating interneurons.

In a control experiment, KCl (3M) was puffed locally in SL and SG with the attempt to excite MFs or interneuron axons with a transient increase of extracellular K$^+$. While glutamate application only recruits somato-dendritic glutamate receptors, KCl application can also excite axons in addition to somata and dendrites which also evoke poly-synaptic responses. Unlike glutamate application, KCl application would yield a qualitatively similar response compared to electrical stimulation (**figure 5.17**).
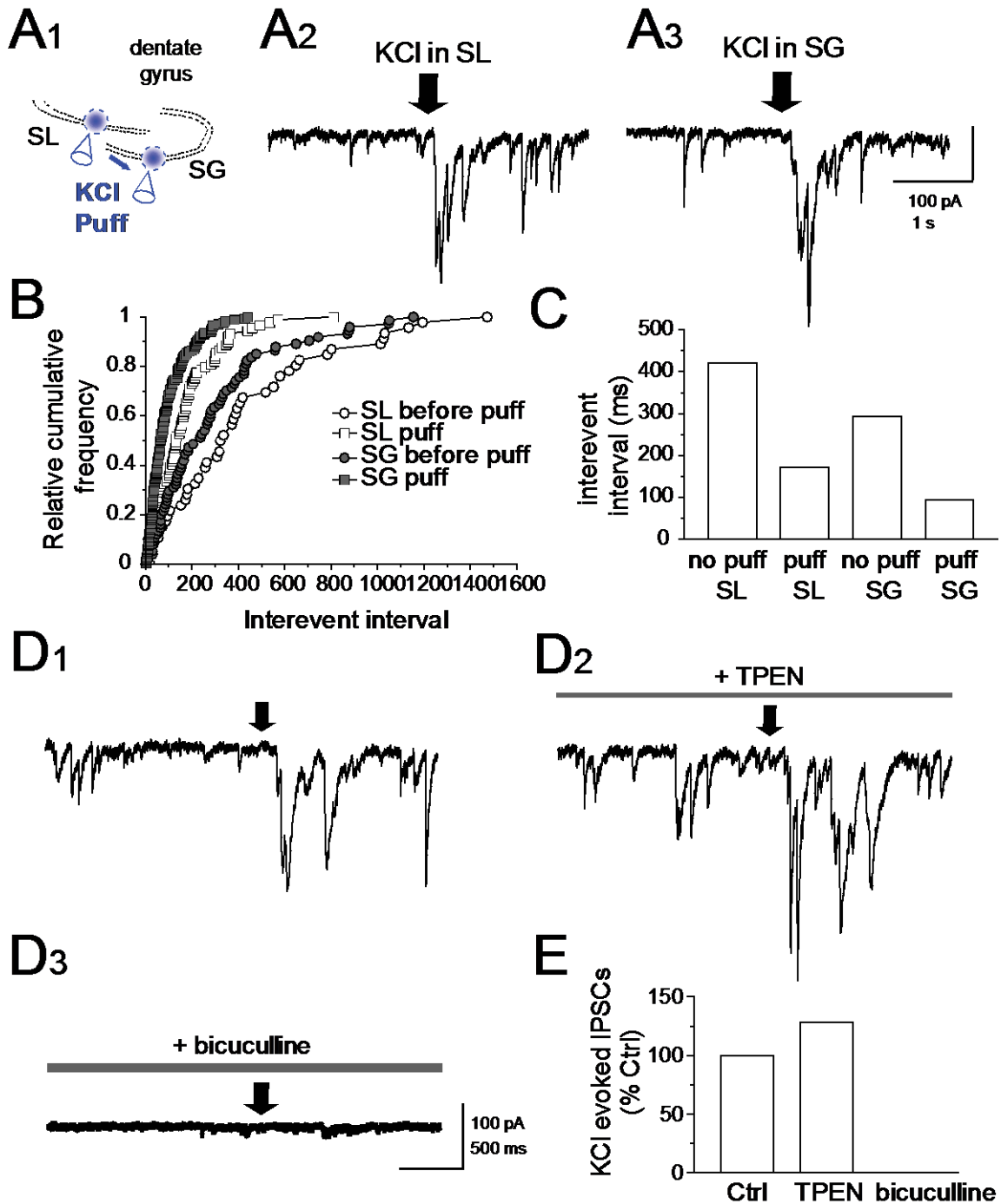
**Figure 5.17** – **Local KCl puff in SL and SG evokes IPSCs in GCs. A1:** Drawing of the outline of the hippocampus and the location of the puff pipette. The KCl-containing puff pipette is moved from SL to SG during the course of the experiment. **A2,3:** Representative current traces show bursts of PSCs in a GC in response to KCl puff in SL or in SG. **B:** Cumulative distributions of inter-event intervals for KCl puffs in SL and SG. **C:** Bar chart comparing the inter-event intervals for KCl puffs in SL and SG. **D1-3:** Current traces showing the effect of TPEN (1µM) and bicuculline (10µM) on the amplitude of KCl evoked PSCs. **E:** Summary bar chart showing the effect of TPEN and bicuculline on the amplitude of KCl evoked IPSCs

Local puffs of KCl in SL evoked bursts of IPSCs in a GC (interevent interval before puff in SL: 421.8ms, after puff 170.9ms, n = 1, **figure 5.17A**). These bursts most likely reflected the antidromic invasion of MFs and subsequent excitation of interneurons projecting onto GCs. When moving the puff electrode to SG while recording from a GC, KCl puffs elicited a similar response compared to those in SL (interevent interval before puff in SG: 294.2ms, after puff 94.6ms, **figure 5.17A-C**). Finally, bath-application of TPEN (1μM) increased KCl evoked IPSCs in GCs by 28.4% (**figure 5.17E**). This result is consistent with the idea that KCl application in SL, unlike glutamate puffs, can excite interneuron-GC circuits, thus mimicking electrical stimulation.

Altogether, the results show that interneurons in SL and SG can be recruited via local glutamate application. When recording from GCs, glutamate puffs in SG evoked IPSCs whereas they did not when glutamate puffs were delivered in SL. In contrast, KCl application in both SL and SG evoked IPSCs, thus mimicking electrical stimulation. Thus, the results suggest that soma and dendrites of interneurons are presumably located in or near SG.

## 5.4. MODULATION OF VOLTAGE-GATED $Ca^{2+}$ CHANNELS

Modulation of NMDARs can only partly provide a mechanism for the facilitation of GABAergic IPSCs in GCs. Alternative molecular targets of endogenous $Zn^{2+}$ which would result in a decrease in GABA release are VGCCs. $Zn^{2+}$ can modulate VGCCs with varying sensitivities depending on their $\alpha 1$ subunit (Sun *et al.*, 2007). At MF synapses, P/Q-type ($Ca_v2.1$), N-type ($Ca_v2.2$) and R-type ($Ca_v2.3$) subunits are primarily expressed at presynaptic boutons (Li *et al.*, 2007), whereas L-type ($Ca_v1.1$-1.4) or T-type ($Ca_v3.1$-3.3) $Ca^{2+}$ channels are mainly found at postsynaptic sites at hippocampal neurons (Hell *et al.*, 1993; Talley *et al.*, 1999). In order to test whether any of the five subtypes of VGCCs are modulated by endogenous $Zn^{2+}$, the two-pathway experiments in GCs were repeated in the background of subunit specific $Ca^{2+}$ channel blockers (**figures 5.18 – 5.22**). In order to block P/Q-type, N-type or R-type VGCCs, slices were incubated with ω-agatoxin IVA (0.5µM), ω-conotoxin GVIA (2µM) or SNX 482 (0.5µM), respectively. Slices were maintained within an interface chamber at least for 2h prior to the beginning of the recording (see Methods).
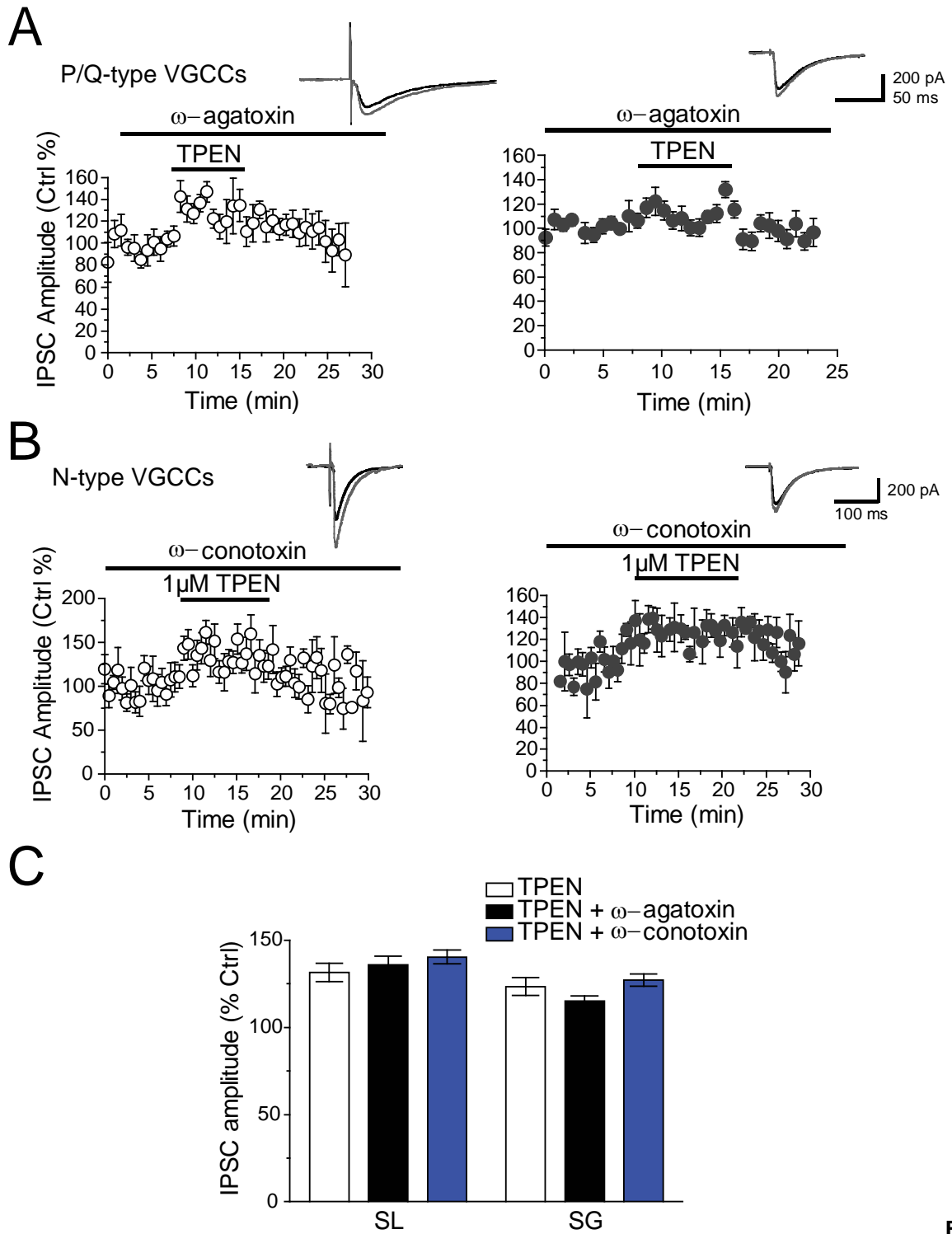
**Figure 5.18 – Effect of the chelator in the presence of the P/Q-type or N-type specific VGCC antagonist ω-agatoxin or ω-conotoxin. A,B:** Plots of the effect of TPEN (1µM) on the SL evoked (white symbols, left) or SG evoked (grey symbols, right) IPSC amplitude in the presence of ω-agatoxin (0.5µM) or ω-conotoxin (2µM) to block P/Q type- (**A**) or N-type- (**B**) VGCCs. Traces are superimposed for control condition (black) and in the presence of TPEN (grey). **C:** Summary bar chart showing a similar extent in IPSC facilitation following perfusion of TPEN, when P/Q-type or N-type VGCCs were left unblocked (white bars) compared to conditions in which they were blocked with ω-agatoxin (black bars) or ω-conotoxin (blue bars).
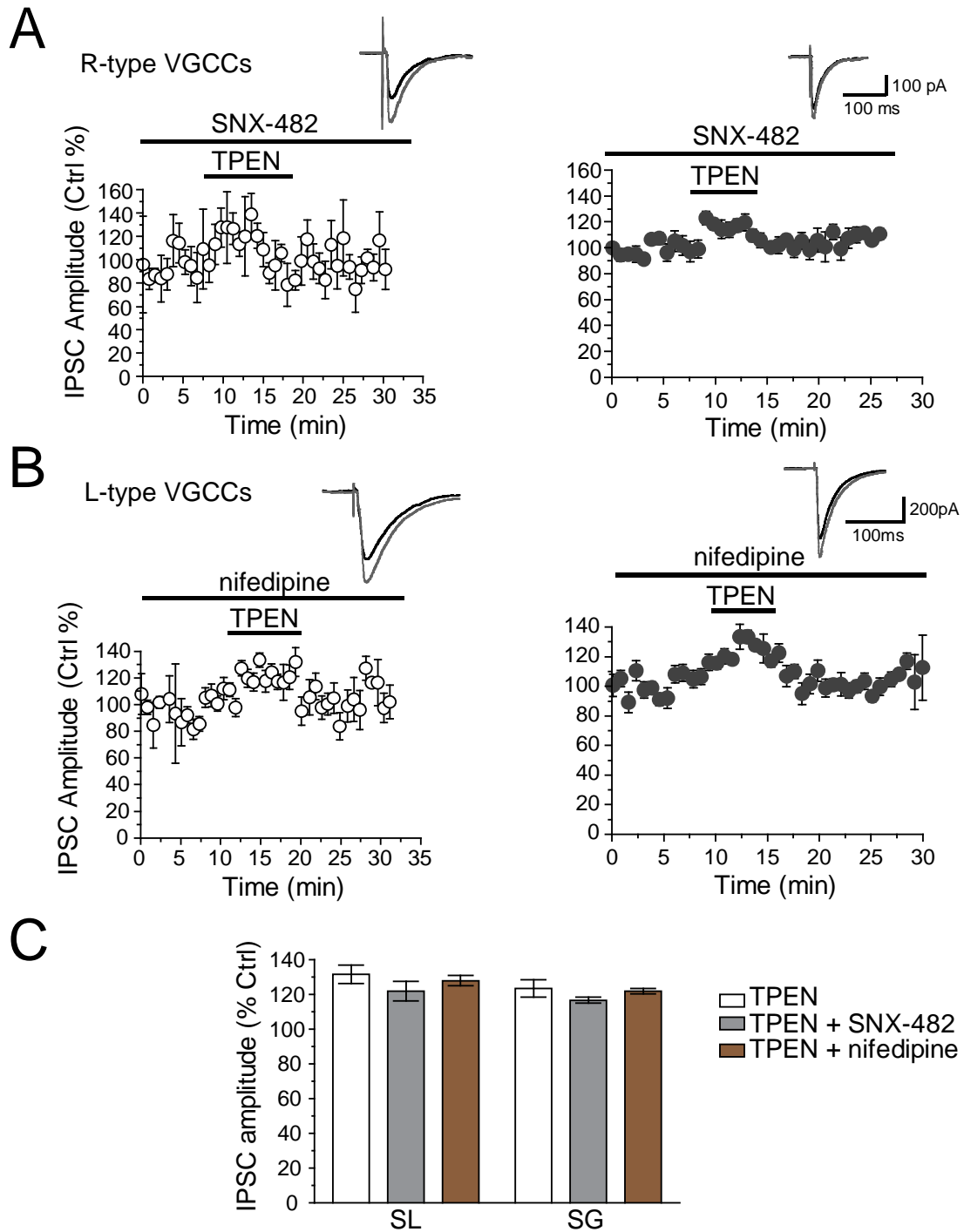
**Figure 5.19 – Effect of the chelator in the presence of the R-type or L-type specific VGCC antagonist SNX-482 or nifedipine. A,B:** Plots of the effect of TPEN (1μM) on the SL evoked (white symbols, left) or SG evoked (grey symbols, right) IPSC amplitude in the presence of SNX-482 (0.5μM) or nifedipine (20μM) to block R-type- (**A**) or L-type- (**B**) VGCCs. Traces are superimposed for control condition (black) and in the presence of TPEN (grey). **C:** Summary bar chart showing a similar extent in IPSC facilitation following perfusion of TPEN, when R-type or L-type VGCCs were left unblocked (white bars) compared to conditions in which they were blocked with SNX-482 (grey bars) or nifedipine (brown bars).
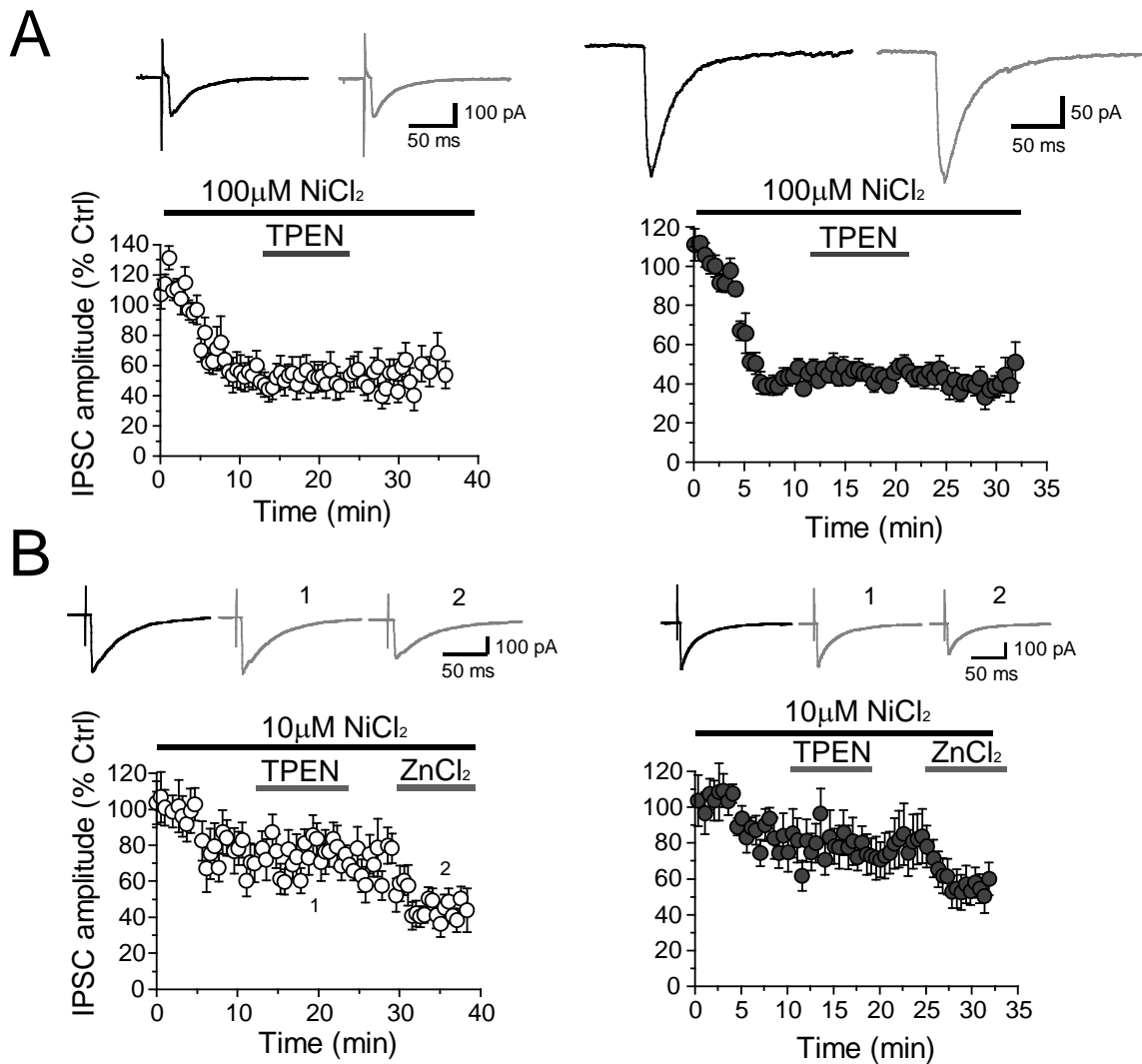
**Figure 5.20 – TPEN does not affect the IPSC amplitude in the presence of different concentrations of NiCl$_2$. A:** Plots of the effect of TPEN (1µM) on SL evoked (white symbols, left) or SG evoked (grey symbols, right) IPSCs in the presence of 100µM NiCl$_2$. Traces are shown in control condition (black) and in TPEN (grey). **B:** Plots of the effects of TPEN and subsequent bath-application of ZnCl$_2$ (10µM) on SL evoked (white symbols, left) or SG evoked (grey symbols, right) IPSCs in the presence of 10µM NiCl$_2$. Traces are shown for control condition (black) and following perfusion of TPEN or ZnCl$_2$ (grey, numbers on plot distinguish between drugs).
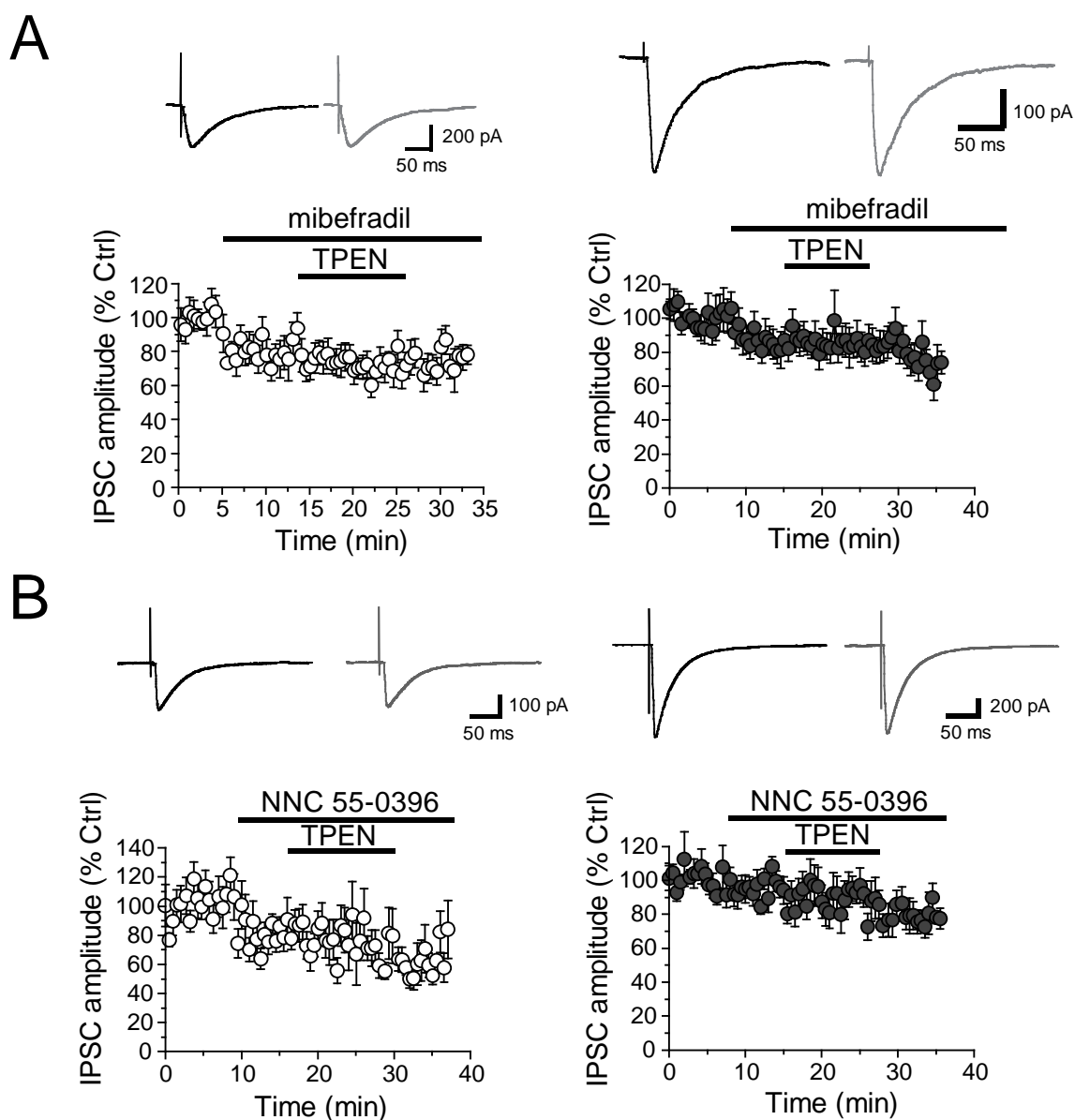
**Figure 5.21 – TPEN does not affect the IPSC amplitude in the presence of the specific T-type channel antagonist mibefradil or NNC 55-0396. A:** Plots of the effect of TPEN (1µM) on SL evoked (white symbols, left) or SG evoked (grey symbols, right) IPSCs in the presence of the specific T-type VGCC antagonist mibefradil (10µM,**A**) or the specific Ca$_v$3.1 T-type VGCC antagonist NNC 55-0396 (10µM,**B**). Traces are shown for control condition (black) and following perfusion of TPEN (grey).

Table 5.1

| TPEN | SL | | SG | |
|---|---|---|---|---|
| | Mean ± SEM | n | Mean ± SEM | n |
| nifedipine (L) | + 28 ± 3% | 5 | + 21.8 ± 1.6% | 4 |
| ω−agatoxin (P/Q) | + 36 ± 4.8% | 5 | + 15 ± 3% | 4 |
| ω−conotoxin (N) | + 40.4 ± 4% | 5 | + 27.1 ± 3.5% | 3 |
| SNX-482 (R) | + 21.8 ± 5.6% | 2 | + 16.6 ± 1.7% | 4 |
| mibefradil (T) | - 1.1 ± 4.9% | 7 | - 4.7 ± 2.9% | 9 |
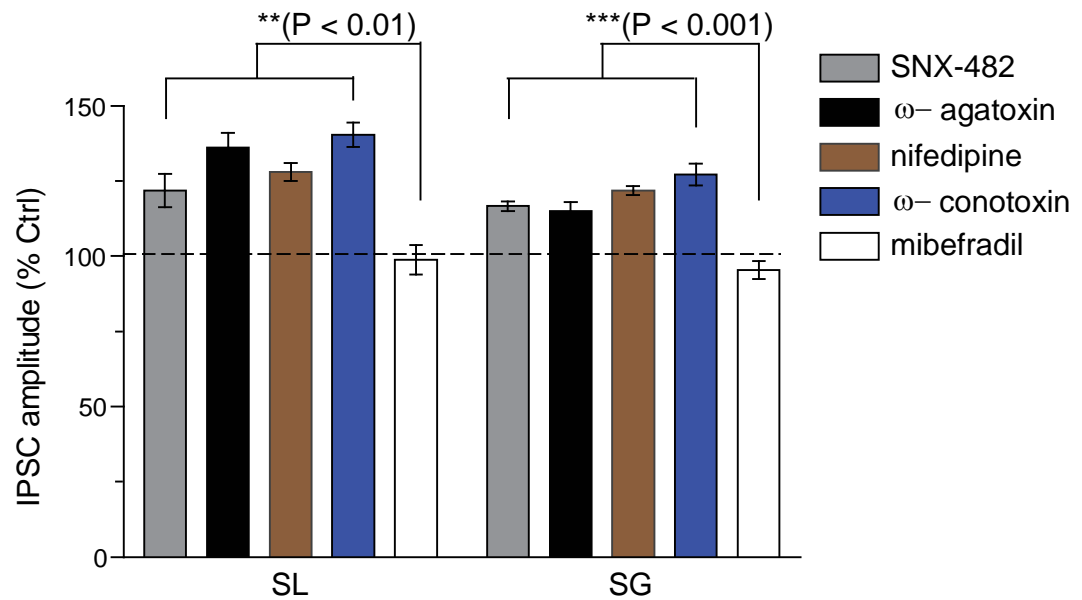


**Figure 5.22 – T-type VGCC antagonism occludes a facilitation of the IPSC amplitude by TPEN in GCs. Table 5.1** and Summary bar chart (**A**) illustrate an occlusion in facilitation of IPSC amplitude following perfusion of TPEN (1µM) when T-type Ca$^{2+}$ channels were blocked. The effect persisted when other VGCC subtypes were blocked (one-way ANOVA, $P < 0.01$ for SL stimulation and $P < 0.001$ for SG stimulation).

Following perfusion of TPEN, the data shown in **figure 5.18 and 5.19** illustrate an increase in IPSC amplitude to a similar extent as in conditions where slices were not incubated with ω-agatoxin IVA (0.5µM), ω-conotoxin GVIA (2µM) or SNX 482 (0.5µM) to leave P/Q type-, N type- or R type VGCCs, respectively, unblocked. Similarly, perfusion of TPEN also increased the IPSC amplitude to a comparable extent as in conditions in which nifedipine (20µM) was perfused in the background to block L-type VGCCs. These results suggest that those VGCC subtypes do not play a major role in the facilitation of IPSC amplitude in GCs. Next, the contribution of T-type $Ca^{2+}$ channels was tested, as those channels have been reported to be inhibited by $Zn^{2+}$ with an $IC_{50}$ = 0.8µM (Traboulsie *et al.*, 2007). Following perfusion of the rather nonspecific T-type $Ca^{2+}$ channel blocker $NiCl_2$ (100µM), there was a significant reduction in IPSC amplitude ([SL] 45.8 ± 4.9% depression, [SG] 57.8 ± 2.1% depression), however when TPEN was perfused in the background of $NiCl_2$, the amplitude of SL or SG evoked IPSCs remained unchanged (T-type VGCCs blocked [SL] 1.6 ± 2.5% depression, n = 11; [SG] 0 ± 1.6%, n = 9, **figure 5.20A**). A lower concentration of $NiCl_2$ (10µM) which has been reported to block T-type $Ca^{2+}$ channels more selectively (Lee *et al.*, 1999), depressed IPSCs by only 22.1 ± 5% (SL stimulation) and 24.8 ± 5.5% (SG stimulation). Again, bath-application of TPEN in the presence of $NiCl_2$ (10µM) prevented a facilitation of IPSC amplitude in GCs (T-type VGCCs blocked [SL] 1.6 ± 2.5% depression, n = 11, *P* > 0.7, [SG] 0 ± 1.6%, n = 9, *P* > 0.1, **figure 5.20B**). To verify that this lack of effect was not due a lack in responsiveness of the tissue (for example as a response to the rather toxic $NiCl_2$), $ZnCl_2$ was applied at the end of the experiment. Bath-application of $ZnCl_2$ depressed IPSC amplitudes ($ZnCl_2$ [SL] 28.5 ± 5% depression, n = 5, P < 0.04, [SG] 30.7 ± 3% depression, n = 6, *P* < 0.05, **figure 5.20B**) suggesting that this was not the case. Prompted by this result, the same experiment was repeated in the background of the T-type selective antagonist mibefradil (10µM). Perfusion of mibefradil depressed IPSCs by 21.8 ± 4.4% (SL stimulation) and 10.8 ± 4.1% (SG stimulation). Again, the facilitation of evoked IPSCs by TPEN was prevented (T-type VGCCs blocked [SL] 1.1 ± 4.9% depression, n = 7, *P* > 0.4, [SG] 4.7 ± 2.9%, n = 9, *P* > 0.9, **figure 5.21A**). Finally, this result was confirmed with the use of the highly selective $Ca_v3.1$ antagonist NNC 55-0396 (10µM) which has

been reported to block Ca$_v$3.1 subunits with an IC$_{50}$ = 6.8µM (Huang *et al.*, 2004). NNC 55-0396 depressed IPSCs by 22.8 ± 3.7% (SL stimulation) and 6.8 ± 3.5% (SG stimulation). Bath-application of TPEN in the background of NNC 55-0396 equally prevented a facilitation in IPSC amplitude (T-type VGCCs blocked [SL] 2.7 ± 7.7% facilitation, n = 7; [SG] 8.3 ± 3% depression, n = 7, **figure 5.21B**).

Together, these results indicate that Zn$^{2+}$-mediated inhibition of T-type Ca$^{2+}$ channels accounts for the facilitation of evoked IPSCs in GCs following Zn$^{2+}$ chelation with TPEN. These results were further strengthened by the fact that selective blockers of other VGCCs did not prevent the facilitation of evoked IPSCs (**figure 5.22**). This may also raise the possibility that a depression of T-type Ca$^{2+}$ channels by Zn$^{2+}$ underlays the effect of Zn$^{2+}$ on NMDARs. An indirect activation of NMDARs by the Ca$^{2+}$ influx through T-type Ca$^{2+}$ channels at subthreshold potentials may contribute.

# 6. Modulation of NMDA receptors and T-type Ca$^{2+}$ channels by Zn$^{2+}$ in dentate interneurons

So far, the results suggest that $Zn^{2+}$ acting on NMDARs and T-type $Ca^{2+}$ channels contributes to a modulation of IPSC amplitude in GCs. Both of these targets may be modulated at MF-interneuron synapses, so direct recordings from dentate interneurons were obtained. Fast-spiking BCs in the dentate gyrus receive most of the $Zn^{2+}$-containing feedback inputs from MFs (Ribak and Peterson, 1991; Seress *et al.*, 2001; Blasco-Ibanez *et al.*, 2000) and have also been reported to mediate most of perisomatic inhibitory inputs to neighbouring GCs, which make them intermediate players in a feedback inhibitory network circuit (Sik *et al.*, 1997).

## 6.1. MODULATION OF NMDA RECEPTORS IN INTERNEURONS

Since BCs in the dentate gyrus have been shown to express NMDARs at proximal dendrites (Koh *et al.*, 1995), it was first asked whether NMDAR-mediated currents are sensitive to endogenous $Zn^{2+}$. Dentate BCs were held in voltage-clamp mode at $V_{holding}$ = +40mV, (**figure 6.1A**) while GABAergic transmission and AMPA- and kainate receptors were blocked by bath-application of bicuculline (10µM), CGP 52432 (5µM) and NBQX (20µM), respectively. As it can be seen in **table 6.1**, positioning the stimulation electrode in SL yielded a low success rate for recording NMDAR-mediated EPSCs in 3 out of 10 cells (30%). When the stimulation electrode was moved towards the hilus, the success rate of recording NMDAR-mediated currents was increased to 10 out of 16 cells (63%).

A
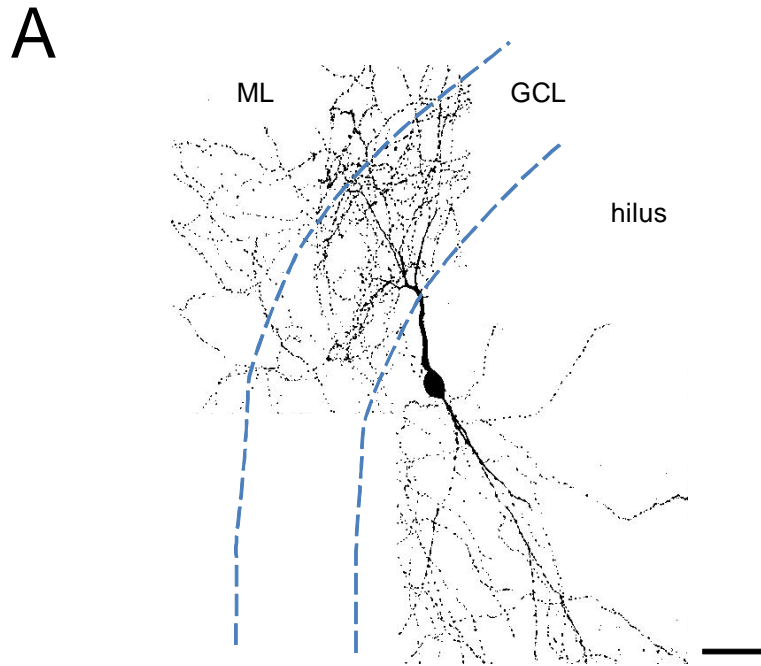


**Table 6.1.** Extracellular stimulation of NMDAR-mediated currents, $I_{NMDA}$ in dentate BCs

| Stimulation | n total | $I_{NMDA}$ | no $I_{NMDA}$ | % $I_{NMDA}$ |
|---|---|---|---|---|
| SL | 10 | 3 | 7 | 30% |
| Hilus | 16 | 10 | 6 | 63% |

**Figure 6.1 – NMDAR-mediated currents in BCs can be evoked by stimulation in the hilus. A:** Morphology of a putative BC in the dentate gyrus. Scale bar 50µm. **B: Table 6.1** illustrates the success rate of evoking NMDAR-mediated currents with a stimulation electrode positioned in SL compared to the hilus.

A



B
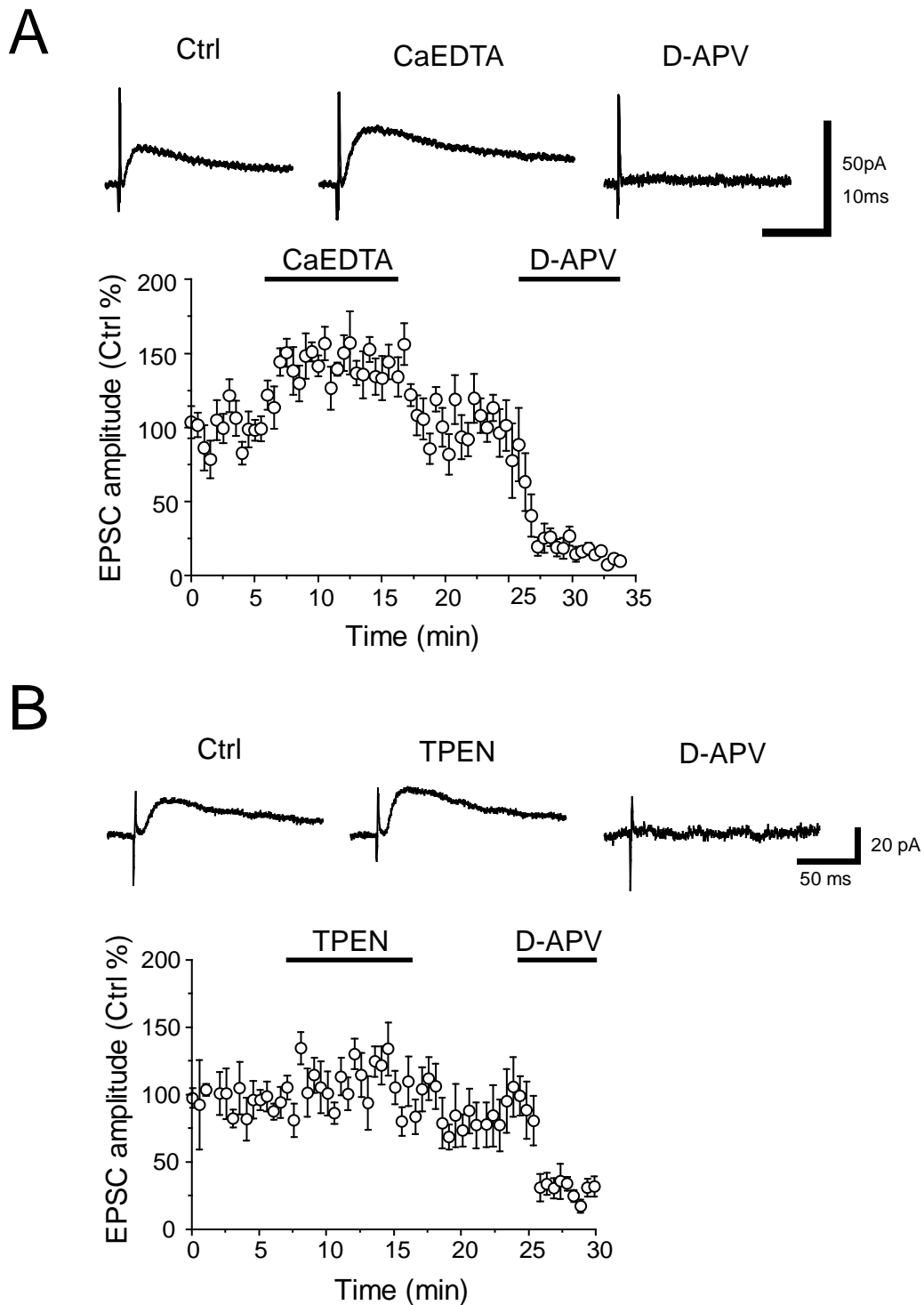


**Figure 6.2 – CaEDTA facilitates NMDAR-mediated EPSCs in dentate BCs. A,B:** Plots of the effect of CaEDTA (2mM, **A**) or TPEN (1µM, **B**) on the NMDAR-mediated EPSC amplitude evoked by a stimulation electrode in the hilus. Bath-application of D-APV (50µM) at the end of the experiment demonstrates that evoked EPSCs are mediated by NMDARs. Traces are shown on top for control condition, following perfusion of CaEDTA, TPEN or D-APV.

Extracellular stimulation in the hilus resulted in NMDAR-mediated EPSCs with a small amplitude and characteristically long decay. Bath-application of CaEDTA (2mM) facilitated NMDAR-mediated EPSCs by $56.5 \pm 9.7\%$ (n = 5, $P < 0.005$) whereas the application of TPEN (1µM) only yielded a small non-significant increase ($13.7 \pm 6.9\%$ facilitation, n = 5, $P > 0.9$, **figure 6.2**). Both currents were abolished with the perfusion of D-APV (50µM) showing that they were mediated by NMDARs. These results show that extracellular $Zn^{2+}$ chelation modulates NMDAR-mediated signalling at synapses formed between dentate MFs and BCs. Since NMDARs are extremely permeable to $Ca^{2+}$, modulation of NMDAR-mediated signalling also alters the $Ca^{2+}$ influx and thus $Ca^{2+}$ signalling.

## 6.2.  MODULATION OF T-TYPE $Ca^{2+}$ CHANNELS

T-type $Ca^{2+}$ channels activate at low-voltages and have been reported to be expressed throughout the forebrain, including the hippocampus and the dentate gyrus (Talley *et al.*, 1999). At MF-CA3 pyramidal cell synapses, R-type VGCCs have been found to be important for the induction of LTP (Dietrich *et al.*, 2003). However, there are no reports about low-voltage activated T-type $Ca^{2+}$ channels and their involvement in synaptic transmission at these synapses. Recently, it was found that T-type $Ca^{2+}$ channels co-localise with $Na^+$ channels at the axon initial segment in interneurons of the dorsal cochlear nucleus, where they have been found to mediate local $Ca^{2+}$ transients which were essential for the generation and timing of action potentials in these bursting cells (Bender and Trussell, 2009). Recordings were obtained from BCs in the dentate gyrus (**figure 6.3A**) to ask whether T-type $Ca^{2+}$ currents are modulated by endogenous $Zn^{2+}$. BCs and GCs were held at $V_{holding}$ = -70mV and experiments were performed in the background of $Na^{2+}$ and $K^+$ channel blockers to isolate low-voltage activated currents (see Methods).
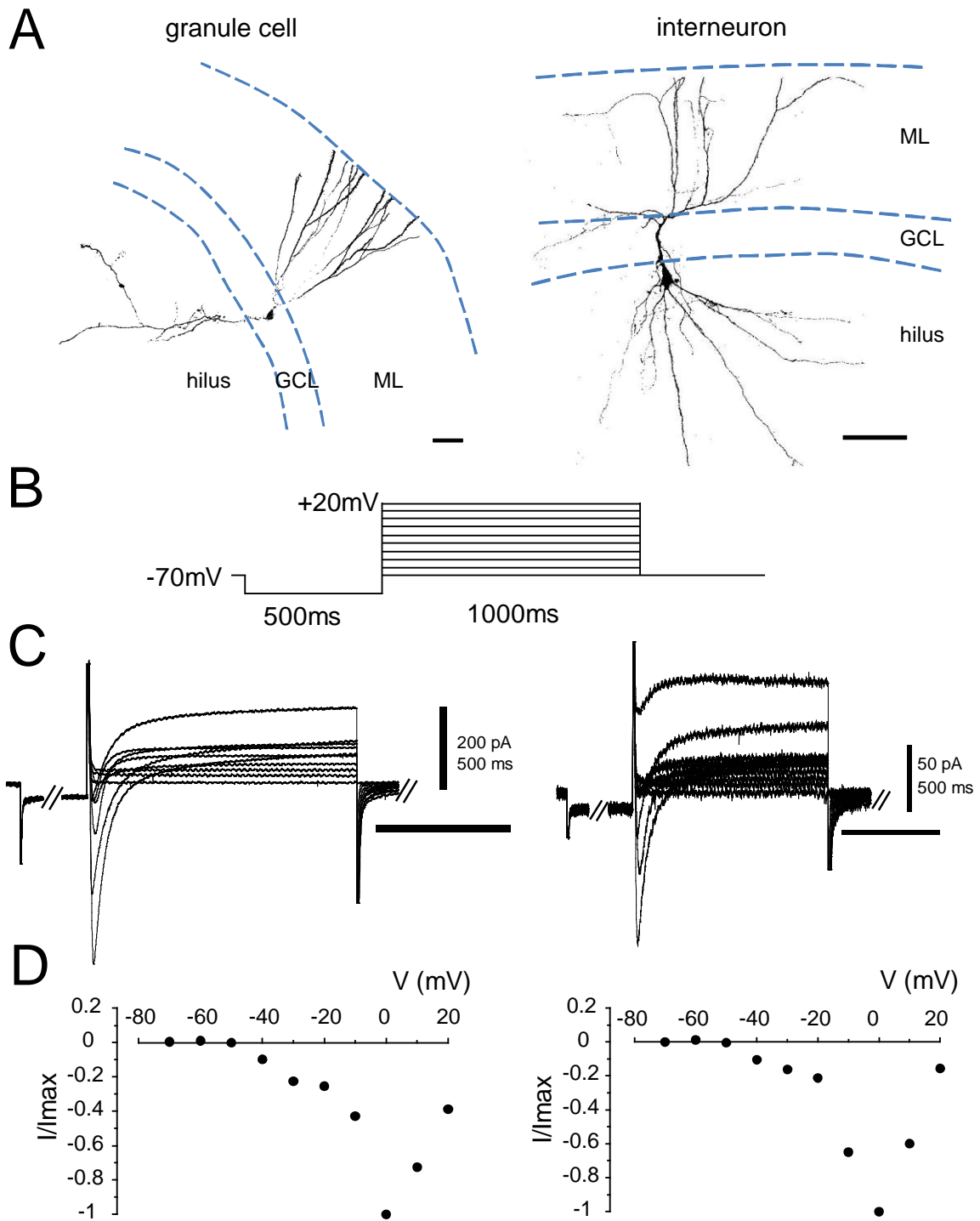
**Figure 6.3 – Recordings of Ca$^{2+}$ currents in GCs and interneurons. A:** Reconstructions of a GC (left) and a dentate interneuron (right) showing the morphology and location in these neurons. **B:** Step protocol to evoke Ca$^{2+}$ currents in both types of neurons. The pipette potential is stepped from $V_{holding}$ = -70mV to a 500ms pre-pulse to -90mV before being stepped up to more depolarised potentials from -70mV to +20mV, in 10mV increments. **C:** Traces showing the responses elicited by the step protocol in a GC (left) and an interneuron (right). Pre-pulses, tail currents and capacitive transients are truncated. **D:** I-V relationship for the data shown in C normalised to the current elicited at $V_{holding}$ = 0mV.

Table 6.2

| Cell type | # Cells | Low-activated current at -40mV (# cells) | mibefradil applied (# cells) | mibefradil-sensitive % (# cells) | mibefradil-insensitive % (# cells) |
|---|---|---|---|---|---|
| Granule cell | 12 | 66% (8) | 5 | 60% (3) | 40% (2) |
| Interneuron | 8 | 88% (7) | 4 | 75% (3) | 25% (1) |

**A**
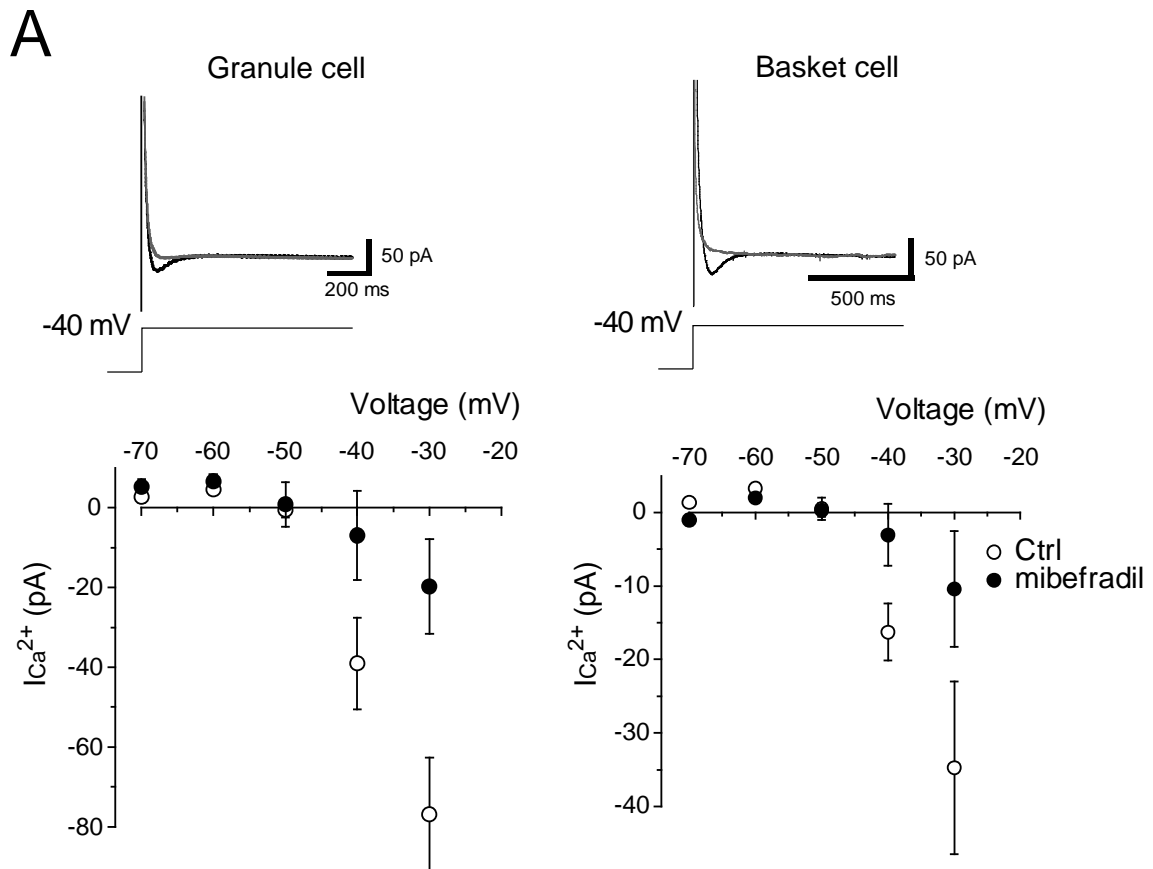


**Figure 6.4 – Low-voltage activated Ca$^{2+}$ currents are sensitive to the T-type Ca$^{2+}$ channel antagonist mibefradil. Table 6.2** shows the percentage of low-voltage activated Ca$^{2+}$ currents in interneurons and GCs exhibiting a sensitivity to mibefradil (10µM). **A:** Plot showing the effect of mibefradil on the amplitude of Ca$^{2+}$ currents at voltages from -70mV to -30mV in control condition (white symbols, Na$^+$ and K$^+$ channels blocked) and in mibefradil (black symbols) for GCs and interneurons. Traces at $V_{holding}$ = -40mV are superimposed for control condition (black) and following perfusion of mibefradil (grey).

The I-V relationship for both GCs and BCs is shown in **figure 6.3D**. Stepping up the pipette potential from -90 to -40 mV to evoke low-voltage activated $Ca^{2+}$ currents (Sanchez-Alonso *et al.*, 2008), elicited mibefradil-sensitive $Ca^{2+}$ currents (**figure 6.4**). In GCs, voltage steps to -50mV did not evoke any current (-0.6 ± 1.9pA, n = 8) whereas stepping to -40mV triggered $Ca^{2+}$ currents of small amplitude (-36.4 ± 7.8pA) in 8 out of 12 cells. In 5 GCs, bath-application of mibefradil (10µM) reduced $Ca^{2+}$ currents from -39 ± 11.5pA to -7 ± 11.2pA (n = 5, *P* < 0.04, **figure 6.4B**) indicating that $Ca^{2+}$ currents at -40mV were largely mediated by T-type $Ca^{2+}$ channels. In interneurons, voltage steps to -50mV did not evoke any current (0.5 ± 1.5pA, n = 7) whereas at -40mV small amplitude $Ca^{2+}$ currents were observed (-13.3 ± 3.9pA) in 7 out of 8 cells. Application of mibefradil (10µM) in 4 cells reduced $Ca^{2+}$ currents from -16.3 ± 3.9pA to -3.1 ± 4.2pA, n = 4, *P* > 0.05, **figure 6.4B**). Again, these results indicate that $Ca^{2+}$ currents at -40mV are largely mediated by T-type $Ca^{2+}$ currents.

To test whether these currents are modulated by $Zn^{2+}$, TPEN was perfused to all those cells that showed T-type-mediated $Ca^{2+}$ currents.
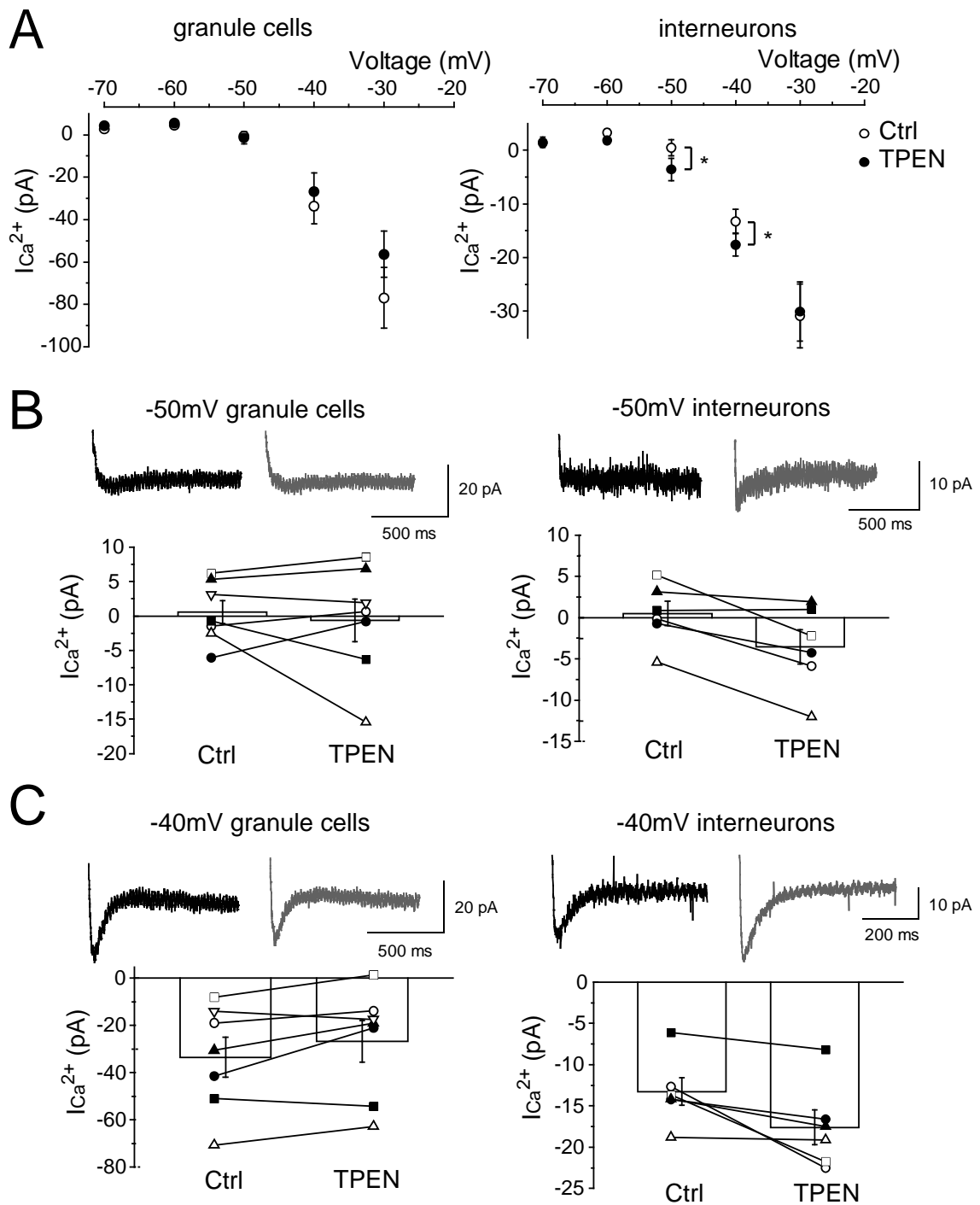
**Figure 6.5 – TPEN enhances mibefradil-sensitive low-voltage activated Ca$^{2+}$ currents in interneurons. A:** Plot showing the effect of TPEN (1µM) on the amplitude of Ca$^{2+}$ currents at voltages from -70mV to -30mV in control condition (white symbols) and in TPEN (black symbols) for GCs (left) and interneurons (right). **B,C:** Summary histograms and data from individual neurons showing the effect of TPEN on the amplitude of Ca$^{2+}$ currents at voltages of -50mV (**B**) and -40mV (**C**) for GCs (left) and interneurons (right). Traces at V$_{holding}$ = -50mV (**B**) and V$_{holding}$ = -40mV (**C**) are shown for control condition (black) and following perfusion of TPEN (1µM, grey).

In interneurons, bath-application of TPEN (1µM) unmasked a small low-threshold current to appear at voltages of -50mV (-50mV: Ctrl 0.5 ± 1.5pA, TPEN -3.6 ± 2.1pA, n = 7, $P$ < 0.03). A significant facilitation of mibefradil-sensitive $Ca^{2+}$ currents was observed at potentials of -40mV (-40mV: Ctrl -13.3 ± 1.7pA, TPEN -17.6 ± 2.1pA, n = 7, $P$ < 0.04, **figure 6.5**), whereas $Ca^{2+}$ currents remained unchanged at potentials of -30mV (-30mV: Ctrl -30.9 ± 6pA, TPEN -30.1 ± 5.5pA, n = 7, $P$ > 0.6). In contrast to interneurons, TPEN caused a depression of mibefradil-sensitive $Ca^{2+}$ currents in GCs (-50mV: Ctrl -0.6 ± 1.9pA, TPEN -1.4 ± 2.8pA, n = 8, $P$ > 0.05; -40mV: Ctrl -33.6 ± 8.5pA, TPEN -26.8 ± 8.7pA, n = 8, $P$ > 0.05, **figure 6.5**). Thus, chelation of $Zn^{2+}$ selectively enhanced T-type-mediated $Ca^{2+}$ currents in interneurons and had little effect in GCs.

To summarise, low-voltage activated $Ca^{2+}$ currents can be recorded in GCs and interneurons in the dentate gyrus. Secondly, these $Ca^{2+}$ currents were largely sensitive to the T-type $Ca^{2+}$ channel antagonist mibefradil. Finally, a selective facilitation of T-type $Ca^{2+}$ currents in interneurons following $Zn^{2+}$ chelation was demonstrated. Currents recorded in GCs remained unchanged or even depressed. These results indicate a selective modulation of T-type $Ca^{2+}$ channels present in interneurons by endogenous $Zn^{2+}$.

Together, these results demonstrate that endogenous $Zn^{2+}$ modulates interneurons via actions on NMDARs and T-type $Ca^{2+}$ channels. Because NMDARs are largely permeable to $Ca^{2+}$, endogenous $Zn^{2+}$ may act to regulate $Ca^{2+}$ influx via these two targets. A modulation in postsynaptic $Ca^{2+}$ signalling may be linked to a modulation of BC excitability which may then translate into changes in neurotransmitter release.

**7. Implications for signal integration in dentate granule cells**

A modulation of the excitability of interneurons by $Zn^{2+}$ may have important consequences for synaptic integration in GCs and therefore spike routing to the hippocampus proper. The following sections describe the effects of $Zn^{2+}$ chelation on the electrical properties of dentate interneurons to complement the results obtained in voltage-clamp.

## 7.1.  SELECTIVE MODULATION OF FIRING PARAMETERS IN FAST-SPIKING INTERNEURONS COMPARED TO GRANULE CELLS

Intrinsic electrical properties such as membrane potential $V_m$, input resistance $R_N$, "sag" ratio, maximum firing frequency or spike amplitude were reported for dentate neurons in **tables 3.1 and 3.3**. To investigate the role of $Zn^{2+}$ chelators on intrinsic properties of GCs and BCs, another set of whole-cell current-clamp recordings was obtained with a K-methanesulphonate-based solution. Spike-width and spike threshold were also analysed to account for changes in cell excitability.

As illustrated in a single cell example in **figure 7.1**, TPEN (1µM) did not alter the membrane potential, $V_m$ nor the I-V relationship in a GC ($V_m$ Ctrl: -73.8mV, TPEN: -74.1mV; $R_N$ Ctrl: 242.9MΩ, TPEN: 247.7MΩ). The "sag" ratio was slightly enhanced (Ctrl: 0.984, TPEN: 0.99) whereas the maximum firing rate (Ctrl: 59Hz, TPEN: 59 Hz) remained unchanged. **Table 7.1** summarises the effect of TPEN on basic electrical properties in several GCs (n = 8).
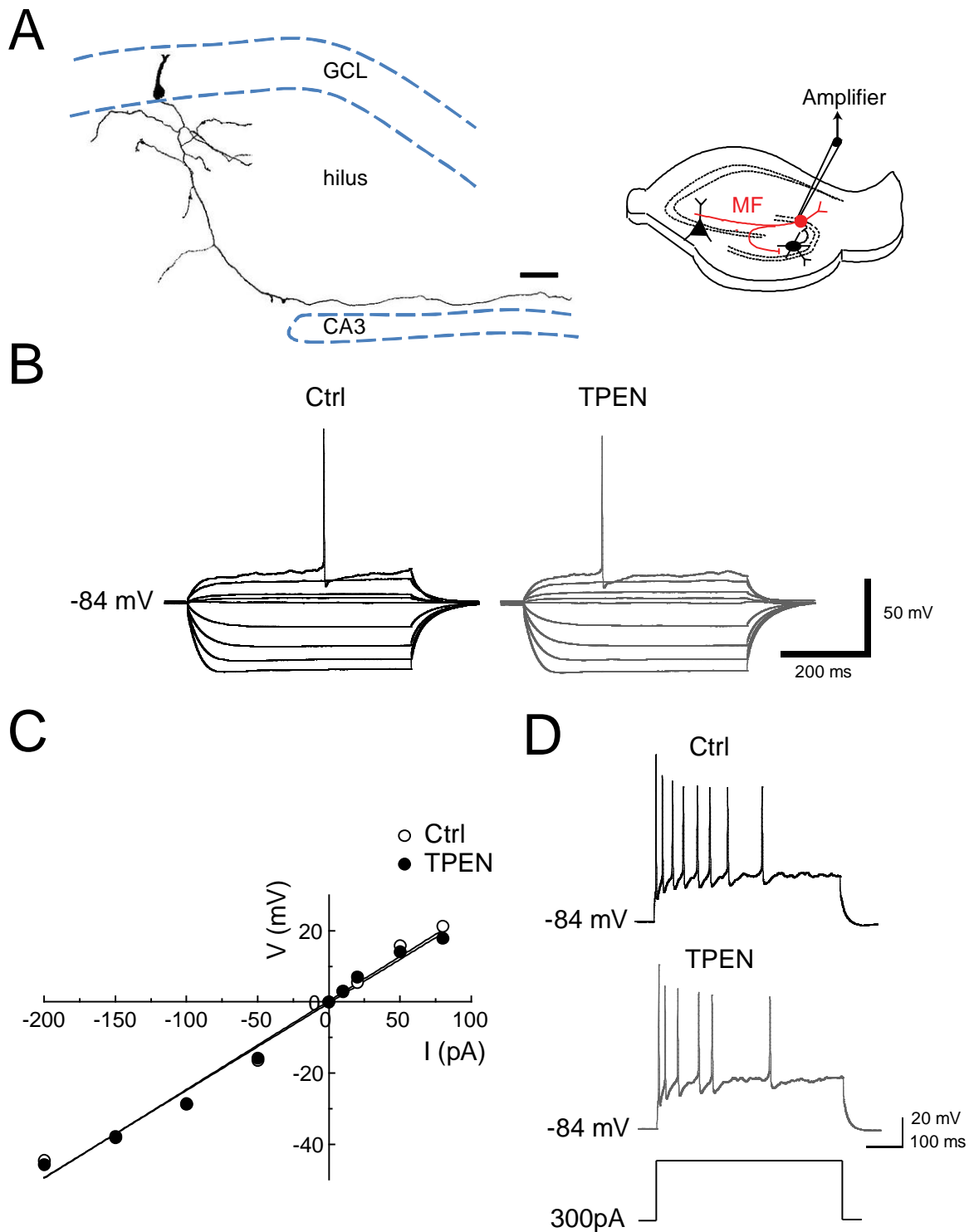
**Figure 7.1 – TPEN does not affect basic electrical properties in GCs. A**: Reconstruction of a GC with the preserved MF and MF collaterals. Scale bar 50μm. Inset: Experimental approach. **B**: Example voltage traces in response to 500ms current steps (-200 to +80pA) in control condition (black traces) and in the presence of TPEN (1μM, grey traces). Traces for -200 to +50pA steps are averages, +80pA steps are single traces. **C**: I-V relationship of the data shown in B. **D**: Voltage response for +300pA step currents in control (black) and in TPEN (grey).

Table 7.1

Effect of TPEN on electrical properties in

granule cells (n = 8) in the dentate gyrus

| Parameter | Mean ± SEM Ctrl | Mean ± SEM TPEN |
|---|---|---|
| resting membrane potential, mV | -88.8, ± 3.7 | -91.3, ± 3 |
| input resistance $R_N$, MΩ | 326 ± 47 | 335 ± 59 |
| "sag" ratio | 0.986 ± 0.005 | 0.971 ± 0.02 |
| maximum firing rate, s$^{-1}$ | 100.1 ± 11.2 | 101.4 ± 9.1 |

Similarly, when recording from fast-spiking interneurons (**figure 7.2A**) $Zn^{2+}$ chelation did not have a significant effect on the membrane potential $V_m$ nor input resistance $R_N$ ($V_m$ Ctrl: 71.2mV, TPEN: 71.8mV; $R_N$ Ctrl: 197.8MΩ, TPEN: 226MΩ, **figure 7.2B,C**). Analysis of the membrane time constant of hyperpolarising potentials of < 10mV showed that $\tau_m$ remained unchanged (Ctrl: 27.45 ± 4.53ms, TPEN: 32.78 ± 9.62ms, n = 4, *P* > 0.5, **table 7.2**) suggesting that TPEN does not alter conductances that are activated by hyperpolarisation, such as $I_h$. Action potentials elicited by supra-threshold depolarising current steps showed little or no adaptation. In this example, the maximum firing rate in the presence of TPEN was slightly increased from 143 to 166 Hz (**figure 7.2D**).
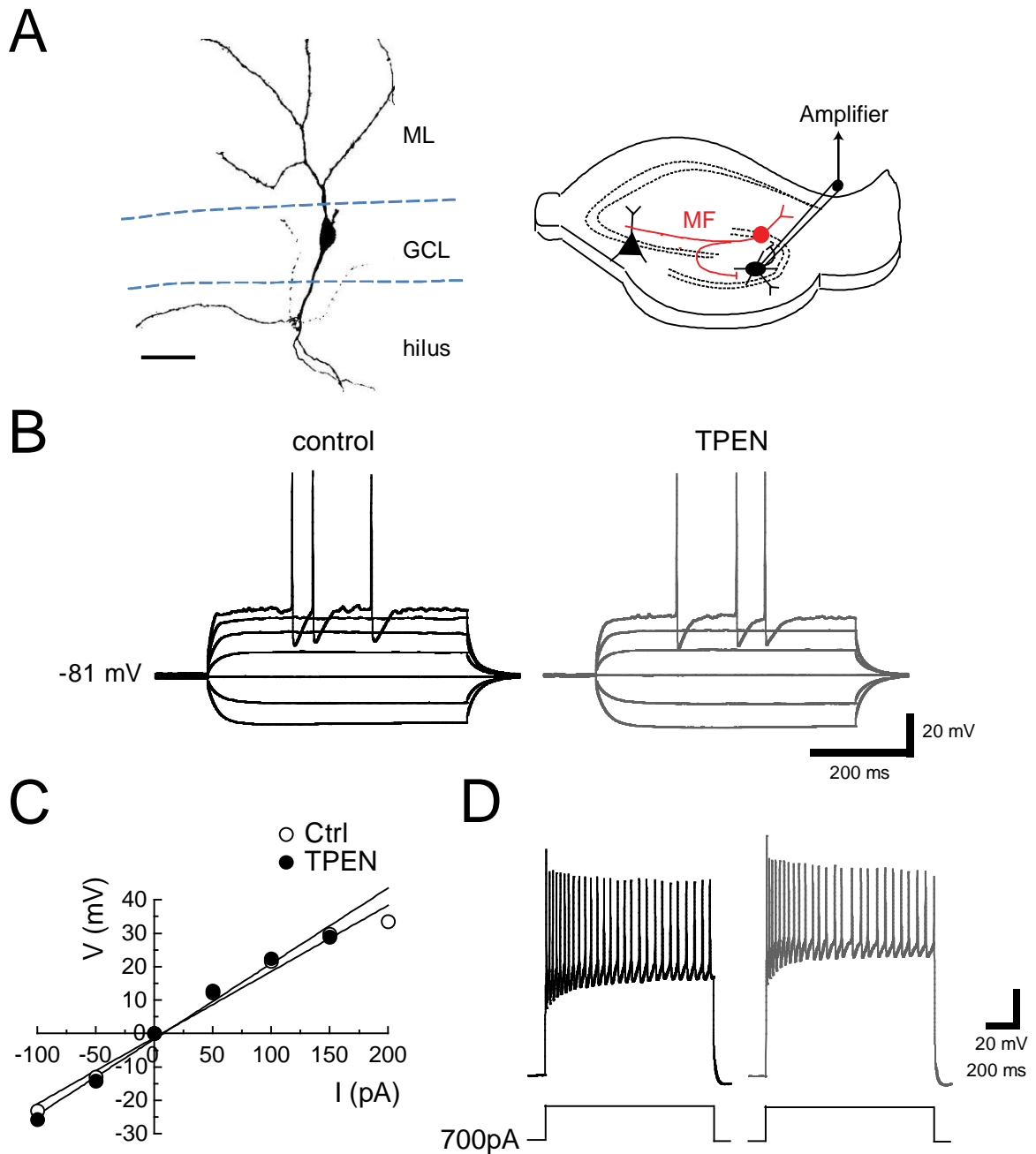
**Figure 7.2 – TPEN does not affect basic electrical properties in fast-spiking interneurons. A**: Reconstruction of a fast-spiking interneuron showing the morphology and the location. Scale bar 50μm. Inset: Drawing of a hippocampal slice showing the experimental approach. **B**: Example voltage traces in response to 500ms current steps (Ctrl: -100 to +200pA, TPEN: -100 to +150pA) in control condition (black traces) and in the background of TPEN (1μM, grey traces). Traces for -100 to +150 (Ctrl) or to +100 (TPEN) are averages, +200 (Ctrl) and +150 (TPEN) are single traces. **C**: I-V relationships of the data shown in **B**. **D**: Voltage traces for a current step of +700pA in control condition (black) and in TPEN (grey).

Data pooled from the entire population of fast-spiking interneurons showed no significant change in basic electrical properties or maximum firing rate (**table 7.2**).

Table 7.2

Effect of TPEN on electrical properties in fast-spiking
interneurons (n = 7) in the dentate gyrus

| Parameter | Mean ± SEM Ctrl | Mean ± SEM TPEN |
|---|---|---|
| resting membrane potential, mV | -77.1, ± 2.9 | -79.2, ± 3 |
| input resistance $R_N$, MΩ | 396 ± 69 | 445 ± 79 |
| membrane time constant, $\tau_m$ | 27.5 ± 4.5 | 32.8 ± 9.6 |
| maximum firing rate, $s^{-1}$ | 131 ± 9 | 130 ± 12 |

However, bath-application of TPEN selectively altered the rheobase current in a subset of fast-spiking interneurons, i.e. the injected current that is required to reach the action potential threshold (**figures 7.3 and 7.4**). As seen in **figure 7.3A**, a current of +50pA was required to elicit 5 action potentials in a fast-spiking interneuron whereas the rheobase current in the background of TPEN was only +20pA, triggering 2 action potentials (+50pA triggered 9 action potentials). This effect was obvious in 3 out of 7 fast-spiking interneurons (highlighted in green in left column, **table 7.3**). The membrane potential remained unchanged. In 6 out of 7 interneurons, injection of the rheobase current in the background of TPEN elicited more action potentials than in control condition (highlighted in green in right column, **table 7.3**). Fitting the I-O relation with a logarithmic function (see Materials and Methods) revealed a reduction in neuronal offset in 6 out of 7 fast-spiking interneurons (Ctrl 154.1 ± 41.3pA; TPEN 142.2 ± 43.3pA, n = 7, $P = 0.03$; **figure 7.5**). Overall, the neuronal gain was not affected by TPEN (Ctrl 43.4 ± 7.1Hz*pA$^{-1}$; TPEN 39.9 ± 6.9Hz*pA$^{-1}$, n = 7, P > 0.05; **figure 7.5D**. These results are consistent with an inhibitory effect of endogenous $Zn^{2+}$ on firing threshold properties in fast-spiking interneurons.

In contrast, in the GC example shown in **figure 7.4A**, a current injection of +80pA was required to elicit 2 action potentials, in control condition and in the background of TPEN. Both the rheobase current and the spike count remained unchanged in GCs following $Zn^{2+}$ chelation with TPEN (**table 7.4**).

# A

fast-spiking interneurons

# cell 3



| Ctrl | TPEN | TPEN |

-83 mV

50pA
20pA          20pA          50pA

20 mV
200 ms
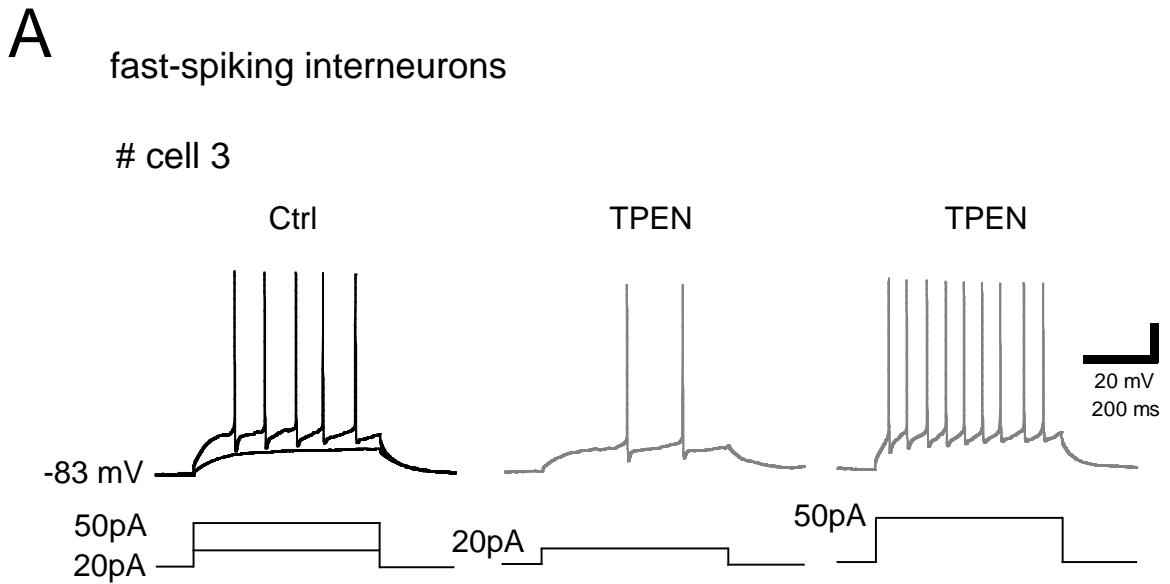
# B

Table 7.3

| cell # | condition | I rheobase (pA) | # spikes rheobase |
|--------|-----------|-----------------|-------------------|
| cell1 | Ctrl | 200 | 4 |
|        | TPEN | 150 (200) | 2 (6) |
| cell2 | Ctrl | 20 | 1 |
|        | TPEN | 20 | 2 |
| cell3 | Ctrl | 50 | 4 |
|        | TPEN | 20 (50) | 2 (9) |
| cell4 | Ctrl | 10 | 1 |
|        | TPEN | 10 | 3 |
| cell5 | Ctrl | 50 | 1 |
|        | TPEN | 50 | 2 |
| cell6 | Ctrl | 20 | 17 |
|        | TPEN | 10 (20) | 9 (14) |
| cell7 | Ctrl | 10 | 4 |
|        | TPEN | 10 | 7 |

**Figure 7.3 – Perfusion of TPEN affects the rheobase and spike count in a subset of fast-spiking interneurons. A:** Representative traces from cell #3 showing the effect of TPEN (1µM) on sub-treshold and supra-threshold voltage responses. The current injected for sub-threshold voltage deflection is +20pA and the rheobase current is +50pA. In the background of TPEN, a rheobase current of +20pA elicited 2 action potentials, whereas a current injection of +50pA triggered 9 action potentials. **B: Table 7.3** summarises the effect of TPEN on rheobase current and spike count at rheobase current. Numbers highlighted in green indicate increases in the corresponding parameters.

## A
granule cells

# cell 4
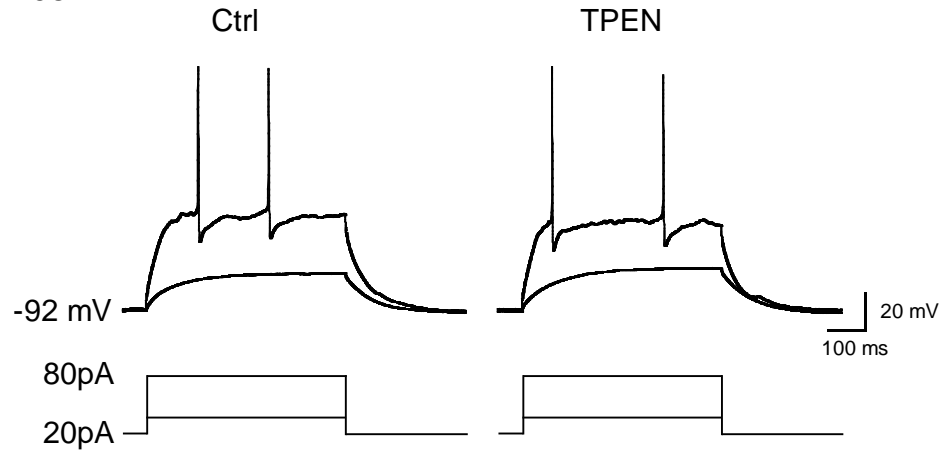


## B
Table 7.4

| cell # | condition | I rheobase (pA) | # spikes rheobase |
|--------|-----------|-----------------|-------------------|
| cell1 | Ctrl | 10 | 1 |
| | TPEN | 10 | 1 |
| cell2 | Ctrl | 50 | 5 |
| | TPEN | 50 | 6 |
| cell3 | Ctrl | 250 | 1 |
| | TPEN | 250 | 1 |
| cell4 | Ctrl | 80 | 2 |
| | TPEN | 80 | 2 |
| cell5 | Ctrl | 50 | 9 |
| | TPEN | 50 | 7 |
| cell6 | Ctrl | 80 | 2 |
| | TPEN | 80 | 1 |
| cell7 | Ctrl | 100 | 1 |
| | TPEN | 100 | 1 |
| cell8 | Ctrl | 80 (100) | 1 (2) |
| | TPEN | 100 | 2 |

**Figure 7.4 – Perfusion of TPEN does not affect the rheobase current nor the spike count in GCs. A:** Representative traces from cell #4 showing the effect of TPEN (1µM) on sub-threshold and supra-threshold voltage responses. The current injected for sub-threshold voltage deflection is +20pA and the rheobase current is +80pA. In the background of TPEN, the rheobase current of +80pA remains unchanged, eliciting the same number of action potentials. **B: Table 7.4** summarises the effect of TPEN on rheobase current and spike count at rheobase current. Numbers highlighted in green indicate increases and in red decreases in the corresponding parameters.
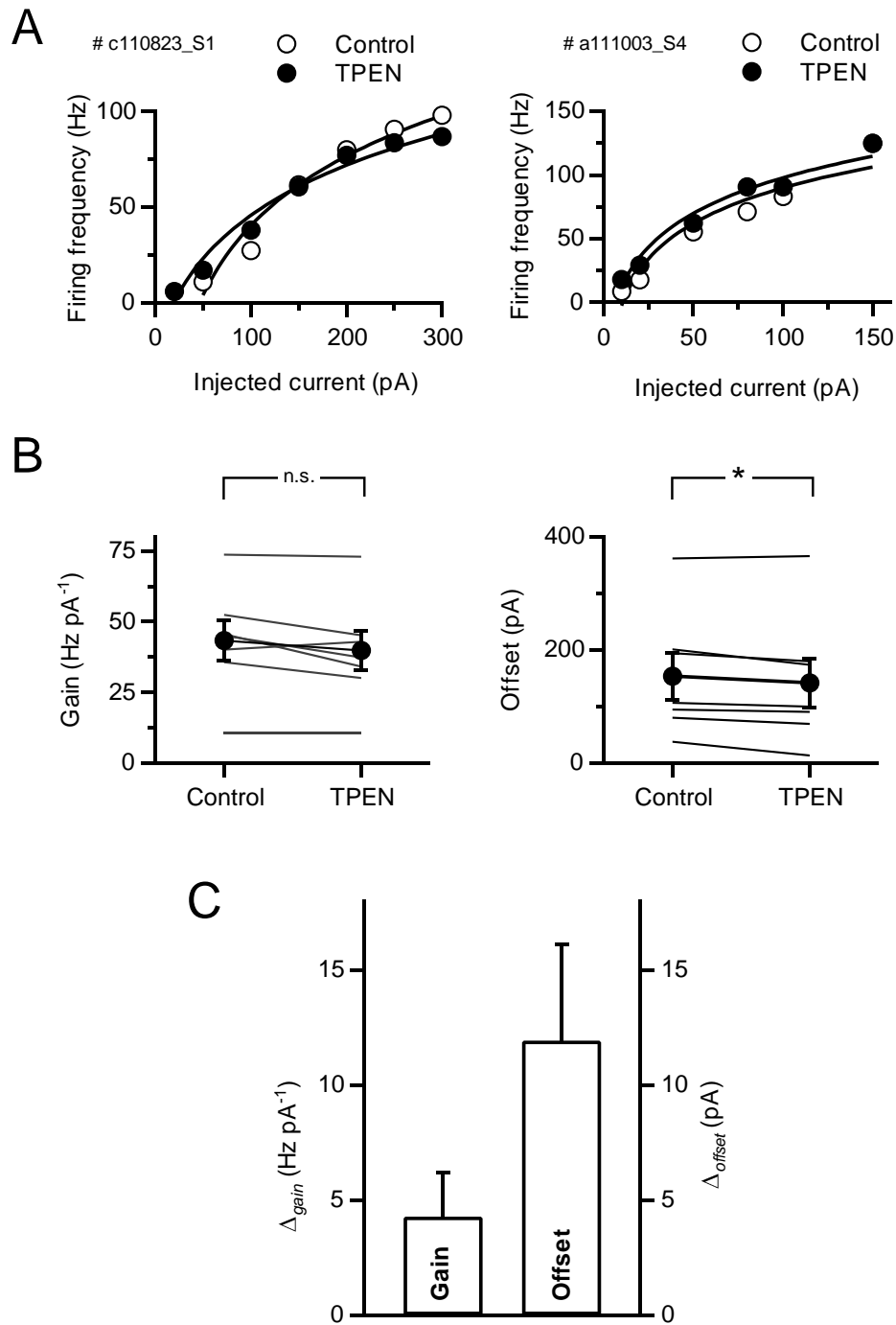
**Figure 7.5 – TPEN modulates neuronal offset but not the gain in fast-spiking interneurons. A:** Examples of input-output relations obtained in 2 fast-spiking interneurons by plotting the injected current against the firing frequency, in control condition and following application of TPEN (1 µM). TPEN modulates neuronal offset and gain in cell #c110823_S1 whereas it solely modulates the offset in cell #a111003_S4. **B:** Summary data from 7 neurons showing a selective reduction in neuronal offset after zinc chelation. Thin lines represent individual experiments, *, $P =$ 0.03, Student's *t*-test. **C:** Same data represented as ∆offset and ∆gain.

So far, the results point towards increased excitability of a population of fast-spiking interneurons in the dentate gyrus. The observation that the same current injection that was sub-theshold in control condition, elicits spikes in TPEN suggests that those interneurons become more excitable. This would be explained by a modulation of voltage-gated channels by $Zn^{2+}$, including $Ca^{2+}$-dependent conductances underlying the action potential. The spike width in GCs and fast-spiking interneurons was analysed based on the reported correlation between $Ca^{2+}$ influx and spike half-duration (Sabatini and Regehr, 1997). $Zn^{2+}$ chelation selectively broadened the spike width in fast-spiking interneurons (Ctrl: 1.50 ± 0.14ms, TPEN: 1.79 ± 0.16ms, n = 7, $P$ < 0.003) without affecting spike amplitude (Ctrl: 110.9 ± 5.26mV, TPEN: 108.1 ± 4.76mV, n = 7, $P$ > 0.3, see **figure 7.6B**). In contrast, these parameters remained unchanged in GCs (spike width Ctrl: 1.59 ± 0.17ms, TPEN: 1.60 ± 0.17ms, n = 8, $P$ > 0.7; spike amplitude Ctrl: 128.1 ± 4.10mV, TPEN: 127.2 ± 3.62mV, n = 8, $P$ > 0.4, **figure 7.6B**).

The observation that a subset of fast-spiking interneurons showed a reduction in the rheobase current in the presence of TPEN also suggests a change in action potential threshold. To analyse whether TPEN altered the action potential threshold, the action potential wave-form was converted into phase-plane plots (Bean, 2007) and compared in both cell groups (**figure 7.7B**). $Zn^{2+}$ chelation with TPEN (1µM) reduced the action potential threshold in fast-spiking interneurons (Ctrl: -40.24 ± 3.1mV, TPEN: -43.83 ± 3.29mV, n = 7, $P$ < 0.001, $\Delta V_{thr}$: -3.59 ± 0.69mV). In contrast, the action potential threshold did not change in GCs (Ctrl: -46.12 ± 2.4mV, TPEN: -47.34 ± 2.19mV, n = 8, $P$ > 0.13, $\Delta V_{thr}$: -1.22 ± 0.74mV). Comparing the changes among both cell types yielded a significant difference (Mann-Whitney U test, $P$ < 0.04). These results suggest that $Zn^{2+}$ chelation reduces action potential threshold which may explain a change in rheobase in a subset of fast-spiking interneurons.
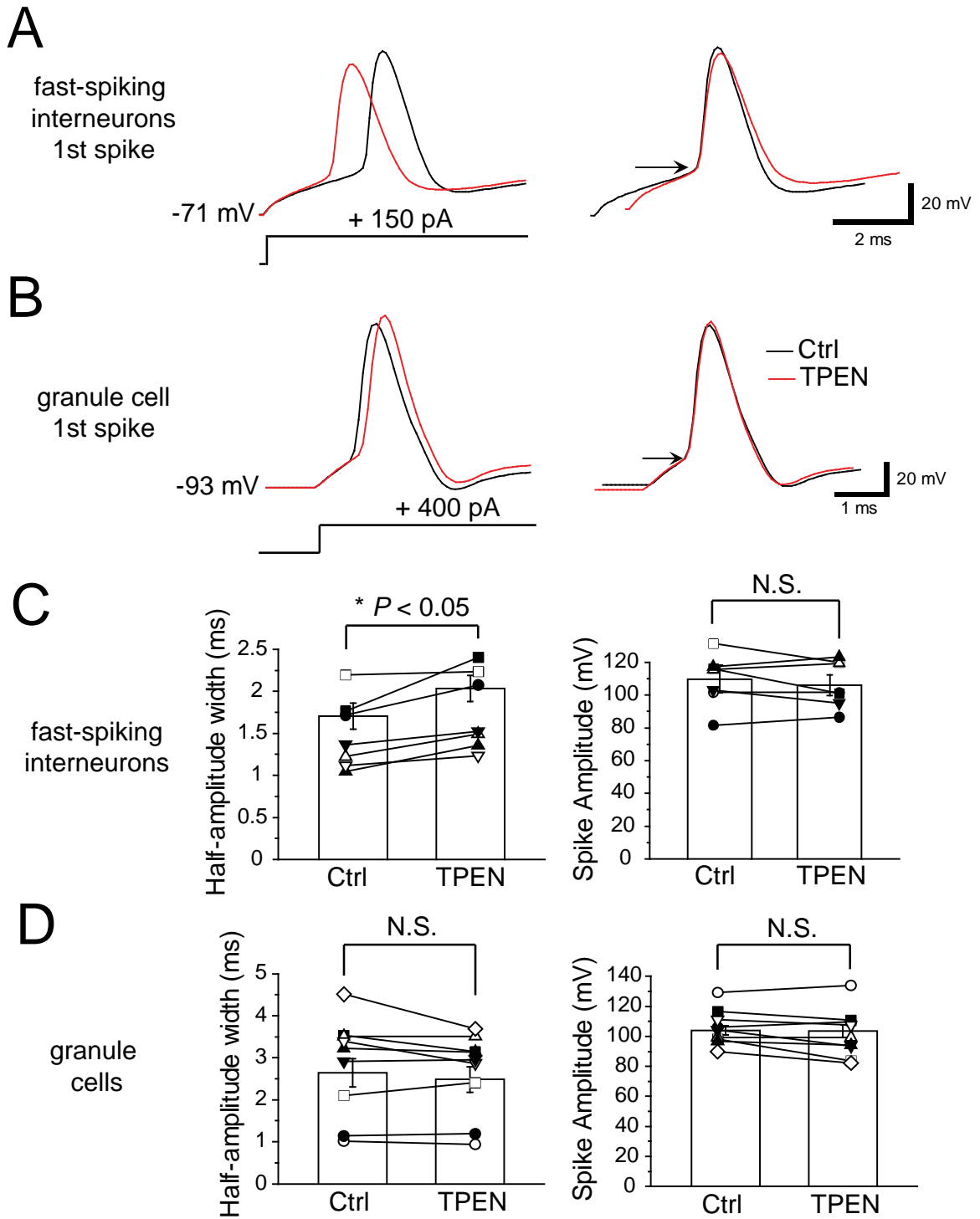
**Figure 7.6 – TPEN selectively alters the half-duration spike width in fast-spiking interneurons. A,B:** Traces of the first spike in a train of spikes aligned to $V_m$ (left) and aligned to $V_{thr}$ (right). **C,D:** Summary bar graphs showing the effect of TPEN (1µM) on half-duration spike width and spike amplitude in fast-spiking interneurons (**C**) and GCs (**D**).

**A**

fast-spiking interneuron

granule cell

-71 mV

20 mV

2 ms

-93 mV

20 mV

2 ms

**B**



—Ctrl
—TPEN

dV/dt (mV*ms$^{-1}$)

V (mV)

**C**

fast-spiking
interneurons

granule
cells

Spike threshold (ΔmV)
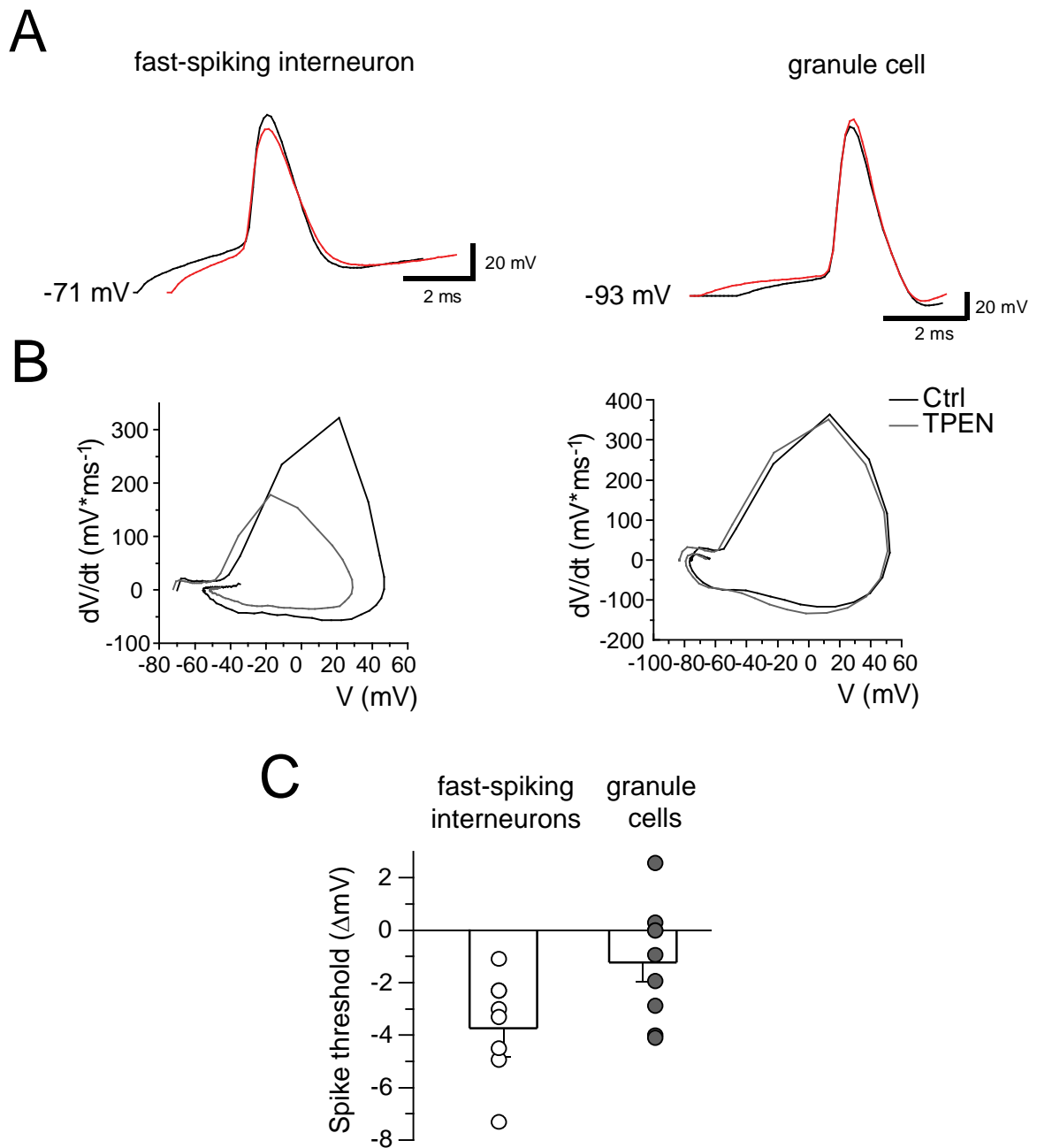
**Figure 7.7 – TPEN modulates the action potential threshold in a subset of fast-spiking interneurons. A:** Superimposed action potential wave-forms generated by intracellular current injection in a fast-spiking interneuron (left) and a GC (right) in control (black) and in TPEN (1µM, red). **B:** Corresponding phase-plane plots showing a small hyperpolarising shift in $V_{thr}$ for fast-spiking interneurons (Ctrl, black: -53.6 mV – corrected for LJP, TPEN, grey: -60.4 mV) compared to GCs (Ctrl, black: -64.7 mV, TPEN, grey: -68.1 mV). **C:** Summary histogram for $\Delta V_{thr}$ in both cell types.

In conclusion, TPEN does not alter the passive properties of GCs or fast-spiking interneurons (eg. $V_m$, $R_N$, "sag" ratio or $\tau_m$, maximum firing rate), but selectively increases the spike width and decreases the action potential threshold in fast-spiking interneurons. Because of the positive correlation between spike width and $Ca^{2+}$ influx, the above results provide the cellular basis for enhanced GABA release and interneuron-GC synapses. Whether low-voltage activated conductances are involved remains to be elucidated.

## 7.2.     ENDOGENOUS $Zn^{2+}$ BROADENS THE WINDOW FOR INTEGRATION OF PERFORANT PATH INPUTS

The results so far indicate a depression of feed-forward and feedback GABAergic circuits by endogenous $Zn^{2+}$ via a selective inhibition of T-type $Ca^{2+}$ currents and NMDAR-mediated currents in interneurons as well as a decrease of GABA release. Because interneurons play a major role in shaping the window for integration of excitatory inputs (Bartos *et al.*, 2011), finally, the question was asked whether $Zn^{2+}$ chelation alters summation of excitatory PSPs and thereby the spike probability of the main excitatory input to the dentate gyrus, the perforant path. In models of microcircuits in which inhibition is mediated by hyperpolarisation, the role of endogenous $Zn^{2+}$ could then be thought as pro-excitatory, as a decrease in the release of GABA from interneurons would result in an increase in GC excitability. However, in the dentate gyrus, where inhibition is mediated by shunting of excitatory inputs, e.g. perforant path EPSPs, IPSPs are evidently depolarising (reversal potential for IPSPs in GCs, $E_{IPSP}$ = 62mV, $E_m$ = 67mV [Misgeld *et al.*, 1986]; extracellular recordings: $E_{GABA}$ = -80mV, $E_m$ = -88mV [Chiang *et al.*, 2012]) and thus raise the membrane potential transiently to more depolarised potentials. Consequently, under these conditions, whether a decrease in the release of GABA caused by endogenous $Zn^{2+}$ has a pro-excitatory (less shunted EPSPs) or anti-excitatory role (greater distance from threshold due to depression in IPSP amplitude) is unclear. Here, the question was asked how $Zn^{2+}$ influences the integration of two synaptic inputs mediated by indirect activation of local interneurons and the perforant path, respectively.

First, the temporal window in which synaptic potentials evoked by stimulation of recurrent MFs and perforant path inputs summated was determined. One stimulation electrode was positioned in SL to activate recurrent MF collaterals and the other in the outer ML to activate the lateral perforant path, respectively (**figure 7.8A**). Whole-cell recordings from GCs were obtained using a KCl-based patch solution and stimulus intensities were set so that the probability for evoking action potentials was ~50% for simultaneous activation of both pathways. The probability for evoking action potentials in response to stimulation of the perforant path or SL alone was registered separately (**figure 7.8B** and see Methods).
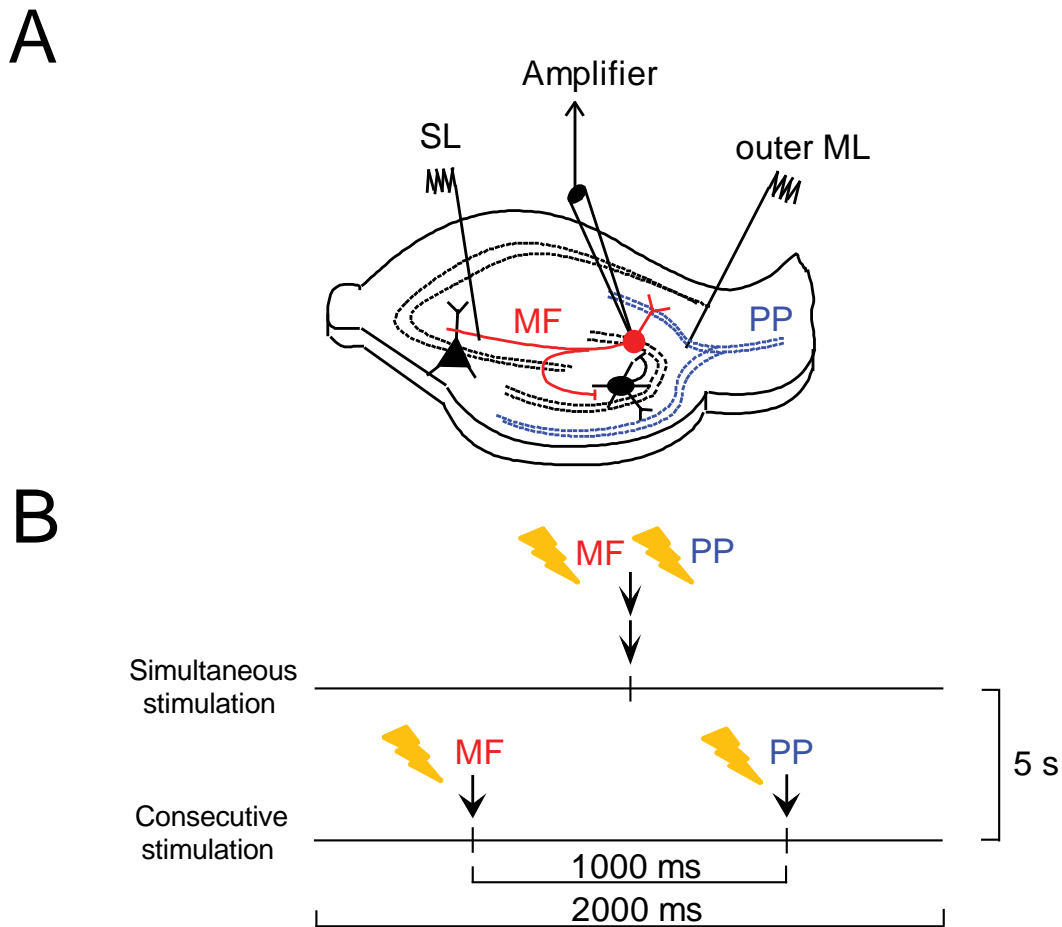
**Figure 7.8 – Experimental approach for spike-timing experiments. A:** Cartoon of a hippocampal slice showing the experimental approach. A stimulation electrode is positioned in SL and the other in the outer ML in order to stimulate MFs and perforant path (PP) inputs. **B:** The stimulation paradigm is designed to simultaneously activate both pathways in one data sampling window and to activate individual pathways in another window (5s apart) with a 1s interval.

Because activation of recurrent MFs elicits depolarising GABAergic IPSPs, supra-threshold stimulation of this pathway triggers action potentials on top of evoked synaptic potentials. Responses elicited at both pathways showed distinct sensitivities to several pharmacological agents. Action potentials which were evoked by SL stimulation were completely abolished following bath-application of bicuculline (10µM), indicating that they occurred as a result of $GABA_AR$-mediated synaptic potentials (**figure 7.9A**). Perfusion of NBQX significantly reduced the probability for evoking action potentials in one recording suggesting that SL

stimulation largely mediated di-synaptic responses. In contrast, the probability of evoking action potentials in response to perforant path stimulation was reduced in response to perfusion of bicuculline, however not abolished (**figure 7.9B**) indicating that stimulation of this pathway also activates feed-forward projections from dentate interneurons. This is in agreement with a study by Ewell and Jones (2010) who showed that perforant path axons have a higher probability to innervate fast-spiking interneurons than GCs providing strong local inhibition to GCs. Bath-application of NBQX (20µM) completely abolished action potentials evoked by perforant path stimulation in one recording. These results indicate that SL stimulation is largely mediated by di-synaptic GABAergic inputs and perforant path stimulation largely mediated by glutamatergic EPSPs.
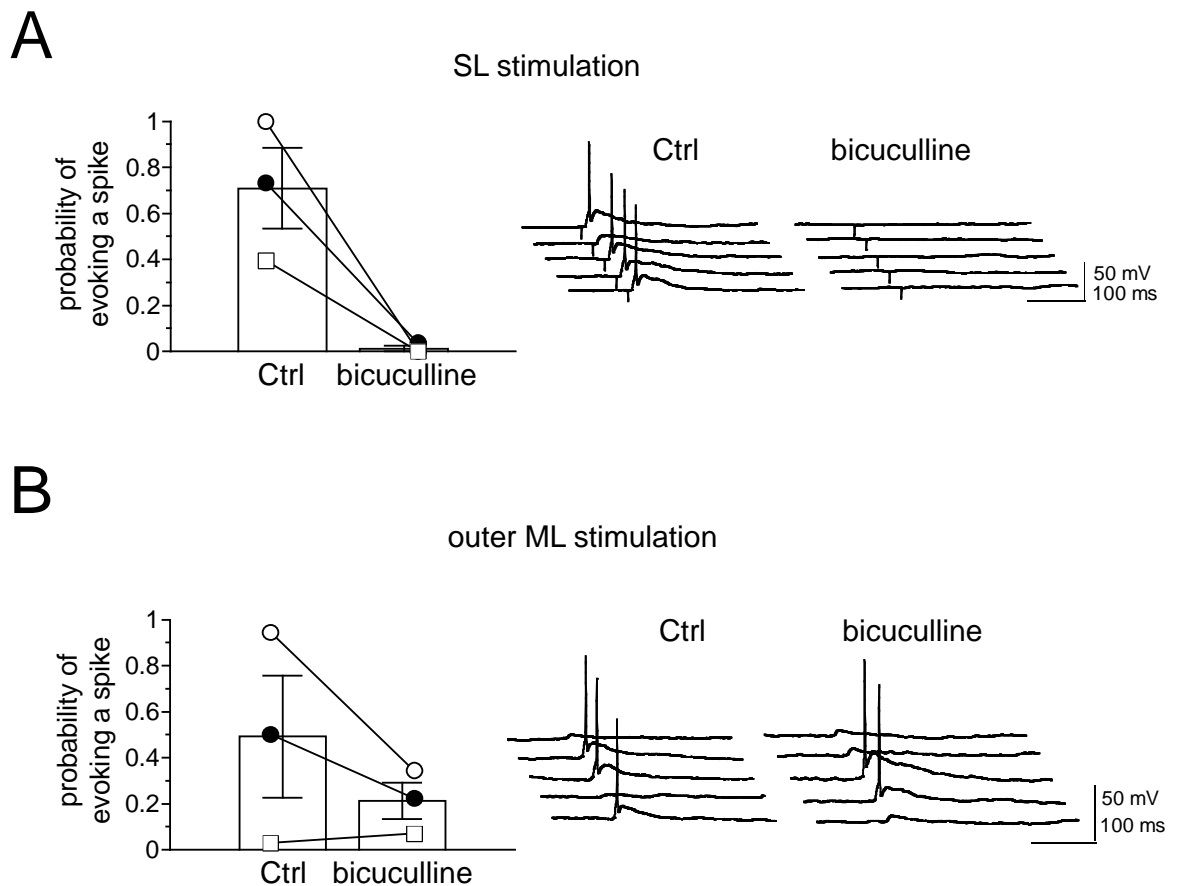


**Figure 7.9 – Pharmacological sensitivities of SL and outer ML evoked responses to bicuculline in GCs. A,B:** Bar charts showing the probability of evoking spikes in response to SL stimulation (**A**) or stimulation in the outer ML (**B**) in control condition and following perfusion of bicuculline (10µM). Traces of 5 consecutive trials in control condition and following perfusion of the corresponding drug are shown on the right.

Next, the question was asked whether activation of recurrent MFs can influence the probability for evoking a spike in response to perforant path stimulation. Simultaneous activation of the perforant path and MFs doubled the probability for evoking an action potential (perforant path only: 0.25 ± 0.08, perforant path + MFs: 0.5 ± 0.13, n = 5, $P < 0.02$, **figure 7.10**) suggesting that the depolarising MF-mediated IPSPs and the perforant path-mediated EPSPs summate and thus significantly increase the occurrence of spikes.
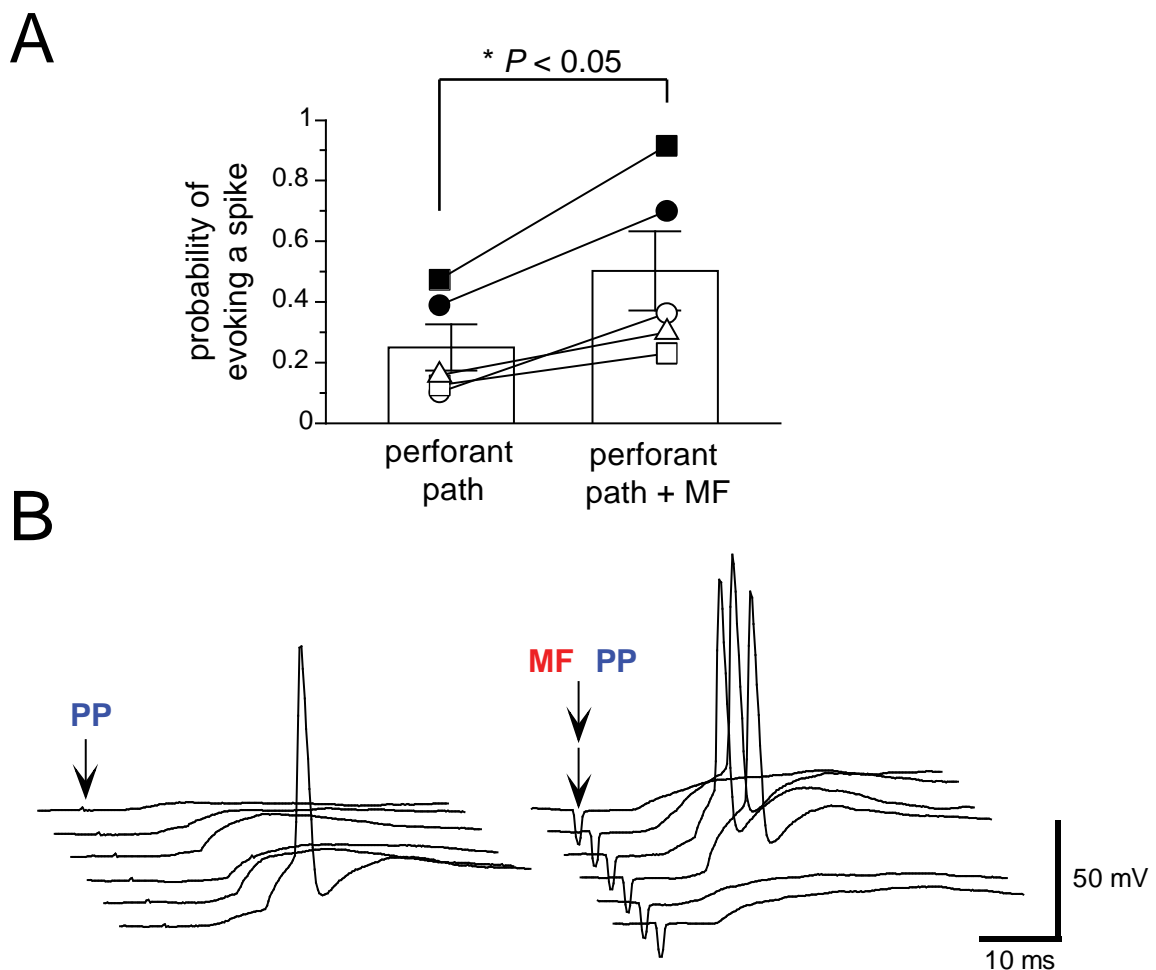


**Figure 7.10 – Simultaneous stimulation in the outer ML and SL increases the probability for evoking spikes in GCs. A:** Bar chart showing that the probability of evoking a spike increases when the outer ML and SL are activated simultaneously compared to the spiking probability when the outer ML is activated alone. **B:** Traces of 6 consecutive trials illustrating that more spikes are elicited when both pathways are activated simultaneously.

Having shown that stimulation of recurrent MF inputs increases the probability for evoking spikes in GCs in response to perforant path stimulation, next it was hypothesised that $Zn^{2+}$ modulates this effect by reducing GABA release. Both pathways were activated individually with an interval of 1s which seemed long enough for the two pathways not to interfere with each other. The stimulation strength was set to ~50% success rate for evoking a spike when both pathways were activated simultaneously. Consequently, the success rate for evoking spikes at individual inputs was set rather low. Chelation of $Zn^{2+}$ selectively increased the success rate for evoking spikes in response to SL stimulation while the probability for evoking spikes in response to perforant path stimulation remained unchanged (SL Ctrl: 0.16 ± 0.05, TPEN: 0.31 ± 0.08, n = 4, $P < 0.04$; perforant path Ctrl: 0.25 ± 0.08, TPEN: 0.23 ± 0.09, n = 5, $P < 0.3$, **figure 7.11**).

A

SL stimulation

* $P < 0.05$

Ctrl    TPEN



50 mV

20 ms

B

outer ML stimulation

N.S.

Ctrl    TPEN



50 mV

20 ms
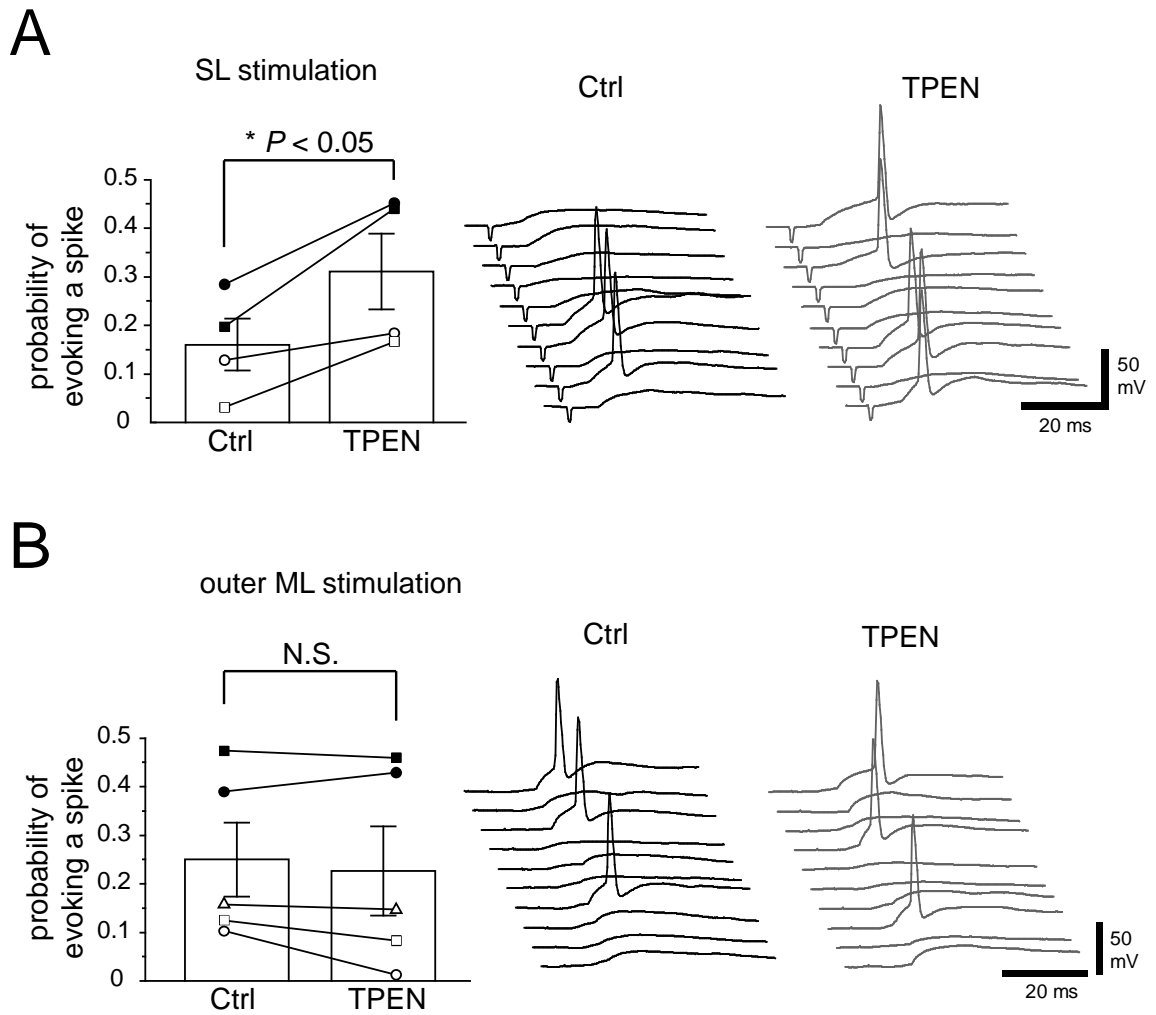
**Figure 7.11 – Zn$^{2+}$ chelation increases the probability for evoking a spike in response to SL stimulation. A,B:** Bar charts showing the probability of evoking a spike following perfusion of TPEN in response to SL stimulation (**A**) or stimulation in the outer ML (**B**). Traces of 10 consecutive trials for each pathway are shown on the right in control condition (black) and following perfusion of TPEN (grey).

These results demonstrate a pathway specific effect of Zn$^{2+}$ chelation on GC spiking. They also suggest that Zn$^{2+}$ chelation may alter the probability for evoking spikes in response to simultaneous activation of both pathways. However, superfusion of TPEN did not affect the probability of spiking when both pathways were activated simultaneously (**figure 7.12**).

A



B₁



B₂
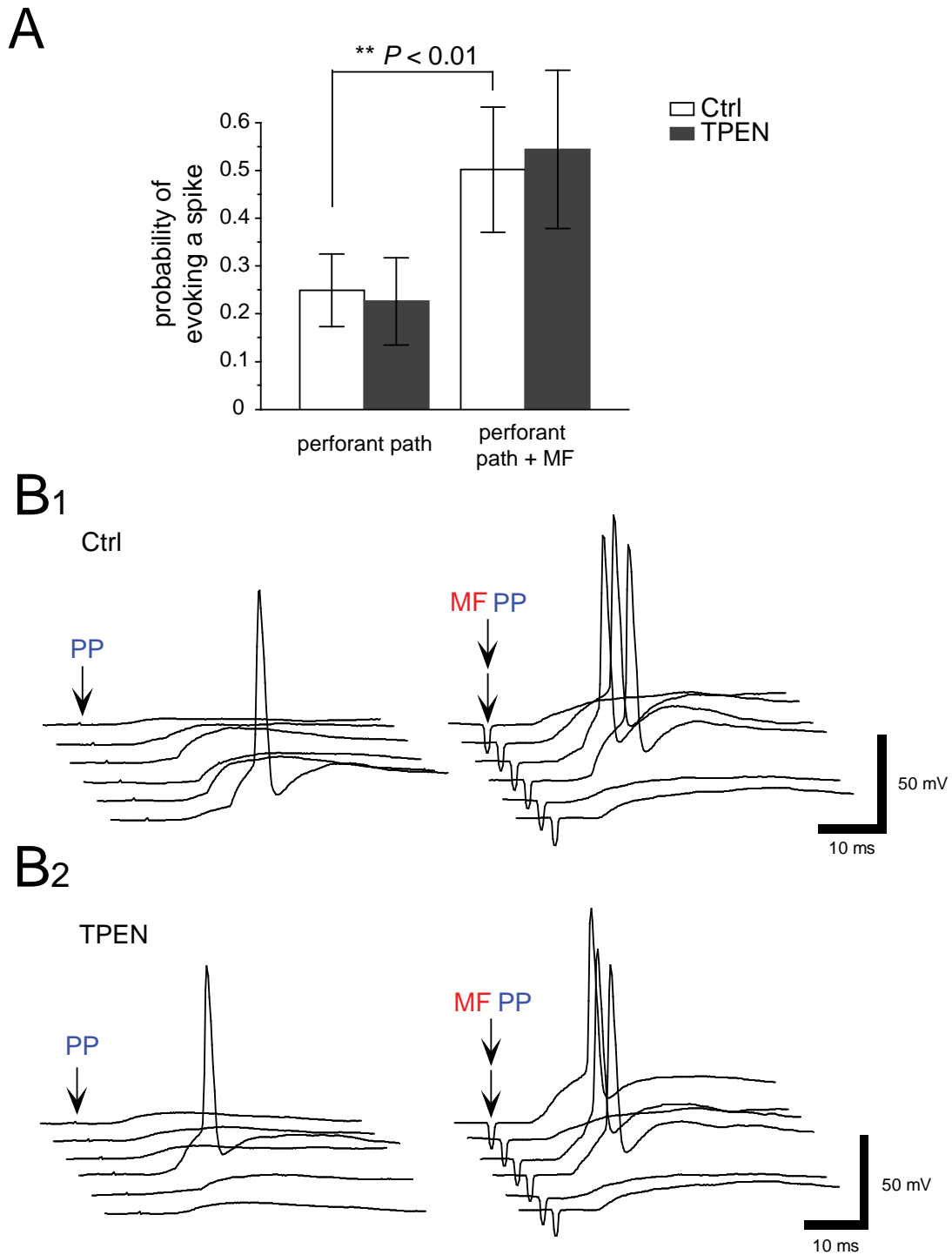


**Figure 7.12 – Effect of TPEN on GC spiking in response to simultaneous stimulation in SL and the outer ML. A:** Bar chart comparing the spiking probability when the outer ML is stimulated alone and when SL and the outer ML are stimulated simultaneously, in control condition (white bars) and following perfusion of TPEN (grey bars). **B1,2:** Traces for 6 consecutive trials showing a similar increase in the number of spikes in control condition (**B1**) and after application of TPEN (**B2**).

These results suggest that the increase in spiking at the MF pathway following $Zn^{2+}$ chelation only minimally translates into an increase in spiking when both pathways are activated, a condition which should yield maximal summation of both depolarising PSPs.

Because it is known from other areas in the hippocampal formation that the window for integration of excitatory inputs is dependent on different conductances, including $I_h$ and T-type $Ca^{2+}$ channels (Pavlov *et al.*, 2011b; Calixto *et al.*, 2008), the stimulation paradigm was altered to ask whether $Zn^{2+}$ modulates the window for integration of perforant path inputs in the dentate gyrus. The two pathways were activated at variable intervals (ranging from -30ms to +30ms in 10ms increments) to answer the question whether TPEN changes the window for integration of perforant path excitatory inputs. Again, the stimulation strength of the two pathways was set to a success rate for evoking a spike of ~50% when activated simultaneously. As shown in **figure 7.13C**, as the interval between stimulating SL and the perforant path became smaller, the probability for evoking spikes in response to perforant path stimulation also increased, following a Gaussian distribution with the maximal spiking probability centred at 0ms. Following bath-application of TPEN, there was a significantly narrower distribution of spiking probability, again with a maximal probability of spiking centred at 0ms.
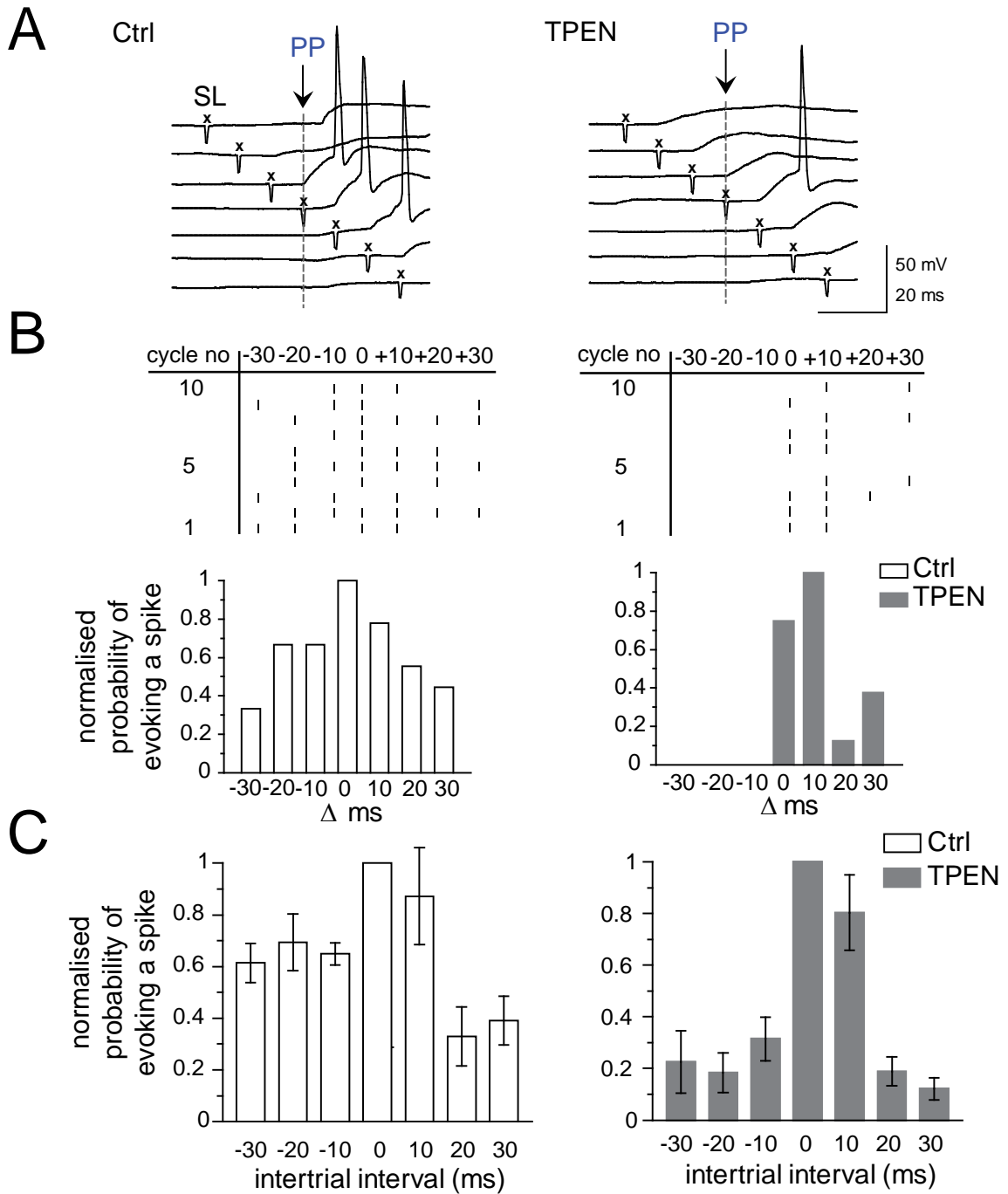
**Figure 7.13 - TPEN narrows the window for integration of perforant path inputs to GCs. A:** Voltage traces for 7 consecutive trials in control condition and after superfusion of TPEN. The perforant path is always activated at t=0ms (arrow) whereas SL stimuli are delivered at different times (x) creating different intertrial intervals (-30, -20, -10, 0, +10, +20, +30ms). The spiking probability increases as the intertrial interval decreases. This window becomes narrower in the presence of TPEN. **B:** (Top) Raster plot illustrating the occurrence of spikes evoked by activation of perforant path synapses for 10 consecutive cycles with different intertrial intervals, in control condition (left) and in the presence of TPEN (right). (Bottom) Bar chart showing the corresponding normalised spike probability against the intertrial interval in control condition (white bars) and TPEN (grey bars). **C:** Summary data from 5 GCs showing the reduction in the probability for evoking an action potential when both pathways are activated at >20ms intervals.

These results indicate that the time window for integration of perforant path inputs in GCs is narrower following $Zn^{2+}$ chelation. Because MFs can rapidly recruit dentate BCs ensuring a precise temporal integration of the excitatory input (Geiger *et al.*, 1997), a possible explanation for the above finding is shunting of perforant path-mediated EPSPs by the $GABA_A$R-mediated conductance activated by recurrent MF inputs. The contribution of each pathway to the overall sub-threshold summated PSP was analysed and expressed relative to their summated amplitude (see green bars in traces in **figure 7.14A**).

**Figure 7.14** shows that the contribution of perforant path-mediated PSPs (shown in blue) to the summated PSPs was significantly smaller and the MF-mediated PSPs (shown in red) were correspondingly bigger following application of TPEN, implying a shift in the excitation-inhibition balance. This change is significant for big intervals of +/-30ms, and the shift can still be observed with an interval of +/-20ms, albeit non-significant. In addition, for intervals in which the MF input preceded the perforant path input (-30 and -20ms), the amplitude of summated PSPs was significantly smaller in the presence of TPEN compared to control condition (**figure 7.15B**).
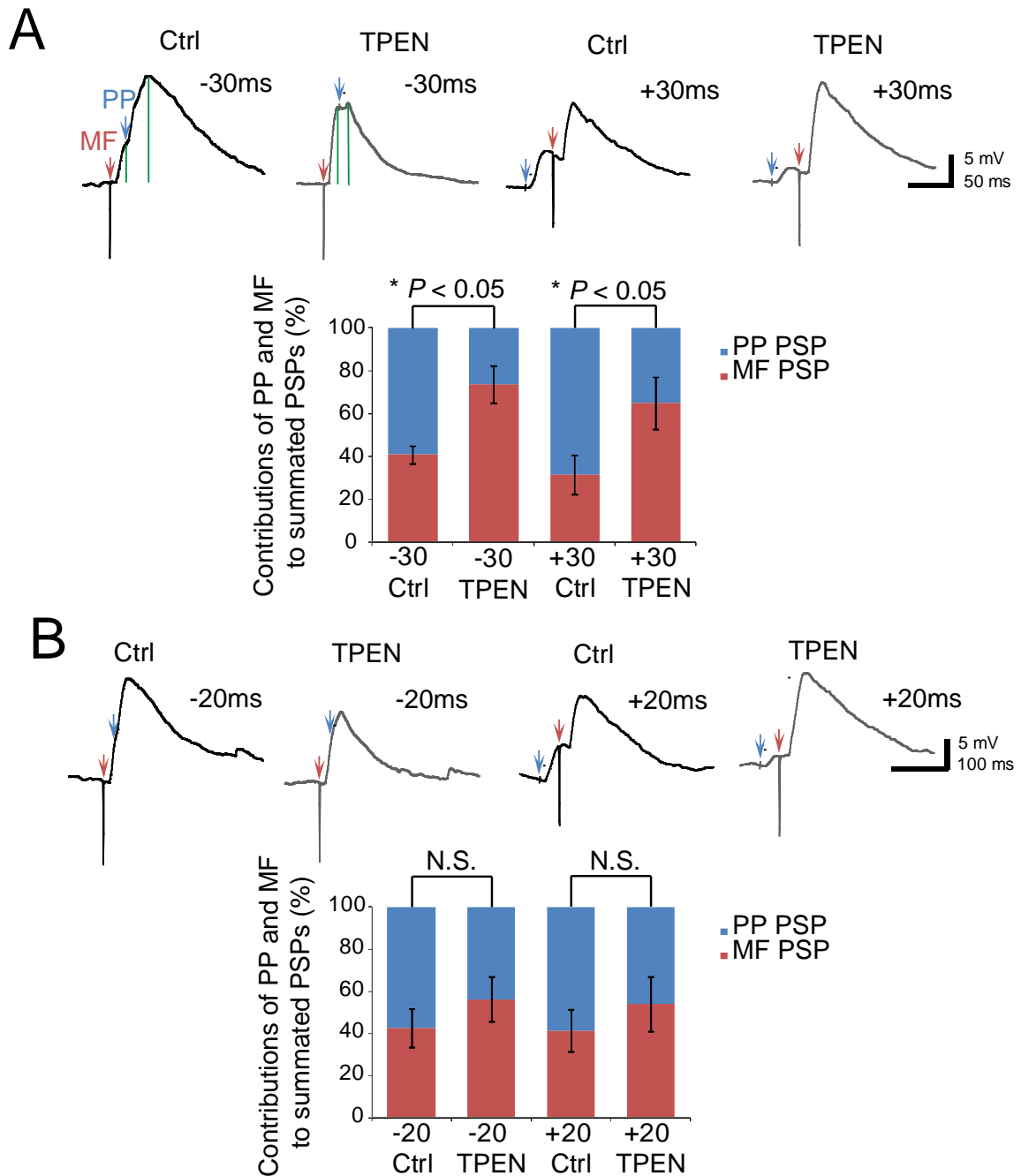
**Figure 7.14 – Sub-threshold PSPs evoked by stimuli delivered in SL or the outer ML contribute differently to summated PSPs at large intervals. A,B:** (Top) Traces showing averaged summated PSPs at large intervals of -30ms and +30ms (**A**) and for -20 and +20ms (**B**) in control (black) and TPEN condition (grey). Arrows indicate when the PP (blue) and MF pathway (red) is activated. Vertical green lines illustrate the contribution of SL stimulation to the amplitude of the summated PSP. (Bottom) Bar charts showing the contribution of ML (blue) and SL (red) evoked PSPs normalised to the amplitude of summated PSPs, at different intertrial intervals.
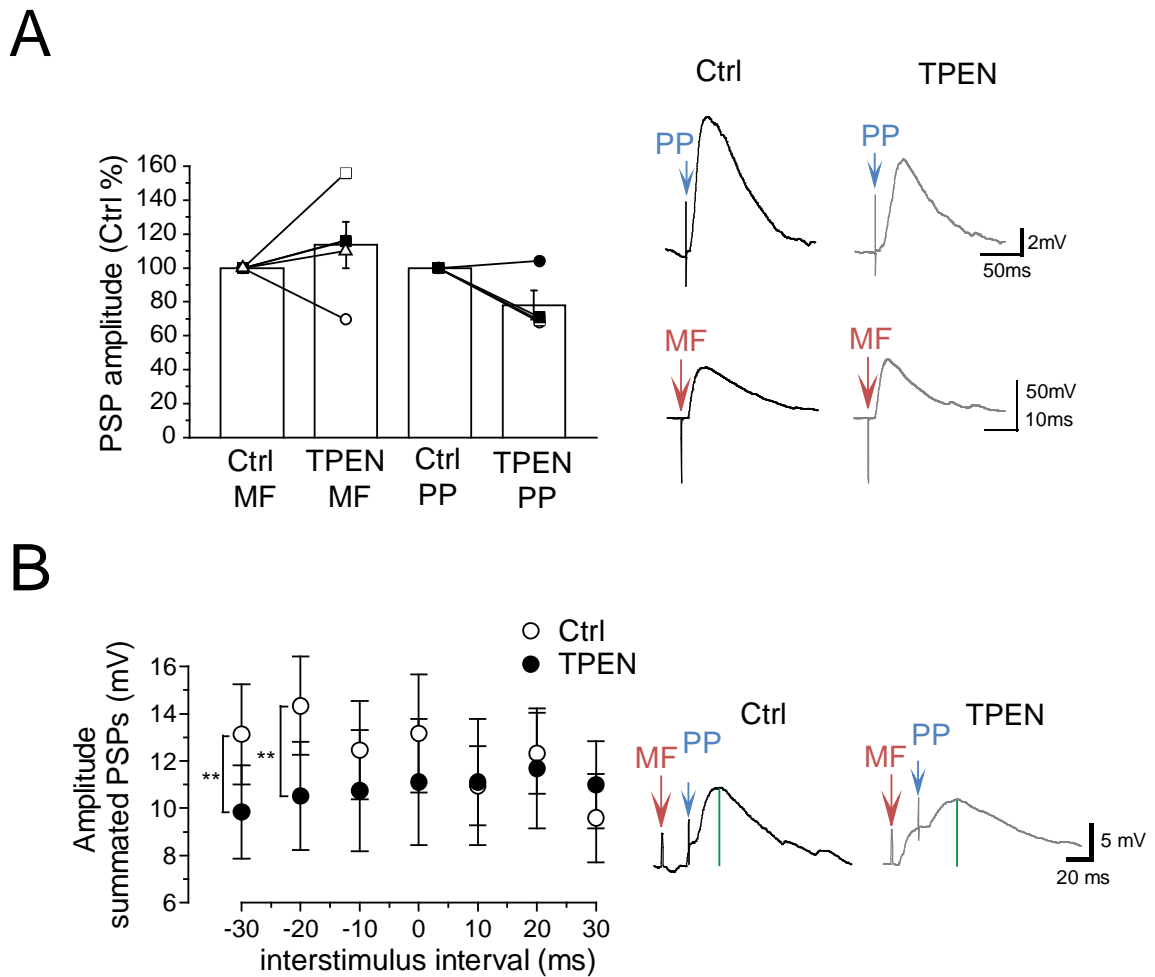
**Figure 7.15 – Effect of TPEN on the amplitude of sub-threshold individual PSPs and summated PSPs. A:** Barplot showing the effect of TPEN on the amplitude of sub-threshold PSPs for SL and outer ML stimulation. Traces are shown on the right in control (black) and in TPEN conditions (grey) for both pathways. **B:** Plot showing the effect of TPEN on the amplitude of summated PSPs for each intertrial interval. Traces (intertrial interval = -30mV) in control condition (black) and in TPEN (grey) are shown on the right.

In conclusion, these data demonstrate that activation of recurrent MF synapses and the main excitatory input to the dentate gyrus, the perforant path, both evoke depolarising PSPs, which summate and yield a significant increase in spiking probability in GCs. When chelating $Zn^{2+}$ with TPEN, there is a significant decrease in the contribution of perforant path inputs to the summated PSP in favour of MF inputs at intervals ≥ 20ms. This observation points towards a shunting effect of the MF-mediated GABAergic conductance.

Overall, an important and previously unknown mechanism was uncovered where endogenous $Zn^{2+}$ broadens the window for integration of excitatory perforant path inputs. This phenomenon has profound functional implications for the integration of synaptic inputs by dentate GCs and for spike routing to the hippocampus proper.

# 8. Discussion and Conclusion

$Zn^{2+}$ is transported into synaptic vesicles in MF terminals in the dentate gyrus and the hippocampus proper. The current view is that it is released at the synapse together with neurotransmitters where it acts on pre- and postsynaptic targets. This study investigated the modulation of interneuronal function by $Zn^{2+}$ and the consequences it has on synaptic integration and network properties in the dentate gyrus.

The results show that $Zn^{2+}$ depresses GABAergic signalling in GCs. This phenomenon was found at two distinct pathways that had different pharmacological properties consistent with mono-synaptic and di-synaptic connections. It was demonstrated that endogenous $Zn^{2+}$ depresses T-type $Ca^{2+}$ channels and NMDARs in fast-spiking interneurons and thus identified these channels and ionotropic receptor as major targets at postsynaptic membranes. Direct whole-bouton recordings suggested a small depression of MF excitability by $Zn^{2+}$ which was not detected using extracellular recordings or whole-cell voltage-clamp recordings from GCs. Moreover, $Zn^{2+}$ modulated GC excitability by reducing the probability for evoking action currents. Direct current-clamp recordings from a population of fast-spiking interneurons revealed that endogenous $Zn^{2+}$ reduced spike width and increased spike threshold. Finally, the results show that $Zn^{2+}$ broadened the window for integration of perforant path inputs in GCs thus altering synaptic processing in dentate GCs and spike routing to the hippocampus proper.

## 8.1. FEEDBACK AND FEED-FORWARD INHIBITORY PATHWAYS IN THE DENTATE GYRUS

Indirect and direct GABAergic synaptic inputs to GCs were evoked by positioning two stimulation electrodes in SL and SG, respectively. Functionally, these inputs can serve as models for feedback and feed-forward inhibitory pathways as shown by the pharmacological analysis of synaptic transmission. The abolishment of PSCs by bicuculline indicated that both inputs were mediated by $GABA_A$Rs which presumably involved local circuit interneurons, such as fast-spiking BCs. $Zn^{2+}$-containing MF collaterals have been previously demonstrated

to preferably form synapses onto these interneurons (Blasco-Ibanez *et al.*, 2000; Seress *et al.*, 2001). IPSCs evoked by SL stimulation had 1) variable latencies, 2) a high sensitivity to the group II mGluR agonist DCG-IV and 3) were abolished following perfusion of the AMPA and kainate receptor antagonist NBQX (**figures 4.3 – 4.5**). These results are consistent with a di-synaptic inhibitory input to GCs. The high sensitivity to DCG-IV was not only comparable to a study by Doherty *et al.* (2004), but also disclaimed major contaminations from inputs which were not mediated by MFs such as back-projecting CA3 collaterals (Scharfman, 2007). In contrast, IPSCs evoked by SG stimulation had 1) less variable latencies and 2) little sensitivity to NBQX. These results are consistent with a mono-synaptic inhibitory input to GCs. Moreover, the relatively little sensitivity to DCG-IV suggested little contamination from MF inputs (**figures 4.3 – 4.5**).

However, there are also disadvantages of using extracellular stimulation to activate bulk MFs. By positioning the stimulation electrode in stratum lucidum, the possibility cannot be excluded that antidromic activation of mossy fibres also activate mossy cells which then impinge onto interneurons (Buckmaster *et al.*, 1996). The SL pathway would then be contaminated by a poly-synaptic circuit which would still be sensitive to DCG-IV. In addition, SL stimulation may also activate those MF that project to local interneurons in stratum lucidum which project their axon into the hilus. These interneurons can either project directly to granule cells (Szabadics and Soltesz, 2009) or can also project to other interneurons or mossy cells. Finally, strong stimulation in SL can bring CA3 pyramidal cells to fire which then project locally to interneurons or mossy cells through hilar projecting collaterals.

Local glutamate puff application demonstrated that local inhibition was mediated by interneurons located in SG. It is unlikely that interneurons in SL also contributed to feedback inhibition to the dentate gyrus (Szabadics and Soltesz, 2009), as glutamate puff application in SL did not evoke IPSCs in GCs (**figure 5.14**). In contrast, local increases in extracellular $K^+$ in both SL and SG evoked IPSCs in GCs. These results showed that elevations in extracellular $K^+$ can recruit dentate interneurons thus mimicking the effect of extracellular stimulation (**figure 5.17**).

## 8.2. $Zn^{2+}$ CHELATION MODULATES GABAergic SIGNALLING

Two different $Zn^{2+}$ chelators were used to show that endogenous $Zn^{2+}$ modulates GABAergic signalling in GCs (**figures 4.7 – 4.9**). Both TPEN and EDTA have a similarly high affinity to $Zn^{2+}$ (TPEN $K_d = 10^{-15.6}$ M and EDTA $K_d = 10^{-16.4}$ M), however differ in their affinity to $Ca^{2+}$ (TPEN $10^{-1.7}$ M and EDTA $10^{-10.6}$ M) and $Mg^{2+}$ (TPEN $10^{-4.4}$ M and EDTA $10^{-8.7}$ M) (Arslan *et al.*, 1985; Dawson RMC *et al.*, 1986). Another difference between the chelators is that TPEN is a lipophilic chelator and thus permeates through membranes thus affecting intracellular $Zn^{2+}$ pools. On the other hand, CaEDTA is negatively charged and only chelates extracellular $Zn^{2+}$. Kay (2003) argued that CaEDTA is too slow to capture $Zn^{2+}$ transients as the kinetics of the chelation process are determined by the slow off-rate constant of $Ca^{2+}$.

The results show that CaEDTA increased the IPSC amplitude to a significantly greater extent than TPEN when SL was stimulated (CaEDTA: 75.2 ± 18.4%; TPEN:  31.6 ± 5.2%, *P* < 0.002, unpaired t-test, **figure 4.9**). An obvious explanation that would account for the difference would be an increase in the extracellular $Ca^{2+}$ concentration due to the exchange of CaEDTA by ZnEDTA. However, CaEDTA has been previously shown not to enhance the extracellular $Ca^{2+}$ concentration during the chelation process (Koh *et al.*, 1996). In addition, the amplitude of IPSCs evoked by stratum radiatum stimulation was not enhanced by perfusion of CaEDTA, arguing against a possible change in the $Ca^{2+}$ concentration. The difference between the chelators may be explained by a difference in selectivity of the chelators to other ions than $Zn^{2+}$, for example $Mg^{2+}$. Alternatively, the fact that TPEN also chelates intracellular $Zn^{2+}$ may explain discrepancies in the magnitude of the effects because $Zn^{2+}$ mediated intracellular action may counteract a potential effect. In the light of these results, it would be interesting to use other extracellular chelators such as tricine (Paoletti *et al.*, 1997) or the newly developed $Zn^{2+}$ chelator ZX1 (Pan *et al.*, 2012) and test whether this difference between extra- and intracellular chelation is a robust observation.

The observation that stratum radiatum evoked IPSCs were chelator-insensitive is in line with a phenomenon which is confined to $Zn^{2+}$-containing synapses such as those in the dentate gyrus (**figure 4.14**). Furthermore, the facilitation of evoked IPSCs was greatly reduced when release probability at MF synapses was lowered pharmacologically with the perfusion of DCG-IV (**figure 4.15**). This result is consistent with $Zn^{2+}$ release from MFs but also raises the possibility that $Zn^{2+}$ may spill-out from MF synapses to extrasynaptic compartments thus contributing to heterosynaptic interactions. On the other hand, there was no evidence for activity-dependent release of $Zn^{2+}$ (**figures 4.16, 4.17, tables 4.1 – 4.3**). Altogether, the results are consistent with a modulation of GABAergic signalling by tonic $Zn^{2+}$ which may be released and recycled at MF terminals.

## 8.3. TARGETS OF ENDOGENOUS $Zn^{2+}$

### 8.3.1. GABA$_A$ receptors at granule cells

It is unlikely that these findings of $Zn^{2+}$–mediated modulation of dentate GC excitability can be explained by an effect of $Zn^{2+}$ on GABA$_A$Rs at somata and dendrites of GCs themselves. The decay–time constant or the somatic holding–current of evoked IPSCs were not affected by $Zn^{2+}$ chelation (**figures 4.11, 4.18**). Also, local GABA application to GC dendrites did not change GABA currents following $Zn^{2+}$ chelation, indicating that synaptic or extrasynaptic GABA$_A$R mediating GABA currents in GCs are not likely to be modulated by endogenous $Zn^{2+}$ (**figure 4.19**). These results are consistent with the low $Zn^{2+}$ sensitivity of GABA$_A$Rs located at GCs (Buhl *et al.*, 1996), and at MF collateral synapses (Molnar and Nadler, 2001a).

### 8.3.2. T-type $Ca^{2+}$ channels

The results show that endogenous $Zn^{2+}$ depresses $Ca^{2+}$ currents mediated by low-voltage activated T-type $Ca^{2+}$ channels. Perfusion of a range of T-type $Ca^{2+}$ channel blockers occluded the effect of $Zn^{2+}$ chelation and thus identified T-type

$Ca^{2+}$ channels as major $Zn^{2+}$ targets (**figures 5.20 – 5.21**). The fact that 100µM NiCl$_2$ reduced the amplitude of evoked IPSCs by 46% and 10µM NiCl$_2$ by 22% (SL stimulation) suggests that a lower concentration of NiCl$_2$ is more selective for T-type $Ca^{2+}$ channels, as reported previously (Lee *et al.*, 1999). To avert any possible saturation of TPEN by $Ni^{2+}$, slices were also perfused with mibefradil (10µM) or the Ca$_v$3.1 selective blocker NNC 55-0396 (10µM). Both antagonists reduced postsynaptic currents by 22% and 23% (SL stimulation), in good agreement with the effects of exogenous $Zn^{2+}$ application (**figure 4.10)**. Importantly, blocking T-type $Ca^{2+}$ channels reduced IPSC amplitude to a similar extent as $Zn^{2+}$ chelators facilitated them. In contrast, other $Ca^{2+}$ channel antagonists did not prevent the modulation by $Zn^{2+}$ implying a selective effect at low-voltage activated channels (**figures 5.22**).

Where are these low-voltage $Ca^{2+}$ channels located? Direct recordings from MFBs have identified T-type $Ca^{2+}$ channels as a minority compared to P/Q and N-type $Ca^{2+}$ channels (Li *et al.*, 2007), so that a presynaptic location of these channels can be excluded. Glutamate puff experiments demonstrated that interneurons which were involved in the activation of microcircuits were located in the dentate gyrus rather than in SL. In accordance with this, there is a high expression of Ca$_v$3.1 – 3.3 in the dentate GCL, where fast-spiking interneurons are located (McKay *et al.*, 2006). In addition, Vinet and Sik (2006) found a high expression of Ca$_v$3.1 in the majority of parvalbumin positive interneurons in the hippocampus, including the dentate gyrus. In line with these reports, recordings from dentate interneurons and GCs indicated that low-threshold T-type $Ca^{2+}$ currents could be detected in both cell types (**figure 6.3 – 6.4**). Importantly, a selective modulation of mibefradil-sensitive $Ca^{2+}$ currents by $Zn^{2+}$ was shown in interneurons but not in GCs (**figure 6.5**). These results raise the possibility that $Zn^{2+}$ regulates low-threshold $Ca^{2+}$ currents in dentate interneurons consistent with the dense innervation of parvalbumin-positive interneurons by $Zn^{2+}$-containing fibres (Seress *et al.*, 2001; Blasco-Ibanez *et al.*, 2000).

### 8.3.3. NMDA receptors

The role of NMDARs in this modulation was also investigated. Recording IPSCs in GCs in the background of the NMDAR antagonist D-APV selectively reduced the chelating effect of CaEDTA (**figure 5.8**). In contrast, bath-application of the GluN2B subunit blocker ifenprodil yielded a similar facilitation in IPSCs compared to conditions in which they were left unblocked (**figure 5.10**). These results suggested that GluN2B subunits were not modulated by endogenous $Zn^{2+}$, offering the possibility that GluN2A subunits play a role. Finally, voltage-clamp recordings from interneurons revealed that NMDARs in putative fast-spiking BCs were sensitive to extracellular $Zn^{2+}$ chelation (**figure 6.2**). This result is consistent with the idea that extracellular $Zn^{2+}$ chelation augments the excitatory drive to interneurons making them more excitable and thus prone to release more GABA onto GCs.

In contrast to extracellular chelation, the blockade of NMDARs by D-APV did not change the amount of facilitation in IPSC amplitude when TPEN was perfused (**figure 5.8**). This result suggests that there are differences in the mechanism of action of the two chelators and that NMDARs may be modulated by extracellular $Zn^{2+}$, while intracellular $Zn^{2+}$ may possibly have counteracting effects. It may be possible that the role of extracellular $Zn^{2+}$ is predominantely to depress its targets T-type $Ca^{2+}$ channels and NMDARs. In contrast, intracellular $Zn^{2+}$ may facilitate an interaction between T-type $Ca^{2+}$ channels and NMDARs by mediating the activation of NMDARs in response to the $Ca^{2+}$ influx through T-type $Ca^{2+}$ channels. Extracellular chelation by CaEDTA would therefore relieve the inhibition of both targets by $Zn^{2+}$. In contrast, additional intracellular $Zn^{2+}$ by TPEN would attenuate the effect of extracellular $Zn^{2+}$ chelation by relieving the activation of NMDARs.

### 8.3.4. Axonal excitability

AfP recordings as well as antidromic whole-cell voltage-clamp recordings showed that there was no obvious change in axonal excitability following $Zn^{2+}$ chelation, indicative by the lack of change in the amplitude of AfPs and a lack of change in

the probability for evoking action currents in response to SL stimulation (**figures 5.1, 5.5**). The short latency wave-form of AfPs indicated that SL stimulation evoked an antidromic population spike which largely persisted when perfused with bicuculline. Similarly, little variability in the short latency and little sensitivity to NBQX of this population of action currents demonstrated that these were mediated by direct stimulation of the axon. In contrast, whole-bouton recordings demonstrated that $Zn^{2+}$ chelation induced a small but significant increase of spike half-width and a reduction of MFB input resistance (**figures 5.6, 5.7**). It is possible that these effects are attributable to the recently identified $K_v3$ $K^+$ channels which have been found to be important for the repolarisation phase of the MF action potential wave-form (Alle *et al.*, 2011). However, other subunits could also be involved (Harrison *et al.*, 1993). It is worth noting that intracellular $Zn^{2+}$ has been shown to potently and reversibly activate large-conductance voltage- and $Ca^{2+}$-activated $K^+$ (BK) channels (Harrison *et al.*, 1993; Hou *et al.*, 2010) which have been shown to reside at MF terminals (Knaus *et al.*, 1996; Alle *et al.*, 2011).

### 8.3.5. Modulation of interneuronal excitability by $Zn^{2+}$

The results indicate that $Zn^{2+}$ selectively modulates intrinsic properties that are critical for controlling the I-O relation in fast-spiking dentate interneurons. Offsetting the I-O relation (an additive operation) allows cells to subtract baseline levels of excitation from an input signal, whereas changing the gain of the I-O relation (a multiplicative operation) alters the sensitivity of a neuron to changes in the excitatory input rate (Kerr and Capogna, 2007; Mitchell and Silver, 2003). Here, chelation of $Zn^{2+}$ with TPEN modulated neuronal offset without affecting the gain (**figures 7.2–7.5**). Removing $Zn^{2+}$ from the extracellular space lowered the threshold of the stimulus independently of changes to the sensitivity of the input. This phenomenon is thought to enhance information encoding in single neurons receiving timed and distributed synaptic events (Carvalho and Buonomano, 2009) and recent evidence has emerged that tonically-active rectifying $GABA_A$Rs in pyramidal cells modulate the offset, not the gain (Pavlov *et al.*, 2009).

Furthermore, chelation of $Zn^{2+}$ decreased spike threshold and enhanced spike-width (**figures 7.6, 7.7**). These indicators point towards increased interneuron excitability and increased GABA release onto GCs as a consequence of $Zn^{2+}$ chelation.

Together, circumstantial evidence was obtained showing that $Zn^{2+}$ chelation augments the excitability of fast-spiking interneurons and that T-type $Ca^{2+}$ channels are involved. Whether these observations are linked remains to be determined.

## 8.4. IMPLICATIONS FOR SIGNAL INTEGRATION

Stimulation of the outer ML of the dentate gyrus recruits largely fibres of the lateral perforant path as previously shown in other studies (Ewell and Jones, 2010; Sambandan *et al.*, 2010). The observation that NBQX abolished spikes evoked by perforant path stimulation and also significantly reduced action potentials elicited by MF synapses indicates that they were both directly or indirectly driven by glutamatergic inputs. In contrast, perfusion of bicuculline abolished MF-mediated action potentials whereas it mildly reduced the probability for evoking action potentials by stimulating the perforant path (**figure 7.9**). This result indicates that 1) depolarising GABAergic inputs onto GCs can make them fire action potentials and 2) that stimulating the outer ML mediates feed-forward inhibition possibly by fast-spiking interneurons which have been shown to be preferentially recruited when stimulating the lateral or medial perforant path (Ewell and Jones, 2010).

Importantly, the observation that $Zn^{2+}$ chelation narrows the window for integration of perforant path inputs (**figure 7.13**) uncovers a novel physiological role for $Zn^{2+}$. The stimulation of fibres from local interneurons activated by the MF input resulted in a $GABA_AR$-mediated conductance that both depolarised and effectively shunted the more strongly depolarising perforant path-mediated PSPs. Therefore, I propose that the tuning of the window for integration is attributed to a greater shunting of excitatory synapses by the $GABA_AR$-mediated conductance

and weakening of EPSPs to spike coupling, resulting in lower spike probability for large intertrial intervals following $Zn^{2+}$ chelation (**figure 7.14, 7.15**).

## 8.5. FUTURE WORK

One of the most controversial and unresolved issues within the $Zn^{2+}$ field is undoubtedly the question whether endogenous $Zn^{2+}$ is released by $Zn^{2+}$-containing neurons and if it is, how much. The distinction between vesicular and non-vesicular $Zn^{2+}$, by utilizing ZnT3 knock-out mice for the experiments is clearly important for the interpretation of the results presented here.

Moreover, the significance of T-type $Ca^{2+}$ channel modulation would need to be best evaluated in transgenic mice that lack these channels. In order to relate the inhibition of T-type $Ca^{2+}$ channels by $Zn^{2+}$ in interneurons to a decrease in GABA release in GCs, paired-recordings between fast-spiking interneurons and GCs would have to be performed, while stimulating MFs. This has not been addressed in the present study because of a low success rate of finding a BC-GC pair. Here, single BCs could be stimulated optogenetically by expressing the light-gated channel channelrhodopsin which would enhance the success rate for finding GC-BC connections.

The main targets for this modulation, T-type $Ca^{2+}$ channels and NMDARs, both have a high permeability for $Ca^{2+}$ and thus activation of these channels enhances the intracellular $Ca^{2+}$ level which may trigger intracellular signalling cascades. Using $Ca^{2+}$ imaging, it could be determined whether these $Ca^{2+}$ signals are also modulated by $Zn^{2+}$ and whether they might enhance cell excitability and other biophysical parameters such as buffering.

Furthermore, it will be important to investigate whether the modulation by $Zn^{2+}$ is dependent on the type of interneuron. Perisomatically targeting interneurons such as BCs may be differentially modulated by $Zn^{2+}$ than dendritically targeting interneurons such as HIPP cells. For that, interneurons would need to be identified according to their physiological and morphological properties, and neurochemical markers.

Finally, a closer investigation of the reconcilement between the broadening of the integration window and a modulation of the reversal potential for synaptic GABAergic inputs would need to be performed in perforated-patch conditions, when the $Cl^-$ environment is left undisturbed.

## 8.6. CONCLUDING REMARKS – ROLE OF $Zn^{2+}$

The findings have shed light onto previously unknown mechanisms by which $Zn^{2+}$ may potentially influence synaptic transmission and integration within the dentate gyrus. The results propose that $Zn^{2+}$ inhibits T-type $Ca^{2+}$ channels, dampens interneuron excitability and decreases GABA release onto GCs. The results propose that when $Zn^{2+}$ is present, a smaller $GABA_AR$-mediated conductance to GCs does not shunt perforant path-mediated EPSPs effectively so that they summate with EPSPs from the perforant path which may then reach action potential threshold. Thus, by increasing summation and decreasing shunting inhibition, $Zn^{2+}$ reduces temporal fidelity from incoming perforant path inputs which in turn increases GC firing (**figure 8.1**).
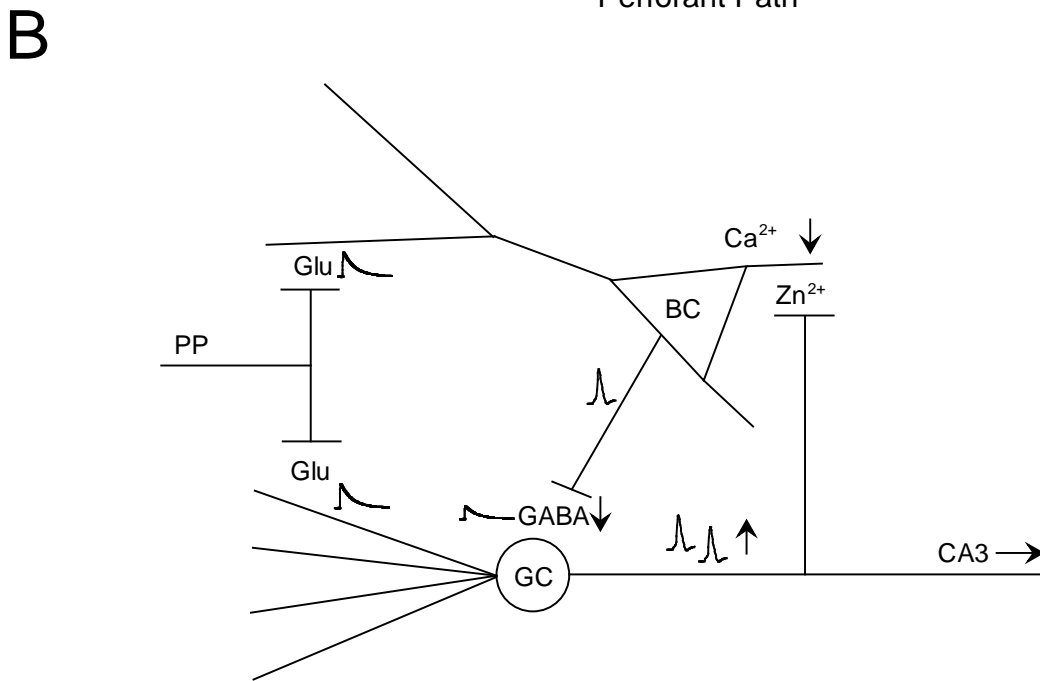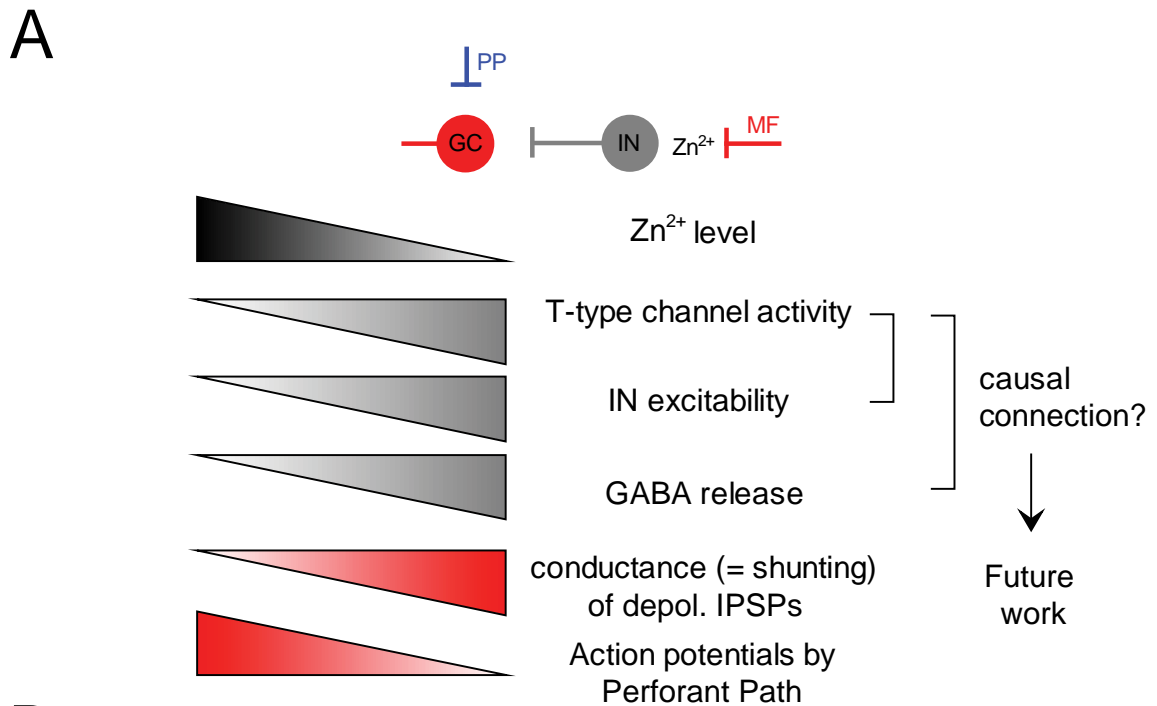
**Figure 8.1 – A novel role for endogenous $Zn^{2+}$ within the dentate gyrus microcircuitry. A:** Diagram of the proposed mechanistic sequence of events involving $Zn^{2+}$. (Left) Right-angled triangles represent high and low levels of $Zn^{2+}$ (black). As $Zn^{2+}$ levels change, effects in interneurons (grey) and in granule cells (red) change accordingly. **B:** Cartoon of a microcircuit between a GC and a BC. Both neurons receive inputs from the perforant path. As GCs become activated by perforant path inputs, they release $Zn^{2+}$ onto MF-BC synapses. $Ca^{2+}$ signalling mediated by T-type $Ca^{2+}$ channels and NMDARs is depressed. $Zn^{2+}$ dampens BC excitability and depresses GABA release at BC-GC synapses. A smaller $GABA_AR$-mediated conductance cannot effectively shunt perforant path-mediated EPSPs resulting in more GC spiking.

Lastly, this study has shown numerous $Zn^{2+}$ actions at the synapse where it is released, but highlights that many other factors such as diffusion, modulation of intrinsic excitability of neurons or the effect on shunting inhibition may also play a role.

Dentate GCs are hyper-excitable in tissues of patients that suffer from temporal lobe epilepsy (Williamson *et al.*, 1995; Gabriel *et al.*, 2004). Factors that are contributing to this abnormally high activity include MF sprouting (Mello *et al.*, 1993; Okazaki *et al.*, 1995), loss of hilar neurons including interneurons (Mello *et al.*, 1993; Blumcke *et al.*, 2000), altered GABAergic transmission between interneurons and GCs (Brooks-Kayal *et al.*, 1998; Zhang and Buckmaster, 2009; Nusser *et al.*, 1998) and increased excitatory transmission onto GCs (Epsztein *et al.*, 2005; Scimemi *et al.*, 2006; Zhang *et al.*, 2012). In addition in models of traumatic brain injury, phasic GABAergic inhibition is also progressively lost (Pavlov *et al.*, 2011a). A speculative hypothesis is that following unusally high excitatory activity of GCs, $Zn^{2+}$ may act as another contributing factor and exacerbates this increased firing in GCs by dampening interneuronal excitability and hampering the filter function of the dentate gyrus.

# References

Reference List

Acsady L, Kamondi A, Sik A, Freund T, Buzsaki G (**1998**) GABAergic cells are the major postsynaptic targets of mossy fibers in the rat hippocampus. *J Neurosci* 18:3386-3403.

Acsady L, Katona I, Martinez-Guijarro FJ, Buzsaki G, Freund TF (**2000**) Unusual target selectivity of perisomatic inhibitory cells in the hilar region of the rat hippocampus. *J Neurosci* 20:6907-6919.

Alle H, Kubota H, Geiger JR (**2011**) Sparse but highly efficient $K_v3$ outpace $BK_{Ca}$ channels in action potential repolarization at hippocampal mossy fiber boutons. *J Neurosci* 31:8001-8012.

Amaral DG (**1978**) A Golgi study of cell types in the hilar region of the hippocampus in the rat. *J Comp Neurol* 182:851-914.

Amaral DG, Ishizuka N, Claiborne B (**1990**) Neurons, numbers and the hippocampal network. *Prog Brain Res* 83:1-11.

Amaral DG, Scharfman HE, Lavenex P (**2007**) The dentate gyrus: fundamental neuroanatomical organization (dentate gyrus for dummies). *Prog Brain Res* 163:3-22.

Amaral DG, Witter MP (**1989**) The three-dimensional organization of the hippocampal formation: a review of anatomical data. *Neuroscience* 31:571-591.

Andersen P, Morris R, Amaral DG, Bliss TV, O'Keefe J (**2007**) The Hippocampus Book. New York: Oxford University Press.

Anderson P, Bliss TV, Skrede KK (**1971**) Lamellar organization of hippocampal pathways. *Exp Brain Res* 13:222-238.

Aponte Y, Bischofberger J, Jonas P (**2008**) Efficient $Ca^{2+}$ buffering in fast-spiking basket cells of rat hippocampus. *J Physiol* 586:2061-2075.

Aponte Y, Lien CC, Reisinger E, Jonas P (**2006**) Hyperpolarization-activated cation channels in fast-spiking interneurons of rat hippocampus. *J Physiol* 574:229-243.

Armstrong C, Szabadics J, Tamás G, Soltesz I (**2011**) Neurogliaform cells in the molecular layer of the dentate gyrus as feed-forward γ-aminobutyric acidergic modulators of entorhinal-hippocampal interplay. *J Comp Neurol* 519:1476-91.

Armstrong C, Krook-Magnuson E, Soltesz I (**2012**) Neurogliaform and ivy cells: a major family of nNOS expressing GABAergic neurons. *Front Neural Circuits* 6:23

Arslan P, Di VF, Beltrame M, Tsien RY, Pozzan T (**1985**) Cytosolic $Ca^{2+}$ homeostasis in Ehrlich and Yoshida carcinomas. A new, membrane-permeant

chelator of heavy metals reveals that these ascites tumor cell lines have normal cytosolic free $Ca^{2+}$. *J Biol Chem* 260:2719-2727.

Assaf SY, Chung SH (**1984**) Release of endogenous $Zn^{2+}$ from brain tissue during activity. *Nature* 308:734-736.

Austin JE, Buckmaster PS (**2004**) Recurrent excitation of granule cells with basal dendrites and low interneuron density and inhibitory postsynaptic current frequency in the dentate gyrus of macaque monkeys. *J Comp Neurol* 476:205-218.

Bartos M, Alle H, Vida I (**2011**) Role of microcircuit structure and input integration in hippocampal interneuron recruitment and plasticity. *Neuropharmacology* 60:730-739.

Bean BP (**2007**) The action potential in mammalian central neurons. *Nat Rev Neurosci* 8:451-465.

Beaulieu C, Dyck R, Cynader M (**1992**) Enrichment of glutamate in zinc-containing terminals of the cat visual cortex. *Neuroreport* 3:861-864.

Bender KJ, Trussell LO (**2009**) Axon initial segment $Ca^{2+}$ channels influence action potential generation and timing. *Neuron* 61:259-271.

Berger T, Schwarz C, Kraushaar U, Monyer H (**1998**) Dentate gyrus basket cell $GABA_A$ receptors are blocked by $Zn^{2+}$ via changes of their desensitization kinetics: an in situ patch-clamp and single-cell PCR study. *J Neurosci* 18:2437-2448.

Bergersen L, Ruiz A, Bjaalie JG, Kullmann DM, Gundersen V (**2003**) GABA and $GABA_A$ receptors at hippocampal mossy fibre synapses. *Eur J Neurosci* 18:931-941.

Besser L, Chorin E, Sekler I, Silverman WF, Atkin S, Russell JT, Hershfinkel M (**2009**) Synaptically released zinc triggers metabotropic signaling via a zinc-sensing receptor in the hippocampus. *J Neurosci* 29:2890-2901.

Birinyi A, Parker D, Antal M, Shupliakov O (**2001**) Zinc co-localizes with GABA and glycine in synapses in the lamprey spinal cord. *J Comp Neurol* 433:208-221.

Bischofberger J, Geiger JR, Jonas P (**2002**) Timing and efficacy of Ca2+ channel activation in hippocampal mossy fiber boutons. *J Neurosci* 22:10593-10602.

Bischofberger J, Engel D, Li L, Geiger JR, Jonas P (**2006**) Patch-clamp recording from mossy fiber terminals in hippocampal slices. *Nat Protoc* 1:2075-2081.

Blasco-Ibanez JM, Martinez-Guijarro FJ, Freund TF (**2000**) Recurrent mossy fibers preferentially innervate parvalbumin-immunoreactive interneurons in the granule cell layer of the rat dentate gyrus. *Neuroreport* 11:3219-3225.

Bliss TV, Collingridge GL (**1993**) A synaptic model of memory: long-term potentiation in the hippocampus. *Nature* 361:31-39.

Bloomenthal AB, Goldwater E, Pritchett DB, Harrison NL (**1994**) Biphasic modulation of the strychnine-sensitive glycine receptor by $Zn^{2+}$. *Mol Pharmacol* 46:1156-1159.

Blumcke I, Suter B, Behle K, Kuhn R, Schramm J, Elger CE, Wiestler OD (**2000**) Loss of hilar mossy cells in Ammon's horn sclerosis. *Epilepsia* 41 Suppl 6:S174-S180.

Brickley SG, Cull-Candy SG, Farrant M (**1996**) Development of a tonic form of synaptic inhibition in rat cerebellar granule cells resulting from persistent activation of $GABA_A$ receptors. *J Physiol* 497 ( Pt 3):753-759.

Brooks-Kayal AR, Shumate MD, Jin H, Rikhter TY, Coulter DA (**1998**) Selective changes in single cell $GABA_A$ receptor subunit expression and function in temporal lobe epilepsy. *Nat Med* 4:1166-1172.

Buckmaster PS, Wenzel HJ, Kunkel DD, Schwartzkroin PA (**1996**) Axon arbors and synaptic connections of hippocampal mossy cells in the rat in vivo. *J Comp Neurol* 366:271-292.

Bucurenciu I, Kulik A, Schwaller B, Frotscher M, Jonas P (**2008**) Nanodomain coupling between $Ca^{2+}$ channels and $Ca^{2+}$ sensors promotes fast and efficient transmitter release at a cortical GABAergic synapse. *Neuron* 57:536-545.

Buhl EH, Otis TS, Mody I (**1996**) Zinc-induced collapse of augmented inhibition by GABA in a temporal lobe epilepsy model. *Science* 271:369-373.

Busselberg D, Platt B, Michael D, Carpenter DO, Haas HL (**1994**) Mammalian voltage-activated calcium channel currents are blocked by $Pb^{2+}$, $Zn^{2+}$, and $Al^{3+}$. *J Neurophysiol* 71:1491-1497.

Buzsaki G (**1984**) Feed-forward inhibition in the hippocampal formation. *Prog Neurobiol* 22:131-153.

Buzsaki G, Czeh G (**1981**) Commissural and perforant path interactions in the rat hippocampus. Field potentials and unitary activity. *Exp Brain Res* 43:429-438.

Calixto E, Galvan EJ, Card JP, Barrionuevo G (**2008**) Coincidence detection of convergent perforant path and mossy fibre inputs by CA3 interneurons. *J Physiol* 586:2695-2712.

Carvalho TP, Buonomano DV (**2009**) Differential effects of excitatory and inhibitory plasticity on synaptically driven neuronal input-output functions. *Neuron* 61:774-85.

Chevaleyre V, Castillo PE (**2002**) Assessing the role of $I_h$ channels in synaptic transmission and mossy fiber LTP. *Proc Natl Acad Sci U S A* 99:9538-9543.

Chiang PH, Wu PY, Kuo TW, Liu YC, Chan CF, Chien TC, Cheng JK, Huang YY, Chiu CD, Lien CC (**2012**) GABA is depolarizing in hippocampal dentate granule cells of the adolescent and adult rats. *J Neurosci* 32:62-7.

Christensen MK, Frederickson CJ (**1998**) Zinc-containing afferent projections to the rat corticomedial amygdaloid complex: a retrograde tracing study. *J Comp Neurol* 400:375-390.

Claiborne BJ, Amaral DG, Cowan WM (**1986**) A light and electron microscopic analysis of the mossy fibers of the rat dentate gyrus. *J Comp Neurol* 246:435-458.

Claiborne BJ, Amaral DG, Cowan WM (**1990**) Quantitative, three-dimensional analysis of granule cell dendrites in the rat dentate gyrus. *J Comp Neurol* 302:206-219.

Cohen-Kfir E, Lee W, Eskandari S, Nelson N (**2005**) Zinc inhibition of gamma-aminobutyric acid transporter 4 (GAT4) reveals a link between excitatory and inhibitory neurotransmission. *Proc Natl Acad Sci U S A* 102:6154-6159.

Cole TB, Wenzel HJ, Kafer KE, Schwartzkroin PA, Palmiter RD (**1999**) Elimination of zinc from synaptic vesicles in the intact mouse brain by disruption of the ZnT3 gene. *Proc Natl Acad Sci U S A* 96:1716-1721.

Conn PJ, Pin JP (**1997**) Pharmacology and functions of metabotropic glutamate receptors. *Annu Rev Pharmacol Toxicol* 37:205-237.

Cote A, Chiasson M, Peralta MR, III, Lafortune K, Pellegrini L, Toth K (**2005**) Cell type-specific action of seizure-induced intracellular zinc accumulation in the rat hippocampus. *J Physiol* 566:821-837.

Craig PJ, Beattie RE, Folly EA, Banerjee MD, Reeves MB, Priestley JV, Carney SL, Sher E, Perez-Reyes E, Volsen SG (**1999**) Distribution of the voltage-dependent calcium channel $\alpha$1G subunit mRNA and protein throughout the mature rat brain. *Eur J Neurosci* 11:2949-2964.

Cueni L, Canepari M, Adelman JP, Luthi A (**2009**) $Ca^{2+}$ signaling by T-type $Ca^{2+}$ channels in neurons. *Pflugers Arch* 457:1161-1172.

Czeh B, Hajnal A, Seress L (**2005**) NADPH-diaphorase positive neurons of the rat hippocampal formation: regional distribution, total number and colocalization with calcium binding proteins. *Prague Med Rep* 106:261-274.

Danscher G (**1981**) Histochemical demonstration of heavy metals. A revised version of the sulphide silver method suitable for both light and electronmicroscopy. *Histochemistry* 71:1-16.

Danscher G (**1984**) Autometallography. A new technique for light and electron microscopic visualization of metals in biological tissues (gold, silver, metal sulphides and metal selenides). *Histochemistry* 81:331-335.

Danscher G, Jo SM, Varea E, Wang Z, Cole TB, Schroder HD (**2001**) Inhibitory zinc-enriched terminals in mouse spinal cord. *Neuroscience* 105:941-947.

Dawson RMC, Elliott DC, Elliott WH, Jones KM (**1986**) Data for biochemical research. New York: Oxford University Press.

Deng W, Aimone JB, Gage FH (**2010**) New neurons and new memories: how does adult hippocampal neurogenesis affect learning and memory? *Nat Rev Neurosci* 11:339-350.

Destexhe A, Contreras D, Steriade M, Sejnowski TJ, Huguenard JR (**1996**) *In vivo*, *in vitro*, and computational analysis of dendritic calcium currents in thalamic reticular neurons. *J Neurosci* 16:169-185.

Dietrich D, Kirschstein T, Kukley M, Pereverzev A, von der BC, Schneider T, Beck H (**2003**) Functional specialization of presynaptic $Ca_V2.3$ $Ca^{2+}$ channels. *Neuron* 39:483-496.

Doherty JJ, Alagarsamy S, Bough KJ, Conn PJ, Dingledine R, Mott DD (**2004**) Metabotropic glutamate receptors modulate feedback inhibition in a developmentally regulated manner in rat dentate gyrus. *J Physiol* 561:395-401.

Draguhn A, Verdorn TA, Ewert M, Seeburg PH, Sakmann B (**1990**) Functional and molecular distinction between recombinant rat $GABA_A$ receptor subtypes by $Zn^{2+}$. *Neuron* 5:781-788.

Dreixler JC, Leonard JP (**1994**) Subunit-specific enhancement of glutamate receptor responses by zinc. *Brain Res Mol Brain Res* 22:144-150.

Edwards RH (**2007**) The neurotransmitter cycle and quantal size. *Neuron* 55:835-58.

Engel D, Jonas P (**2005**) Presynaptic action potential amplification by voltage-gated Na+ channels in hippocampal mossy fiber boutons. *Neuron* 45:405-417.

Epsztein J, Represa A, Jorquera I, Ben-Ari Y, Crepel V (**2005**) Recurrent mossy fibers establish aberrant kainate receptor-operated synapses on granule cells from epileptic rats. *J Neurosci* 25:8229-8239.

Evstratova A, Toth K (**2011**) Synaptically evoked $Ca^{2+}$ release from intracellular stores is not influenced by vesicular zinc in CA3 hippocampal pyramidal neurones. *J Physiol* 589:5677-5689.

Ewell LA, Jones MV (**2010**) Frequency-tuned distribution of inhibition in the dentate gyrus. *J Neurosci* 30:12597-12607.

Farrant M, Nusser Z (**2005**) Variations on an inhibitory theme: phasic and tonic activation of $GABA_A$ receptors. *Nat Rev Neurosci* 6:215-229.

Fisher JL, Macdonald RL (**1998**) The role of an alpha subtype M2-M3 His in regulating inhibition of GABA$_A$ receptor current by zinc and other divalent cations. *J Neurosci* 18:2944-2953.

Frederickson C (**2003**) Imaging zinc: old and new tools. *Sci STKE* 2003:e18.

Frederickson CJ, Giblin LJ, Krezel A, McAdoo DJ, Mueller RN, Zeng Y, Balaji RV, Masalha R, Thompson RB, Fierke CA, Sarvey JM, de VM, Prough DS, Zornow MH (**2006**) Concentrations of extracellular free zinc (pZn)$_e$ in the central nervous system during simple anesthetization, ischemia and reperfusion. *Exp Neurol* 198:285-293.

Frederickson CJ, Kasarskis EJ, Ringo D, Frederickson RE (**1987**) A quinoline fluorescence method for visualizing and assaying the histochemically reactive zinc (bouton zinc) in the brain. *J Neurosci Methods* 20:91-103.

Frederickson CJ, Koh JY, Bush AI (**2005**) The neurobiology of zinc in health and disease. *Nat Rev Neurosci* 6:449-462.

Frederickson CJ, Suh SW, Silva D, Frederickson CJ, Thompson RB (**2000**) Importance of zinc in the central nervous system: the zinc-containing neuron. *J Nutr* 130:1471S-1483S.

Frerking M, Ohliger-Frerking P (**2002**) AMPA receptors and kainate receptors encode different features of afferent activity. *J Neurosci* 22:7434-7443.

Freund TF, Buzsaki G (**1996**) Interneurons of the hippocampus. *Hippocampus* 6:347-470.

Fricke RA, Prince DA (**1984**) Electrophysiology of dentate gyrus granule cells. J Neurophysiol 51:195-209.

Fukushima T, Shingai R, Ogurusu T, Ichinose M (**2003**) Inhibition of willardiine-induced currents through rat GluR6/KA-2 kainate receptor channels by Zinc and other divalent cations. *Neurosci Lett* 349:107-110.

Gabriel S, Njunting M, Pomper JK, Merschhemke M, Sanabria ER, Eilers A, Kivi A, Zeller M, Meencke HJ, Cavalheiro EA, Heinemann U, Lehmann TN (**2004**) Stimulus and potassium-induced epileptiform activity in the human dentate gyrus from patients with and without hippocampal sclerosis. *J Neurosci* 24:10416-10430.

Geiger JR, Jonas P (**2000**) Dynamic control of presynaptic Ca$^{2+}$ inflow by fast-inactivating K$^+$ channels in hippocampal mossy fiber boutons. *Neuron* 28:927-939.

Geiger JR, Lubke J, Roth A, Frotscher M, Jonas P (**1997**) Submillisecond AMPA receptor-mediated signaling at a principal neuron-interneuron synapse. *Neuron* 18:1009-1023.

Gibbs JW, III, Shumate MD, Coulter DA (**1997**) Differential epilepsy-associated alterations in postsynaptic GABA$_A$ receptor function in dentate granule and CA1 neurons. *J Neurophysiol* 77:1924-1938.

Gielen M, Le GA, Stroebel D, Johnson JW, Neyton J, Paoletti P (**2008**) Structural rearrangements of NR1/NR2A NMDA receptors during allosteric inhibition. *Neuron* 57:80-93.

Gielen M, Siegler RB, Mony L, Johnson JW, Paoletti P (**2009**) Mechanism of differential control of NMDA receptor activity by NR2 subunits. *Nature* 459:703-707.

Gulyas AI, Miles R, Hajos N, Freund TF (**1993**) Precision and variability in postsynaptic target selection of inhibitory cells in the hippocampal CA3 region. *Eur J Neurosci* 5:1729-1751.

Gulyas AI, Sik A, Payne JA, Kaila K, Freund TF (**2001**) The KCl cotransporter, KCC2, is highly expressed in the vicinity of excitatory synapses in the rat hippocampus. *Eur J Neurosci* 13:2205-2217.

Gutierrez R (**2000**) Seizures induce simultaneous GABAergic and glutamatergic transmission in the dentate gyrus-CA3 system. *J Neurophysiol* 84:3088-3090.

Halasy K, Somogyi P (**1993**) Subdivisions in the multiple GABAergic innervation of granule cells in the dentate gyrus of the rat hippocampus. *Eur J Neurosci* 5:411-429.

Han ZS, Buhl EH, Lorinczi Z, Somogyi P (**1993**) A high degree of spatial selectivity in the axonal and dendritic domains of physiologically identified local-circuit neurons in the dentate gyrus of the rat hippocampus. *Eur J Neurosci* 5:395-410.

Harrison NL, Radke HK, Tamkun MM, Lovinger DM (**1993**) Modulation of gating of cloned rat and human $K^+$ channels by micromolar $Zn^{2+}$. *Mol Pharmacol* 43:482-486.

Haug FM (**1967**) Electron microscopical localization of the zinc in hippocampal mossy fibre synapses by a modified sulfide silver procedure. *Histochemie* 8:355-368.

Hell JW, Westenbroek RE, Warner C, Ahlijanian MK, Prystay W, Gilbert MM, Snutch TP, Catterall WA (**1993**) Identification and differential subcellular localization of the neuronal class C and class D L-type calcium channel $\alpha$1 subunits. *J Cell Biol* 123:949-962.

Henze DA, Wittner L, Buzsaki G (**2002**) Single granule cells reliably discharge targets in the hippocampal CA3 network in vivo. *Nat Neurosci* 5:790-795.

Hershfinkel M, Kandler K, Knoch ME, gan-Rabin M, Aras MA, bramovitch-Dahan C, Sekler I, Aizenman E (**2009**) Intracellular zinc inhibits KCC2 transporter activity. *Nat Neurosci* 6:725-727.

Hershfinkel M, Moran A, Grossman N, Sekler I (**2001**) A zinc-sensing receptor triggers the release of intracellular $Ca^{2+}$ and regulates ion transport. *Proc Natl Acad Sci U S A* 98:11749-11754.

Hesse GW (**1979**) Chronic zinc deficiency alters neuronal function of hippocampal mossy fibers. *Science* 205:1005-1007.

Hesse GW, Hesse KA, Catalanotto FA (**1979**) Behavioral characteristics of rats experiencing chronic zinc deficiency. *Physiol Behav* 22:211-215.

Hirzel K, Muller U, Latal AT, Hulsmann S, Grudzinska J, Seeliger MW, Betz H, Laube B (**2006**) Hyperekplexia phenotype of glycine receptor $\alpha$1 subunit mutant mice identifies $Zn^{2+}$ as an essential endogenous modulator of glycinergic neurotransmission. *Neuron* 52:679-690.

Hosie AM, Dunne EL, Harvey RJ, Smart TG (**2003**) Zinc-mediated inhibition of $GABA_A$ receptors: discrete binding sites underlie subtype specificity. *Nat Neurosci* 6:362-369.

Hou S, Vigeland LE, Zhang G, Xu R, Li M, Heinemann SH, Hoshi T (**2010**) $Zn^{2+}$ activates large conductance $Ca^{2+}$-activated $K^+$ channel via an intracellular domain. *J Biol Chem* 285:6434-6442.

Howell GA, Welch MG, Frederickson CJ (**1984**) Stimulation-induced uptake and release of zinc in hippocampal slices. *Nature* 308:736-738.

Hu H, Martina M, Jonas P (**2010**) Dendritic mechanisms underlying rapid synaptic activation of fast-spiking hippocampal interneurons. *Science* 327:52-58.

Huang L, Keyser BM, Tagmose TM, Hansen JB, Taylor JT, Zhuang H, Zhang M, Ragsdale DS, Li M (**2004**) NNC 55-0396 [(1S,2S)-2-(2-(N-[(3-benzimidazol-2-yl)propyl]-N-methylamino)ethyl)-6-fluoro-1,2, 3,4-tetrahydro-1-isopropyl-2-naphtyl cyclopropanecarboxylate dihydrochloride]: a new selective inhibitor of T-type calcium channels. *J Pharmacol Exp Ther* 309:193-199.

Huang YZ, Pan E, Xiong ZQ, McNamara JO (**2008**) Zinc-mediated transactivation of TrkB potentiates the hippocampal mossy fiber-CA3 pyramid synapse. *Neuron* 57:546-558.

Izumi Y, Auberson YP, Zorumski CF (**2006**) Zinc modulates bidirectional hippocampal plasticity by effects on NMDA receptors. *J Neurosci* 26:7181-7188.

Jonas P, Bischofberger J, Fricker D, Miles R (**2004**) Interneuron Diversity series: Fast in, fast out-temporal and spatial signal processing in hippocampal interneurons. *Trends Neurosci* 27:30-40.

Jung MW, McNaughton BL (**1993**) Spatial selectivity of unit activity in the hippocampal granular layer. *Hippocampus* 3:165-182.

Kantheti P, Qiao X, Diaz ME, Peden AA, Meyer GE, Carskadon SL, Kapfhamer D, Sufalko D, Robinson MS, Noebels JL, Burmeister M (**1998**) Mutation in AP-3 delta in the mocha mouse links endosomal transport to storage deficiency in platelets, melanosomes, and synaptic vesicles. *Neuron* 21:111-122.

Kapur A, Yeckel MF, Gray R, Johnston D (**1998**) L-Type calcium channels are required for one form of hippocampal mossy fiber LTP. *J Neurophysiol* 79:2181-2190.

Kay AR (**2003**) Evidence for chelatable zinc in the extracellular space of the hippocampus, but little evidence for synaptic release of Zn. *J Neurosci* 23:6847-6855.

Kay AR, Toth K (**2006**) Influence of location of a fluorescent zinc probe in brain slices on its response to synaptic activation. *J Neurophysiol* 95:1949-1956.

Kerr AM, Capogna M (**2007**) Unitary IPSPs enhance hilar mossy cell gain in the rat hippocampus. *J Physiol* 578:451-470.

Knaus HG, Schwarzer C, Koch RO, Eberhart A, Kaczorowski GJ, Glossmann H, Wunder F, Pongs O, Garcia ML, Sperk G (**1996**) Distribution of high-conductance $Ca^{2+}$-activated $K^+$ channels in rat brain: targeting to axons and nerve terminals. *J Neurosci* 16:955-963.

Kneisler TB, Dingledine R (**1995**) Spontaneous and synaptic input from granule cells and the perforant path to dentate basket cells in the rat hippocampus. *Hippocampus* 5:151-164.

Kodirov SA, Takizawa S, Joseph J, Kandel ER, Shumyatsky GP, Bolshakov VY (**2006**) Synaptically released zinc gates long-term potentiation in fear conditioning pathways. *Proc Natl Acad Sci U S A* 103:15218-15223.

Koh DS, Geiger JR, Jonas P, Sakmann B (**1995**) $Ca^{2+}$-permeable AMPA and NMDA receptor channels in basket cells of rat hippocampal dentate gyrus. *J Physiol* 485 (Pt 2):383-402.

Koh JY, Suh SW, Gwag BJ, He YY, Hsu CY, Choi DW (**1996**) The role of zinc in selective neuronal death after transient global cerebral ischemia. *Science* 272:1013-1016.

Komatsu K, Kikuchi K, Kojima H, Urano Y, Nagano T (**2005**) Selective zinc sensor molecules with various affinities for $Zn^{2+}$, revealing dynamics and regional distribution of synaptically released $Zn^{2+}$ in hippocampal slices. *J Am Chem Soc* 127:10197-10204.

Kraushaar U, Jonas P (**2000**) Efficacy and stability of quantal GABA release at a hippocampal interneuron-principal neuron synapse. *J Neurosci* 20:5594-5607.

Krishek BJ, Moss SJ, Smart TG (**1998**) Interaction of $H^+$ and $Zn^{2+}$ on recombinant and native rat neuronal $GABA_A$ receptors. *J Physiol 507* ( Pt 3):639-652.

Krueppel R, Remy S, Beck H (**2011**) Dendritic integration in hippocampal dentate granule cells. *Neuron* 71:512-528.

Kullmann DM (**2001**) Presynaptic kainate receptors in the hippocampus: slowly emerging from obscurity. *Neuron* 32:561-564.

Kyrozis A, Reichling DB (**1995**) Perforated-patch recording with gramicidin avoids artifactual changes in intracellular chloride concentration. *J Neurosci Methods* 57:27-35.

Larimer P, Strowbridge BW (**2010**) Representing information in cell assemblies: persistent activity mediated by semilunar granule cells. *Nat Neurosci* 13:213-222.

Lauri SE, Bortolotto ZA, Nistico R, Bleakman D, Ornstein PL, Lodge D, Isaac JT, Collingridge GL (**2003**) A role for Ca2+ stores in kainate receptor-dependent synaptic facilitation and LTP at mossy fiber synapses in the hippocampus. *Neuron* 39:327-341.

Lavoie N, Peralta MR, III, Chiasson M, Lafortune K, Pellegrini L, Seress L, Toth K (**2007**) Extracellular chelation of zinc does not affect hippocampal excitability and seizure-induced cell death in rats. *J Physiol* 578:275-289.

Lawrence JJ, Grinspan ZM, McBain CJ (**2004**) Quantal transmission at mossy fibre targets in the CA3 region of the rat hippocampus. *J Physiol* 554:175-193.

Lee JH, Gomora JC, Cribbs LL, Perez-Reyes E (**1999**) Nickel block of three cloned T-type calcium channels: low concentrations selectively block $\alpha$1H. *Biophys J* 77:3034-3042.

Lei S, McBain CJ (**2002**) Distinct NMDA receptors provide differential modes of transmission at mossy fiber-interneuron synapses. *Neuron* 33:921-933.

Li L, Bischofberger J, Jonas P (**2007**) Differential gating and recruitment of P/Q-, N-, and R-type $Ca^{2+}$ channels in hippocampal mossy fiber boutons. *J Neurosci* 27:13420-13429.

Li XG, Somogyi P, Ylinen A, Buzsaki G (**1994**) The hippocampal CA3 network: an in vivo intracellular labeling study. *J Comp Neurol* 339:181-208.

Li Y, Hough CJ, Suh SW, Sarvey JM, Frederickson CJ (**2001**) Rapid translocation of $Zn^{2+}$ from presynaptic terminals into postsynaptic hippocampal neurons after physiological stimulation. *J Neurophysiol* 86:2597-2604.

Lien CC, Jonas P (**2003**) $K_v3$ potassium conductance is necessary and kinetically optimized for high-frequency action potential generation in hippocampal interneurons. *J Neurosci* 23:2058-2068.

Liu L, Wong TP, Pozza MF, Lingenhoehl K, Wang Y, Sheng M, Auberson YP, Wang YT (**2004**) Role of NMDA receptor subtypes in governing the direction of hippocampal synaptic plasticity. *Science* 304:1021-1024.

Long Y, Hardwick AL, Frederickson CJ (**1995**) Zinc-containing innervation of the subicular region in the rat. *Neurochem Int* 27:95-103.

Lopantsev V, Wenzel HJ, Cole TB, Palmiter RD, Schwartzkroin PA (**2003**) Lack of vesicular zinc in mossy fibers does not affect synaptic excitability of CA3 pyramidal cells in zinc transporter 3 knockout mice. *Neuroscience* 116:237-248.

Low CM, Zheng F, Lyuboslavsky P, Traynelis SF (**2000**) Molecular determinants of coordinated proton and zinc inhibition of N-methyl-D-aspartate NR1/NR2A receptors. *Proc Natl Acad Sci U S A* 97:11062-11067.

Lu YM, Taverna FA, Tu R, Ackerley CA, Wang YT, Roder J (**2000**) Endogenous $Zn^{2+}$ is required for the induction of long-term potentiation at rat hippocampal mossy fiber-CA3 synapses. *Synapse* 38:187-197.

Lubke J, Frotscher M, Spruston N (**1998**) Specialized electrophysiological properties of anatomically identified neurons in the hilar region of the rat fascia dentata. *J Neurophysiol* 79:1518-1534.

Maccaferri G, Tóth K, McBain CJ (**1998**) Target-specific expression of presynaptic mossy fiber plasticity. *Science* 279:1368-70.

Magistretti J, Castelli L, Taglietti V, Tanzi F (**2003**) Dual effect of $Zn^{2+}$ on multiple types of voltage-dependent $Ca^{2+}$ currents in rat palaeocortical neurons. *Neuroscience* 117:249-264.

Manzoni OJ, Castillo PE, Nicoll RA (**1995**) Pharmacology of metabotropic glutamate receptors at the mossy fiber synapses of the guinea pig hippocampus. *Neuropharmacology* 34:965-971.

Markwardt SJ, Wadiche JI, Overstreet-Wadiche LS (**2009**) Input-specific GABAergic signaling to newborn neurons in adult dentate gyrus. *J Neurosci* 29:15063-72.

Markwardt SJ, Dieni CV, Wadiche JI, Overstreet-Widiche L (**2012**) Ivy/neurogliaform interneurons coordinate activity in the neurogenic niche, *Nat Neurosci* 14:1407-9.

Martina M, Schultz JH, Ehmke H, Monyer H, Jonas P (**1998**) Functional and molecular differences between voltage-gated $K^+$ channels of fast-spiking interneurons and pyramidal neurons of rat hippocampus. *J Neurosci* 18:8111-8125.

Martina M, Vida I, Jonas P (**2000**) Distal initiation and active propagation of action potentials in interneuron dendrites. *Science* 287:295-300.

Mathie A, Sutton GL, Clarke CE, Veale EL (**2006**) Zinc and copper: pharmacological probes and endogenous modulators of neuronal excitability. *Pharmacol Ther* 111:567-583.

Mayer ML, Vyklicky L, Jr., Westbrook GL (**1989**) Modulation of excitatory amino acid receptors by group IIB metal cations in cultured mouse hippocampal neurones. *J Physiol* 415:329-350.

McKay BE, McRory JE, Molineux ML, Hamid J, Snutch TP, Zamponi GW, Turner RW (**2006**) $Ca_v3$ T-type calcium channel isoforms differentially distribute to somatic and dendritic compartments in rat central neurons. *Eur J Neurosci* 24:2581-2594.

Mello LE, Cavalheiro EA, Tan AM, Kupfer WR, Pretorius JK, Babb TL, Finch DM (**1993**) Circuit mechanisms of seizures in the pilocarpine model of chronic epilepsy: cell loss and mossy fiber sprouting. *Epilepsia* 34:985-995.

Mellor J, Nicoll RA, Schmitz D (**2002**) Mediation of hippocampal mossy fiber long-term potentiation by presynaptic Ih channels. *Science* 295:143-147.

Melzer S, Michael M, Caputi A, Eliava M, Fuchs EC, Whittington MA, Monyer H (**2012**) Long-range-projecting GABAergic neurons modulate inhibition in the hippcampus and entorhinal cortex. *Science* 335:1506-10.

Miller PS, Beato M, Harvey RJ, Smart TG (**2005**) Molecular determinants of glycine receptor $\alpha\beta$ subunit sensitivities to $Zn^{2+}$-mediated inhibition. *J Physiol* 566:657-670.

Misgeld U, Deisz RA, Dodt HU, Lux HD (**1986**) The role of chloride transport in postsynaptic inhibition of hippocampal neurons. *Science* 232:1413-1415.

Mitchell SJ, Silver RA (**2003**) Shunting inhibition modulates neuronal gain during synaptic excitation. *Neuron* 38:433-445.

Mody I, Otis TS, Staley KJ, Kohr G (**1992**) The balance between excitation and inhibition in dentate granule cells and its role in epilepsy. *Epilepsy Res Suppl* 9:331-339.

Molnar P, Nadler JV (**2001a**) Lack of effect of mossy fiber-released zinc on granule cell $GABA_A$ receptors in the pilocarpine model of epilepsy. *J Neurophysiol* 85:1932-1940.

Molnar P, Nadler JV (**2001b**) Synaptically-released zinc inhibits N-methyl-D-aspartate receptor activation at recurrent mossy fiber synapses. *Brain Res* 910:205-207.

Monyer H, Burnashev N, Laurie DJ, Sakmann B, Seeburg PH (**1994**) Developmental and regional expression in the rat brain and functional properties of four NMDA receptors. *Neuron* 12:529-540.

Moore KA, Nicoll RA, Schmitz D (**2003**) Adenosine gates synaptic plasticity at hippocampal mossy fiber synapses. *Proc Natl Acad Sci U S A* 100:14397-14402.

Moosmang S, Biel M, Hofmann F, Ludwig A (**1999**) Differential distribution of four hyperpolarization-activated cation channels in mouse brain. *Biol Chem* 380:975-980.

Moriyoshi K, Masu M, Ishii T, Shigemoto R, Mizuno N, Nakanishi S (**1991**) Molecular cloning and characterization of the rat NMDA receptor. *Nature* 354:31-37.

Mortensen M, Smart TG (**2006**) Extrasynaptic $\alpha\beta$ subunit GABA$_A$ receptors on rat hippocampal pyramidal neurons. *J Physiol* 577:841-856.

Mott DD, Benveniste M, Dingledine RJ (**2008**) pH-dependent inhibition of kainate receptors by zinc. *J Neurosci* 28:1659-1671.

Muller TH, Misgeld U, Swandulla D (**1992**) Ionic currents in cultured rat hypothalamic neurones. *J Physiol* 450:341-362.

Nelson MT, Woo J, Kang HW, Vitko I, Barrett PQ, Perez-Reyes E, Lee JH, Shin HS, Todorovic SM (**2007**) Reducing agents sensitize C-type nociceptors by relieving high-affinity zinc inhibition of T-type calcium channels. *J Neurosci* 27:8250-8260.

Noh JH, Chung JM (**2003**) Zinc reduces low-threshold $Ca^{2+}$ currents of rat thalamic relay neurons. *Neurosci Res* 47:261-265.

Nozaki C, Vergnano AM, Filliol D, Ouagazzal AM, Le GA, Carvalho S, Reiss D, Gaveriaux-Ruff C, Neyton J, Paoletti P, Kieffer BL (**2011**) Zinc alleviates pain through high-affinity binding to the NMDA receptor NR2A subunit. *Nat Neurosci* 14:1017-1022.

Nusser Z, Hajos N, Somogyi P, Mody I (**1998**) Increased number of synaptic GABA$_A$ receptors underlies potentiation at hippocampal inhibitory synapses. *Nature* 395:172-177.

Nusser Z, Mody I (**2002**) Selective modulation of tonic and phasic inhibitions in dentate gyrus granule cells. *J Neurophysiol* 87:2624-2628.

Okazaki MM, Evenson DA, Nadler JV (**1995**) Hippocampal mossy fiber sprouting and synapse formation after status epilepticus in rats: visualization after retrograde transport of biocytin. *J Comp Neurol* 352:515-534.

Palmiter RD, Cole TB, Quaife CJ, Findley SD (**1996**) ZnT-3, a putative transporter of zinc into synaptic vesicles. *Proc Natl Acad Sci U S A* 93:14934-14939.

Palmiter RD, Findley SD (**1995**) Cloning and functional characterization of a mammalian zinc transporter that confers resistance to zinc. *EMBO J* 14:639-649.

Pan E, Zhang XA, Huang Z, Krezel A, Zhao M, Tinberg CE, Lippard SJ, McNamara JO (**2011**) Vesicular zinc promotes presynaptic and inhibits postsynaptic long-term potentiation of mossy fiber-CA3 synapse. *Neuron* 71:1116-1126.

Paoletti P, Ascher P, Neyton J (**1997**) High-affinity zinc inhibition of NMDA NR1-NR2A receptors. *J Neurosci* 17:5711-5725.

Paoletti P, Vergnano AM, Barbour B, Casado M (**2009**) Zinc at glutamatergic synapses. *Neuroscience* 158:126-136.

Pavlov I, Savtchenko LP, Kullmann DM, Semyanov A, Walker MC (**2009**) Outwardly rectifying tonically active $GABA_A$ receptors in pyramidal cells modulate neuronal offset, not gain. *J Neurosci* 29:15341-50.

Pavlov I, Huusko N, Drexel M, Kirchmair E, Sperk G, Pitkanen A, Walker MC (**2011a**) Progressive loss of phasic, but not tonic, $GABA_A$ receptor-mediated inhibition in dentate granule cells in a model of post-traumatic epilepsy in rats. *Neuroscience* 194:208-219.

Pavlov I, Scimemi A, Savtchenko L, Kullmann DM, Walker MC (**2011b**) $I_h$-mediated depolarization enhances the temporal precision of neuronal integration. *Nat Commun* 2:199.

Penttonen M, Kamondi A, Sik A, Acsady L, Buzsaki G (**1997**) Feed-forward and feed-back activation of the dentate gyrus in vivo during dentate spikes and sharp wave bursts. *Hippocampus* 7:437-450.

Perez-Clausell J, Danscher G (**1985**) Intravesicular localization of zinc in rat telencephalic boutons. A histochemical study. *Brain Res* 337:91-98.

Perkins KL, Wong RK (**1995**) Intracellular QX-314 blocks the hyperpolarization-activated inward current $I_q$ in hippocampal CA1 pyramidal cells. *J Neurophysiol* 73:911-915.

Peters S, Koh J, Choi DW (**1987**) Zinc selectively blocks the action of N-methyl-D-aspartate on cortical neurons. *Science* 236:589-593.

Pouille F, Scanziani M (**2004**) Routing of spike series by dynamic circuits in the hippocampus. *Nature* 429:717-723.

Prasad AS (**2003**) Zinc deficiency. *BMJ* 326:409-410.

Qian J, Noebels JL (**2005**) Visualization of transmitter release with zinc fluorescence detection at the mouse hippocampal mossy fibre synapse. *J Physiol* 566:747-758.

Qian J, Noebels JL (**2006**) Exocytosis of vesicular zinc reveals persistent depression of neurotransmitter release during metabotropic glutamate receptor

long-term depression at the hippocampal CA3-CA1 synapse. *J Neurosci* 26:6089-6095.

Quinta-Ferreira ME, Matias CM (**2004**) Hippocampal mossy fiber calcium transients are maintained during long-term potentiation and are inhibited by endogenous zinc. *Brain Res* 1004:52-60.

Rachline J, Perin-Dureau F, Le GA, Neyton J, Paoletti P (**2005**) The micromolar zinc-binding domain on the NMDA receptor subunit NR2B. *J Neurosci* 25:308-317.

Ramón y Cajal (**1911**) Histologie du système nerveux de l'homme et des vertébrés. Paris.

Regehr WG, Delaney KR, Tank DW (**1994**) The role of presynaptic calcium in short-term enhancement at the hippocampal mossy fiber synapse. *J Neurosci* 14:523-37.

Ribak CE, Peterson GM (**1991**) Intragranular mossy fibers in rats and gerbils form synapses with the somata and proximal dendrites of basket cells in the dentate gyrus. *Hippocampus* 1:355-364.

Ribak CE, Seress L (**1983**) Five types of basket cell in the hippocampal dentate gyrus: a combined Golgi and electron microscopic study. *J Neurocytol* 12:577-597.

Ribak CE, Vaughn JE, Saito K (**1978**) Immunocytochemical localization of glutamic acid decarboxylase in neuronal somata following colchicine inhibition of axonal transport. *Brain Res* 140:315-332.

Ruiz A, Campanac E, Scott RS, Rusakov DA, Kullmann DM (**2010**) Presynaptic GABA$_A$ receptors enhance transmission and LTP induction at hippocampal mossy fiber synapses. *Nat Neurosci* 13:431-438.

Ruiz A, Walker MC, Fabian-Fine R, Kullmann DM (**2004**) Endogenous zinc inhibits GABA$_A$ receptors in a hippocampal pathway. *J Neurophysiol* 91:1091-1096.

Sabatini BL, Regehr WG (**1997**) Control of neurotransmitter release by presynaptic waveform at the granule cell to Purkinje cell synapse. *J Neurosci* 17:3425-3435.

Safiulina VF, Fattorini G, Conti F, Cherubini E (**2006**) GABAergic signaling at mossy fiber synapses in neonatal rat hippocampus. *J Neurosci* 26:597-608.

Salin PA, Scanziani M, Malenka RC, Nicoll RA (**1996**) Distinct short-term plasticity at two excitatory synapses in the hippocampus. *Proc Natl Acad Sci U S A* 93:13304-9.

Sambandan S, Sauer JF, Vida I, Bartos M (**2010**) Associative plasticity at excitatory synapses facilitates recruitment of fast-spiking interneurons in the dentate gyrus. *J Neurosci* 30:11826-11837.

Sanchez-Alonso JL, Halliwell JV, Colino A (**2008**) ZD 7288 inhibits T-type calcium current in rat hippocampal pyramidal cells. *Neurosci Lett* 439:275-280.

Sandler R, Smith AD (**1991**) Coexistence of GABA and glutamate in mossy fiber terminals of the primate hippocampus: an ultrastructural study. *J Comp Neurol* 303:177-192.

Santoro B, Chen S, Luthi A, Pavlidis P, Shumyatsky GP, Tibbs GR, Siegelbaum SA (**2000**) Molecular and functional heterogeneity of hyperpolarization-activated pacemaker channels in the mouse CNS. *J Neurosci* 20:5264-5275.

Saxena NC, Macdonald RL (**1996**) Properties of putative cerebellar gamma-aminobutyric acid A receptor isoforms. *Mol Pharmacol* 49:567-579.

Scharfman HE (**2007**) The CA3 "backprojection" to the dentate gyrus. *Prog Brain Res* 163:627-637.

Schmitz D, Frerking M, Nicoll RA (**2000**) Synaptic activation of presynaptic kainate receptors on hippocampal mossy fiber synapses. *Neuron* 27:327-338.

Schmitz D, Mellor J, Nicoll RA (**2001**) Presynaptic kainate receptor mediation of frequency facilitation at hippocampal mossy fiber synapses. *Science* 291:1972-1976.

Schmitz D, Mellor J, Breustedt J, Nicoll RA (**2003**) Presynaptic kainate receptors impart an associative property to hippocampal mossy fiber long-term potentiation. *Nat Neurosci* 6:1058-1063.

Schwarzer C, Sperk G (**1995**) Hippocampal granule cells express glutamic acid decarboxylase-67 after limbic seizures in the rat. *Neuroscience* 69:705-709.

Scimemi A, Schorge S, Kullmann DM, Walker MC (**2006**) Epileptogenesis is associated with enhanced glutamatergic transmission in the perforant path. *J Neurophysiol* 95:1213-1220.

Scott R, Rusakov DA (**2006**) Main determinants of presynaptic Ca2+ dynamics at individual mossy fiber-CA3 pyramidal cell synapses. *J Neurosci* 26:7071-81.

Semyanov A, Walker MC, Kullmann DM, Silver RA (**2004**) Tonically active GABA$_A$ receptors: modulating gain and maintaining the tone. *Trends Neurosci* 27:262-269.

Sensi SL, Paoletti P, Bush AI, Sekler I (**2009**) Zinc in the physiology and pathology of the CNS. *Nat Rev Neurosci* 10:780-791.

Seress L, Abraham H, Paleszter M, Gallyas F (**2001**) Granule cells are the main source of excitatory input to a subpopulation of GABAergic hippocampal neurons

as revealed by electron microscopic double staining for zinc histochemistry and parvalbumin immunocytochemistry. *Exp Brain Res* 136:456-462.

Seress L, Pokorny J (**1981**) Structure of the granular layer of the rat dentate gyrus. A light microscopic and Golgi study. *J Anat* 133:181-195.

Sik A, Penttonen M, Buzsaki G (**1997**) Interneurons in the hippocampal dentate gyrus: an *in vivo* intracellular study. *Eur J Neurosci* 9:573-588.

Sik A, Ylinen A, Penttonen M, Buzsaki G (**1994**) Inhibitory CA1-CA3-hilar region feedback in the hippocampus. *Science* 265:1722-1724.

Sim JA, Cherubini E (**1990**) Submicromolar concentrations of zinc irreversibly reduce a calcium-dependent potassium current in rat hippocampal neurons in vitro. *Neuroscience* 36:623-629.

Sindreu C, Palmiter RD, Storm DR (**2011**) Zinc transporter ZnT-3 regulates presynaptic Erk1/2 signaling and hippocampus-dependent memory. *Proc Natl Acad Sci U S A* 108:3366-3370.

Sindreu CB, Varoqui H, Erickson JD, Perez-Clausell J (**2003**) Boutons containing vesicular zinc define a subpopulation of synapses with low AMPAR content in rat hippocampus. *Cereb Cortex* 13:823-829.

Slomianka L (**1992**) Neurons of origin of zinc-containing pathways and the distribution of zinc-containing boutons in the hippocampal region of the rat. *Neuroscience* 48:325-352.

Slomianka L, Danscher G, Frederickson CJ (**1990**) Labeling of the neurons of origin of zinc-containing pathways by intraperitoneal injections of sodium selenite. *Neuroscience* 38:843-854.

Smart TG, Constanti A (**1990**) Differential effect of zinc on the vertebrate $GABA_A$-receptor complex. *Br J Pharmacol* 99:643-654.

Smart TG, Hosie AM, Miller PS (**2004**) $Zn^{2+}$ ions: modulators of excitatory and inhibitory synaptic activity. *Neuroscientist* 10:432-442.

Soriano E, Frotscher M (**1994**) Mossy cells of the rat fascia dentata are glutamate-immunoreactive. *Hippocampus* 4:65-69.

Stell BM, Brickley SG, Tang CY, Farrant M, Mody I (**2003**) Neuroactive steroids reduce neuronal excitability by selectively enhancing tonic inhibition mediated by δ subunit-containing $GABA_A$ receptors. *Proc Natl Acad Sci U S A* 100:14439-14444.

Sun HS, Hui K, Lee DW, Feng ZP (**2007**) $Zn^{2+}$ sensitivity of high- and low-voltage activated calcium channels. *Biophys J* 93:1175-1183.

Szabadics J, Soltesz I (**2009**) Functional specificity of mossy fiber innervation of GABAergic cells in the hippocampus. *J Neurosci* 29:4239-4251.

Takahashi K, Akaike N (**1991**) Calcium antagonist effects on low-threshold (T-type) calcium current in rat isolated hippocampal CA1 pyramidal neurons. *J Pharmacol Exp Ther* 256:169-175.

Talley EM, Cribbs LL, Lee JH, Daud A, Perez-Reyes E, Bayliss DA (**1999**) Differential distribution of three members of a gene family encoding low voltage-activated (T-type) calcium channels. *J Neurosci* 19:1895-1911.

Timm F (**1958**) [Histochemistry of the region of Ammon's horn]. *Z Zellforsch Mikrosk Anat* 48:548-555.

Traboulsie A, Chemin J, Chevalier M, Quignard JF, Nargeot J, Lory P (**2007**) Subunit-specific modulation of T-type calcium channels by zinc. *J Physiol* 578:159-171.

Uchigashima M, Fukaya M, Watanabe M, Kamiya H (**2007**) Evidence against GABA release from glutamatergic mossy fiber terminals in the developing hippocampus. *J Neurosci* 27:8088-100.

Ueno S, Tsukamoto M, Hirano T, Kikuchi K, Yamada MK, Nishiyama N, Nagano T, Matsuki N, Ikegaya Y (**2002**) Mossy fiber $Zn^{2+}$ spillover modulates heterosynaptic N-methyl-D-aspartate receptor activity in hippocampal CA3 circuits. *J Cell Biol* 158:215-220.

Vandenberg RJ, Mitrovic AD, Johnston GA (**1998**) Molecular basis for differential inhibition of glutamate transporter subtypes by zinc ions. *Mol Pharmacol* 54:189-196.

Vinet J, Sik A (**2006**) Expression pattern of voltage-dependent calcium channel subunits in hippocampal inhibitory neurons in mice. *Neuroscience* 143:189-212.

Vogt K, Mellor J, Tong G, Nicoll R (**2000**) The actions of synaptically released zinc at hippocampal mossy fiber synapses. *Neuron* 26:187-196.

Walker MC, Ruiz A, Kullmann DM (**2001**) Monosynaptic GABAergic signaling from dentate to CA3 with a pharmacological and physiological profile typical of mossy fiber synapses. *Neuron* 29:703-715.

Walker MC, Ruiz A, Kullmann DM (**2002**) Do mossy fibers release GABA? *Epilepsia* 43 Suppl 5:196-202.

Weisskopf MG, Nicoll RA (**1995**) Presynaptic changes during mossy fibre LTP revealed by NMDA receptor-mediated synaptic responses. *Nature* 376:256-259.

Wenzel HJ, Cole TB, Born DE, Schwartzkroin PA, Palmiter RD (**1997**) Ultrastructural localization of zinc transporter-3 (ZnT-3) to synaptic vesicle membranes within mossy fiber boutons in the hippocampus of mouse and monkey. *Proc Natl Acad Sci U S A* 94:12676-12681.

Westbrook GL, Mayer ML (**1987**) Micromolar concentrations of $Zn^{2+}$ antagonize NMDA and GABA responses of hippocampal neurons. *Nature* 328:640-643.

White JA, Alonso A, Kay AR (**1993**) A heart-like $Na^+$ current in the medial entorhinal cortex. *Neuron* 11:1037-1047.

Wiebe SP, Staubli UV (**1999**) Dynamic filtering of recognition memory codes in the hippocampus. *J Neurosci* 19:10562-10574.

Williams K (**1996**) Separating dual effects of zinc at recombinant N-methyl-D-aspartate receptors. *Neurosci Lett* 215:9-12.

Williams PA, Larimer P, Gao Y, Strowbridge BW (**2007**) Semilunar granule cells: glutamatergic neurons in the rat dentate gyrus with axon collaterals in the inner molecular layer. *J Neurosci* 27:13756-13761.

Williamson A, Spencer SS, Spencer DD (**1995**) Depth electrode studies and intracellular dentate granule cell recordings in temporal lobe epilepsy. *Ann Neurol* 38:778-787.

Xie X, Smart TG (**1994**) Modulation of long-term potentiation in rat hippocampal pyramidal neurons by zinc. *Pflugers Arch* 427:481-486.

Zhang W, Buckmaster PS (**2009**) Dysfunction of the dentate basket cell circuit in a rat model of temporal lobe epilepsy. *J Neurosci* 29:7846-7856.

Zhang W, Huguenard JR, Buckmaster PS (**2012**) Increased excitatory synaptic input to granule cells from hilar and CA3 regions in a rat model of temporal lobe epilepsy. *J Neurosci* 32:1183-1196.

# Publications, presentations and awards

# PUBLICATIONS AND PRESENTATIONS

**Grauert, A.**, Engel, D., Ruiz, A. Endogenous zinc depresses feedback GABAergic transmission and broadens the time-window for integration of excitatory synaptic inputs. In preparation for submission to *J Neurosci*

**Grauert, A.,** Engel, D., Ruiz, A. (**2011**) Mossy fiber zinc modulates di-synaptic GABAergic transmission and tunes the integration window of excitatory synaptic input. UCL Neuroscience Symposium 2011, Institute of Education, London, July 1st

**Grauert, A.**, Ruiz, A. (**2010**) Endogenous zinc modulates feedback inhibition in dentate granule cells. 2nd ZINC-UK Meeting, UCL Institute of Ophthalmology, London, October 15th

**Grauert, A.,** Engel, D., Ruiz, A. (**2010**) Endogenous zinc modulates dentate gyrus feed-back inhibition. 7th FENS Forum of European Neuroscience, RAI Convention Centre, Amsterdam, July 3rd – 7th

**Grauert, A.,** Ruiz, A. (**2009**) Endogenous Zinc modulates GABAergic inhibition at a cortical pathway. International Society for Zinc Biology Meeting, Mishkenot Sha'ananim international cultural center, Jerusalem, December 1st-6th

# AWARDS

Best poster presentation at the UCL School of Pharmacy PhD Research Day, London, September 2010.

Best poster presentation at the Neuroscience Retreat, Department of Pharmacology, UCL School of Pharmacy in Cambridge, July 2010.